# Atmospheric Impacts of a Close Cometary Encounter

**Natasha Marie Aylett**

Submitted in accordance with the requirements for the degree of

Doctor of Philosophy

The University of Leeds
School of Chemistry

May 2019

The candidate confirms that the work submitted is his/her own, except where work which has formed part of jointly-authored publications has been included. The contribution of the candidate and the other authors to this work has been explicitly indicated below. The candidate confirms that appropriate credit has been given within the thesis where reference has been made to the work of others.

This copy has been supplied on the understanding that it is copyright material and that no quotation from the thesis may be published without proper acknowledgement.

The right of Natasha M Aylett to be identified as Author of this work has been asserted by her in accordance with the Copyright, Designs and Patents Act 1988.

# Acknowledgements

# Contributions

My own contributions and those of other researchers, fully and explicitly indicated in the thesis, have been:

In the optical properties of iron oxide meteoric smoke analogues (Chapters 2 and 3), including the associated publications:

*Aylett, T., Brooke, J. S. A., James, A. D., Nachbar, M., Duft, D., Leisner, T., Plane, J. M. C., Optical properties of meteoric smoke analogues, Atmos. Chem. Phys. Discuss., 2019 https://doi.org/10.5194/acp-2019-240*

*Nachbar, M., Wilms, H., Duft, D., Aylett, T., Kitajima, K., Majima, T., Plane, J. M. C., Rapp, M., and Leisner, T.: The impact of solar radiation on polar mesospheric ice particle formation, Atmos. Chem. Phys., 19, 4311-4322, 2019 https://doi.org/10.5194/acp-19-4311-2019*

*PAFS experimental system:*

- Modification of the PAFS experimental apparatus to include an optical-bypass system.
- Carried out laboratory experiments and performed data analysis.
- Conducted photochemical modelling to derive refractive indices.
- Characterisation of the MSP analogues with TEM, EELS and EDX spectroscopy, assisted by Dr Andy Brown. Data for the iron oxide standards was recorded by Dr Andy Brown.

*TRAPS experimental system:*

- The TRAPS system is located at the Karlsruhe Institute of Technology (KIT). It was developed and used mainly by Dr Mario Nachbar and Dr Denis Duft at KIT.
- Addition of the laser setup at 405 nm and 660 nm to the TRAPS apparatus, including alignment and calibration.
- Carried out laboratory experiments at 405 nm, and 660 nm, with Dr Mario Nachbar. Laboratory experiments at 488 nm were carried out by Dr Mario Nachbar and Kensei Kitajima.
- Analysis of experimental data at 405 nm and 660 nm presented in this thesis, with guidance from Dr Mario Nachbar. Data analysis for the associated publication was performed by Dr Mario Nachbar.
- Assisted in the SEM analysis of the $Fe_2O_3$ sample, with Dr Mario Nachbar and support from Dr Alexei Kiselev. NEXAFS measurements and associated analysis performed by Dr Mario Nachbar.

In the global-climate modelling of the Halley encounter (Chapters 4, 5, and 6):

*WACCM 1.06 modelling (Chapter 5):*

- CABMOD simulations to generate the MIF were run by Dr Juan Diego Carrillo Sánchez.
- Model spin up and initialisation was performed by Dr Wuhu Feng.
- Coding for the implementation of the Halley MIF in WACCM.
- Calculation of, and coding for the implementation of the heating tendency in WACCM.
- All model simulations performed, including associated data processing, generation of figures and interpretation of results.

*WACCM-CARMA modelling (Chapter 6):*

- Set up of the model case for the Halley simulation, with support from Dr James Brooke.
- Set up of the model case for the control simulation.
- Both model simulations were executed on the university supercomputing facilities by Dr Wuhu Feng.
- Data processing, generation of figures and interpretation of results.

Throughout these studies I was supervised by Prof John Plane, Prof Dan Marsh, Dr Wuhu Feng, Prof Martyn Chipperfield and Prof Piers Forster.

# **Abstract**

This thesis comprises both experimental and modelling investigations relating to the atmospheric impacts of a close cometary encounter. Two laboratory techniques were used to study the optical properties of iron oxide meteoric smoke particle (MSP) analogues: the Photochemical Aerosol Flow System (PAFS) and the Molecular flow Ice Cell in the Trapped Reactive Atmospheric Particle Spectrometer (MICE/TRAPS). Results from the two experiments were combined using an iterative photochemical model to derive complex refractive indices for the nanoparticles.

A number of sensitivity simulations were performed using the global climate model, WACCM (the Whole Atmosphere Community Climate Model) to simulate the effects of a cometary dust-loading following a close encounter with Halley's comet at a distance of 100,000 km. The effects of a chemical perturbation (a metal injection) and a dynamical perturbation (a heating tendency) on the mesosphere-lower thermosphere (MLT) were investigated. The increase in metal density following the chemical perturbation caused the destruction of up to 100 % of the ozone ($O_3$), atomic hydrogen (H) and water ($H_2O$) in the MLT, and up to around 30 % of the atomic oxygen (O). This affected the chemical heating rates, leading to changes in temperature and changes to global transport and mixing. The dynamical perturbation produced up to a ~200 K temperature increase that led to small changes to the densities of O and $O_3$. When the two perturbations were combined, the dynamical perturbation essentially amplified the effects of the chemical perturbation.

The effects of an injection of meteoric sulfur (S) and MSPs on the middle atmosphere were also investigated. Notable perturbations to both gas-phase sulfur chemistry and aerosol size distributions were observed. The injection also produced large increases in the surface area density of MSPs and mixed sulfate aerosol. No significant changes to the total aerosol deposition pattern were observed. However, a significant increase in the S deposited *via* this aerosol was seen compared to observations in a Greenlandic ice-core.

# Contents

# List of Figures

# List of Tables

# List of Abbreviations

AIM - aeronomy of ice in the mesosphere

AU - astronomical unit

CABMOD - chemical ablation model

CARMA - community aerosol and radiation model for atmospheres

CAM(4) - Community Atmosphere Model (version 4)

CCD - charged coupled device

CESM(1) - Community Earth System Model (version 1)

CPC - condensation particle counter

DMA - differential mobility analyser

ECOMA - existence and charge state of meteoric smoke particles in the middle atmosphere

EDX - energy dispersive X-Ray (spectroscopy)

EELS - electron energy loss spectroscopy

EUV - extreme ultra-violet

GOMOS - global ozone measurement by occultation of stars

HTC - Halley type comet

IR - infra red

IRAS - infrared astronomy satellite

JFC - Jupiter family comet

JPL - Nasa's Jet Propulsion Laboratory

LIDAR - a detection system that works on the principle of radar, but using laser light

LPC - long period comet

MAVEN - Mars atmosphere and volatile evolution (spacecraft)

MICE - molecular flow ice cell

MIF - meteoric input function

MLT - mesosphere-lower thermosphere

MOZART - Model for Ozone and Related Chemical Tracers (version 3)

MSIS - mass spectrometer-incoherent scatter (model)

MSP - meteoric smoke particle

NEO - near Earth object

NEXAFS - near edge X-ray absorption fine structure

OCC - oort cloud comet

OD - optical density

OSIRIS - optical spectrograph and infra-red imager system (spectrometer)

PAFS - photochemical aerosol flow system

PMC - polar mesospheric cloud

PSC - polar stratospheric cloud

QE - quantum efficiency

RDG - Rayleigh-Debye-Gans (approximation)

RI - refractive index

SAD – surface area density

SCIAMACHY - scanning imaging absorption spectrometer for atmospheric chartography

SEM - scanning electron microscopy

SMPS - scanning mobility particle sizer

SOFIE - solar occultation for ice experiment

SSA - stratospheric sulfate aerosol

TEM - transmission electron microscopy

TOF - time of flight (mass spectrometer)

TRAPS - trapped reactive atmospheric particle spectrometer

UMSLIMCAT - a global climate model

UV - ultra violet

WACCM - whole atmosphere community climate model

# Mineral Compositions

Hematite - $\alpha$-$Fe_2O_3$

Maghemite - $\gamma$-$Fe_2O_3$

Magnetite - $Fe_3O_4$

Wüstite - $FeO$

Goethite - $FeOOH$

Olivine - $Mg_{2x}Fe_{2-2x}SiO_4$, $0<x<1$ (end members: Fayalite - $Fe_2SiO_4$ & Forsterite - $Mg_2SiO_4$)

Silica - $SiO_2$

# Chapter 1

# Introduction

This chapter describes our current understanding of the processing of cometary dust, beginning with its ejection from a cometary nucleus, and ending with its deposition at the Earth's surface. Dust emitted from comets represents the majority of the total input of interplanetary dust to Earth, though usually meteor showers make up only a small fraction of the total mass. However, in the case of a close encounter with a comet, a dramatic increase in the total dust influx might be observed. When material enters the Earth's atmosphere, a fraction (typically ~20 %) of the incoming meteoroids undergo ablation in the mesosphere-lower thermosphere (MLT) at around 70 - 120 km in altitude (Figure 1.1). This processing leads to the formation of mesospheric metal layers and meteoric smoke particles (MSPs), the latter of which are transported down through the stratosphere, where they can become entrained in aerosol particles. MSPs are eventually deposited to the surface *via* sedimentation or precipitation.

It should be noted that the term 'dust' is used throughout this work to describe fine particulate matter, which takes many forms, both cosmic and terrestrial. Due to the wide range of phenomena relating to the processing of cosmic dust as it passes through the atmosphere, this chapter is not intended to be a comprehensive overview of previous work related to the processes implicated in or affected by this transformation. Rather, through discussion of the relevant literature, relevant concepts and techniques related to this work will be introduced. Scientific questions, to be addressed in later chapters, are then presented and an outline of the project aims is described.
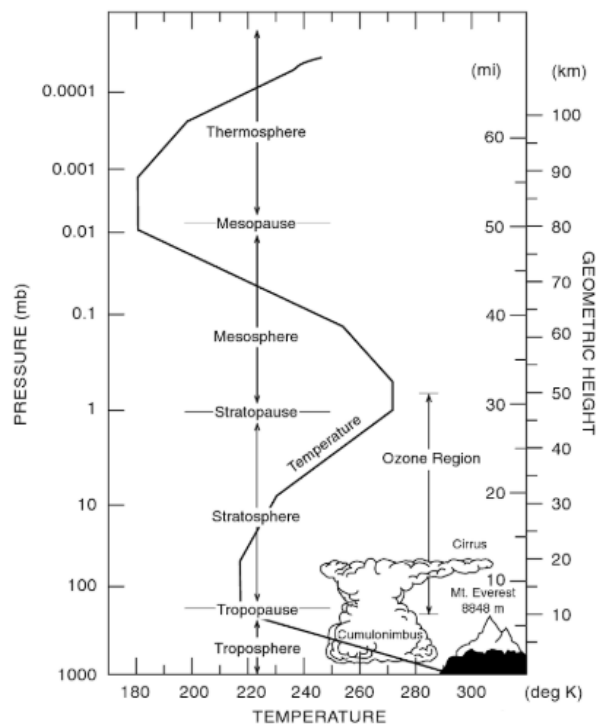


Figure 1.1. The layers of the atmosphere, including the thermosphere, mesosphere, stratosphere and troposphere, and their approximate altitudes. Approximate temperatures at each altitude are also shown (K). Figure adapted from *Brasseur and Solomon* [1986].

## 1.1 Cometary Dust in the Solar System

### 1.1.1 Sources of Dust

Dust grains are a crucial component of the galaxy, and are mainly found in interstellar clouds, where they play a role in establishing the thermodynamics and chemical composition by providing a substrate for the rich and varied chemistry which is observed [*Williams et al.*, 2007]. They are thus implicated in the collapse of these clouds into new stars, comets, asteroids, planetismals and planets, essentially determining both the nature and behaviour of the interstellar medium as well as the process of star formation which creates the galaxies themselves [*Draine*, 2003; *Williams and Herbst*, 2002]. Within our Solar System the dust manifests itself in various forms. These include the asteroid belt, the Kuiper belt, dispersed cometary dust, and interstellar dust passing through the Solar System. Decaying comets releasing dust *via* sublimation and asteroids freeing dust *via* collisions are considered to be the main sources of the interplanetary dust that enters the Earth's atmosphere [*Nesvorný et al.*, 2010; *Nesvorný et al.*, 2011; *Pokorný et al.*, 2014], with cometary dust constituting around 70 - 95 % of this total [*Carrillo-Sanchez et al.*, 2016; *Nesvorný et al.*, 2010; *Rowan-Robinson and May*, 2013; *Yang and Ishiguro*, 2015].

### 1.1.2 Comets

#### 1.1.2.1 Evolution

To understand the formation and behaviour of comets, it is important to consider the evolution of dust grains from interstellar clouds. Interstellar dust grains typically contain a silicacious core with a shell of refractory organics, upon which an icy mantle is deposited containing molecules such as water ($H_2O$), carbon monoxide (CO), ammonia ($NH_3$) and simple organics such as methane ($CH_4$) [*Burke and Brown*, 2010]. During its lifetime, each grain passes through a wide range of environments where interactions, both constructive and destructive, ultimately lead to varied compositions and structures [*Burke and Brown*, 2010; *Greenberg and Li*, 1998]. A schematic of the physical and chemical processing of interstellar dust is shown in Figure 1.2. Since comets are thought to be formed by processing of dust grains in the protoplanetary disk orbiting a star during the early formation of a planetary system [*Engrand et al.*, 2016], this variation in dust-grain composition is reflected in cometary compositions.
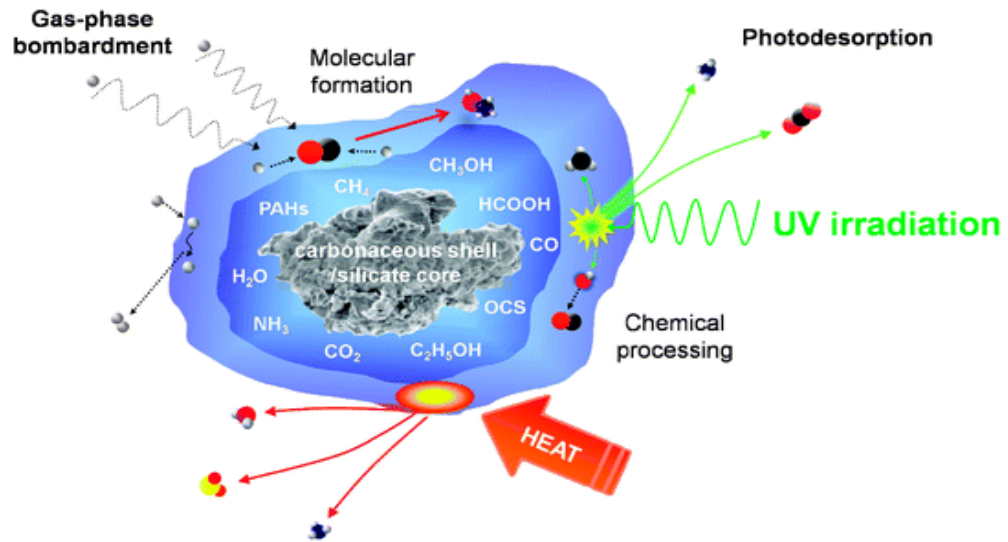
Figure 1.2. Schematic of a dust grain, showing the composition and the thermal and chemical processing [*Burke and Brown*, 2010].

### 1.1.2.2  Orbital Characteristics

Two main populations of comets can be found in the Solar System: the first, at the edge of the Sun's original protoplanetary disk, is the Kuiper belt at approximately 30 - 50 astronomical units (AU) away from the Sun and the second is the Oort cloud, which extends to the gravitational 'edge' of the Solar System at approximately 10,000 – 100,000 AU [*Lisse*, 2015]. A schematic of the relative size and orientation of the Kuiper belt and the Oort cloud is shown in Figure 1.3.
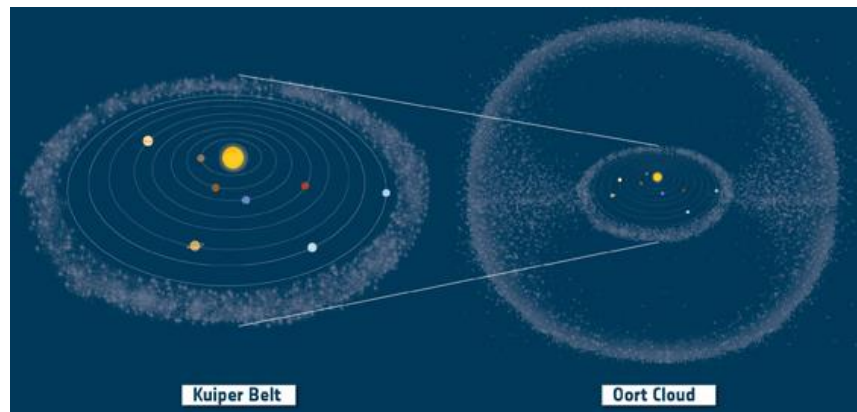


Figure 1.3. An illustration showing the two main reservoirs of comets in the Solar System: the Kuiper Belt and the Oort cloud. Image reproduced from *ESA* [2014].

A number of important parameters characterise a comet's orbit: the eccentricity ($e$), inclination ($i$), semi-major axis ($a$), orbital period ($p$) and perihelion distance ($q$). The eccentricity is a measure of the elliptical nature of the orbit with a value of 0 indicating a perfectly spherical orbit. A value between 0 and 1 characterises an elliptical orbit, and 1 or >1 represent parabolic and hyperbolic trajectories, respectively. The orbital inclination describes the deviation of the orbit

from the plane of the ecliptic (Figure 1.4). The perihelion and aphelion of a comet on an elliptical orbit refer to the closest and furthest points from the Sun respectively. The semi-major axis of such an orbit is essentially the radius of the orbit between the two most distant points.
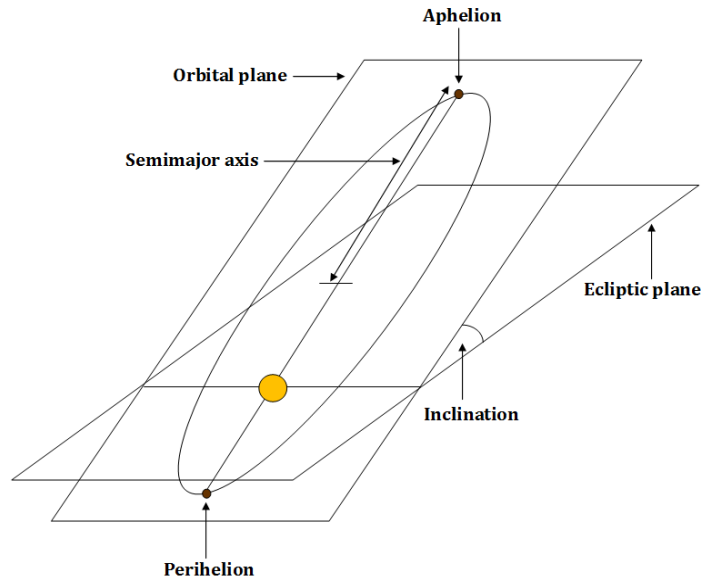


Figure 1.4. Orbital characteristics of a comet (represented by brown circles) orbiting around the sun (yellow circle).

The orbital period refers to the length of time it takes to complete one rotation about the Sun. Comets have been traditionally defined according to this parameter, with those having orbital periods <200 years being defined as short-period comets. If a comet has an orbital period of <20 years and an inclination <30° it is further classified as a Jupiter-family comet (JFC). JFCs are Kuiper belt objects that have been captured by the gravity of Jupiter. As such, their aphelion is close to Jupiter, and they exhibit low eccentricities and very short periods [Jewitt, 2002]. Comets with orbital periods >200 years and more highly eccentric orbits are termed long-period comets (LPCs). This population has a range of inclinations (from 0 to 180°) and is generally found in the Oort cloud. Note that an inclination greater than 90° indicates a retrograde orbit – where an orbit proceeds in the opposite direction to that of the planets. Halley-type comets (HTCs) are comets which have orbital periods between 20 and 200 years. They originate primarily from the Oort cloud but can also be formed in the Kuiper belt. Like the Oort cloud comets (OCCs), HTCs have a range of inclinations from 0 to 180°. Comet 1P/Halley (hereafter referred to as Halley) is the most prominent member of this family of comets. It has a highly inclined (162.24°) and an eccentric (0.967) orbit with an orbital period of 76.0 years and a perihelion distance of 0.587 AU. The high inclination of Halley's comet leads to fast encounter velocities for Halley dust; in the case of a close flyby with the Earth, material would be expected to enter the atmosphere at around 66.5 km s$^{-1}$ [*Kissel et al.*, 1986a].

### 1.1.2.3 Physical Characteristics

#### 1.1.2.3.1 Observational and Theoretical Studies

Although comets have been studied for millennia, it was the pioneering work of *Whipple* [1950; 1951] which led to the famous 'dirty snowball' hypothesis. In this seminal work, Whipple introduced the idea that comets were formed of a solid nucleus, composed of a conglomerate of intimately mixed cosmic dust and ices such as $H_2O$, $NH_3$, $CH_4$, CO and carbon dioxide ($CO_2$). He supposed that the ices were vaporised by externally applied solar wind and radiation pressure to form a cometary atmosphere (coma) with dust released from the nucleus as a result of this evaporation forming the observed dust tails. At around the same time, observations of a cometary tail pointing radially away from the sun led *Biermann* [1951] to speculate that the interaction of a cometary nucleus with the solar wind results in the formation of a plasma tail, and to develop a model to describe this process [*Biermann et al.*, 1967]. A schematic representation of these phenomena is shown in Figure 1.5.
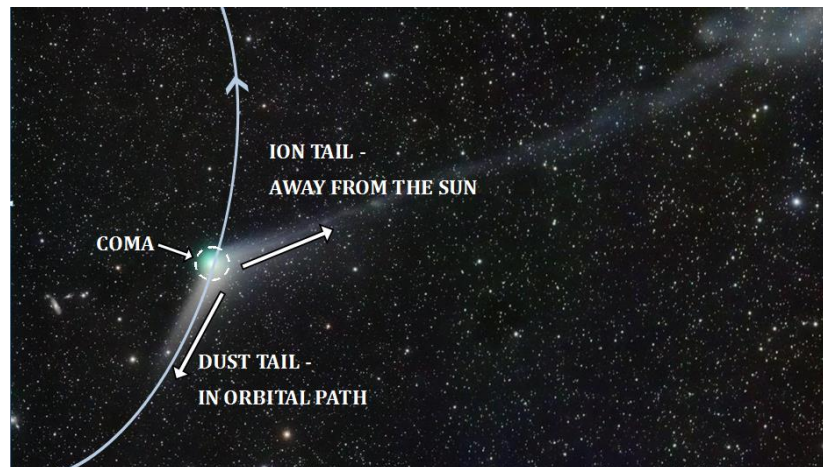


Figure 1.5. Illustration of the two types of cometary tail - dust tails and plasma (ion) tails - showing their orientation with respect to the orbit of a comet. Image: edited from *Chambó* [2016].

#### 1.1.2.3.2 In Situ Studies

Although these ideas were widely accepted, it was not until the 1980s and the first *in situ* studies of comets that these theories were evidenced. The Russian VeGA 1 & 2, European Giotto and the Japanese Suisei and Sakigake missions to comet Halley (the 'Halley Armada') significantly advanced our understanding of a number of phenomena, including the fundamental properties of the nucleus, localisation of surface activity and interactions with the solar wind. Mass spectral measurements from dust particles encountered by the Vega 1 & 2 and Giotto spacecraft revealed the cometary dust to be formed of carbon (C), oxygen (O), sodium (Na), magnesium (Mg), silicon (Si) and iron (Fe), most likely in metal oxides and silicates [*Geiss and Altwegg*, 1998; *Kissel et al.*, 1986a; *Kissel et al.*, 1986b]. Images returned by Giotto showed a clear solid nucleus, with surface activity largely on the sunward side, localised into jets [*Keller et al.*, 1988; *Keller et al.*,

1986]. The icy material released from the surface was found to be composed of predominantly of $H_2O$ (see Figure 1.6) and the detection of strong plasma wave turbulence demonstrated the process of solar wind mass-loading by photoionization of gas released from the nucleus [*Galeev et al.*, 1986; *Yumoto et al.*, 1986].
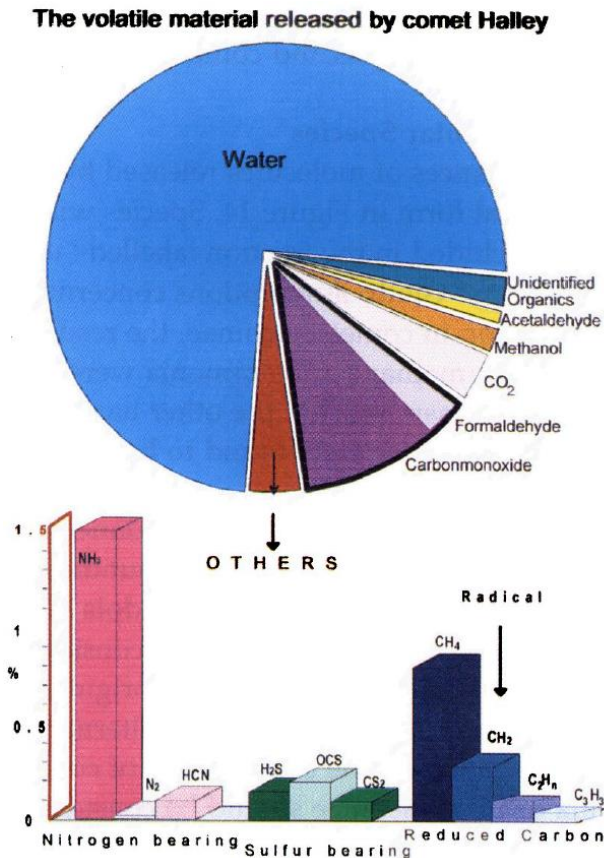


Figure 1.6. Fractional abundances of molecules identified in the coma of comet Halley. The total number of molecules coming out of the nucleus, evaporating near the nucleus, or released by grains up to 5000 km from the nucleus are included. Figure from *Geiss and Altwegg* [1998], data compiled from references therein.

In the last 20 years, missions such as Deep Space One [*Soderblom et al.*, 2002], Stardust [*Brownlee et al.*, 2006], Deep Impact [*A'Hearn et al.*, 2005], EPOXI [*A'Hearn et al.*, 2011] and Stardust NExT [*Veverka et al.*, 2013] have further advanced cometary science (see Figure 1.7 for a schematic of these missions). Through the study of this small number of cometary bodies, remarkable diversity of the size, shape, composition and activity has been revealed. Key advances in this field have improved our understanding of where comets formed, their evolution and where they are found today [*Hsieh and Jewitt*, 2006; *Morbidelli*, 2005]. The culmination of these previous cometary missions has been the unprecedented Rosetta mission [*Jones et al.*, 2017], which is the only spacecraft to have entered into orbit around a comet. Observation of comet 67P/Churyumov-Gerasimenko (hereafter 67P) over 26 months revealed the dynamic nature of the nucleus and coma over an extended time period, in contrast to all previous missions which captured only a 'snapshot' of the comets.

Imaging of dust grains throughout the Rosetta mission has contributed to our current understanding of cometary dust – that grains are formed of sub-μm aggregates with varying morphologies, from highly porous to relatively compact [*Bentley et al.*, 2016; *Langevin et al.*, 2016; *Rotundi et al.*, 2015]. Typically, the composition of the refractory organic matter within comets is comparable, with measurements from 67P demonstrating that most of the main elements exhibit roughly a chondritic ratio (within a factor of 3), except for an enrichment in C and N [*Bardyn et al.*, 2017; *Levasseur-Regourd et al.*, 2018]; this is in broad agreement with data from Halley. These properties suggest that cometary dust is composed of matter from the outer edges of the protoplanetary nebula, mixed with material that has been processed in the inner solar system and then transported outward.
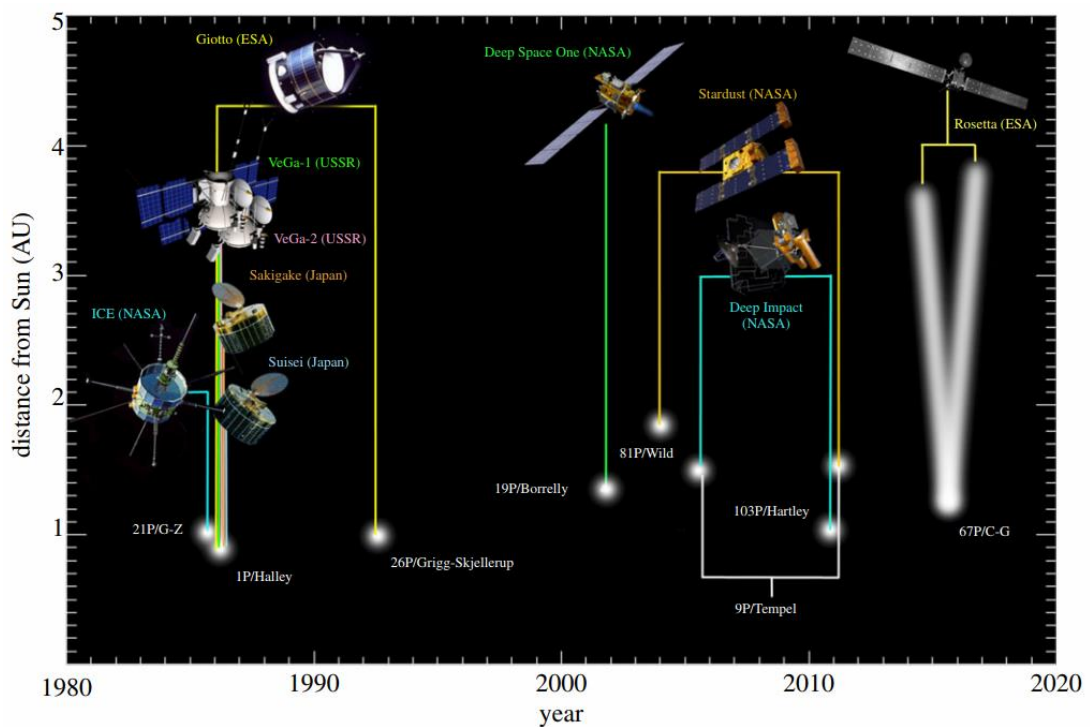


Figure 1.7. Timeline showing previous dedicated cometary missions, from the International cometary Explorer (ICE), to the 'Halley Armada' (Giotto, VeGa 1 & 2, Sakigake and Suisei), and more recent missions: Deep Space One, Stardust, Deep Impact and Rosetta. Image credit: *Jones et al.* [2017].

### 1.1.2.4 Likelihood of Encounter

Awareness of the impact hazard of comets and asteroids is a recent phenomenon and has only been recognised since the mid twentieth century. Widespread interest from both scientists and the public has only really developed since the 1980s and the identification of a cosmic impact as the cause of the mass extinction ~65 million years ago at the end of the cretaceous period [*Alvarez et al.*, 1980]. Attempts to quantify the statistical risk posed to Earth by an encounter with a comet or asteroid vary widely between studies, from one in ten thousand to one in hundreds of millions of years, depending on the nature of the encounter and the size of the body [*Chapman and Morrison*, 1994; *Napier*, 2015; *Nesvorný and Roig*, 2017; *Toon et al.*, 1997]. The risk posed by

near Earth objects, or NEOs, is difficult to calculate due to the large degree of uncertainty involved. Impact fluxes can be estimated from the cratering record of the moon or inner planets (e.g. *Neukum et al.* [2001]), or alternatively from dynamical models of the orbital evolution of the impactor population (e.g. *Nesvorný and Roig* [2017]) though both of these methods have their limitations. The former can determine impactor probabilities, though it cannot determine their source. It is also based on the assumptions that the population of NEOs is in a steady state and that impacts occur at a constant rate over astronomical time. The latter may not be able to accurately represent the population of small bodies due to either a lack of observations, computational limitations or uncertainties in dynamical processes. Furthermore, these studies largely focus on the population of (and associated risk from) asteroidal bodies, whose population is far better constrained than that of comets, particularly those originating from the Oort cloud. A consequence of this is that there is likely to be significantly less warning in the case of a cometary encounter, with this likely measured in weeks or months rather than decades or centuries for a well-mapped near-earth asteroid population [*Napier and Asher*, 2009]. Thus, the risk posed by comets is likely to be significantly higher and more unpredictable than that from asteroids.

Though the flux of near-Earth comets is estimated at only a few percent of the asteroid flux (for objects of the same size), comets tend to be travelling much faster: typically 30-40 km s$^{-1}$ for short-period comets, and 50-60 km s$^{-1}$ for long-period comets, compared to 20 km s$^{-1}$ for asteroids [*Chapman and Morrison*, 1994]. Comets can therefore deposit significantly more kinetic energy into the atmosphere; for Giotto encountering dust from comet Halley at 68.4 km s$^{-1}$, a grain with a radius of 1 mm would impart around the same amount of energy at impact as a motorbike and its rider colliding with a wall at 40 mph [*Geiss and Altwegg*, 1998]. A grain twice this size would penetrate 8 cm through solid aluminium [*ESA*, 2013]. Besides, whilst an asteroid only poses a risk in the event of a collision, a close encounter with a comet could still lead to significant dust loading to the atmosphere, since cometary comas can extend for hundreds of thousands of km. Dust trails from comets can also persist in the inner solar system for thousands of years – the passage through which can lead to periodic meteor showers (see section 1.2.1.3.1).

### 1.1.2.5 Previous Encounters

The Earth has experienced a number of encounters with extra-terrestrial bodies throughout its past: from historical impact events such as the late-heavy bombardment and those believed to have caused the Cretaceous/Tertiary mass extinction [*Alvarez et al.*, 1980; *Hildebrand et al.*, 1991] and the Younger Dryas cooling [*Napier*, 2010; *Wolbach et al.*, 2018], to more recent events such as the Tunguska and Chelyabinsk airbursts in 1908 and 2013 respectively [*Brown et al.*, 2013; *Turco et al.*, 1981]. The record for the closest ever approach of a comet is held by comet D/1770 L1 (Lexell's comet), a long period comet which passed the Earth at a distance of 1,800,000 km in 1770 [*Minor-Planet-Center*, 2019]. Although cometary encounters are rare

enough to be beyond personal experience, the statistical risk posed by such events over long timescales is significant, as exemplified by the numerous previous encounters throughout history.

Encounters of comets with other bodies in the Solar system have also been observed. One such encounter is the impact of the fragmented comet D/1993 F2 (Shoemaker Levy) with Jupiter in 1994, where prominent fireballs were observed despite the occurrence of the collisions on the far side of Jupiter relative to Earth [*Crawford et al.*, 1995]. Debris from the collisions resulted in impact scars (i.e. dark spots) on the order of 10,000 km (approximately the size of the 'great red spot'), which persisted for many months. Changes to the temperature and stratospheric chemical composition were also observed [*Bézard*, 1997; *McGrath et al.*, 1996]. Another notable event was the close encounter of Comet C/2013 A1 (comet Siding Spring) with Mars in 2014. First detected in 2013 at the Siding Spring Observatory, it was initially classified as an asteroid. However, subsequent observations revealed a faint tail [*Manca et al.*, 2016]. It was soon discovered that Siding Spring would undergo a close encounter with Mars late the following year, with a closest approach distance on the order of 130,000 km – providing the first and only opportunity to observe the effects of the close flyby of a planet by a comet.

Before the encounter, a number of groups developed models to predict the risk posed to spacecraft and the planet from ejected material. *Moorhead et al.* [2014] produced a simple analytical model to describe the size and spatial distributions of dust in a cometary coma, which was able to reproduce the meteoroid fluxes experienced by Giotto and Stardust during their encounters with Halley and 81P/Wild to within an order of magnitude (see Figure 1.8). Other models developed by *Vaubaillon et al.* [2014], *Tricarico et al.* [2014] and *Ye and Hui* [2014] used different numerical approaches to calculate the dust fluence. Whilst *Vaubaillon et al.* [2014] significantly over-predicted (by a factor of $10^6$) the dust fluence measured by the Mars Atmosphere and Volatile Evolution (MAVEN) spacecraft ($0.5$-$3 \times 10^{-5}$ m$^{-2}$ [*Schneider et al.*, 2015]), other models fared better. *Moorhead et al.* [2014] and *Tricarico et al.* [2014] under-predicted the total fluence by a factors of 3-20 and 30, although the top of the predicted size distributions were factors of 1200 and 30 times too large, respectively. *Ye and Hui* [2014] over-predicted the dust fluence by a factor of 3-20, however they under-predicted the maximum particle size by a factor of $10^9$, concluding that the flyby of Siding Spring past Mars posed no risk to spacecraft and the dust flux experienced at Mars would be no different to the sporadic background influx.

An intense ground- and space-based campaign monitored the close encounter, with more than 19 spacecraft observing the comet, and around 13 reporting detections ranging from X-ray to IR wavelengths. The comet appeared to have no detectable reaction to the close flyby, though *in situ* measurements from MAVEN suggested between 2.7 and 16 tons of dust was injected into the Martian atmosphere (MAVEN orbits Mars on an elliptical orbit, with a closest approach to Mars'surface at periapse of 150–200 km) [*Schneider et al.*, 2015]. A recent reanalysis has revised this fluence estimate to 82 tons [*Crismani et al.*, 2018]. The MAVEN spacecraft's Imaging Ultra-Violet Spectrograph (IUVS) captured spectra of the planet's upper atmosphere above 50 km, detecting intense emission from Mg, Mg$^+$, Fe and Fe$^+$ peaking at an altitude of around 100 - 120

km [*Schneider et al.*, 2015]; spectra obtained before and after the closest approach (Figure 1.9) demonstrated the formation of a temporary, global ionospheric layer. While such emissions had not been observed in the Martian atmosphere before, the spectra closely resemble those recorded in the Earth's upper atmosphere attributed to metal atoms added *via* meteoric ablation (see section 1.2.1.3.2) [*Dymond et al.*, 2003].
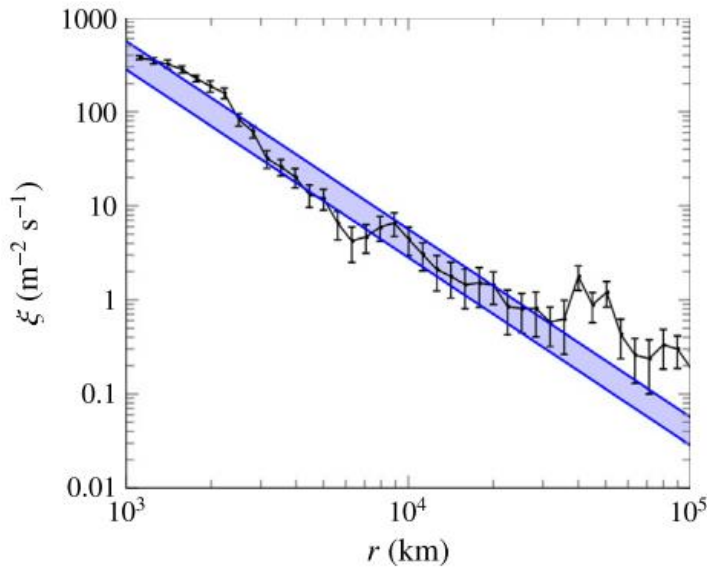


Figure 1.8. Dust flux ($\xi$/ m$^{-2}$ s$^{-1}$) calculated by *Moorhead et al.* [2014] in the coma of comet Halley, as a function of cometocentric distance, *r*. The upper and lower limits of the blue region correspond to a coma radius of 100,000 km and 200,000 km respectively. Black data points and error bars are measurements from Giotto, reproduced from *Fulle et al.* [2000]. Image from *Moorhead et al.* [2014].
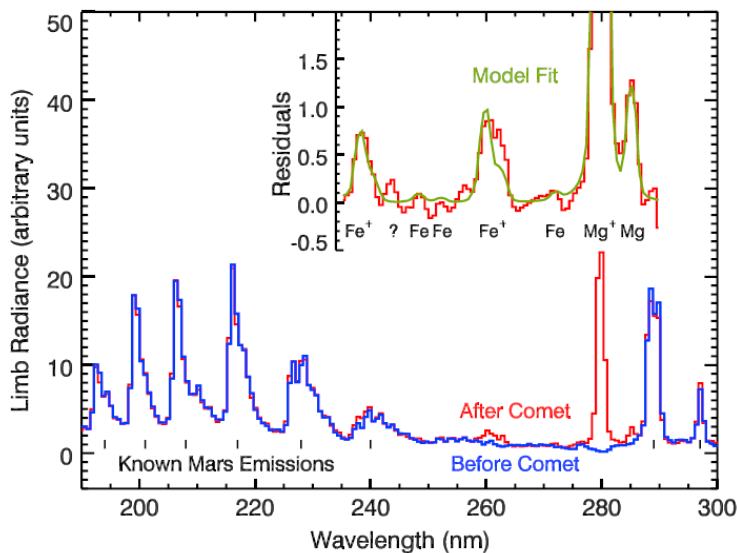


Figure 1.9. Scaled and background corrected spectra from Mars' atmosphere before and after the closest approach of Siding Spring showing emissions of Mg, Mg$^+$, Fe and Fe$^+$. Both spectra were recorded near a tangent altitude of 119 km at approximately 14 h local time and a zenith angle of ~60 °. The inset shows a comparison of a model spectrum with the smoothed residual spectrum on an expanded vertical scale [*Schneider et al.*, 2015].

## 1.2 Cometary Dust in the Earth's Atmosphere

### 1.2.1 The Mesosphere-Lower-Thermosphere

The mesosphere is a region of the atmosphere that comprises altitudes from the stratopause at 50 km to the mesopause at around 90 km; the thermosphere extends from 90 km to about 600 km (Figure 1.1). The region between 70 km and about 110 km is commonly referred to as the mesosphere-lower thermosphere (MLT), since the lower and upper mesosphere are physically and chemically distinct from each other. Furthermore, phenomena such as airglow layers, meteoric ablation, the mesospheric metal layers and polar mesospheric clouds (PMCs) typically occur close to or span the boundary between these regions (the mesopause) [*Plane*, 2003] – these phenomena are discussed further in this section. Within the MLT (at ~110 km) lies the turbopause – one description of where the edge of space begins. The MLT experiences the direct effects of a constant influx of cosmic material, which contributes to the physical and chemical characteristics of this region of the atmosphere.

#### 1.2.1.1 Physical and Dynamical Characteristics

The dynamics of the MLT is driven by atmospheric waves, such as planetary waves, gravity waves and atmospheric tides [*Smith*, 2012; *Vincent*, 2015]. As these waves propagate upwards from their sources lower in the atmosphere, their amplitudes grow to offset the decrease in density [*Andrews et al.*, 1987]. Momentum deposition from wave-breaking generates large-scale meridional circulation in the mesosphere. The breaking gravity waves exert drag on the zonal wind, which causes residual circulation from the summer to winter pole and generates an upwelling of air in the summer high latitudes to feed this flow [*Andrews et al.*, 1987; *Plane et al.*, 2015]. As it rises, this air experiences adiabatic expansion leading to temperatures of around 120 K or lower – the summer mesopause region is in fact the coldest place on earth. A downwelling of air in the winter high latitudes funnels air down into the stratosphere, where adiabatic contraction leads to the higher temperatures observed. The residual transport in the MLT is shown in Figure 1.10, which displays output from the Whole Atmosphere Community Climate Model (WACCM) – discussed in detail in Chapter 4. WACCM is a 'high-top' coupled global chemistry-climate model used for research on the MLT region, since it spans altitudes from the surface up to $6 \times 10^{-6}$ hPa (~140 km). It is produced by the National Center for Atmospheric Research (NCAR) in Boulder, Colorado [*Hurrell et al.*, 2013; *Marsh et al.*, 2013b].
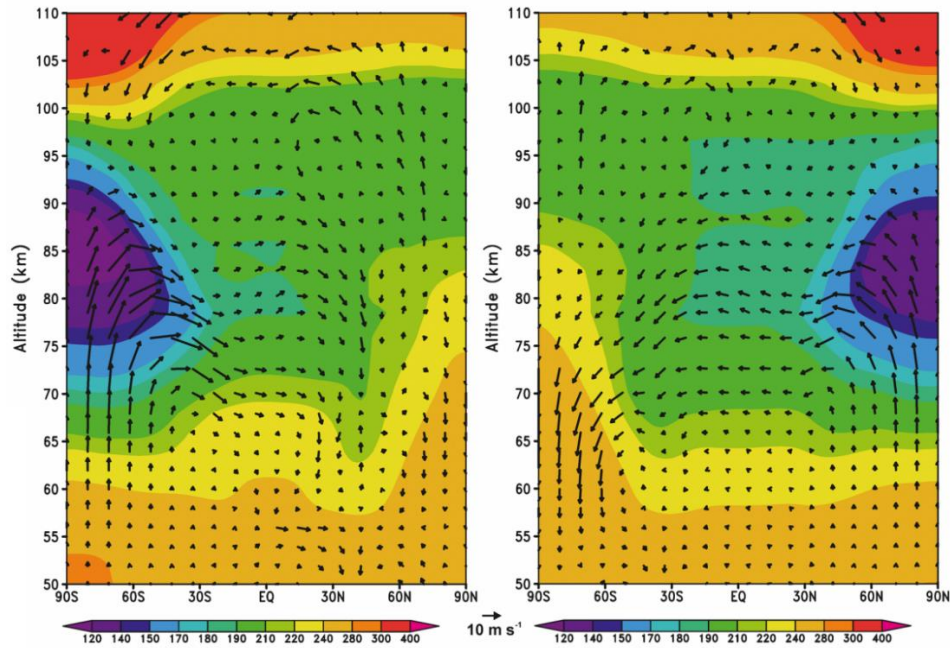
Figure 1.10. Output from the Whole Atmosphere Community Climate Model (WACCM) showing the temperature (K) as a function of altitude and latitude in the MLT for January (left) and July (right) (averaged from 2004 to 2011). Wind vectors (ms$^{-1}$) showing the residual circulation are also shown, with the vertical wind multiplied by 500 for visualisation purposes. Image from *Plane et al.* [2015].

### 1.2.1.2   Dominant Chemistry

The chemistry of the MLT is dominated by atomic O, which is plays a crucial role in a number of processes: it regulates the concentrations of atomic hydrogen (H) and HO$_x$ radicals such as OH and HO$_2$; it enables the formation of neutral and ionic metal layers; it participates in the reactions that contribute to airglow emission reactions; it facilitates the charging of MSPs below 90 km; and it establishes the radiative balance of the MLT through chemical heating and radiative cooling [*Plane et al.*, 2015]. Absorption in the Schumann-Runge continuum (in the wavelength range $130 < \lambda < 175$ nm) and the Schumann-Runge bands (175-195 nm) generates O *via* photolysis during the daytime [*Brasseur and Solomon*, 1986];

R1.1    $O_2 + hv \rightarrow O + O$

R1.2    $O_2 + hv \rightarrow O(^1D) + O$ ($\lambda < 175$ nm)
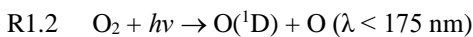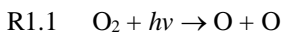
and atomic O is predominantly removed by the reactions;

R1.3    $O + O_2 (+M) \rightarrow O_3 (+M)$     (where M is a third body i.e. N$_2$ or O$_2$)

R1.4    $H + O_3 \rightarrow OH + O_2$

R1.5    $O + OH \rightarrow H + O_2$

R1.6    $H + O_2 (+M) \rightarrow HO_2 (+M)$

R1.7    $O + HO_2 \rightarrow OH + O_2$
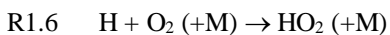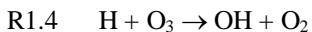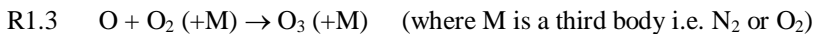
rather than the reactions;

R1.8    $O + O (+M) \rightarrow O_2 (+M)$

R1.9    $O + O_3 (+M) \rightarrow 2\ O_2 (+M)$
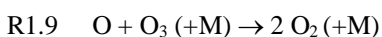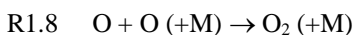
which typically proceed slowly in the MLT. The reaction cycles R1.3-R1.4-R1.5 and R1.6-R1.7-R1.5 facilitate the recombination of two O atoms into molecular oxygen ($O_2$). Both of these reaction cycles are catalysed by H, which is produced in the MLT by the photolysis of $H_2O$ (R1.10) – see Figure 1.11 [*Brasseur and Solomon*, 1986]:

R1.10   $H_2O + h\nu \rightarrow H + OH$ ($\lambda < 200$ nm)
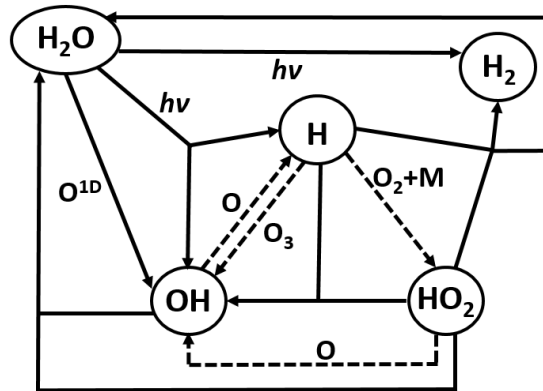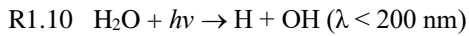


Figure 1.11. The principal reactions of $HO_x$ compounds in the MLT region. Dashed lines represent reactions involved in the catalytic removal of O [*Brasseur and Solomon*, 1986].

The density of O is ultimately controlled by the pressure dependent reaction R1.3 since this is the rate-determining step in the reaction cycle. Above ~80 km, the time constant for this reaction is longer than 12 hours, generating an 'oxygen ledge', above which no significant diurnal variation is observed [*Plane et al.*, 2015]. H exhibits a similar profile, due to the close coupling of these two species in the aforementioned reactions, and the pressure dependence of reaction R1.6. Contrastingly, ozone ($O_3$) displays little diurnal variation below ~75 km, but above ~80 km a ten-fold decrease is observed during the day due to photolysis (R1.11 and R1.12, see Figure 1.12) [*Brasseur and Solomon*, 1986; *Plane et al.*, 2015]. The density of $H_2O$ in the MLT is controlled by a balance between transport and photolysis. $H_2O$ is formed in the lower mesosphere as a result of $CH_4$ oxidation, propagating upwards from lower altitudes in the stratosphere; the residual circulation leads to an increase in $H_2O$ in summer (approximately 3 fold, see Figure 1.13) [*Brasseur and Solomon*, 1986; *Plane et al.*, 2015]. However, above ~80 km, the mixing ratio decreases as a result of photodissociation – predominantly due to the absorption of solar Lyman-$\alpha$ radiation (R1.10).

R1.11    $O_3 + h\nu \rightarrow O + O_2$

R1.12    $O_3 + h\nu \rightarrow O(^1D) + O_2(^1\Delta_g)$  ($\lambda < 300$ nm)
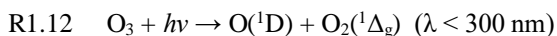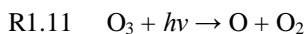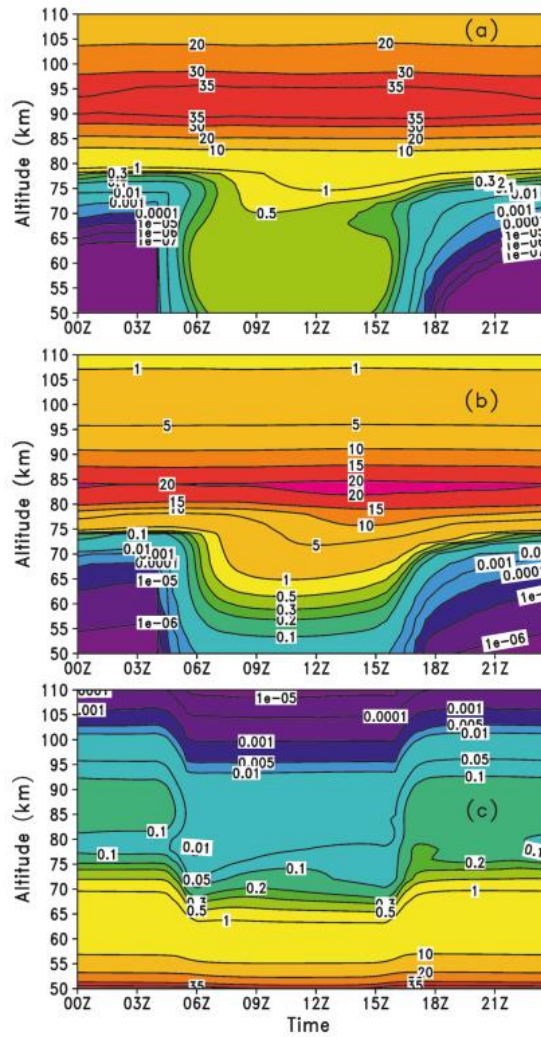
Figure 1.12. Top panel: Diurnal variation in O density ($10^{10}$ atoms cm$^{-3}$) as a function of altitude (km). Middle panel: Diurnal variation in H density ($10^7$ atoms cm$^{-3}$) as a function of altitude (km). Bottom panel: Diurnal variation in $O_3$ density ($10^9$ atoms cm$^{-3}$) as a function of altitude (km). Data from 54° N, 12° E (Kühlungsborn, Germany), averaged from 2004 to 2011. output from the Whole Atmosphere Community Climate Model [*Plane et al.*, 2015].
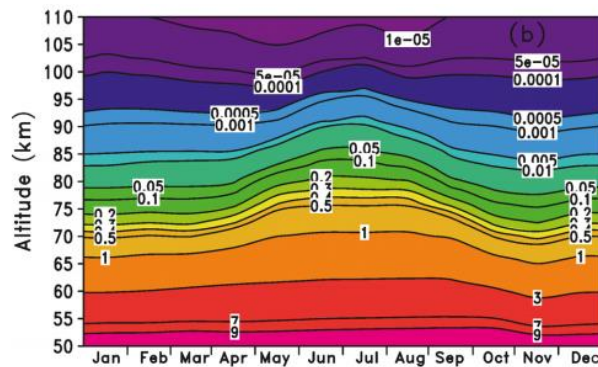


Figure 1.13. Seasonal variation in $H_2O$ density as a function of altitude ($10^7$ atoms cm$^{-3}$). Output from the Whole Atmosphere Community Climate Model, averaged from 2004-2007 at 54° N [*Plane et al.*, 2015].

Appreciable concentrations of positive ions, negative ions and electrons occur in the MLT, in two distinct regions. In the D region, between around 70 km and 90 km, the ions are dominated by

positively charged cluster ions such as proton hydrates, negatively charged MSPs, and electrons. Above this, the E region (95-170 km) is dominated by $O_2^+$ and $NO^+$, with all of the negative charge in the form of free electrons (see Figure 1.14) [*Shuman et al.*, 2015]. Photoionization is the main source of plasma, with the ionization in the E region dominated by the absorption of solar X-rays and extreme ultra-violet (EUV) radiation by the dominant neutral species, $N_2$, O and $O_2$. A 'window' in the $O_2$ spectrum (i.e. a weak absorption) at the wavelength of solar Lyman- α radiation (121.6 nm) allows this wavelength to penetrate deeper into the atmosphere. Below 90 km, it is absorbed by NO, providing the main source of ionization in the D region (in addition to ionization by cosmic rays) [*Shuman et al.*, 2015].

The dominant chemistry in the lower thermosphere involves exothermic reactions of N and O-containing atomic and diatomic species (see Figure 1.15, left panel). The main loss process for ions in this atmospheric region is *via* dissociative recombination of diatomic cations. Recombination of $NO^+$ and $O_2^+$ with electrons is very exothermic, so the atoms can be formed in electronically excited states, which then upon radiative decay produce the visible airglow (see Figure 1.15, right panel). Similar chemistry to that occurring in the thermosphere occurs in the mesosphere, but here the concentration of neutral species is large enough that the N and O-containing ions form clusters with ambient $H_2O$ molecules to form a range of hydrated positively charged ions. In this region, negatively charged ions are also formed *via* a complex scheme of reactions initiated by electron attachment to $O_2$ [*Shuman et al.*, 2015].
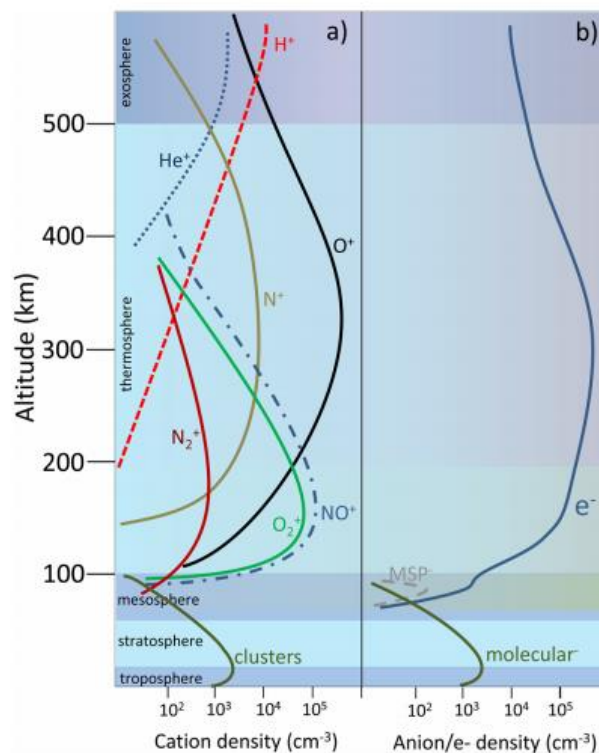


Figure 1.14. Typical positive and negative ion densities as a function of altitude. Significant diurnal, seasonal and latitudinal fluctuations are observed in the ion densities – the values shown are typical for midlatitudes during daytime. Figure adapted from *Shuman et al.* [2015].
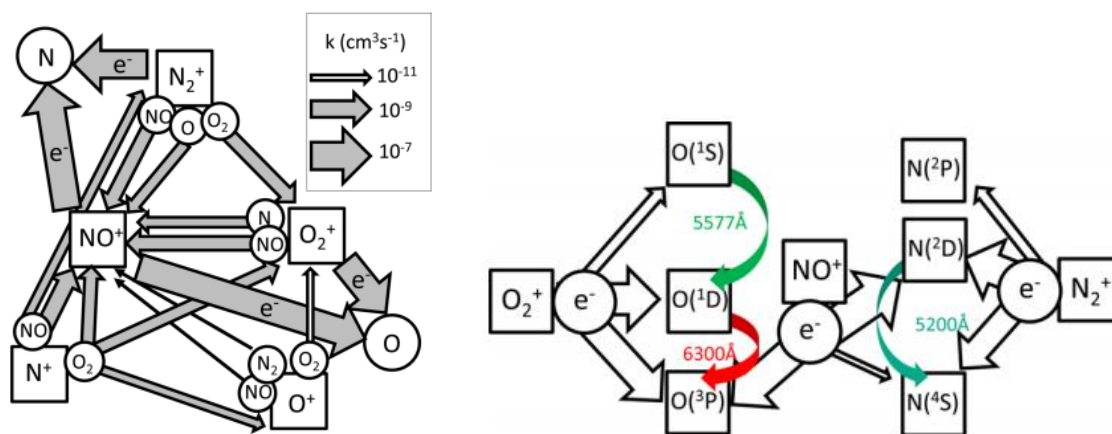
Figure 1.15. Left panel: Schematic diagram of the chemistry of the E region, showing ion-molecule and dissociative recombination reactions (only ground-state species are considered for simplicity). The thickness of the arrows scales roughly with the rate constants, as detailed in the legend. Right panel: The production of metastable N and O from the dissociative recombination of $O_2^+$, $NO^+$ and $N_2^+$. Approximate branching ratios are indicated by the thickness of each arrow, and the radiative decay constituting the visible airglow are also shown. Figures from *Shuman et al.* [2015].

### 1.2.1.3 Dust input

#### 1.2.1.3.1 Meteor Showers

Meteors are distinct from meteoroids – the latter being a general term for incoming cosmic dust particles and former being the optical and/or radar signal observed when a meteoroid enters the atmosphere. Particles larger than ~1 mm become incandescent upon atmospheric entry, resulting in a bright streak of light. These normally occur during meteor showers, when the Earth passes through a 'fresh' dust tail, produced by a comet that crossed the Earth's orbit recently (less than 100 years ago). There are many annual meteor showers associated with particular comets, such as the Eta-Aquarids, Perseids and Leonoids showers, associated with the comets Halley, Swift–Tuttle, and Tempel-Tuttle respectively. Each year the Earth takes several weeks to pass through one of the strongest streams of dust in the inner solar system, the Taurid meteor shower, which is thought to originate from the break-up of a giant comet (Comet 2P/Encke) which disintegrated some 20,000 - 30,000 years ago [*Babadzhanov et al.*, 2008; *Bailey et al.*, 1990; *Whipple*, 1940; 1954]. The fact that the Earth is still experiencing the effects of a cometary break-up from so long ago demonstrates the pronounced effect that such events can have in the solar system.

In the event of a close cometary flyby with the Earth, intense meteor showers would be observed. Numerous factors would affect the strength of the shower, including but not limited to: the cometary mass, composition and activity; the nature of its orbit including the inclination, curvature and direction of rotation (prograde or retrograde) with respect to that of the Earth; the speed of the comet and the distance between the two bodies at the point of intersection between the two orbits. The high degree of variability in such parameters means the nature of a close cometary encounter is unpredictable, and the magnitude of the atmospheric impacts will vary significantly with these parameters. This makes it difficult to make general predictions regarding

the implications of a terrestrial cometary flyby – especially with the lack of precedent, since there are no observations that can provide a calibration.

### 1.2.1.3.2   Meteoric Ablation

Dust from sources other than meteor showers gives rise to a continuous input of sporadic meteoroids; the incident mass of material to the Earth is largely due to this steady rain of meteoroids with masses ranging from $10^{-10}$ to $10^{-1}$ g and speeds of $11 - 72$ km s$^{-1}$ (see Figure 1.16) [*Carrillo-Sanchez et al.*, 2015; *Carrillo-Sanchez et al.*, 2016]. Because of this very wide range in mass distribution, which cannot be observed by a single instrument, recent estimates of the dust input vary by nearly 2 orders of magnitude, depending on the measurement technique used (see *Plane* [2012] and references therein). However, current estimates suggest the total dust flux entering the atmosphere is $43 \pm 14$ t d$^{-1}$ (tons per day) [*Carrillo-Sanchez et al.*, 2016].
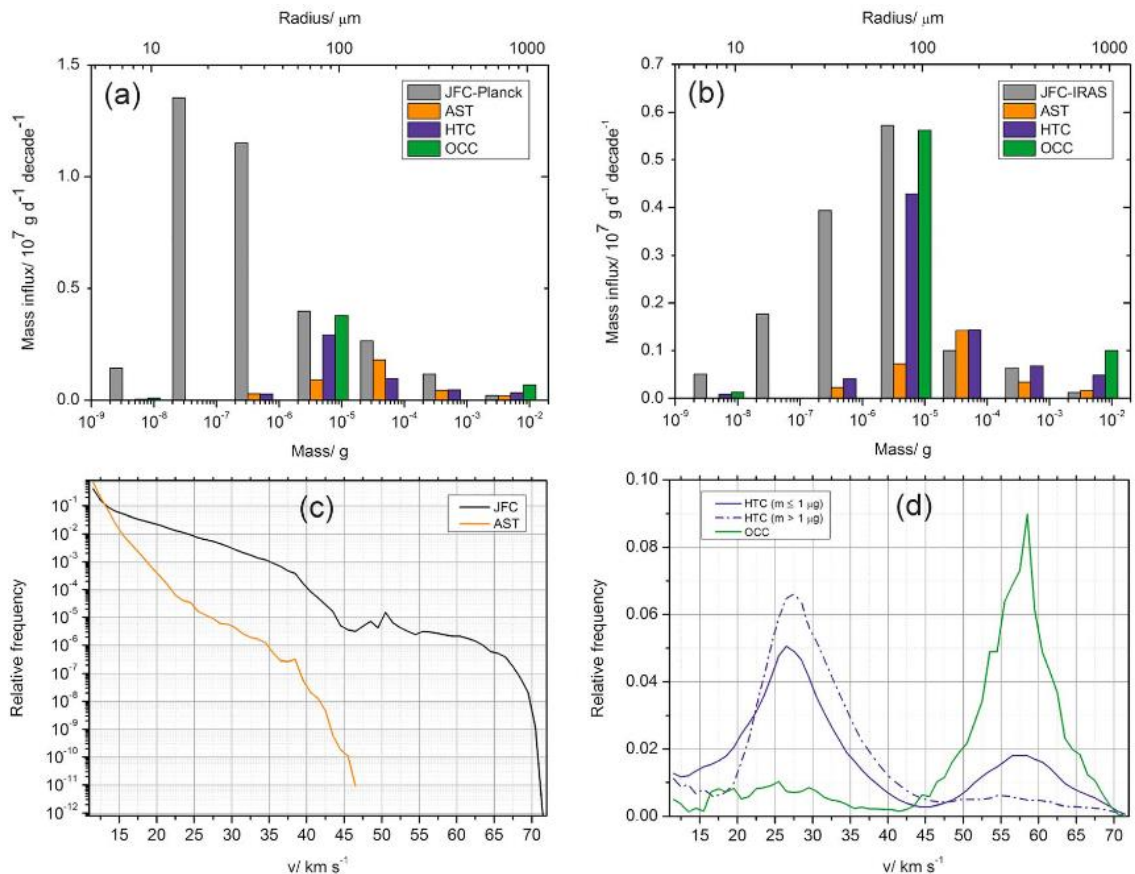


Figure 1.16. Top panels: histograms showing the mass input rate for the four sources of dust - JFCs, HTCs, OCCs and asteroids (AST) - derived from measurements from the Planck telescope (a) and the Infrared astronomy satellite (IRAS) (b) as a function of mass and size. Bottom panels: velocity distributions illustrating the entry speed for meteoroids from JFCs (black), HTCs (blue) and OCCs (green) and asteroids (orange). Diagram from *Carrillo-Sanchez et al.* [2016].

Around 8 t d$^{-1}$ of this material undergoes a process termed differential ablation – the main mass loss mechanism which deposits material into the MLT [*Carrillo-Sanchez et al.*, 2016; *Janches et*

*al.*, 2009]. When a meteoroid collides with air molecules, it experiences rapid frictional heating. If the temperature exceeds the melting point of the constituent minerals (~1800 K), vaporization will occur. At first, while the temperature is still relatively low, only the least refractory elements - potassium (K) and sodium (Na) - are ablated. Then the main elements - iron (Fe), silicon (Si) and magnesium (Mg) - ablate around 2000 K. The most refractory elements - calcium (Ca), aluminium (Al) and titanium (Ti) - come off at the lowest altitudes, if a sufficiently high temperature (~2200 K) is reached. The process of meteoric ablation has been described with the Chemical Ablation Model (CABMOD), developed at the University of Leeds – this model is discussed in detail in Chapter 4, section 4.1.2. The high entry speeds of meteoroids lead to a fraction of the ablated material becoming ionized through collisions with $N_2$ and $O_2$, with the ionization fraction varying for each metal [*Janches et al.*, 2017; *Jones*, 1997]. A significant amount of fragmentation may also occur before a meteoroid melts [*Campbell-Brown and Koschny*, 2004], though currently this process is not represented in CABMOD. Any meteoroids which only partially melted, or melted but did not completely evaporate and then solidified, sediment out of the atmosphere at rates dependent on their size. These are termed scoriaceous meteorites and cosmic spherules, respectively.

### 1.2.1.3.3   Metal Chemistry

The deposition of metals into the MLT *via* ablation results in the formation of metal layers that occur globally at altitudes between ~80 and 105 km. At the layer peaks (84 - 92 km), the neutral atomic metals are the dominant species, with typical peak densities ranging from 10 $cm^{-3}$ for Ca to $10^4$ $cm^{-3}$ for Fe. In contrast to the other metals, Si reacts rapidly with $O_2$ to form SiO, and so SiO is the counterpart of the other neutral metal atoms such as Fe, Mg and Na. Above the neutral metal layers, which have half-widths of approximately 5-10 km, ionic chemistry dominates and the metals are present predominantly as their atomic ions. These ions are largely formed *via* charge transfer between the neutral metals and $NO^+$ or $O_2^+$ (see Figure 1.17), and removed by the formation of cluster ions which can then undergo dissociative recombination with electrons. Below the neutral metal layers, reactions involving $O_3$, $H_2O$ and H transform the neutral metals to the stable reservoir species (eg. FeOH, $Mg(OH)_2$, $NaHCO_3$, $Si(OH)_4$). Reactions involving atomic O and H with both neutral and ionic metal species are also prevalent. The chemistry of the metal layers has been established through a combined effort of observational, laboratory and modelling studies: WACCM has predominantly been used to simulate the vertical and seasonal distribution of the metal layers, using reaction rate coefficients measured in the laboratory, and making comparisons to Lidar (laser radar), satellite and sounding-rocket measurements [*Plane et al.*, 2015].
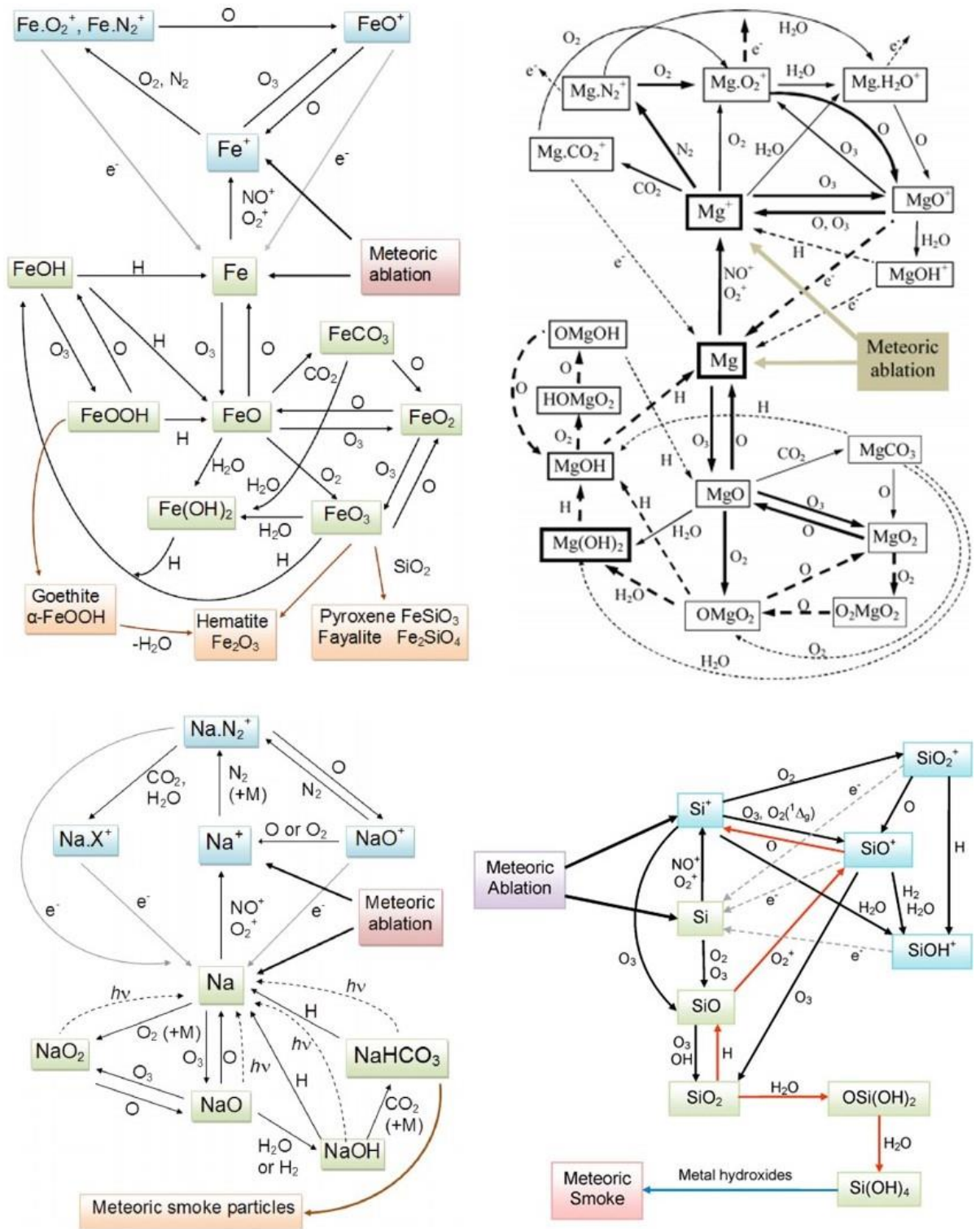
Figure 1.17. Schematic diagram showing the chemistry of Fe, Mg, Na and Si in the MLT. Figure compiled from *Plane and Whalley* [2012]; *Plane et al.* [2015]; *Plane et al.* [2016].

The metal layers were first quantitatively detected in the 1950s using ground-based photometry that measured fluorescence from transitions of metal atoms excited by solar radiation [*Hunten*, 1967]. Vertical profiles of Na, K, Fe and Ca$^+$ were established with this technique using emission

lines from airglow measurements during twilight when the solar terminator passed through the MLT. Since the 1970s and the development of tuneable lasers, resonance lidars have been used to record density profiles for Na, K, Li, Ca, Ca$^+$, Fe, and most recently Ni (see *Collins et al.* [2015]; *Gerding et al.* [2019]; *Plane et al.* [2015] and references therein). Lidar operates by firing a pulsed laser beam (tuned to a known spectroscopic transition) upwards through the atmosphere where it is Rayleigh scattered by air molecules, and resonantly scattered by the metal atoms. A small fraction of the light returns to the ground, where it is collected by time-resolved photon counting to provide the height of the scattering layer, and the absolute metal density is determined relative to the Rayleigh signal from the stratosphere [*Plane*, 2003]. Currently there are around 25 Lidar stations operating across the globe (see *Plane et al.* [2015] and references therein).

Sounding rocket flights currently provide the only *in situ* measurements of metals, since the MLT is inaccessible to direct sampling by high-altitude balloons or satellites, which reach a maximum of ~45 km and a minimum of ~150 km respectively [*Plane*, 2003]. However, the nature of this technique can lead to difficulties with contamination, payload launch/recovery and incur significant costs. Furthermore, due to the high speeds (> 1 km s$^{-1}$) only a brief snapshot can be recorded and fast instrument response times are necessary. Nevertheless, a number of measurements have been made of the altitude profiles of Fe$^+$, Mg$^+$, Ca$^+$, and Na$^+$ with rocket flights [*Kopp*, 1997]. Significant progress has also been made with satellite-borne optical spectrometers in the last 15 years. Odin's Optical Spectrograph and Infra-red Imager System (OSIRIS) spectrometer (Na, K), Envisat's Scanning Imaging Absorption Spectrometer for Atmospheric Chartography (SCIAMACHY, Mg and Mg$^+$) and the Global Ozone Measurement by Occultation of Stars (GOMOS) spectrometer (Na) have enabled near-global coverage of the metal layers through limb measurements of solar-pumped resonance fluorescence or stellar occultation (see *Plane et al.* [2015] and references therein).

This set of observations, over a range of latitudes and seasons, has enabled global models of the metal layers to be tested in detail. *Feng et al.* [2013] and *Marsh et al.* [2013a] updated the chemistry scheme in WACCM to include the reactions of neutral and ionic Fe and Na, respectively. The influx of metals to WACCM is defined by a MIF which is itself derived from CABMOD, taking into account variations in the astronomical sources of meteoroids, their mass, velocity, entry angle and the ablation efficiencies of the different metal constituents. In both modelling studies, Na and Fe were found to exhibit a wintertime maximum and summertime minimum, through a combination of temperature-dependent chemistry and the meridional transport of metallic species from the summer to winter hemisphere (Figure 1.18). In 2015, the chemistry of Mg was modelled with WACCM, and was also found to exhibit a wintertime maximum and summer minimum (Figure 1.19) [*Langowski et al.*, 2015]. The chemistry of Si has been established most recently [*Plane et al.*, 2016], and displays different seasonal behaviour to the other metals, showing a late summertime maximum and wintertime minimum (see Figure 1.19). This results from an increase in photoionization (R1.13) during the longer periods of sunlight in summer generating more Si$^+$, which is closely coupled to SiO (see Figure 1.17).

R1.13  $Si + h\nu \rightarrow Si^+ + e^-$
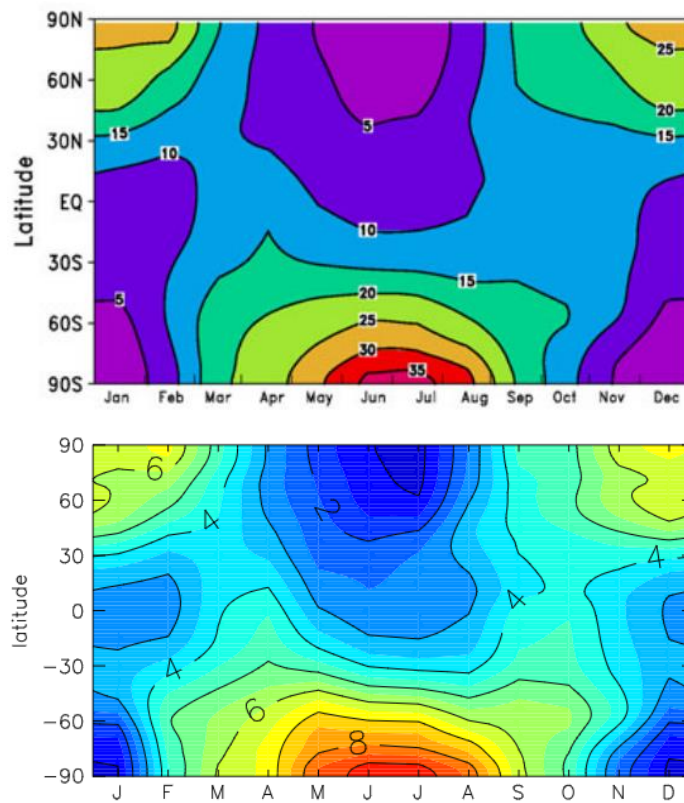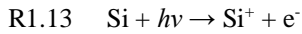


Figure 1.18. Top panel: Output from WACCM showing the mean Fe column abundance ($10^9$ cm$^{-2}$) between 70 and 120 km. Bottom panel: Output from WACCM showing the monthly mean Na total column abundance ($10^9$ cm$^{-2}$) between 70 and 120 km.
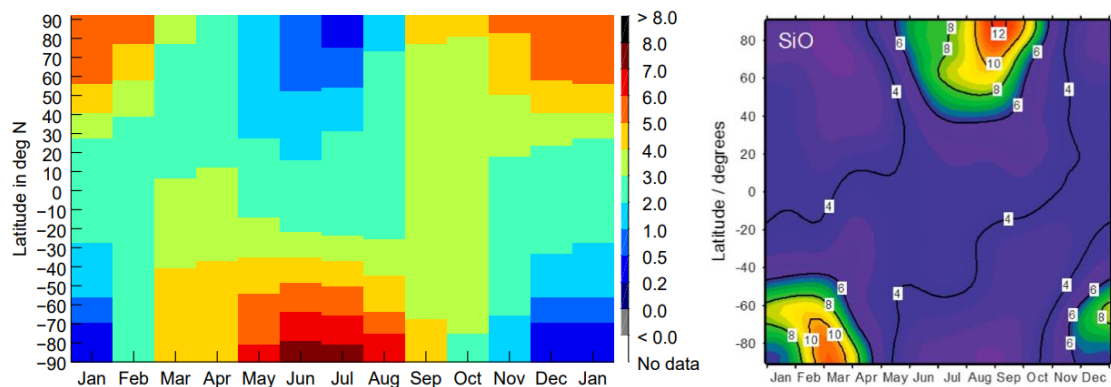


Figure 1.19. Left panel: Output from WACCM showing the Mg column density (in $10^9$ cm$^{-2}$) as a function of latitude and time. Figure from *Langowski et al.* [2015]. Right panel: Output from WACCM showing the SiO column density (in $10^9$ cm$^{-2}$) as a function of latitude and time. Figure from *Plane et al.* [2016].

#### 1.2.1.3.4    Meteoric Smoke Particles

Over a timescale of several days, the stable metal reservoir species can react, condense and coagulate to form MSPs – thought to be 'fluffy', porous, fractal-like agglomerates [*Saunders and Plane*, 2006]. MSPs are thought to have radii on the order of 1-10 nm in the MLT, and to coagulate

to larger sizes as they sediment to lower altitudes [*Bardeen et al.*, 2008; *Megner*, 2008; *Plane et al.*, 2014]. The physical and chemical properties of these particles are still unclear, though it is important to establish their composition and behaviour because MSPs participate in a number of atmospheric processes (discussed below). The sampling and characterisation of MSPs has been particularly challenging due to the inherent difficulties with performing *in situ* studies in the MLT. Currently only two techniques have had any success: rocket-borne instruments and remote sensing with optical spectroscopy – note that 'optical' spectroscopy here (and throughout this thesis) refers to measurements in the visible as well as the UV and infra-red (IR) regions of the spectrum. Sounding rocket flights currently provide the only direct sampling of MSPs, though only charged particles have been detected. The ECOMA (Existence and Charge state Of Meteoric smoke particles in the middle Atmosphere) rocket campaign employed a Faraday cup detector combined with a photoionization instrument to constrain MSP size (~0.5 –3 nm at ~80 - 105 km) and the work function (∼4 - 4.6 eV). Subsequent electronic structure calculations suggested the most likely composition to be Fe and Mg hydroxide clusters with low silica content [*Rapp et al.*, 2012; *Rapp et al.*, 2011; *Rapp et al.*, 2010].

Major progress has been made with optical spectroscopy – the SOFIE (Solar Occultation for Ice Experiment) on the AIM (Aeronomy of Ice in the Mesosphere) satellite has carried out solar occultation measurements from 2007 to present, conducting the first remote observations of MSPs in the MLT [*Hervig et al.*, 2009]. Optical extinction measurements (discussed further in section 1.2.2.4) at 330 nm, 867 nm and 1037 nm suggest that MSPs are formed of iron-rich oxides (magnetite ($Fe_3O_4$), wüstite (FeO), magnesiowüstite ($Mg_xFe_{1-x}O$, x=0-0.6)) or iron-rich olivine ($Mg_{2x}Fe_{2-2x}SiO_4$, x=0.4 - 0.5) – see Figure 1.20 [*Hervig et al.*, 2017]. However, these compositions should not be considered a definitive list of MSP candidates, since the measurements have large uncertainties (particularly at 330 nm) and around 12 % of the measured data (ratios of extinctions at pairs of wavelengths) cannot be explained with any the compositions considered. Moreover, it cannot be definitively established using current techniques whether mixed smoke compositions are present (considering this possibility, the measured data can be replicated with an extensive list of possible mixtures).

This technique also relies on the use of refractive indices (RIs) previously measured in the literature for bulk (crystalline) minerals, and therefore necessitates an important assumption: that these RIs are applicable to MSPs, despite evidence that they are likely to be structurally amorphous [*Saunders and Plane*, 2006]. This assumption is currently still under debate, and so measurements of RIs for candidate smoke species formed under atmospherically relevant conditions would be desirable. It is especially important to measure RIs for iron-rich analogues, since MSPs are likely to be iron-rich, with the major components being Fe, Mg, Si and O – either as a single olivinic composition, or as a mixture of metal oxides and silica. The extinction from pure $SiO_2$ is significantly smaller than that from iron-rich compounds [*Saunders and Plane*, 2006], meaning that if MSPs are composed of multiple distinct phases, the optical properties of iron oxides are likely to be of particular importance.
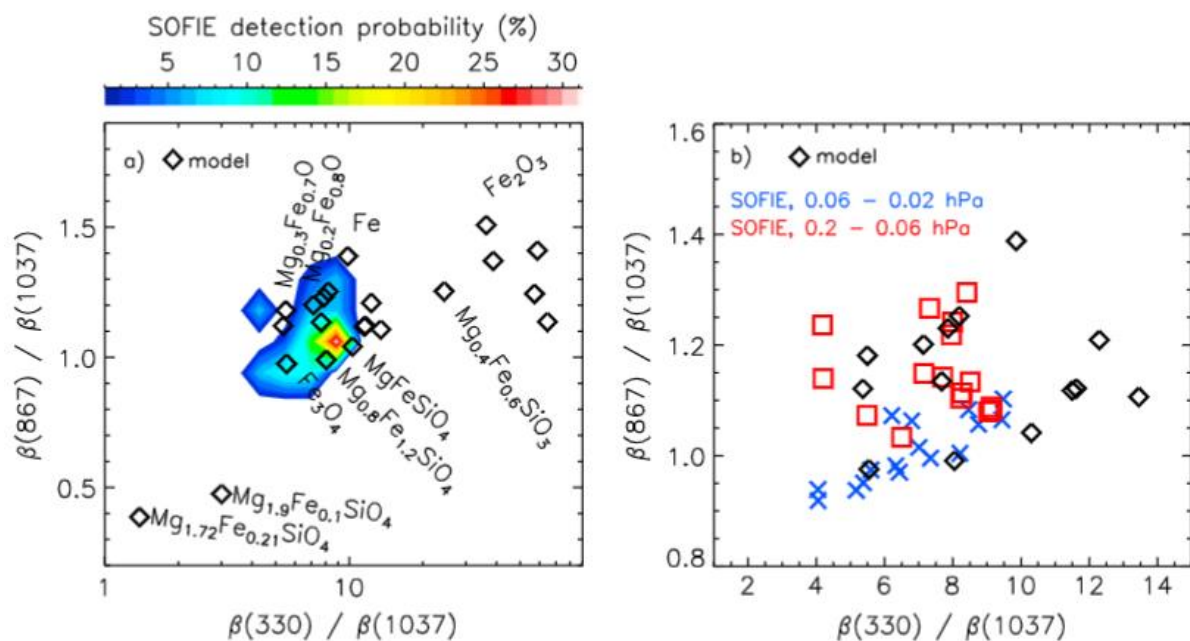
Figure 1.20. The extinction ratio between the three wavelengths probed by the SOFIE experiment on the AIM satellite (330 nm, 867 nm and 1027 nm). Data shown as 15 day averages from April-May 2011 (~70 °S), compared to simulated results for various MSP compositions. The left panel shows the SOFIE measurements as a probability distribution at pressures between 0.2 - 0.02 hPa. Modelled data are shown as black diamonds, though not all points are labelled for clarity. The right panel shows the SOFIE results as discrete datapoints for either 0.2 - 0.06 hPa or 0.06 - 0.02 hPa, with model points shown but not labelled. Note the different scales for the left and right panels. Figure adapted from *Hervig et al.* [2017].

In light of the uncertainties that remain regarding the structure and composition of MSPs, two notable laboratory techniques have been developed for producing MSP analogues, and evaluating their optical properties. First, a low-pressure, non-thermal microwave resonator has recently been used to generate a number of crystalline MSP analogues with radii on the order of ~2 nm [*Nachbar et al.*, 2018b; *Nachbar et al.*, 2016]. So far, iron oxide ($Fe_2O_3$), silica ($SiO_2$) and iron silicates ($Fe_xSi_{(1-x)}O_3$ where $0 \leq x \leq 1$) have been produced with this setup [*Nachbar et al.*, 2018b]. After particle production, MSP analogues are transferred to a low-pressure supersaturated particle trap: the Molecular flow Ice Cell in the Trapped Reactive Atmospheric Particle Spectrometer (MICE/TRAPS). This apparatus enables particle properties to be determined such as absorption efficiencies and ice nucleating characteristics, and has been used in this work to determine the absorption of iron oxide MSP analogues (see Chapter 2 for further details of the methods used).

The second technique used to study MSP analogues is the Photochemical Aerosol Flow System (PAFS), which has previously generated amorphous particles *via* the photolysis, and subsequent agglomeration of, metal precursors such as iron pentacarbonyl ($Fe(CO)_5$) in the presence of $O_2/O_3$. Agglomerates with iron oxide ($Fe_2O_3$), goethite (FeOOH), fayalite ($Fe_2SiO_4$) and silica ($SiO_2$) compositions have been produced [*Saunders and Plane*, 2006; 2010; 2011]. Particle size distributions were recorded with a Scanning Mobility Particle Sizer (SMPS) and the optical extinction was measured, for comparison to values determined using Mie theory with literature RIs for the unidentified particles (for further discussion of Mie theory see section 1.2.2.4.1). While the work of *Saunders and Plane* [2006; 2010] was able to reproduce the experimental size

distributions of particles generated with the PAFS using an agglomeration model [*Jacobson*, 2005], there was significant uncertainty in the measured distribution. As such, though the measured extinction (of $Fe_2O_3$ and $Fe_2SiO_4$) could be replicated using Mie theory for a log-normal size distribution, it could not be replicated with the measured distributions. Another reason for this could be due to the particle morphology – imaging with Transmission Electron Microscopy (TEM) revealed the particles to be structurally amorphous and fractal-like in nature (Figure 1.21). The techniques developed by *Saunders and Plane* [2006; 2010; 2011] have been extended in this work such that smaller particle extinctions could be measured, and an iterative photochemical model has been developed to derive refractive indices for the particles.
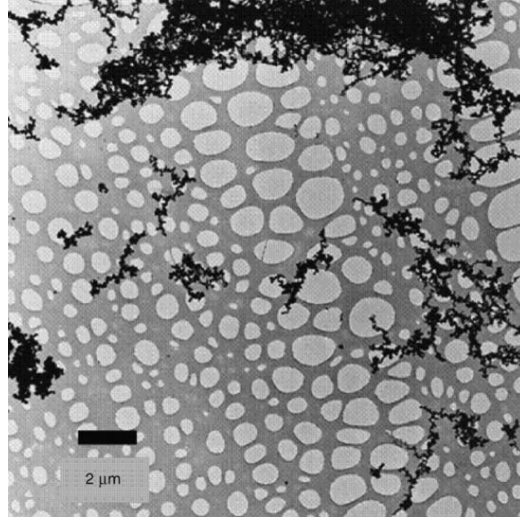


Figure 1.21. TEM image obtained of $Fe_2O_3$ agglomerates (black particles) produced from a mixture of $Fe(CO)_5$ and $O_2/O_3$. The particles are deposited on a holey carbon grid (light grey holes and webbing) [*Saunders and Plane*, 2006].

### 1.2.1.3.5   Polar Mesospheric Clouds

An important reason for studying MSPs in the MLT is their connection to PMCs. These clouds have been appearing since 1885 with increased frequency, brightness and latitudinal extent, and are widely considered to be an unambiguous signal of climate change [*Thomas and Olivero*, 2001]. PMCs form in the summer mesosphere at ~85 km when the temperature in the polar mesosphere is at its coldest (<150 K) and the frost point of $H_2O$ is reached. Though water ice is the primary component of PMCs [*Hervig et al.*, 2001], the nucleation of this ice in such a dry region of the atmosphere long puzzled the research community because supersaturation ratios are not considered high enough for homogeneous nucleation to occur except under extreme conditions (<110 K) [*Murray and Jensen*, 2010]. Heterogeneous nucleation via pre-existing condensation nuclei is therefore deemed necessary [*Megner*, 2008] and MSPs are widely considered to be the most likely nuclei. There is strong evidence that PMCs cause depletion of the Fe, Na, and K layers due to heterogeneous removal onto ice aerosol [*Murray and Plane*, 2005; *Plane et al.*, 2004]. However, understanding the interactions between the metal layers, MSPs and PMCs is not trivial, since the phenomena are interlinked by feedback mechanisms and performing *in situ* studies is difficult. Furthermore, the structure and composition of MSPs is still unclear.

Elucidating the structure and composition of MSPs is thus important for understanding PMCs. In the context of an extreme dust-loading, a significant disruption to mesospheric metal chemistry and the MSP density or size distribution could affect the brightness and occurrence-frequency of PMCs, which may then have feedbacks on the metal layers. Any change to the typical meridional circulation could also affect the availability of nuclei. However, this is an avenue for future research since these interactions are not parametrised in the global-climate model used in this study.

## 1.2.2 The Stratosphere

### 1.2.2.1 Physical and Dynamical Characteristics

In the mesosphere, the temperature increases with decreasing altitude (Figure 1.10) down to the stratopause, at which a local temperature maximum is observed. In contrast, stratospheric temperatures decrease with decreasing altitude, down to an altitude of ~30 km where they approach the local minimum that occurs at the tropopause (~10-12 km, see Figure 1.1). Breaking gravity and planetary waves generate a meridional circulation that transports material into the stratosphere and down the winter polar vortex. Similar wave processes drive stratospheric circulation from the equator to the poles (Figure 1.22) [*Bönisch et al.*, 2011] and also lead to localized patches of 3-D turbulence and thus mixing of chemical species [*Haynes*, 2005]. These transport patterns lead to a strong enhancement of meteoric material at high latitudes, which has been measured *in situ* [*Weigel et al.*, 2014] and modelled with WACCM [*Bardeen et al.*, 2008; *Gómez Martín et al.*, 2017].
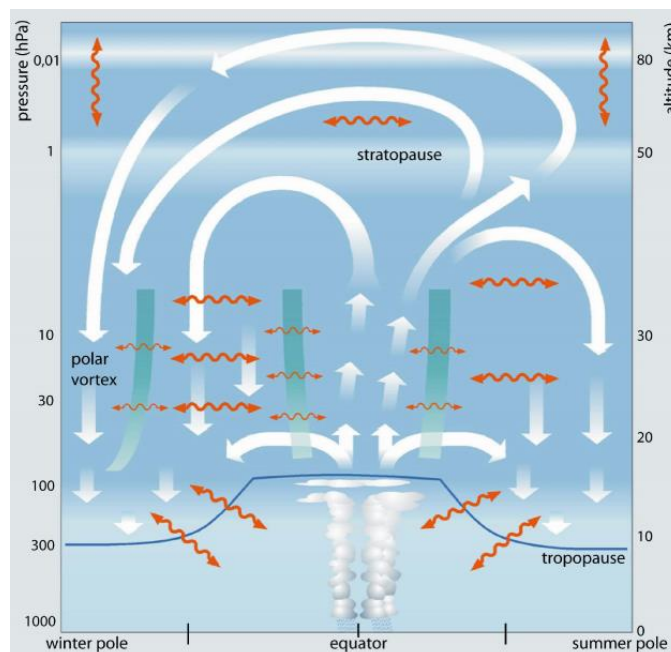


Figure 1.22. Schematic showing the residual circulation and mixing in the stratosphere and mesosphere. Thick white arrows represent the residual circulation (net mass transport) patterns and the wavy orange arrows show two-way mixing. Thick green lines indicate transport and mixing barriers. Image from *Bönisch et al.* [2011].

## 1.2.2.2 Gas-Phase Chemistry

The cold temperatures (< 230 K) in the stratosphere at altitudes of ~ 20 km facilitate condensation of sulfates to form a layer of SSA that exists predominantly in the form of $H_2SO_4/H_2O$ droplets [*Junge and Manson*, 1961; *Junge et al.*, 1961]. This phenomenon leads to a relatively low concentration of $H_2SO_4$ in the gas-phase ($10^4$ - $10^5$ cm$^{-3}$ outside of periods of major volcanic activity). As the temperature increases between 30 and 35 km, the amount of gas-phase $H_2SO_4$ increases to $10^6$ - $10^7$ cm$^{-3}$ [*Saunders et al.*, 2012]. However, above this altitude the concentration unexpectedly falls; data from balloon flights above 40 km indicate concentrations between $10^4$ and $10^5$ cm$^{-3}$ [*Arijs et al.*, 1983; 1985]. A number of explanations have been proposed to explain this decrease, although uptake onto MSPs is a strong candidate (see section 1.2.2.3.1).

Stratospheric aerosol is formed by the uptake of $H_2SO_4$, which is itself formed by the sequential oxidation of various sulfur sources – either meteoric S or terrestrial sources such as dimethyl sulphide (DMS) from oceanic emissions, or OCS and $SO_2$ from explosive volcanism or anthropogenic emissions (see Figure 1.23). The density of S in the MLT is typically very small due to the rapid oxidation of meteoric S by $O_2$ (R1.14). As such, the most abundant S species in the MLT is SO, which forms a layer at ~92 km (peak abundance ~$1.5 \times 10^5$ cm$^{-3}$). SO is further oxidised by R1.15 to form the comparatively inert $SO_2$. Since there are few sinks of SO or $SO_2$, their spatiotemporal distribution is controlled by transport, and these species are transported down to lower altitudes, predominantly in the winter polar vortex. $SO_3$ is formed indirectly from $SO_2$, *via* the intermediate $HOSO_2$ (R1.16 & R1.17) though the density of this intermediate species is insignificant compared to the other S oxides. The addition of $H_2O$ finally leads to the formation of $H_2SO_4$ (R1.18). Photolysis facilitates the reduction of $H_2SO_4$, $SO_3$, $SO_2$ and SO to their counterpart species with lower oxygen content.

R1.14     $S + O_2 \rightarrow SO + O$

R1.15     $SO + OX \rightarrow SO_2 + X$     (where X is O, $O_2$ or H)

R1.16     $SO_2 + OH (+M) \rightarrow HOSO_2 (+M)$

R1.17     $HOSO_2 + O_2 \rightarrow HO_2 + SO_3$

R1.18     $SO_3 + H_2O \rightarrow H_2SO_4$
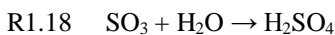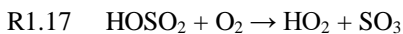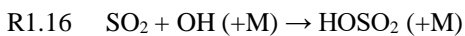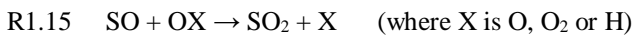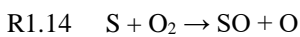
A sulfur (S) MIF and this gas-phase chemistry scheme have recently been incorporated into WACCM to study the impact of meteoric S from the thermosphere to the stratosphere (~20-120 km) [*Gómez Martín et al.*, 2017]. Results from the simulations were compared to observations to establish the global influx of cosmic S (~1.0 t d$^{-1}$) – two orders of magnitude smaller than the flux from terrestrial sources. However, the focusing of this S into the polar vortices by the residual circulation means that cosmic S constitutes a substantial fraction of the sulfur dioxide ($SO_2$) in the winter polar upper stratosphere (~30 % at 50 km). The Antarctic sulfate aerosol layer was thus found to be very sensitive to an increase in the S-MIF, particularly in springtime.
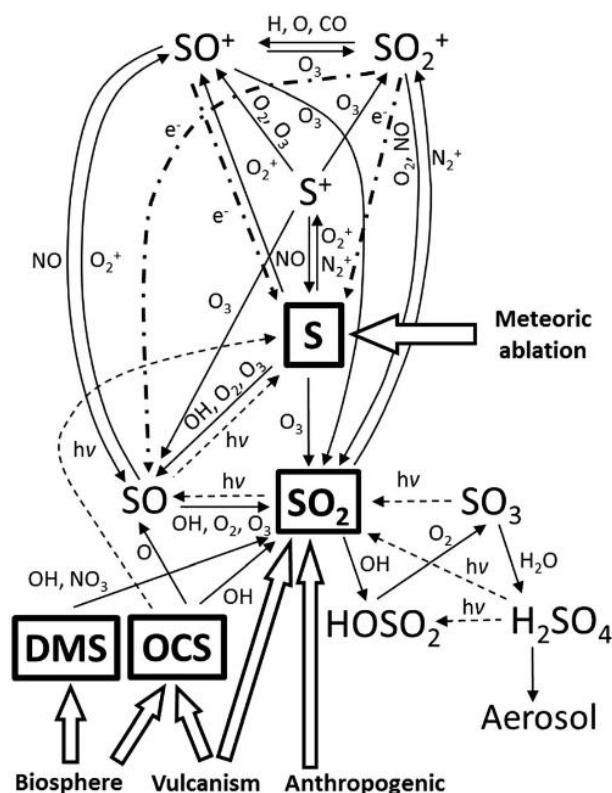
Figure 1.23. Schematic diagram showing the atmospheric S cycle. Solid lines indicate chemical processes, dashed lines indicate photolysis and dot-dash indicates recombination reactions. Sources/emissions of sulfur compounds are surrounded by a square box [*Gómez Martín et al.*, 2017].

### 1.2.2.3 Aerosols

#### 1.2.2.3.1 Uptake to MSPs

Through 1-D modelling, *Turco et al.* [1981] introduced the idea that meteoric dust could be an important constituent of stratospheric aerosol and affect their observable properties. A more recent 2-D modelling study of $H_2SO_4$ photolysis [*Mills et al.*, 2005] found that none of the proposed photolysis mechanisms could account for the observations above 40 km, similarly suggesting an additional, permanent loss mechanism such as neutralisation by meteoric dust. *In situ* observations in the lower stratosphere have shown that more than 50 % of stratospheric aerosol contains Mg and Fe at 20 km, with this fraction becoming more important with increasing altitude [*Murphy et al.*, 2007]. This was confirmed by the observations of *Hervig et al.* [2009] who demonstrated the first observations of MSPs in the upper stratosphere. A relatively recent study by *Neely et al.* [2011] performed 3-D modelling with WACCM coupled to some elements of the Community Aerosol and Radiation Model for Atmospheres (CARMA) module for aerosol microphysics (discussed further in Chapter 4, section 4.3). This study derived aerosol extinction profiles with and without MSPs, and compared these to observations, concluding that MSPs contribute a significant proportion to the observed aerosol extinction down to altitudes of ~ 25 - 30 km at mid-latitudes and 35 km in the tropics.

The loss of SSA to MSPs has also been explored by *Saunders et al.* [2012] through a combined laboratory-modelling approach. The modelling part of the study probed the MSP distribution needed to explain the available observations with the global climate model UM-SLIMCAT. The laboratory work measured dissolution rates of MSP analogues in $H_2SO_4/H_2O$ solutions. Using these two approaches the $H_2SO_4$ decrease above 40 km was accounted for with a global meteoric input of 20 t d$^{-1}$ and an uptake coefficient $\geq 0.01$. Since the uptake of gas-phase species such as $H_2SO_4$ onto MSPs is significant at the typical ambient concentrations of these species in the middle atmosphere, there are likely to be notable effects on aerosol processes following a significant disruption to these species from the simulated close encounter with Halley's Comet explored in the present study. The interaction of these species will be investigated by probing the effects of an increased input of both MSPs and meteoric S on gas-phase and aerosol chemistry.

MSPs have also been implicated in the uptake of other species to form SSA; *Prather and Rodriguez* [1988] first proposed that MSPs provide an important sink for $HNO_3$ in the middle atmosphere, and both recent modelling and laboratory studies have confirmed this. Modelling work has shown that heterogeneous aerosol chemistry is required to explain the discrepancy between observed and modelled gas-phase $HNO_3$ – the concentration of which is over-predicted in models when only accounting for gas-phase chemistry [*Funke et al.*, 2011; *Jucks et al.*, 1999]. Recently, *Frankland et al.* [2015] measured uptake coefficients for a number of MSP analogues (e.g. $MgFeSiO_4$ and $Fe_2O_3$) in the laboratory, using a Knudsen cell apparatus. These were then included in WACCM simulations, coupled with CARMA. Introducing heterogeneous uptake of $HNO_3$ to the model resulted in significant seasonal losses in gas phase $HNO_3$ (across the winter hemisphere), compared to a control simulation without this interaction [*Frankland et al.*, 2015; *James*, 2016]; the uptake of $HNO_3$ on MSPs *via* the formation of metal nitrates was suggested to be the most important loss process for $HNO_3$ within the polar vortex from 30 - 60 km.

The uptake of $HO_2$ onto MSPs has also been shown to be important in the winter polar vortex, potentially helping to explain the discrepancy between modelled and observed $HO_2$ concentrations in the middle atmosphere (the "HO$_x$ dilemma") [*Millán et al.*, 2015]. A recent combined laboratory and modelling study measured uptake coefficients for $HO_2$ on various olivinic MSP analogues [*James et al.*, 2017]. A dependence on composition was observed for the MSP analogues, which electronic structure calculations revealed was most likely a result of preferable binding to Fe sites. However, as for the uptake of $H_2SO_4$ and $HNO_3$, the extent of this effect is difficult to quantify in the atmosphere due to the current lack of knowledge regarding the composition, structure and total influx of MSPs; this leads to uncertainties in both the surface area available for heterogeneous reaction and the uptake coefficients for the adsorbing species. Furthermore, the uptake of $HNO_3$ and $HO_2$ to MSPs is inherently linked since the gas-phase reactions of HO$_x$ and NO$_x$ involve a number of the same species (e.g. OH, NO). As such, any effect on (or uncertainty in) one of these can alter the balance of the other.

**1.2.2.3.2    Polar Stratospheric Clouds**

MSPs have been implicated in the nucleation of PSCs, which are formed from different types of particles that consist of $H_2O$, $H_2SO_4$ and $HNO_3$ [*James et al.*, 2018; *Peter and Grooß*, 2012]. These clouds are formed in the winter polar stratosphere at altitudes between around 15 - 25 km and temperatures below ~210 K. PSCs are thought to facilitate heterogeneous chemistry that can lead to the activation of halogen radicals that catalytically destroy ozone [*Solomon*, 1999]. This can occur *via* heterogeneous reactions such as reaction R1.19, or by the removal of nitrates from the gas phase, either temporarily *via* condensation (e.g. R1.20) or permanently *via* sedimentation of these particles (denitrification) [*Peter*, 1997]. This slows down the formation of $ClONO_2$ (*via* reactions such as R1.21), thus preventing the deactivation of ClO, and leading to increased $O_3$ destruction [*Wegner et al.*, 2012]. Given that MSPs are possible nuclei for PSCs, a close cometary encounter is likely to impact the occurrence of PSCs and thus affect $O_3$ chemistry, having the potential to alter the radiative balance of the atmosphere. These effects have not been explored in this work, as appropriate parametrisations have not yet been developed for the interactions of PSCs in the global climate model used. However, this would be an interesting avenue for future development.

R1.19    $XNO_3 + H_2O \rightarrow HNO_3 + HOX$    (where X is Cl or Br)

R1.20    $N_2O_5 + H_2O \rightarrow 2HNO_3$

R1.21    $ClO + NO_2 (+ M) \rightarrow ClONO_2$
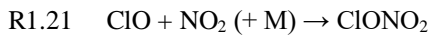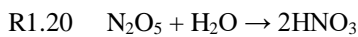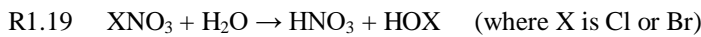
**1.2.2.4    Light Extinction & Radiative Balance**

The studies discussed in section 1.2.2.3 demonstrate that MSPs represent an important component of atmospheric aerosols, with the ability to affect both aerosol processes and related gas-phase chemistry. The interaction of light with aerosols is an important process that can affect the global balance of incident and outgoing radiation (radiative balance) in the atmosphere, and this remains one of the main sources of uncertainty in the prediction of current and future climate scenarios [*Myhre et al.*, 2013]. Aerosols can have both direct and indirect effects on radiative forcing (the extent to which the radiative balance is affected) by either direct interaction with incident light, or by influencing the properties of clouds. As such, elucidating the properties of MSPs and their role in the formation both aerosols and clouds is of wider interest than to just the scientific community whose research directly relates to cosmic dust.

**1.2.2.4.1    The Interaction of Light with Particles**

There are a number of possible interactions of light with particles. However, the processes of absorption and scattering of light not only define the radiative properties of a particle but can also be used for the purposes of characterisation. Scattering is defined as the re-radiation of incident light by a medium – either elastically, i.e. at the same energy, or inelastically, i.e. with a different energy. Absorption is the transformation of part of the incident electromagnetic energy into

another form, such as thermal energy [*Bohren and Huffman*, 1983]. These processes are represented schematically in Figure 1.24. The extent to which light is perturbed as it passes through a medium is described by the complex refractive index (RI);

E1.1
$$m = n + ik$$

where the real part (*n*) describes the extent of scattering and the imaginary part (*k*) describes the extent of absorption. These are not mutually independent processes and are related by the Kramers-Kronig relations such that *n* is related to the differential of *k*. *n* is a measure of the speed of light in a vacuum (*c*) compared to its propagation speed in a medium (*v*), and is thus always greater than 1 (as $n = c / v$ ) [*Bohren and Huffman*, 1983]. Both absorption and scattering depend on the microscopic properties of the material such as the mass density of molecules, the polarizability and the local electric field experienced by particles [*Liu and Daum*, 2008]. As such, RIs are characteristic of an individual substance. For a particular medium, the measured RI varies with wavelength ($\lambda$). Small variations with temperature and pressure can also be observed, though these are typically much less pronounced than variations with wavelength.
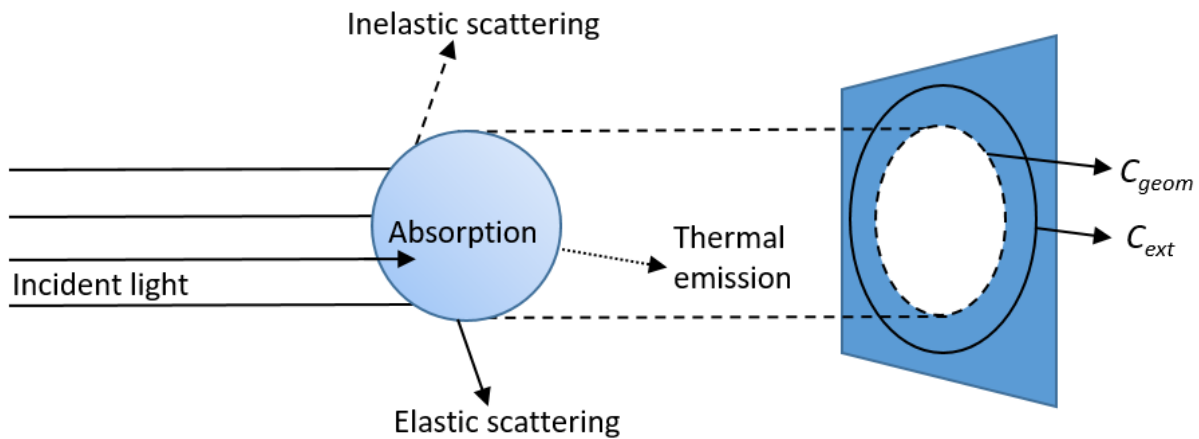


Figure 1.24. Schematic representing the interactions of a particle with incident light, including a representation of the extinction cross section ($C_{ext}$) with respect to the geometric cross section ($C_{geom}$).

The optical properties of a material also vary with size, and can be characterised by the ratio between the particle radius (*r*) and the illumination wavelength:

E1.2
$$x = \frac{2\pi r}{\lambda}$$

This size parameter (*x*) defines certain size regimes in which different levels of theory can be applied to calculate the absorption and scattering of particles. When particles are significantly smaller than the wavelength of incident light ($< \sim\lambda/20$) they are said to exhibit Rayleigh scattering – an elastic scattering mechanism that is more efficient at short wavelengths and is independent of particle shape. When particles are on the order of, or larger than, the incident wavelength, their behaviour can be described by Mie theory. Mie scattering exhibits an angular dependency, with stronger scattering in the forward direction. Mie theory provides an exact solution in both size regimes, though under the assumption that particles are - or can be treated as - homogeneous spheres in an isotropic medium [*Sorensen*, 2001]. For this reason, Mie theory is widely used in

atmospheric science since, unlike Rayleigh theory, it has no upper size limit. In either size regime, the amount of light interacting with a particle can be expressed as the absorption ($C_{abs}$) and scattering ($C_{sca}$) cross sections, expressed in units of area – these can differ from the geometric cross section ($C_{geom}$). The extinction cross section ($C_{ext}$) represents the sum of the contributions from absorption and scattering (E1.3) and can be thought of as the 'shadow' cast by the illuminated object (Figure 1.24) [*Bohren and Huffman*, 1983].

E1.3 $$C_{ext} = C_{abs} + C_{sca}$$

### 1.2.2.4.2   Light Extinction in the Atmosphere

Modelling the effects of a large dust loading into the terrestrial atmosphere has focused on the after effects of nuclear war, predicting the occurrence of a large atmospheric dust cloud (composed of black carbon) with damaging consequences for the planet: surface temperature, precipitation and insolation reductions large enough to stimulate destruction of the global ozone layer, the collapse of global agriculture, and the starvation of billions of people [*Mills et al.*, 2014; *Robock et al.*, 2007]. In an analogous manner, there are a number of studies on the atmospheric impacts of an asteroidal or cometary impact event. These studies have largely been from the perspective of quantifying the risk to life or property and establishing energy thresholds for environmental catastrophe [*Brown et al.*, 2013; *Gi et al.*, 2018; *Toon et al.*, 1997]. It has been found that even small (~tens of metres) objects could cause significant damage [*Chapman and Morrison*, 1994] and that effects related to dust-loading are likely to be the most significant manner by which the atmosphere is perturbed in such events (with the dust either injected directly during atmospheric entry or as a consequence of mass biomass burning) [*Toon et al.*, 1997].

The atmospheric implications of a cosmic dust loading have been investigated previously in the context of assessing the possible role of MSPs in the initiation of glaciation episodes in the Neo-Proterozoic era (1000–540 million years ago). *Saunders et al.* [2007] used a 1-D particle physics model to analyse the hypothesis of *Pavlov et al.* [2005] that the passage of the Earth through a large molecular cloud could have resulted in sufficiently large negative direct radiative forcing to initiate a global ice age. This study demonstrated that the optical effects of a cosmic dust loading are likely to be significantly reduced if fractal-like MSPs are considered rather than spherical ones (see Figure 1.25). As such, they concluded that MSPs were unlikely to have initiated the ice-ages unless the flux was ~250 times present day levels (note the dust loading considered in this thesis (see Chapter 4) represents ~10,000 times the daily input injected over ~1 hour, or ~25 times the annual flux if averaged across one year). However, if MSPs are effective ice nuclei, then subsequent indirect forcing through ice-cloud formation could have made a more significant contribution to the onset of the glaciation episodes. Furthermore, a 1-D model does not take into account the significant latitudinal variation in the stratospheric MSP density. A 3-D modelling approach would therefore provide a much greater insight into the impacts of a high dust flux on

the radiative forcing – though it is important to first constrain the optical properties of MSPs in order for such a study to yield a reasonable representation of the possible effects.
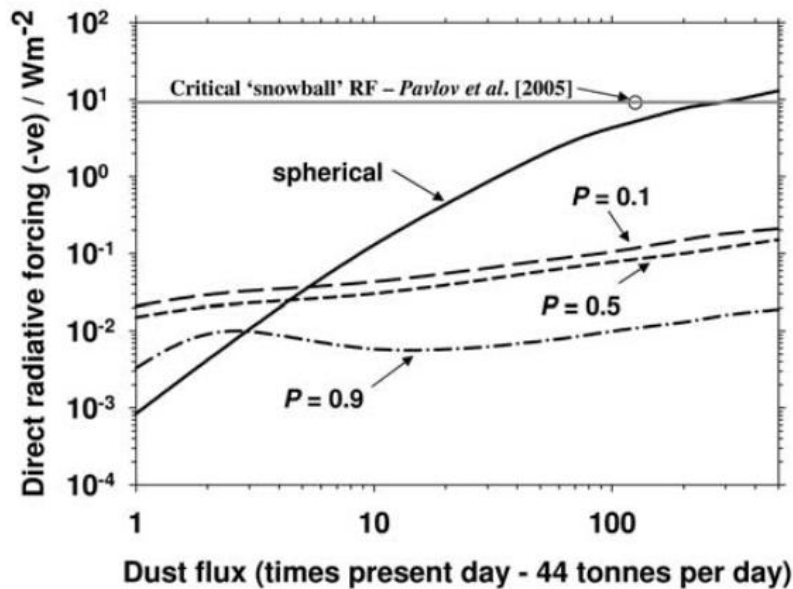


Figure 1.25. Radiative forcing (RF) resulting from the light extinction by fayalite MSPs, as a function of the influx of material to the atmosphere. Values are shown for spherical and fractal particles with different porosities (P). The critical level of radiative forcing required to initiate the global ice-age (9.3 W m$^{-2}$, calculated by *Pavlov et al.* [2005]) is indicated with a solid line [*Saunders et al.*, 2007].

Another context in which the climatic effects of an atmospheric dust loading has been explored is the field of volcanology. Explosive volcanic eruptions can inject dust and gases such as $SO_2$ directly into the stratosphere, where they form aerosols *via* reaction with ambient molecules. These aerosols can lead to short-term cooling at both regional and global scales, caused both directly by the absorption and scattering of light, and indirectly through the formation of clouds or as a catalyst for ozone depletion (as discussed in section 1.2.2.3). The dynamical and climatic effects of volcanic eruptions are strongly dependent on geographic location, though the complexities of these effects are still poorly understood [*Cooper et al.*, 2018]. Whilst similar in a number of ways, an explosive volcanic eruption or impact event differs from a cometary close encounter since the emitted dust would likely be preferentially injected into the stratosphere and troposphere, rather than to the MLT. The atmospheric implications would likely be considerably different in each case, and thus specific studies on a close encounter are necessary to be able to quantify these differences.

### 1.2.2.5   Global Cooling Event of 536 AD

A number of classical sources collated by *Stothers and Rampino* [1983] reference a range of environmental catastrophes between latitudes 30-41 °N, during the period 536-538 AD. These included a significant reduction in sunlight, 4 hour days, weather anomalies, widespread crop

failures and famine in Europe [*Budge*, 1932; *Chabot*, 1901; *Dewing*, 1916; *Hamilton and Brooks*, 1899; *Wachsmuth*, 1897]. After the identification of these historical records, it was suggested that the climatic consequences were due to a 'mystery cloud' that obscured the suns light and was caused by a large tropical volcanic eruption (the 'super-volcano argument') [*Stothers*, 1984]. This sparked widespread interest from the scientific community and the public that is still prominent today [*Bruner*, 2018; *Williams*, 2018]. Numerous attempts to characterise or explain the source of the 'mystery cloud' and corresponding temperature decrease have been published over the last 35 years, since despite evidence that this was one of - if not the most - severe and protracted short term cooling events in the last 2000 years, no definitive cause has been identified [*Larsen et al.*, 2008; *Scuderi*, 1993; *Sigl et al.*, 2015]. However, advances in modern technology and multi-proxy analysis approaches (using a combination of both tree-ring and ice core chronologies with historical records) have facilitated developments in the last 5 years that have propelled us ever closer to understanding the events of the 6th century 'dark ages'. This has been through the re-dating of sulfate layers in ice cores [*Sigl et al.*, 2015] and confirming the existence of the mystery cloud through the study of carbon isotope in tree-rings [*Helama et al.*, 2018].

### 1.2.2.5.1    Developments Since the 1980s

In the 20 years following the work of *Stothers* [1983; 1984], evidence was found in both Greenlandic [*Clausen et al.*, 1997; *Hammer*, 1984; *Zielinski et al.*, 1994] and Antarctic [*Hammer et al.*, 1997] ice core records that it was argued supported the super-volcano argument; sulfate deposits were located in the years $504 \pm 40$ AD [Hammer et al., 1997], 508 AD [*Zielinski et al.*, 1994], 528 AD and 533 A.D [Clausen et al., 1997]. However, there were significant uncertainties surrounding the dating of the layers. Additionally, none of them were sufficiently strong that they could be attributed to a volcano large enough to produce the reported effects, or the magnitude of the temperature anomaly implied by the analysis of tree-rings in the northern hemisphere (up to ~3 °C) [*Briffa et al.*, 1990; *Scuderi*, 1993]. The 536 AD eruption was postulated to be twice as large as the infamous Tambora eruption of 1815 [*Stothers*, 1984]. However, although this latter eruption produced a dim sun there was no reduction in the length of the day [*Rampino et al.*, 1988]. Furthermore, reductions in surface temperatures after Tambora and other large historic eruptions are typically on the order of a few tenths of a degree (see Figure 1.26) [*Self et al.*, 1981; *Swingedouw et al.*, 2017] - the climatic consequences of the mystery cloud far exceed that of any other volcanic cloud from the last three millennia.
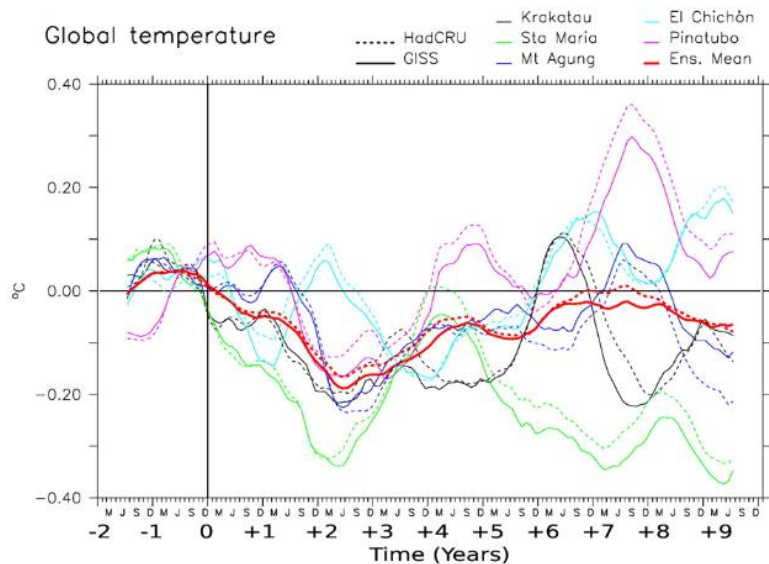
Figure 1.26. Temperature anomalies (°C) with respect to the three years prior to each eruption, for five major volcanic eruptions in the instrumental era: Krakatau (1883), Santa María (1902), Agung (1963), El Chichón (1982) and Pinatubo (1991). The vertical black line indicates the year in which the eruption occurs. Image from *Swingedouw et al.* [2017], temperature reconstruction data from the GISS and HadCRU models (*Hansen et al.* [2010] and [*Morice et al.*, 2012] respectively).

The uncertainties in the dating of the ice core sulfate deposits led to much speculation regarding the possible causes of the 6th century cooling; there have been various explanations proposed, including a large volcanic eruption, a cometary impact or a combination of the two. *Rigby et al.* [2004] reasoned that an airbursting comet (diameter ~300 m) could account for the cooling, based upon modelling simulations showing the formation of a plume that would focus energy and debris high into the atmosphere (Figure 1.27), though they had to make a number of important assumptions in their calculations (e.g. dust density, particle size, dust-to-gas ratio and transport rates). *Baillie* [2007] also made the case for a cometary impact based upon inconsistencies in the ice-core data, historical observations of comets in 539 and 541 AD and multiple accounts of meteor showers recorded by Chinese astronomers who noted that "stars fell like a shower" in the early 530s [*Imoto and Hasegawa*, 1958]. However, this work was largely speculative in nature.
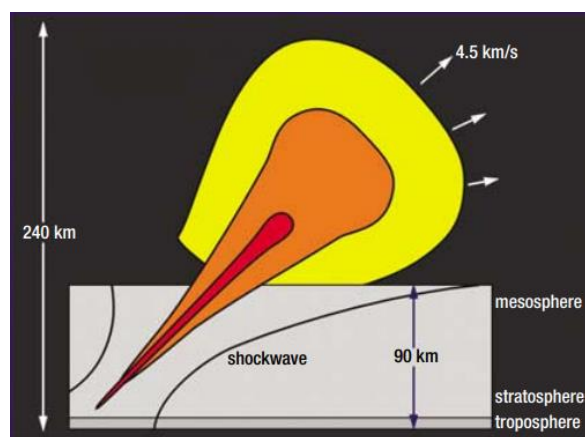


Figure 1.27. Schematic of a cometary airburst showing plume formation over the Earth 100 s after impact [*Rigby et al.*, 2004].

In the following few years, two further studies made the case for a large tropical volcanic eruption; sulfate deposits were identified in Greenlandic and Antarctic ice cores ($529 \pm 2$ and $533/534 \pm 2$ AD [*Larsen et al.*, 2008] and $531 \pm 15$ AD [*Ferris et al.*, 2011] in Greenland and Antarctica respectively). Nonetheless, *Abbott et al.* [2014a, 2014b] concluded both cometary and volcanic dust contributed to the global dimming in AD 536. They attributed part of the cooling to a low-latitude cometary explosion in the ocean, based on the elevated levels of Ni-rich particles and cosmic spherules detected in the GISP2 Greenland ice core, where the sulfate peak, dated at $539.2 \pm 3$ AD, was approximately the same size as that corresponding to the Tambora eruption. The elemental abundances observed suggested cometary material, well preserved marine diatoms, $CaCO_3$ and feldspar (most likely from a low-latitude source) were also found in the high latitude GISP2 ice-core – though given the small sample sizes these were found at high but not unprecedented levels, and it is possible that they could have been transported from low latitudes without any extra-terrestrial influence.

Though orbital calculations using the model of *Chambers* [1999] suggested the Eta-Aquarids was an important source of cometary debris in the sixth century, and observations detail that the apparition of Halley's comet in 530 AD had one of the highest absolute magnitudes of all apparitions between 239 B.C and 1682 AD [*Kronk*, 1984], there were still inconsistencies with the timing of the maximum dust loading (533 AD) observed by *Abbott et al.* [2014a]; *Abbott et al.* [2014b], and both their observations in the ice-cores and historical accounts of the 'mystery cloud'. It should be noted, however, that in recent work unrelated to the 536 AD cooling event, dynamical simulations of dust streams produced by Halley's comet have determined that there was an exceptionally strong visible outburst in the Eta-Aquarids meteor shower in 531 AD resulting from old dust streams produced during three different perihelion passages (295, 374 and 451 AD) [*Kinsman and Asher*, 2017]. This was noted to be the strongest meteor outburst from Halley's comet during the period from 250–600 AD, and supports the idea that cometary material could be at least partly responsible for the 6th century 'mystery cloud'. This idea that there could be a cometary contribution to the 6th century dust-loading will be explored in this work – for further discussion see section 1.3.2.

### 1.2.2.5.2   Developments Since the Initiation of this Project

Controversy continued between volcanologists and dendrochronologists [*Büntgen et al.*, 2014] until 2015, when - although first suggested by *Baillie and McAneney* [2015] - a more widely renowned study by *Sigl et al.* [2015] proposed re-dating the ice-core records in Greenland and Antarctica by up to 11 and 14 years respectively on the basis of combined evidence from radioisotopes, tree rings, tephra analyses, and historical accounts (see Figure 1.28 which shows these updated records). This study resolved the inconsistencies between the various proxies by using an automated layer counting algorithm tied to historical accounts at 536, 626 and 939 AD, proposing multiple North American eruptions in 536 AD and a large tropical eruption in 540 AD

as the cause of the climate downturn. However, there remain large differences in the estimated temperature response reconstructed from the different chronologies, which vary between 1.4 and 2.7 °C depending on the method used (i.e. from tree ring or ice core data).
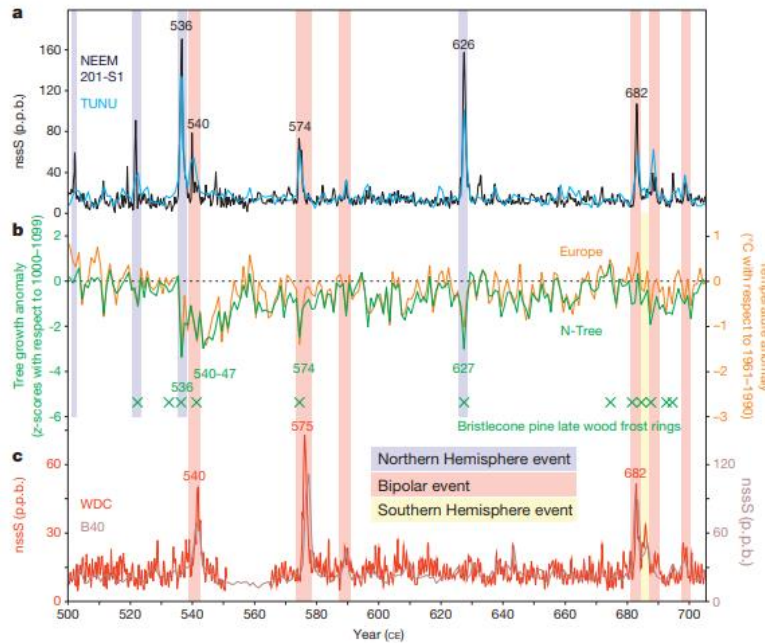


Figure 1.28. a) Non sea salt sulfur (nssS) deposits in Greenland (NEEM-2011-S1 (black) and TUNU2013 (blue)). b) Summer temperature anomalies in Europe (orange), tree-growth anomalies (green) – an index developed to measure the response of trees to changes in temperature, and the occurrence of frost rings in North American bristlecone pine trees (green crosses). c) nssS deposits from Antarctica (WDC (red), B40 (pink)). Blue and pink shaded regions indicate northern and southern hemispheric events based on the collocation of deposits in the Greenland and Antarctic ice cores [*Sigl et al.*, 2015].

It is possible to generate a reasonable reproduction of observed temperature anomalies (Figure 1.29, A) by constructing a volcanic forcing time series using a coupled aerosol-general circulation model (MAECHAM5-HAM) with simulated eruptions at either 46 °N or 56 °N in 536 AD and 15 °N in 540 AD, injecting 30 Tg and 50 Tg respectively at 30 hPa. *Toohey et al.* [2016] used this prescribed forcing in 12 ensemble simulations with the Max Plank Institute Earth System Model (MPI-ESM) to model the climate response. Significant spatial and seasonal variation was observed in the temperature response following the modelled eruptions, with the maximum summer cooling at mid-latitudes over land masses, and the winter cooling exacerbated by positive sea-ice anomalies. Whilst this work supports the idea of a volcanic cause of the climate downturn, since strong cooling was observed after both eruptions, the magnitude and extent of the cooling observed in tree-ring chronologies could not be replicated, particularly in 540 AD. This was attributed to either biological memory effects in tree rings or an under-representation of feedbacks in the model, though this leaves room for interpretation of different possible explanations.
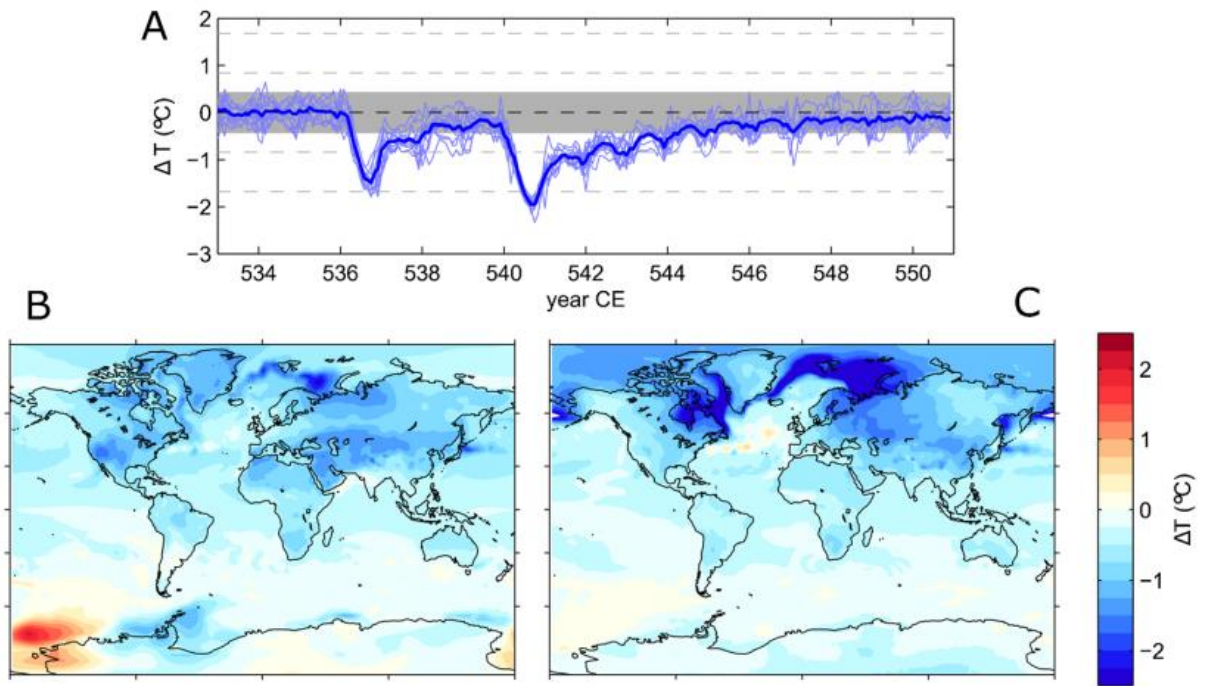
Figure 1.29. Surface temperature anomalies following the reconstructed volcanic forcing for the 536 and 540 AD eruptions using the MPI-ESM model. A) Mean monthly surface temperature anomalies with individual simulations shown in light blue and the ensemble mean shown in bold blue. $\pm 2\sigma$ variability is shown with grey shading and the dashed lines represent $\pm 4\sigma$ and $\pm 8\sigma$. B) and C) show global maps of the boreal summer and winter mean temperature anomalies respectively. Figure from *Toohey et al.* [2016].

Last year a new ultra-high resolution analysis of the Colle-Gniffetti ice core in the Swiss Alps [*Loveluck et al.*, 2018] found two microscopic tephra particles that are chemically similar to those previously found both in peat bogs and lakes in Europe, and in the NEEM-2011-S1 ice core by *Sigl et al.* [2015]. In the latter of these sources, the particles were interpreted as evidence for the 536 AD eruption. Though some believe the particles found in the Swiss ice core constitute evidence of an Icelandic eruption in 536 A.D., *Sigl* is reportedly not convinced [*Gibbons*, 2018], highlighting that the controversy surrounding this event is still ongoing today. Though there is growing evidence linking volcanic eruptions to this time period, no volcanoes have been satisfactorily linked to the cooling, despite the possibility that this was one of the most explosive eruptions in history. As such, there is still cause for further investigation and it is clear that a multi-disciplinary approach is not only preferable, but necessary in order to prove or disprove possible hypotheses regarding this case study.

### 1.2.3   The Troposphere & Surface Deposition

In the lower stratosphere, eddies generated by breaking planetary waves rapidly mix meteoric material to low and mid latitudes (see Figure 1.22) where the majority of stratospheric-tropospheric exchange occurs. This exchange is driven by deep convection around mountain ranges and storm tracks over the North Atlantic, Pacific and Southern oceans, and leads to significant zonal asymmetry in the deposition pattern of meteoric material – the strongest

deposition occurring at northern and southern mid-latitudes [*Brooke et al.*, 2017; *Dhomse et al.*, 2013]. The surface deposition of particles represents the last steps in the chain of events initiated on entry into the atmosphere, and must be considered for a full understanding of both the atmospheric effects derived from cosmic material and the processing of the particles themselves. Determining the composition and deposition flux of cosmic material requires a large, unbiased and well-preserved deposit of known age. Such deposits are difficult to find, considering that meteoric material is usually present in low concentrations and often undergoes rapid weathering, which leads to large uncertainties in deposition fluxes [*Taylor et al.*, 2000].

The two preferred strata in which to search for meteoric material are deep-sea sediments and frozen ice-cores. In ice-cores the deposition rate can be derived from the concentration of cosmic spherules [*Taylor et al.*, 1998] and several trace elements by using the snow accumulation rate to determine the flux; measurements of Ir and Pt isotopes [*Gabrielli et al.*, 2006; *Gabrielli et al.*, 2004] and super-paramagnetic Fe [*Lanci et al.*, 2012] have been used for this purpose, since terrestrial material is depleted in these elements compared to typical cosmic abundances [*Ganapathy et al.*, 1978]. A similar analysis of cosmic spherules [*Prasad et al.*, 2013] or siderophiles such as Ir and Os in deep-sea sediments can also provide a measure of the deposition rate [*Kyte*, 2002]. However, volcanic emissions can also be enriched in minerals such as Ir and Pt, complicating the identification process [*Brooke et al.*, 2017].

Deposition typically occurs *via* two mechanisms: dry deposition - i.e. direct sedimentation - and wet deposition, whereby material is deposited through precipitation. Wet deposition is thought to be more important for meteoric material, due to the relatively high levels of precipitation as MSPs are transported poleward in the troposphere [*Brooke et al.*, 2017] and the higher deposition rates in Greenland (where the snowfall is typically higher) compared to Antarctica [*Dhomse et al.*, 2013]. However, significant discrepancies between modelled and measured fluxes of meteoric material remain, even changing various model parameters relating to the deposition scheme, the MSP flux or composition, or including a simple representation of PSC interactions; similar results have been obtained using the models WACCM, the United Kingdom's (UK) Unified Model (UM), or the UM-United Kingdom Chemistry and Aerosols (UKCA) [*Brooke et al.*, 2017; *Dhomse et al.*, 2013].

An MSP injection rate 2-6 times larger than current estimates is required to reproduce the measured deposition (in Greenland [*Gabrielli et al.*, 2004; *Lanci and Kent*, 2006] and Antarctica [*Lanci et al.*, 2007; *Lanci et al.*, 2012]). This discrepancy highlights the large uncertainties regarding the transport and both atmospheric and terrestrial processing of MSPs and their derivatives, and the need for further studies on their classification and behaviour. This is important, not only for establishing the deposition flux, but because fertilisation of the oceans with cosmic material can generate climate feedbacks through the stimulation of phytoplankton growth, particularly in the Southern ocean where the supply of bio-available Fe is limited [*Dhomse et al.*, 2013; *Johnson*, 2001]. Phytoplankton activity facilitates the removal of $CO_2$ from the atmosphere which can have significant climate implications because when the organisms die

this $CO_2$ is transferred to the deep ocean and sea floor [*Smetacek et al.*, 2012]. Furthermore, phytoplankton produce DMS, which contributes to the formation of atmospheric aerosol and subsequently cloud condensation nuclei (see section 1.2.2.2 and Figure 1.23). Although the deposition flux of cosmic material is small compared to the continental dust input (~1.5 μmol Fe $m^{-2}$ $year^{-1}$ vs 30 μmol Fe $m^{-2}$ $year^{-1}$ [*Lancelot et al.*, 2009]) the stratospheric processing of MSPs in SSA generates a highly soluble form of Fe (e.g. $FeSO_4$ and $Fe_2(SO_4)_3$) meaning the bioavailable Fe injected could be between 50 and 400 % of the soluble Aeolian dust input [*Dhomse et al.*, 2013; *Saunders et al.*, 2012]. This could be an important mechanism through which indirect climate feedbacks are generated in the case of an elevated dust flux following a close cometary encounter.

## 1.3  Project Aims

This literature review has introduced the nature of cometary 'dust' and discussed both the likelihood of a cometary encounter and previous known encounters with the Earth and other planets in the Solar System. The mechanisms by which dust enters the Earth's atmosphere have been presented, along with the range of processes directly or indirectly affected by the passage of this dust (and its derivatives) through the atmosphere. Gaps in knowledge regarding our current understanding of these processes have been highlighted through this discussion, which leads now to the introduction of the specific questions that will be addressed in this thesis.

### 1.3.1  The Optical Properties of Meteoric Smoke Analogues

#### 1.3.1.1  Motivation and Importance

MSPs are of wide interest within the scientific community, since they are implicated in an extensive range of atmospheric processes, from their formation in the MLT to their deposition at the Earth's surface. In the MLT, MSPs are of interest regarding the quantification of the total influx of cosmic material to the atmosphere, the chemistry of the metal layers, and the formation of PMCs. In the stratosphere, they are thought to play a key role in regulating the concentrations of gas phase species such as $H_2SO_4$, $HNO_3$, $HO_2$ and $O_3$. They are also involved in the formation of stratospheric sulfate aerosol particles and PSCs, having subsequent effects on $O_3$ chemistry and potentially the radiative balance of the atmosphere in the case of a significantly elevated dust flux. The processing of MSPs in the stratosphere leads to the formation of bioavailable iron sulfates, which have further potential to impact the climate through the activity of phytoplankton in the oceans.

Despite the wide range of processes in which MSPs are implicated, surprisingly little is known about their physical and chemical properties. As such, studies on the physical, chemical and optical properties of candidate MSP species are of particular interest and importance to the

scientific community within a number of different fields of study. Current observational work suggests that MSPs are most likely to be formed of iron-rich oxides and silicates [*Hervig et al.*, 2017], though it is not known whether these compounds are intimately mixed as olivines or in separate distinct phases. In any case, the optical properties of iron oxides are highly relevant, as the absorption and extinction of iron-containing species is significantly greater than that of pure silica [*Saunders and Plane*, 2006]. Furthermore, parameters such as the complex RIs are required to test potential candidate MSP species against the optical extinction recorded from MSPs in the atmosphere.

It is currently assumed that the bulk properties of minerals accurately represent nanoparticles (MSPs) with a similar composition. This is the best approximation available, given the sparsity of laboratory studies on the optical properties of relevant compounds in this particular context. However, MSPs are likely to be structurally amorphous, fractal-like agglomerates with sizes on the order of tens of nanometres. Particles of this nature do not necessarily behave in the same manner as their bulk counterparts, and as such, it is important to study the formation and optical properties of MSP analogues under atmospherically relevant conditions.

Laboratory studies of this nature are necessary to:

1) Determine the most likely products from the reaction and agglomeration of suitable precursors under atmospherically relevant conditions
2) Probe the interaction of these products with light, deriving complex RIs to describe the processes of absorption, scattering and extinction
3) Aid with the process used for the characterisation of atmospheric MSPs, and shed light on whether this method is valid

### 1.3.1.2   Thesis Outline

The two laboratory techniques described in section 1.2.1.3.4 have been employed in this work to study the formation, agglomeration and optical properties of iron oxide MSP analogues. Nanoparticles have been produced with both experimental setups: the MICE/TRAPS and the PAFS. Whilst the first of these experiments has previously produced iron oxide nanoparticles, this work additionally presents absorption efficiencies derived for the particles. The second technique has also been used previously to produce iron oxide particles, reporting on their optical extinction. However, this method has been adapted by adding an optical bypass system, to measure smaller extinctions than in this previous work. Furthermore, the absorption and extinction data from the MICE/TRAPS and PAFS, respectively were combined for the purposes of deriving complex RIs using an iterative photochemical model. The methods used for both experiments are presented in Chapter 2, and the corresponding results are discussed in Chapter 3.

### 1.3.2 Global Climate Modelling of a Simulated Close Encounter

#### 1.3.2.1 Motivation and Importance

The multiple impacts and encounters of extraterrestrial bodies with planets that have been observed throughout history demonstrate that the statistical likelihood of these encounters is not negligible. Furthermore, these events have been linked (albeit sometimes controversially) to effects such as environmental destruction, changes to atmospheric processes, cultural reorganisation and even mass extinctions. Recently, the passage of comet Siding Spring past Mars at a distance of ~130,000 km was shown to have a pronounced effect on the atmosphere of this inner planet. Despite this (to the author's knowledge), there have been no previous studies on the effects of a close cometary encounter on the terrestrial atmosphere. This work is therefore the first study of its kind, and represents a novel and important investigation into the atmospheric impacts of a close cometary encounter.

The high degree of variability in the nature of a close cometary encounter means that the development of some thresholds to quantify the extent of the possible effects for different encounter scenarios would be advantageous. However, it also inhibits the practicality of such studies, since a more simplistic modelling approach would be required, that would not necessarily be able to accurately gauge the effects of an encounter on the complex network of atmospheric phenomena likely to be involved. As such, it is more prudent to first probe the effects of one well-constrained encounter scenario, to assess the important mechanisms through which the atmospheric impacts are derived. This can then serve as a basis for future work to expand upon.

This work focuses on the simulation of a hypothetical scenario: a close encounter with Halley's comet with a closest approach distance of 100,000 km – arbitrarily chosen so as to be on the order of that for Siding Spring's encounter with Mars. Halley is one of the most active short period comets [*Keller et al.*, 2004]; hence, significantly more dust (by a factor of ~4900 – see Chapter 4) would be injected in the event of a close encounter than was experienced at Mars during the Siding Spring event. An encounter of this magnitude has not been experienced at the Earth in recorded history, and the meteor shower that would result would be the strongest ever recorded. Halley's comet was chosen for this scenario because of the availability of information regarding the nature and distribution of its dust; a model has been developed that has been shown to reasonably reproduce the dust distribution within its coma [*Moorhead et al.*, 2014]. Additionally, it has also been implicated (tangentially) in the 6th century cooling discussed in section 1.2.2.5.

#### 1.3.2.2 Aims and Thesis Outline

The aim of this work is to assess the impacts of the simulated encounter with Halley's comet on relevant chemical and dynamical processes in the Earth's atmosphere. In order to achieve this, a number of sensitivity simulations have been performed with the global climate model WACCM. This modelling work is split into two parts – the first assessing the implications for the upper

atmosphere, and the second assessing the impacts on the middle and lower atmosphere, including surface deposition. A different modelling approach is used in each, appropriate to the phenomena being probed in each case. Details of the methodology used and simulations performed for both parts are presented in Chapter 4.

The impact of the close encounter on the upper atmosphere has been explored through four WACCM runs. A chemical perturbation (i.e. a metal injection) and a dynamical perturbation (i.e. a heating tendency) were added to the model in order to assess the effects on a range of atmospheric phenomena:

1) The chemistry of the metal layers
2) The chemistry of other ambient species in the MLT such as O, $O_3$, H and $H_2O$
3) Changes to the temperature
4) Changes to the residual atmospheric circulation

The results from these simulations are presented in Chapter 5.

A different model configuration where WACCM is coupled to the CARMA module for aerosol microphysics was then used to probe the effects of the close encounter on the middle and lower atmosphere. Two sensitivity simulations were performed, to explore the effects of an injection of both meteoric sulfur and MSPs on a number of atmospheric phenomena:

1) The gas-phase sulfur chemistry of the mesosphere and stratosphere
2) The particle size distributions for MSPs and stratospheric sulfate aerosol
3) The deposition pattern of the meteoric aerosols and sulfur

The third point will be explored in the context of assessing whether an event such as a cometary close encounter could have had a measurable effect on sulfate deposition, in order to evaluate whether an event of this nature could have contributed towards the global cooling event in the 6th century. The results of these simulations are presented in Chapter 6.

# Chapter 2
# Experimental Methods

Accurate determination of the optical properties of analogues for MSPs is important for their observation and characterization in the atmosphere. In this study, a photochemical aerosol flow reactor, modified from the setup described in *Saunders and Plane* [2006; 2010; 2011], has been used to study the optical extinction of iron oxide meteoric smoke analogues in the wavelength range 325-675 nm. The particles were produced photochemically and coagulate into larger, fractal-like agglomerates with mobility radii on the order of 100 nm. Particle size distributions were recorded using a scanning mobility particle size analyser (SMPS) and samples were collected and analysed using Transmission Electron Microscopy (TEM), Energy Dispersive X-ray spectroscopy (EDX) and Electron Energy Loss Spectroscopy (EELS).

A very different system, the Molecular Flow Ice Cell/Trapped Reactive Atmospheric Particle Spectrometer (MICE/TRAPS), was used to study the optical absorption of iron oxide particles with radii on the order of 2 nm. In this setup, nanoparticles are generated using a microwave resonator and held within a low pressure, supersaturated particle trap. Through the use of time resolved mass spectrometry measurements, the adsorption of $H_2O$ vapour onto the nanoparticle surface over time and desorption of this water *via* absorption of laser light (at 405 nm, 488 nm & 660 nm), particle absorption coefficients can be calculated.

## 2.1   Optical Extinction: Photochemical Aerosol Flow System

### 2.1.1   Particle Generation

The photochemical aerosol flow system (PAFS) used by Saunders and Plane has been developed further to study the agglomeration and optical properties of iron oxide particles. The experimental setup (Figure 2.1) used to generate analogue MSPs consists of a cylindrical glass photolysis cell with quartz end windows (4 cm x 25 cm) into which a combined flow of iron pentacarbonyl vapour ($Fe(CO)_5$) and $O_3/O_2$ was introduced. The $Fe(CO)_5$ was generated by passing a flow of $N_2$ (1.1 sccm) through a round-bottomed flask containing ~3 $cm^3$ of liquid $Fe(CO)_5$ (Aldrich) cooled in a water-ice bath to 0 °C. The round-bottomed flask and ice-bath were covered to prevent any premature photolysis (and subsequent build-up of material on the flow tube walls). $O_3$ was produced by photolysing $O_2$ at 185 nm, by passing a flow of $O_2$ (50 sccm) through a glass cell with a quartz window in front of a mercury (Hg) pen lamp. Once in the photolysis cell, the gases were irradiated using a 1000 W ozone-free Xenon arc lamp. Variable $N_2$ 'curtain' flows were passed across each of the cell windows such that the total flow rate was 550 sccm (1 sccm = 1 $cm^3$ $min^{-1}$ at standard temperature and pressure (293 K and 1 atm)). After photolysis of the precursors, agglomeration of amorphous, fractal-like iron oxide particles proceeds throughout the experimental system.
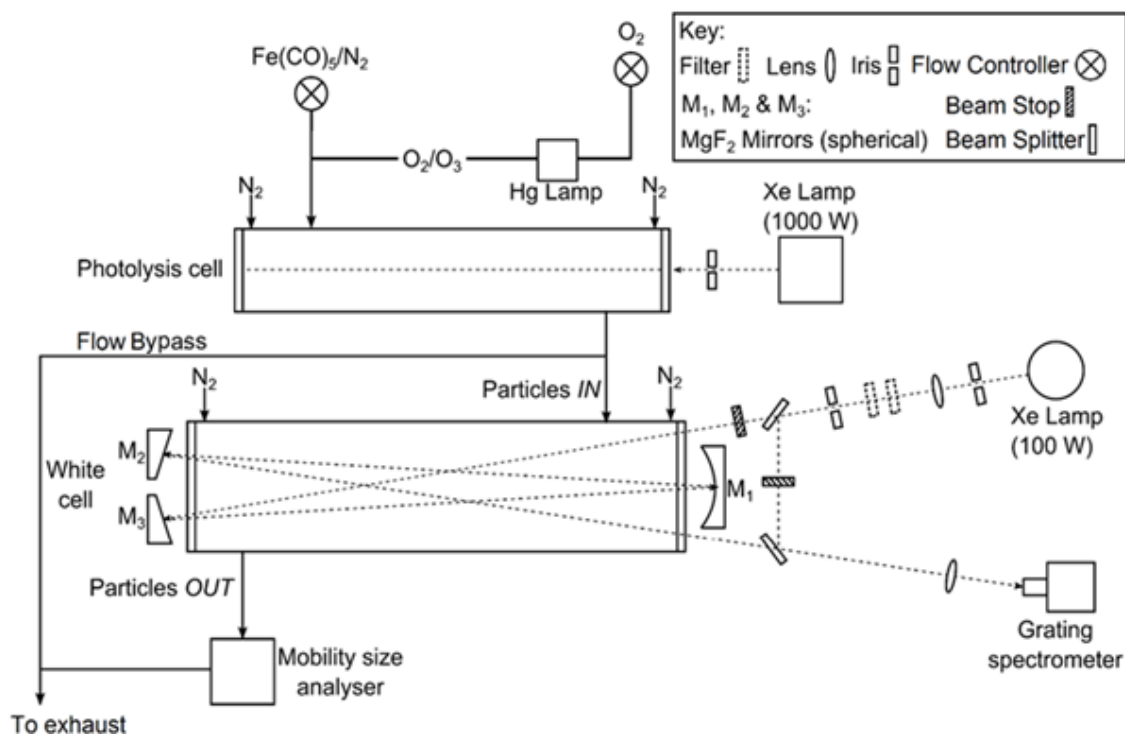
Figure 2.1: Schematic diagram of the experimental system used for the generation and optical detection of MSP analogues.

## 2.1.2 Spectral and Size Analysis

After leaving the photolysis cell the particle flow was directed through an absorption cell (10 cm × 48 cm) with White cell optics in which the optical extinction of the particles was measured (hereafter referred to as the White cell). On exit from the White cell, particle size distributions were recorded using a SMPS consisting of a differential mobility analyser (DMA) and a condensation particle counter (CPC) – this instrument was kindly loaned by Professor Dwayne Heard at University of Leeds. The DMA sheath and aerosol flow rates were 3 L min$^{-1}$ and 0.3 L min$^{-1}$ respectively, with a scan taken every 3 minutes (a scan time of 120 seconds and retrace of 30 s was used).

Light from a 100 W Xenon arc lamp (SLS401, Thorlabs) was focused into the White cell using a quartz lens (focal length 75 cm). The lamp intensity could be controlled by the insertion of a selection of neutral density filters, and stray lamp light was eliminated using an iris. During experiments, the system was operated in the dark and the White cell was also covered with black cloth to further minimise any stray light. Borosilicate White cell windows prevented further photolysis by the spectroscopy lamp, and excluded second-order light at wavelengths below ~330 nm from entering the spectrometer and potentially contaminating the spectra. N$_2$ curtain flows (500 sccm) were passed across the windows to prevent aerosol deposition. Particle extinction was measured between 325 and 675 nm.  A total optical path length (*l*) of 624 cm was achieved by folding the light path 12 times between three concave mirrors comprising the White cell. The number of reflections was indicated by observing the number of 'spots' visible on the mirror M1.

One spot was visible when there was 4 beam-passes through the cell, and a further two spots were observed for every additional 4 passes. The exit beam was focused with a quartz lens onto a fibre optic coupled to an Acton Research Spectra Pro 500i spectrometer, in which the light was dispersed using a grating (150 groove mm$^{-1}$) onto a CCD camera (back-illuminated, Roper Scientific). The exposure time was 0.1 s, with 57 accumulations per spectrum generating 9 spectra per minute. An example spectrum is shown in Figure 2.2. The shape of the profile is created from a combination of the 100 W Xe-lamp power spectrum and the quantum efficiency of the CCD detector, which both decrease dramatically below 450 nm (see Figure 2.3).
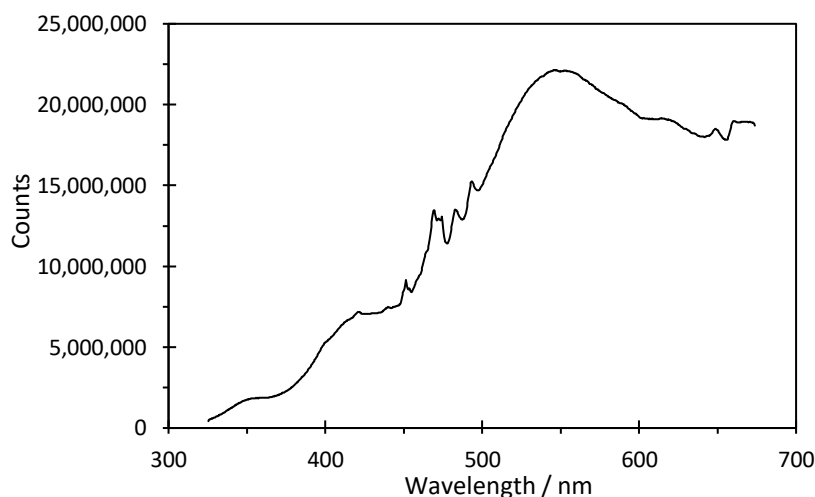


Figure 2.2: Example raw transmission spectrum for iron oxide particles from the photochemical aerosol flow system (PAFS), as a function of wavelength.
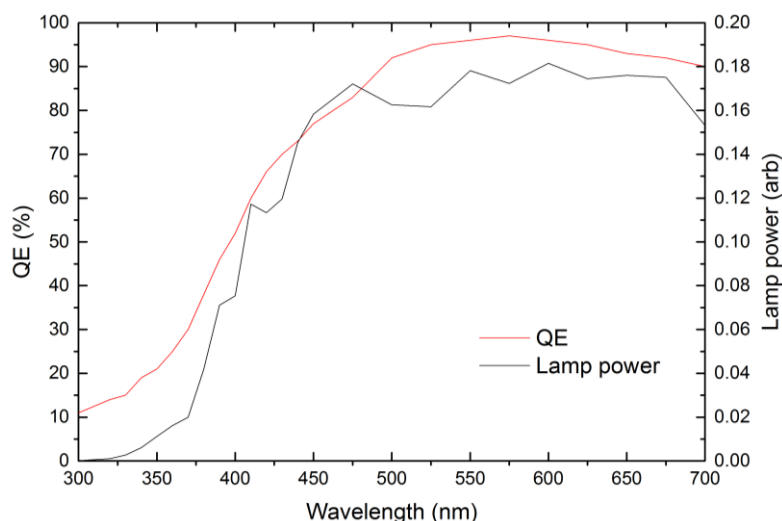


Figure 2.3: Quantum efficiency (QE) of the CCD detector, and the power of the 100 W Xe lamp as a function of wavelength across the region of interest for the PAFS. Data for plot obtained from equipment manufacturers.

In addition to correcting each of the measured spectra by removing the dark counts, a correction was applied to normalise for drifts in the Xe lamp spectrum with time. This correction was

introduced such as to measure smaller levels of optical extinction than in previous work with the PAFS (Saunders and Plane, 2006, 2010, 2011). For this correction, the measured intensity through the cell was normalised by that from a bypass measurement. However, as separate measurements through the cell and bypass could not be measured simultaneously using the same apparatus, beam stops were used to create three different beam-configurations (see Figure 2.4), from which the separate signals could be extracted. Spectra were recorded in three minute cycles with one minute of spectra taken using each configuration: (a) the beam directed through the cell and additionally through the bypass ($I_a$); (b) the beam directed only through the bypass ($I_b$); and (c) the beam directed only through the cell ($I_c$).
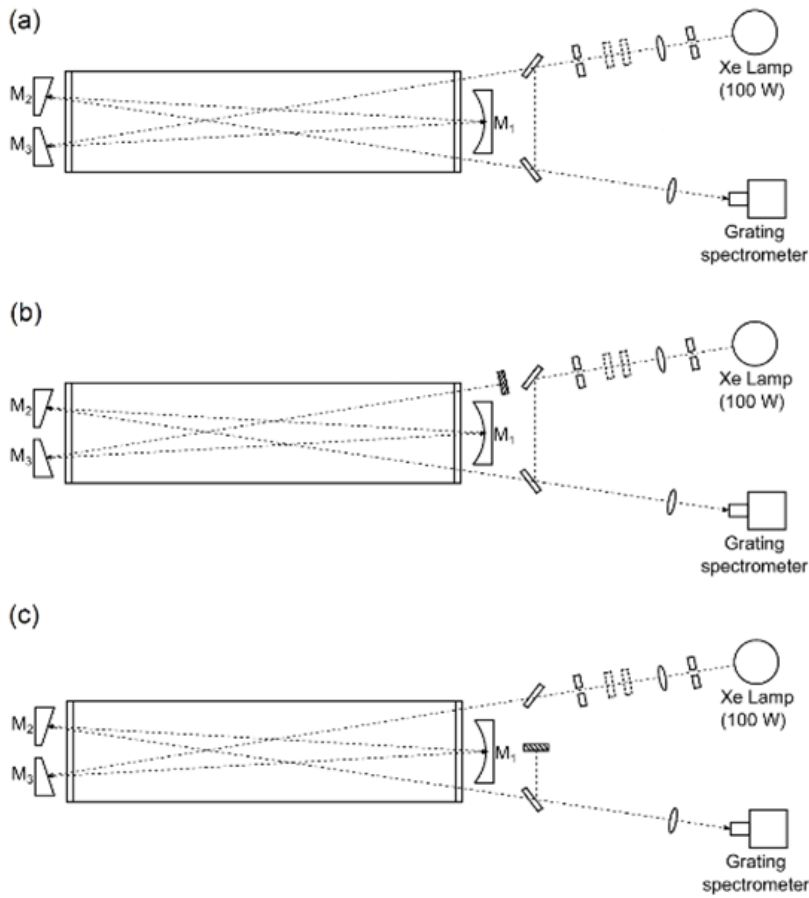


Figure 2.4: Beam configurations thorough the White cell. (a) Beam passing through the cell and the bypass. (b) Beam passing through the bypass only (c) Beam passing through the cell only.

The first spectrum of the 9 spectra generated in each configuration was removed to allow for the time taken to change configuration, and the remaining 8 spectra were summed to generate one spectrum each minute ($I_{tot,a}$, $I_{tot,b}$ and $I_{tot,c}$ - see equation E2.1).

E2.1
$$I_{tot,x}\ (\lambda, t) = \sum_2^9 I_x(\lambda, t) \qquad where\ x = a, b\ or\ c$$

Subsequently correcting the cell measurement ($I_C$, equation E2.2) using the bypass measurement ($I_B$, equation $E2.3$) enabled one normalised spectrum ($I_{Cn}$, equation E2.4) to be generated every three minutes.

E2.2 $$I_C(\lambda, t) = I_{tot,a}(\lambda, t) - I_{tot,b}(\lambda, t)$$

E2.3 $$I_B(\lambda, t) = I_{tot,a}(\lambda, t) - I_{tot,c}(\lambda, t)$$

E2.4 $$I_{Cn}(\lambda, t) = I_C(\lambda, t) / I_B(\lambda, t))$$

The gas-phase spectrum for the $Fe(CO)_5$ precursor was measured with a PerkinElmer Lamda 90 UV/Vis spectrometer in a $1 \times 1$ cm gas cuvette. Due to the wide range covered by the absorption cross section in the measured wavelength range (4 orders of magnitude), the final spectrum was a composite of two spectra; the low-wavelength end of the spectrum ($\lambda < 280$ nm) was an average of three low pressure measurements ($P \sim 2$ Torr) and the high wavelength portion ($\lambda > 280$ nm) was an average of two higher pressure measurements ($P \sim 20\text{-}30$ Torr). A reference spectrum for the empty cuvette was removed from each individual spectrum before averaging.

## 2.1.3  Experimental Technique

In a typical experiment, the sample flows were switched on, with the particle flow initially diverted through the flow bypass (to an exhaust) rather than through the White cell (see Figure 2.1). With the SMPS measurements initiated so that a background size distribution was being measured every 3 minutes, extinction measurements were initiated. Approximately 30 minutes of 'reference' spectra were recorded. The particle flow was then directed through the White cell, and a further 21 minutes of 'sample' measurements were recorded. Thereafter, the particle flow was diverted back to the exhaust and background measurements resumed for around 45 minutes. A repeat sample measurement was recorded followed by approximately 30 minutes of reference measurements until the peak of the recorded size distribution had stabilized to within 1 %.

## 2.1.4  Microscopic Analysis

Particles formed in the PAFS were collected by diverting the flow bypass through a round-bottomed flask containing a suspended transmission electron microscopy (TEM) grid (copper (Cu) mesh with a holey carbon film coating). The grids were then stored under vacuum in the dark prior to imaging. Particles were analysed using TEM with energy dispersive X-ray (EDX) spectroscopy and electron energy loss spectroscopy (EELS) at the University of Leeds (FEI Titan3 Themis 300).

## 2.2 Optical Absorption: MICE/TRAPS Apparatus

### 2.2.1 TRAPS

The MICE/TRAPS apparatus was used as part of a short placement at the Karlsruhe Institute of Technology (KIT), based in Professor Thomas Leisner's research group, within the Institute of Meteorology and Climate Research. The TRAPS (Figure 2.5) consists of a nanoparticle source, in which singly charged nanoparticles were produced by mixing vapour from a volatile precursor heated to ~353 K (solid ferrocene, $Fe(C_2H_5)_2$) with a flow of helium and oxygen (1 l min$^{-1}$). This mixture then flowed through a low pressure (~60 mbar) non-thermal microwave resonator (350 W, 2.45 GHz) to create a plasma in which metastable exited Fe was oxidised to produce $Fe_xO_y$ particles. Previous studies (*Baumann et al.* [2006]; *Giesen et al.* [2005]; *Janzen et al.* [2002]) using similar methodology have demonstrated that particles produced are singly charged, spherical and compact, with little agglomeration. A portion of the flow ($< 20$ %) was then passed into the vacuum chamber through a flow-limiting orifice, and the nanoparticles were separated from the residual gas using an aerodynamic lens. An octupole ion guide was used to prevent expansion of the particle beam.

Particles of a chosen size were deflected and trapped into a cloud of ~1 mm radius within the MICE using a quadrupole deflector ($DF_1$) operating at voltages between 10 V and 150 V. A typical filling time of 1-4 seconds allowed ~$10^7$-$10^8$ particles into the trap (max. capacity ~$8x10^8$ particles) where a He bath gas was used to thermalize the trapped particles. Within the MICE, there were two surfaces, on which before each experiment a $H_2O$ ice layer was deposited. The temperature difference between these two surfaces determined the particle temperature and $H_2O$ supersaturation (the ratio between the vapour pressure and the chamber pressure of $H_2O$). Small numbers of particles were extracted from the trap at regular time intervals by lowering the potentials of the exit lens (~$10^5$ particles, 1.5-8 seconds between pulses per pulse). A quadrupole ($DF_2$) guided the extracted particles to a Daly-type detector and Time-of-Flight (TOF) mass spectrometer that measures particle mass as a function of time.

For further information on the design and characterisation of the TRAPS apparatus the reader is referred to: *Duft et al.* [2015]; *Meinen et al.* [2010a]; *Meinen et al.* [2010b]; *Nachbar et al.* [2016]. Modification of the TRAPS apparatus to include the MICE is described in detail in *Duft et al.* [2015], with the up to date methodology for particle production outlined in *Nachbar et al.* [2018b]. Theoretical concepts are discussed in *Nachbar et al.* [2016] and *Nachbar et al.* [2019] provides details of the methodology for the determination of absorption efficiencies.
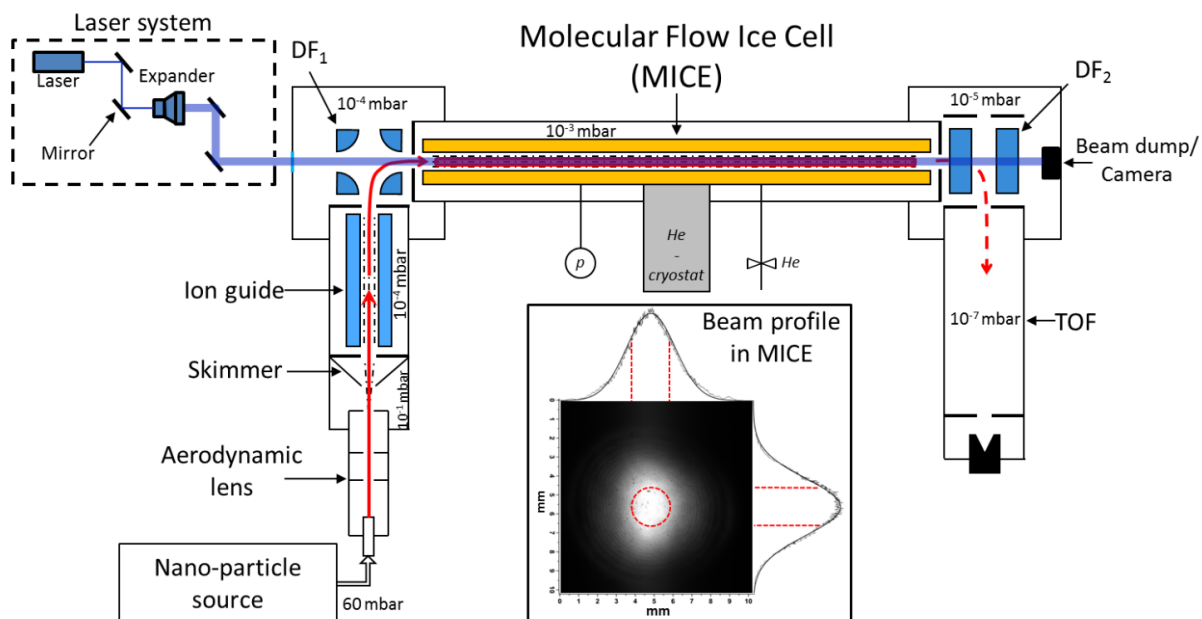
Figure 2.5. A schematic diagram of the TRAPS apparatus from KIT, including the MICE. DF$_1$ and DF$_2$ indicate quadrupole detectors used to guide the particle beam into and out of the apparatus. TOF indicates the time-of-flight mass spectrometer (image from [*Nachbar et al.*, 2019]).

## 2.2.2 MICE

Within the TRAPS, the MICE (Figure 2.6) ion trap allowed particles to be held in a supersaturated environment. The trap (~7 mm radius) was created using a 'cold wall' ($T_c$ ~ 133 K) consisting of four 480 mm gold-plated copper electrodes (2) mounted onto a copper tube (1) using SHAPAL™ ceramic spacers (3), which are electrically insulating but with high thermal conductivity. The copper tube is in turn mounted onto a helium closed-cycle cryostat. The application of radio frequency AC potentials to the ion-trap electrodes generated the fields required to trap particles into a cloud of ~ 1 mm radius. The spaces between the quadrupole electrodes contain the 'warm wall' ($T_w$ ~ 150 K, (4)), an additional gold-plated copper tube, which was held at ground potential. PEEK™ spacers (5), with a low thermal conductivity, were used to mount this to the outer wall. The warm wall was heated using heating foils (6) positioned such as to minimise any temperature gradients along the MICE, with the temperature set and monitored using calibrated sensors in cavities along its length (7).

In order to produce supersaturated conditions inside the MICE, before each experiment and with the system held at a low temperature ($T < Tc$), a hollow stainless steel tube (8) was inserted into the apparatus to deposit a layer of $H_2O$ onto the trap walls. This tube has four longitudinal rows of laser drilled 100 μm diameter holes, oriented at 90° to one another, such as to preferentially deposit particles onto the warm wall. Each row has 100 holes spaced 5 mm apart covering the length of the trap. A $H_2O$ vapour pressure inside the deposition tube of ~30 mbar means that around 10 minutes of deposition generates a layer 20 to 30 μm thick.
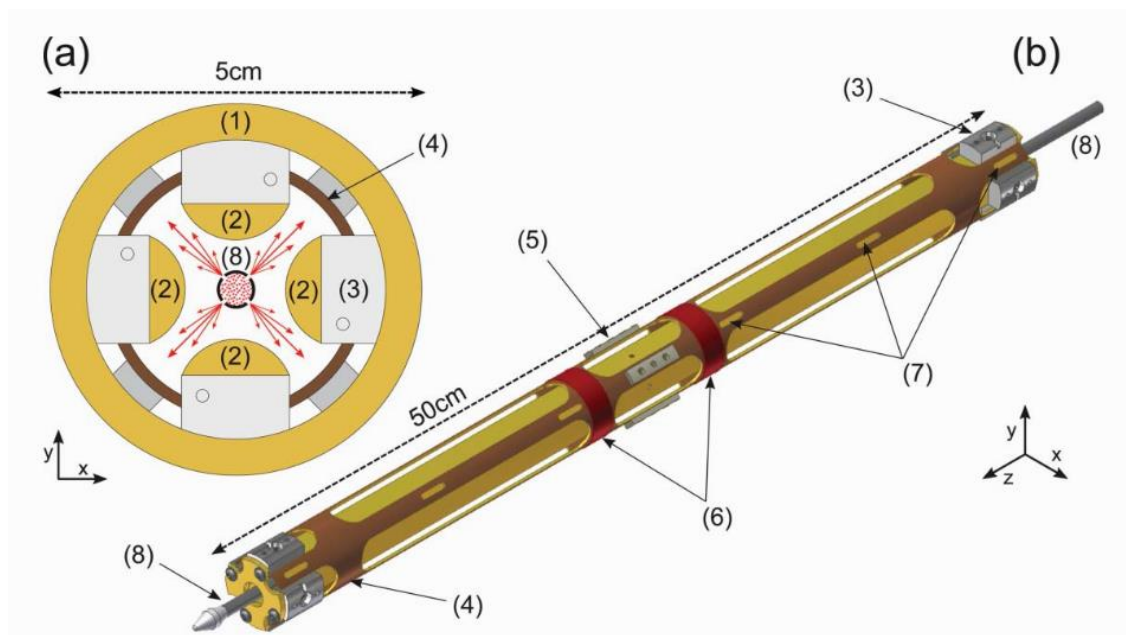
Figure 2.6. Schematic diagram of the MICE, as part of the TRAPS apparatus from KIT: cross section (a) and overall design excluding outer cooling tube (b). (1) Cooling tube (2) Quadrupole electrodes (3) SHAPAL™ spacers (4) heated electrode (5) PEEK™ spacers (6) heating foils (7) temperature sensor cavities (8) retractable vapour applicator tube [*Duft et al.*, 2015].

The low pressures and temperatures used in the trap are such that nanoparticles were in the free molecular flow regime (the mean free path of particles is greater than the distance between the electrodes), meaning a stable region was produced in the centre of the trap, with well-defined pressure (typically (1-3) $\times$ $10^{-3}$ mbar), temperature and supersaturation [*Brown and Schowengerdt*, 1979; *Duft et al.*, 2015]. A slight temperature gradient across the width of MICE lead to a particle temperature uncertainty of ~0.4 K and an uncertainty in the $H_2O$ concentration of ~ 7 %.

## 2.2.3 Experimental Technique

One experimental run consisted of allowing a number of particles into the apparatus, and periodically extracting small numbers of particles with increasing trapping time. At the end of a run, the particles in the chamber were pumped away and the apparatus was refilled with fresh particles, ready for a new run. With increasing trapping time during each experimental run, $H_2O$ molecules adsorb onto the surface of the iron oxide nanoparticles within the MICE until an equilibrium of adsorbing and desorbing particles is reached. A number of repeat runs were then performed under the same conditions, irradiating the particle cloud using optical laser light with increasing power. Optically pumped continuous wave semiconductor lasers (OBIS LX, Coherent) were used at wavelengths of 405 nm, 488 nm and 660 nm for this irradiation, which were directed through the apparatus (Figure 2.5) onto a beam dump using four silver coated (488 nm & 660 nm)

or UV-enhanced Aluminium (405 nm) mirrors (Thorlabs) and a broadband beam expander (Techspec 10X VIS, Edmund Optics).

The light intensity in the MICE was calibrated by measuring beam profile and laser-power in MICE using a power-meter (Coherent PM USB PS19Q) and a CCD camera (Thorlabs 4070M-GETE). A typical beam profile for the (expanded) beam at 488 nm is shown in Figure 2.5. The maximum calculated ion cloud diameter ($d = 2$ mm) is shown with red dashed lines [*Majima et al.*, 2012; *Nachbar et al.*, 2019]. Allowing for a beam misalignment of 0.5 mm, the ion cloud was assumed to be located within a diameter of 3 mm from the centre of the laser beam. The irradiation intensity was thus calculated from the mean of the intensity values at $d = 3$ mm and the beam centre, with the associated uncertainty being defined by the difference between these two values.

Absorption of the laser light by the nanoparticles causes differing amounts of $H_2O$ desorption from the particle surface, which was monitored as a function of time using the TOF. From this data, the mass of adsorbed $H_2O$ at equilibrium and the initial mass of particles could be calculated. With these parameters known, parameters such as the desorption energy and the particle temperature change due to irradiation could then be calculated. Further analysis then leads to the extraction of particle absorption coefficients (described in detail in Chapter 3).

# Chapter 3

# Optical Properties of Iron Oxide Meteoric Smoke Analogues

Whilst MSPs are implicated in a number of atmospheric processes, their composition is yet to be definitively determined. Current best-estimates of MSP composition are derived using optical spectroscopy. However, this technique relies on the availability of accurate refractive indices for candidate MSP species, since these are used to evaluate possible compositions against satellite data; at present the most likely MSP compositions are thought to be iron-rich oxides or olivines. Chapter 2 described the production of iron oxide nanoparticles, as analogues for MSPs, in the laboratory using two complementary experimental systems: the Photochemical Aerosol Flow System (PAFS) and the Molecular flow Ice Cell within the Trapped Reactive Atmospheric Particle Spectrometer (MICE/TRAPS). In this chapter, the optical extinction and absorption are presented for the PAFS and MICE/TRAPS respectively. Solid-state and optical analysis techniques are used to infer the most likely particle composition, and RIs are derived using optical data from both experiments.

## 3.1   Optical Extinction: Photochemical Aerosol Flow System

### 3.1.1   Microscopy

Inspection of particles collected with the PAFS using TEM showed that the particles were non-spherical, with a fractal-like morphology. The particles ranged in size from a few nanometres to microns in radius (Figure 3.1, left panel) and their form ranged from relatively compact to more open, porous (or even filament-like) structures. Agglomerates were composed of a large number of primary spheres, the average size of which was calculated by taking measurements from high resolution images of different agglomerates (one such image is shown in Figure 3.1, right panel). In each of three images, the primary particle size was estimated by averaging the radius measured for 15 spheres, chosen from the visible 'edge' of the agglomerate, where a well-defined spherical shape was observed. The average primary particle radius ($r_0$) obtained from the three images was $1.65 \pm 0.15$ nm. This is consistent with previous work on $Fe_2O_3$ particles using the PAFS, where an upper limit of $r_0 = 3.3$ nm was derived with particle growth modelling [*Saunders and Plane*, 2006].
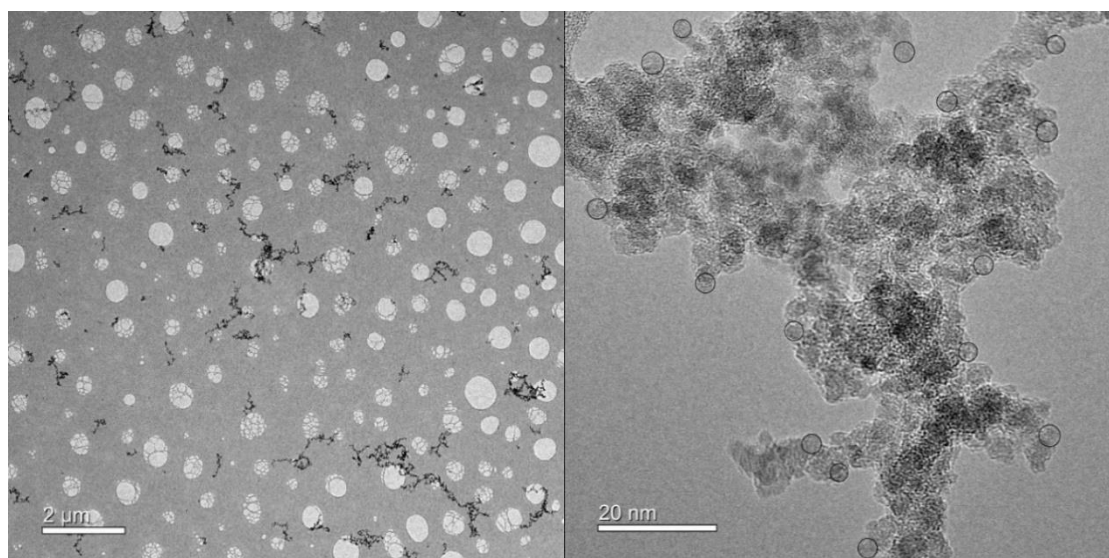
Figure 3.1.(Left panel) Low resolution TEM image showing the size-range of iron oxide agglomerates collected on a holey-carbon grid. Note the dark grey/black particles are particle agglomerates, whereas the light grey structure within the holes is part of the holey-carbon grid. (Right panel) High resolution TEM image showing the primary particles forming an agglomerate. Black circles indicate measured primary spheres used for size characterisation.

Electron energy loss spectroscopy (EELS) exposes a sample to an electron beam that has a well-defined, narrow range of kinetic energies. The electron beam can induce ionization of inner-shell electrons, which causes an energy loss in the transmitted electron beam. This facilitates sample characterisation since different materials cause different characteristic energy losses. After an inner electron is excited in this manner, an electron from an outer, higher-energy shell can 'fall down' to fill the electron hole left from the ejected inner-shell electron. This process results in the emission of an X-ray with an energy characteristic of the energy difference between the high and low energy electron shells. Energy dispersive X-ray (EDX) spectroscopy probes the energies of these emitted X-rays, and is thus also able to determine the elemental composition of a sample.

Low-loss deconvolved, background-subtracted electron energy loss (EEL) spectra showing the Fe L-edge and O K-edges are shown in Figure 3.2. These 'edges' are a result of transitions from the $2p \leftarrow 3d$, and $1s \leftarrow 2p$ orbitals respectively. Comparison of these spectra to equivalent spectra from iron oxide standards [*Brown et al.*, 2001; *Brown et al.*, 2017] allows the most likely composition to be inferred. Since the position of the peaks designated as a and b in the Fe L-edge and O K-edge respectively do not change for the iron oxide standards, the spectra have been aligned using the energy loss for this peak. Examination of peak *a* in the O K-edges allows for hematite-like and wüstite-like compositions to be excluded, since the former exhibits a higher edge-onset energy and different peak shape, and the latter displays a double-peak pattern not present in the sample spectrum. Inspection of peak *a* in the Fe L-edge confirms this, as for wüstite a broad shoulder is observed on the high energy side, and for hematite a well-defined shoulder is observed on the low energy side of the peak. However, as there are no distinguishing features in either EEL spectra to differentiate between maghemite or magnetite, it is not possible to determine

the sample composition based solely upon the EEL spectra. The similarity in the literature EEL spectra for magnetite and maghemite is because these conformers are based upon the same inverse spinel crystal structure. Magnetite contains mixed valence iron ($Fe^{2+}$ and $Fe^{3+}$) with a mixture of tetrahedral and octahedral environments, whereas maghemite contains only $Fe^{3+}$, with octahedral iron site vacancies [*Brown et al.*, 2017].
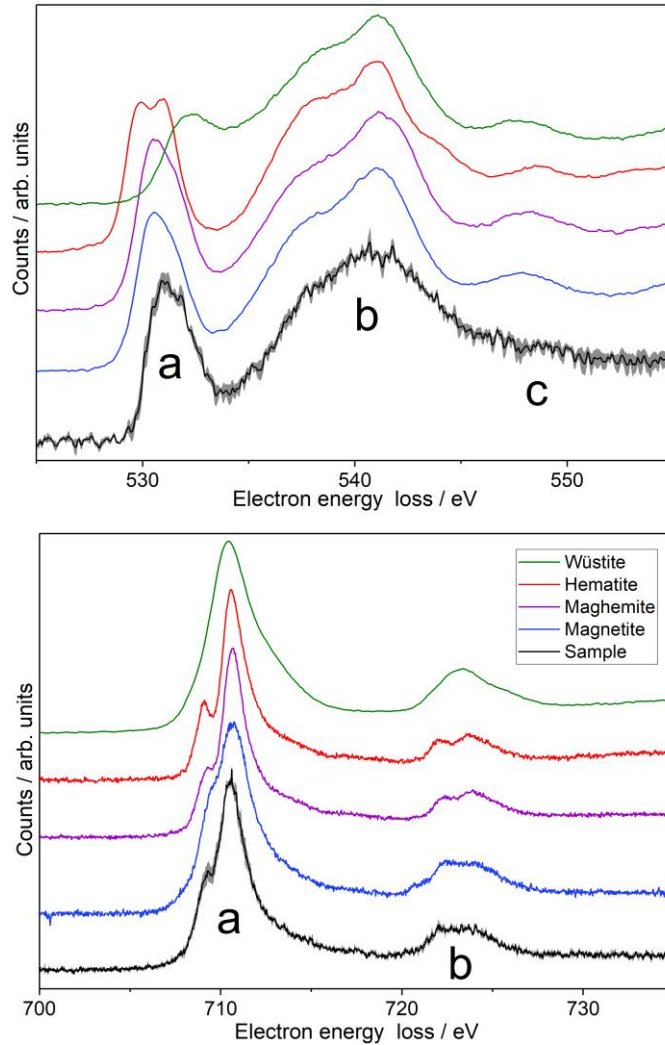


Figure 3.2. Electron energy loss spectra measured with the TEM (black) compared to spectra for iron oxide standards: wűstite (green), hematite (red), maghemite (purple), and magnetite (blue) [*Brown et al.*, 2001; *Brown et al.*, 2017]. Top panel: O K-edge. Bottom panel: Fe L edge. Grey shaded region indicates the experimental uncertainty. Major peaks in each spectrum are indicated with a & b (bottom panel) and a, b & c (top panel).

The sample O K-edge does not show a well-defined peak c, which may be a possible consequence of the poor crystallinity of agglomerates. The degree of crystallinity can be probed by inspection of the electron diffraction pattern; for amorphous particles, broad concentric rings are typically observed rather than distinct spots. For the iron oxide agglomerates, two broad rings can be clearly seen in the diffraction pattern (Figure 3.3, left panel). These rings appear at inter-planar distances

of 2.60 Å and 1.47 Å (allowing for a camera calibration error of 6 %) and correspond to the intense reflections of maghemite or magnetite. These are near to the 311 and 440 diffraction planes respectively, which were measured for a maghemite standard (Alfa-Aesar) to occur at distances of 2.57 Å and 1.52 Å. A faint ring at an inter-planar distance of 2.09 Å is also observed, close to the 400 diffraction plane at 2.11 Å. Due to the similarity in the structure of maghemite and magnetite, the diffraction pattern does not divulge any additional information to distinguish between these two compositions. However, it does corroborate that the sample composition is similar to one or other of these minerals. Elemental quantification using EELS resulted in a Fe/O ratio of 0.48 $\pm$ 0.12 which is more oxygen rich than any of the possible compositions hematite/maghemite, magnetite or wüstite; the oxides have Fe/O ratios of 0.67, 0.75 and 1, respectively (Fe:O 2:3, 3:4 and 1:1). Accordingly, the composition is most likely to be maghemite-like, although potentially with additional oxidation or oxygen contamination (discussed later in this section).
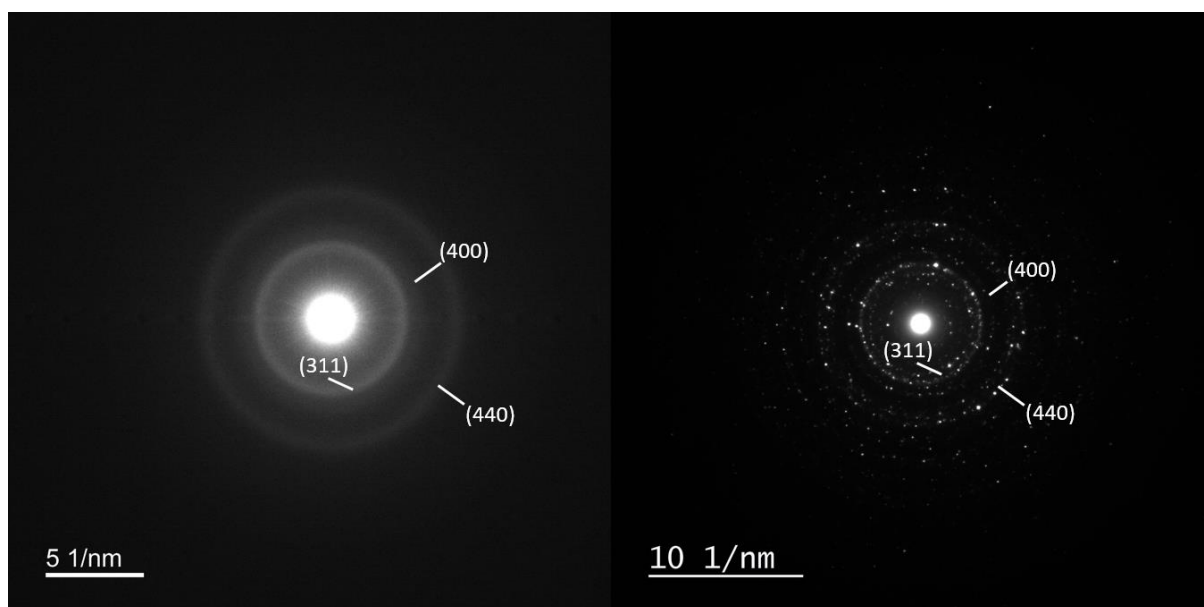


Figure 3.3. Left panel: Electron diffraction pattern for an iron oxide agglomerate taken with the transmission electron microscope showing intense reflections close to the 311, 400 and 440 planes of maghemite/magnetite. Right panel: Electron diffraction pattern for a maghemite standard.

The EDX spectrum (Figure 3.4) confirms the presence of Fe and O in the sample. However, some differences in the peak intensities are observed upon comparison with a spectrum for a maghemite standard. A difference in the ratio of the Fe K-peak to the Fe L-peak is observed. This may be a result of secondary X-ray fluorescence induced by the absorption of the characteristic X-rays emitted from a copper (Cu) grid bar. The partial absorption of such X-rays by a sample can cause the emission of additional X-rays with a lower energy. This process is not typically very efficient. However, it can significantly affect the relative amounts of radiation emitted by some compounds – in particular when elements with quite similar atomic numbers are present [*Goodhew et al.*,

2001]. If fluorescence is observed, this typically means the sampling volume (the volume of the sample from which X-rays are emitted) may be bigger than the interaction volume (the volume of the sample penetrated by electrons) which could be a consequence of the amorphous nature of the sample [*Goodhew et al.*, 2001]. This effect may be present to differing degrees in the sample and standard spectra, since the sample depth (tens of nm) is significantly thinner than that of the maghemite standard (~150 nm), so the relative amount of Cu present is greater in the sample spectrum.
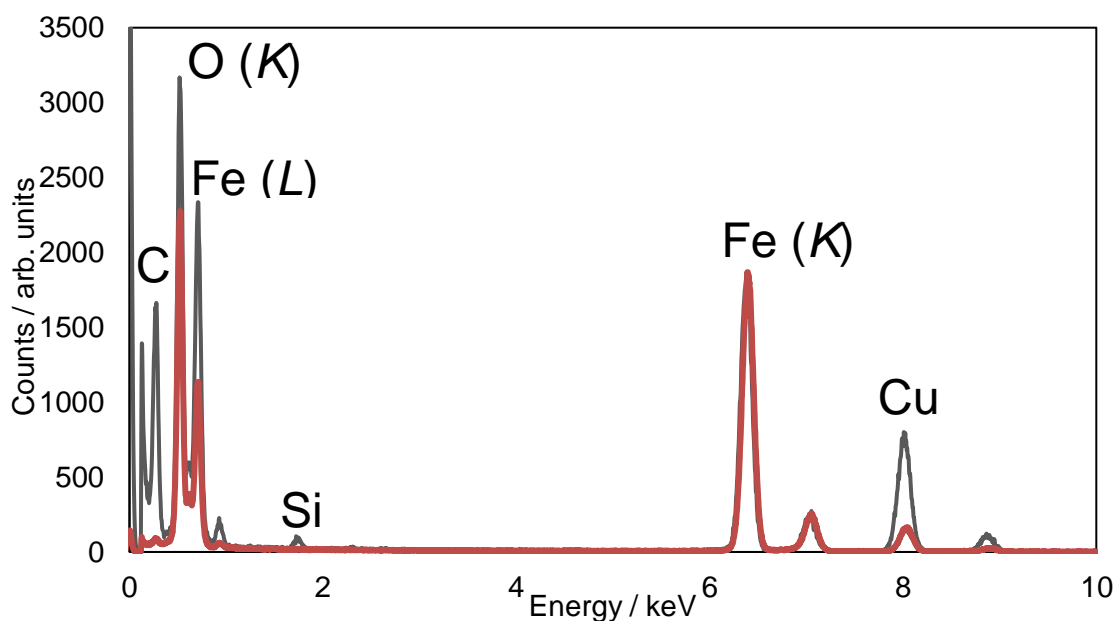


Figure 3.4. EDX spectrum of the iron oxide particles produced in the PAFS (grey) overlaid with an equivalent spectrum for the maghemite standard (orange). The latter spectrum has been scaled to the Fe K peak for the purposes of visualisation.

The sample is more oxygen-rich than the standard which could be for a number of reasons. First, it could be a result of contamination, which could have been introduced to the sample after deposition, prior to TEM imaging. A significant carbon peak is observed in the sample spectrum, suggesting the contamination could be from a C and O rich hydrocarbon source (e.g. volatile organic compounds, or VOCs). Since the TEM grids were very small (~ 1 mm) and were necessarily transferred into/out of the experimental apparatus, a storage vessel, and the TEM itself, this is the most likely point at which the sample would have become contaminated. On the other hand, it is possible that oxygen could have been introduced within the experimental apparatus, *via* reaction or coordination with an oxygen-rich species such as $O_3$, forming an oxide coating on the agglomerates. $Fe_2O_3$ is thought to form *via* the oxidation of Fe by $O_3$ (i.e. Fe $\rightarrow$ FeO $\rightarrow$ $FeO_2$ $\rightarrow$ $FeO_3$) since the rate of these gas-phase reactions is fast [*Self and Plane*, 2003]. Polymerization and additional restructuring in the solid phase is suggested to follow the Fe oxidation [*Saunders and Plane*, 2006; 2010]. With this in mind, it may be that there has been

incomplete re-ordering of the $FeO_3$ in the iron oxide particles from the present work, thus leading to the increased Fe/O ratio. In previous work using the PAFS under comparable experimental conditions, a Fe/O ratio of $0.65 \pm 0.06$ was obtained [*Saunders and Plane*, 2006] which was attributed to hematite particle formation. However, this ratio would also be consistent with the formation of maghemite. Furthermore, for nanoparticles with radii less than ~8 nm, maghemite is the more stable conformer as it has a lower surface enthalpy than hematite [*Navrotsky et al.*, 2008]. In light of this, a maghemite-like composition is thus the most likely composition for the iron oxide MSP analogues produced with the PAFS.

### 3.1.2  Data Analysis

The exponential attenuation of the irradiance of a beam of light from $I_0$ to $I$ as it traverses a distance $l$ through an absorbing medium can be expressed with the Beer-Lambert law [*Beer*, 1852; *Lambert*, 1760; *Rees*, 1989];

E3.1
$$\frac{I}{I_0} = exp(-a_{ext} \cdot l)$$

where the extinction coefficient ($\alpha_{ext}$) arises from both absorption and scattering:

E3.2
$$\alpha_{ext} = n \cdot (C_{abs} + C_{sca})$$

$n$ is the number of particles per unit volume of gas, and $C_{abs}$ and $C_{sca}$ are the absorption and scattering cross sections per unit volume of particle – these are measures of the absorption and scattering efficiencies, respectively. The Beer-Lambert law is used in a rearranged form to extract the optical density (or 'extinction') as a function of wavelength $\lambda$ and time $t$ ($OD(\lambda,t)$) from experimental spectra:

E3.3
$$OD(\lambda, t) = ln \frac{I_0(\lambda,t)}{I_{Cn(\lambda,t)}}$$

At each wavelength, the transmitted intensity at time $t$ is given by the sample spectrum recorded with the particle flow directed through the White cell ($I_{Cn}(\lambda,t)$). A straight line reference fitted to the background measurements yields the incident intensity at time $t$ ($I_0(\lambda,t)$), enabling the time and wavelength-dependent OD to be extracted from raw spectra (see Figure 3.5).

When particles are directed through the White cell, the normalised intensity in Figure 3.5 drops until the point where a steady state is reached and the signal plateaus. After the flow is switched back to the flow-bypass, the signal rises until it returns to the reference value. This enables the wavelength dependent OD to be extracted from the raw data at each time step (see Figure 3.6). After the particle size distribution had stabilised and a steady state was reached, these spectra were averaged to obtain one OD spectrum (see Figure 3.7). The uncertainty for this OD was calculated from the standard deviation of the steady state spectra and the detection limit for the experiment (the average standard deviation of 6 half-hour reference measurements).

The uncertainty in the OD and the detection limit both increased significantly at low wavelengths because of the reduction in both the intensity of the spectroscopic lamp and the quantum efficiency of the detector. As such, the optical data below 350 nm was discarded. Data above 550 nm was also discarded since the OD decreased below the detection limit. The OD spectrum was also corrected for contributions from any residual precursors present in the White cell. The OD of residual $O_3$ was negligible over the range of usable experimental data (350 nm $< \lambda <$ 500 nm) [*Burrows et al.*, 1999]. However, it was necessary to subtract the Fe(CO)$_5$ spectrum. Inspection of the literature did not yield appropriate data, so the Fe(CO)$_5$ absorption cross section was measured (Figure 3.7, top panel). The extent of Fe(CO)$_5$ photolysis was calculated using the flow rates, the lamp irradiance and the wavelength-dependent absorption cross sections.
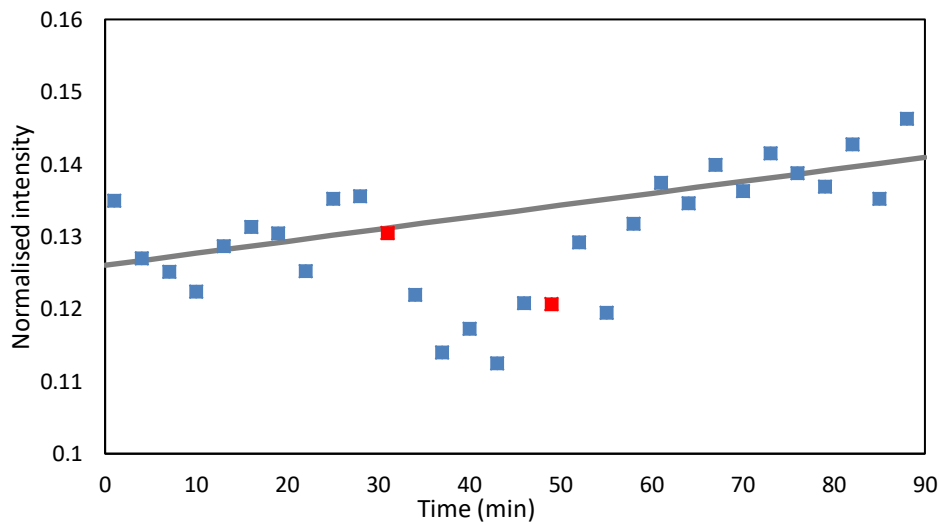


Figure 3.5: Example plot for iron oxide particles showing the normalised intensity ($I_{Cn}$) as a function of time at 350 nm (blue). The red data points indicate where the flow was switched from the flow-bypass to through the White cell, and vice versa. Also shown is the straight line fit to the reference data (grey line).
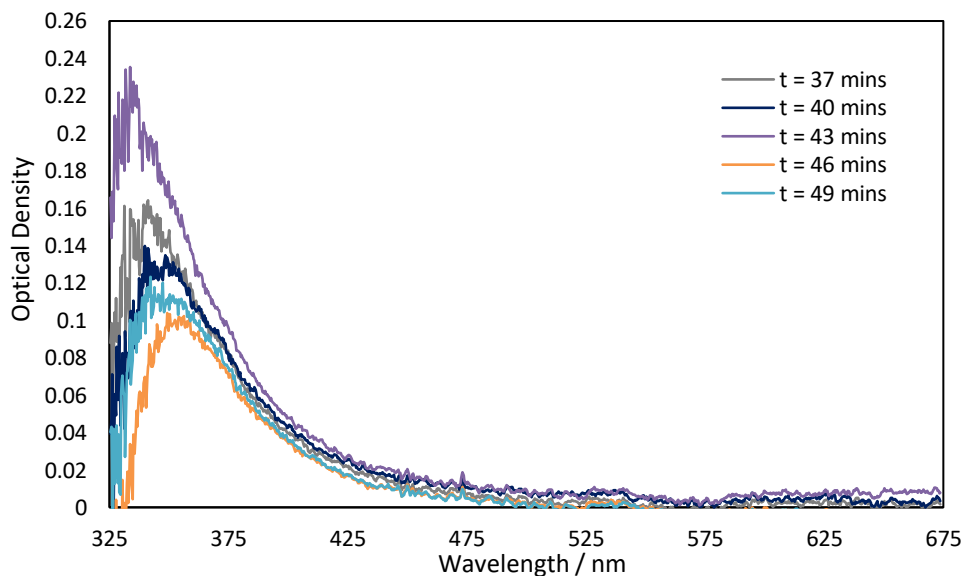


Figure 3.6: Iron oxide particle spectra for times between 37 and 49 minutes, where the signal has plateaued and the system is in steady state.
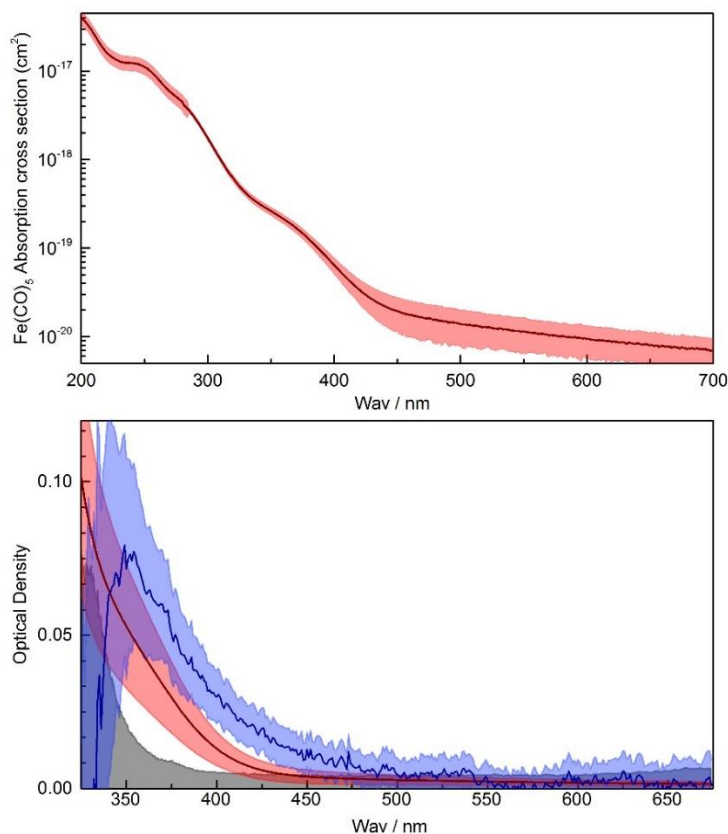
Figure 3.7. (Top panel) Measured $Fe(CO)_5$ absorption cross section ($cm^2$) with uncertainty indicated by red shading. (Bottom panel) Iron oxide particle extinction with the precursor spectrum removed (blue line). Experimental uncertainty is indicated by light blue shading. Also shown is the spectrum for the $Fe(CO)_5$ (red line) present in the absorption cell, with uncertainty indicated by red shading. The experimental detection limit is shown with the black line and shading.

## 3.1.3   Results and Discussion

The particle size distribution measured with the SMPS (Figure 3.8) follows a lognormal distribution, with its peak at a radius of 100 nm. The SMPS records the mobility radius – a measure of how fast particles travel in an electric field. For spherical particles this is equivalent to the outer radius. However, for amorphous particles, the mobility radius is typically larger than the fractal (outer) radius since they experience higher drag compared to a sphere with the same mass [*DeCarlo et al.*, 2004]. Thus, the mobility radius would represent an upper limit to the fractal radius. Nonetheless, a number of very large agglomerates were observed using TEM. This could be for a number of reasons. First, it may be that large particles are more efficiently deposited on the TEM grids, or secondly it could be a result of additional agglomeration after deposition. Alternatively, it may be that due to the filament-like structure of the particles the agglomerates may actually experience less drag than a sphere of equivalent mass. In any case, it may not be appropriate to use the measured size-distribution to calculate the particle optical density.
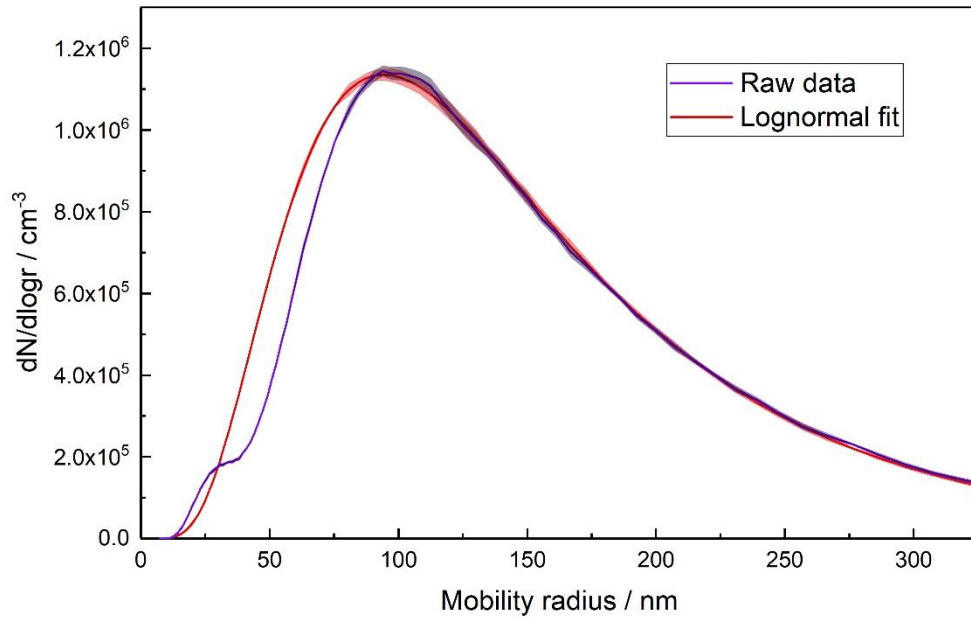
Figure 3.8. The experimental size distribution (purple) and a lognormal fit to the measured data (red). Shaded areas indicate the experimental uncertainty.

As exemplified in Figure 3.9 (dotted lines), modelling the measured size distribution using Mie theory over predicts the OD by at least an order of magnitude when using complex refractive index (RI) data for iron oxides available in the literature (hematite, magnetite, and wüstite [*Fontijn et al.*, 1997; *Henning and Mutschke*, 1997; *Hsu and Matijevic*, 1985; *Huffman and Stapp*, 1973; *Longtin et al.*, 1988; *Querry*, 1985]). Note that data from *Bedidi and Cervelle* [1993] have not been used for hematite since the data only goes down to a wavelength of 400 nm. A similar calculation cannot be performed for maghemite because there are no RIs available in the literature.

A method commonly used to calculate the OD of amorphous agglomerates is the Rayleigh-Debye-Gans (RDG) approximation [*Sorensen*, 2001] whereby an agglomerate is treated as a monodisperse distribution of primary spheres. The overall particle OD is calculated from a sum of the OD for the individual primary particles calculated using Mie theory. This approach assumes no multiple internal scattering and compares favourably to calculations where this is accounted for if the primary particle radius lies within the Rayleigh limit ($x \leq 0.3$) [*Farias et al.*, 1996]. For the particles considered in this study, this would mean an upper limit of $r_0 = 16.7$ nm at $\lambda = 350$ nm. For the experimental data, a concentration ($C_0 = 4.3 \times 10^{11}$ cm$^{-3}$) of the monomers (with average $r_0 = 1.65$ nm) can be calculated from the total integrated volume of particles in the measured size distribution, assuming spherical particles. Multiplying the OD calculated using Mie theory for a 1.65 nm particle by this concentration yields the ODs shown by dashed lines in Figure 3.9; again, the OD is over predicted by around an order of magnitude, although the decrease in the sample OD with increasing wavelength is better captured than when using Mie theory on the assumption that the measured size distribution was composed of spherical particles rather than agglomerates.
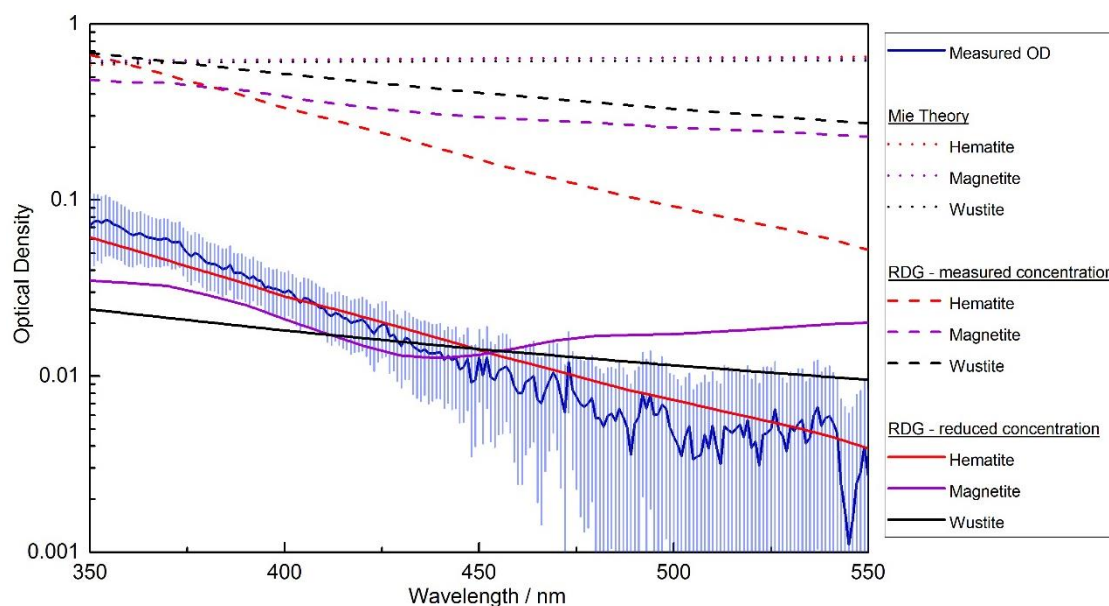
Figure 3.9. The measured wavelength dependent OD (blue), compared to the average OD calculated from literature data for hematite (red) [*Hsu and Matijevic*, 1985; *Longtin et al.*, 1988; *Querry*, 1985], magnetite (purple) [*Fontijn et al.*, 1997; *Huffman and Stapp*, 1973; *Querry*, 1985] and wüstite (black) [*Henning and Mutschke*, 1997]. Dotted lines indicate that the optical density has been calculated using Mie theory with the measured size distribution, dashed lines represent where the Rayleigh-Debye-Gans (RDG) approximation has been used with a monomer concentration derived from the measured size distribution, and solid lines indicate where the RDG approximation has been used with a monomer concentration fitted to experimental data.

If the measured size distribution were made up of fractal-like agglomerates rather than solid spheres, the monomer concentration would be significantly less than the previous estimate, as only a fraction of the volume of each sphere would be occupied by particles. Reducing the monomer concentration obtains significantly better fits to the measured OD for all iron oxides considered, with the best fit attained using hematite literature RIs (Figure 3.9, dashed lines). As mentioned previously, no RIs are available for maghemite in the literature. However, some absorption data is available for $5.1 \pm 1.5$ nm [*Jain et al.*, 2009] and 8.7 nm particles [*Tang et al.*, 2003]. For particles with sizes on the order of a few nanometres, absorption dominates over scattering (for the iron oxides, scattering $< 0.01$ % absorption) and the scattering contribution to the OD can be neglected. Thus, assuming the RDG approximation holds, a comparison can be made between this (arbitrarily scaled) absorbance data and the measured OD (Figure 3.10), since scaling the absorbance data is equivalent to changing the monomer concentration in the RDG approximation. Using this method, there is good agreement between the maghemite literature data and the experimental OD.

The optical analysis demonstrates that the best-fit to the experimental data is achieved through using hematite or maghemite RIs. The next-best fit is attained with wüstite RIs, and magnetite RIs give the worst fit to the data. However, the microscopic analysis definitively excludes a hematite-like or wüstite-like sample composition, suggesting the sample is closest to maghemite or magnetite. Of these two possible conformers, the TEM analysis suggests the most likely

composition is maghemite. Thus, considering these two analysis techniques, the sample is concluded to be maghemite-like in composition.
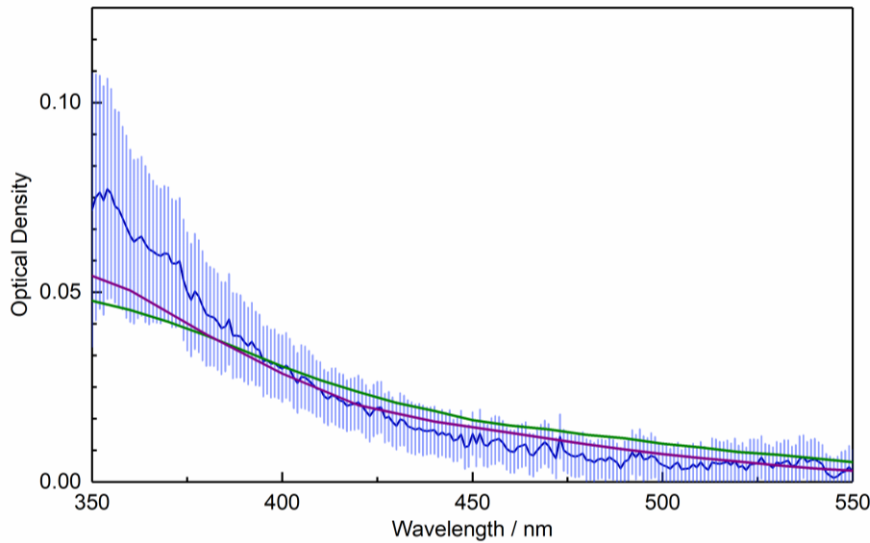


Figure 3.10. Comparison of the measured wavelength dependent OD (blue), and the scaled maghemite OD from *Jain et al.* [2009] (green) and *Tang et al.* [2003] (purple).

## 3.2   Optical Absorption: MICE/TRAPS Apparatus

### 3.2.1   Microscopy

Nanoparticles generated using the MICE/TRAPS apparatus were collected and analysed using scanning electron microscopy (SEM) [*Nachbar*, 2018]. For the iron oxide particles, analysis using EDX spectroscopy gave a Fe:O ratio close to 2:3, which is in good agreement with previous data using similar experimental techniques [*Chou and Phillips*, 1992; *David et al.*, 2012; *Nadeem et al.*, 2012]. Of these experiments, *David et al.* [2012] demonstrated the production of maghemite particles with XRD, Raman and Mössbauer spectroscopy. Furthermore, as mentioned previously, the formation of maghemite is thought to be thermodynamically favourable for particles with radii less than 8 nm [*Navrotsky et al.*, 2008]. To confirm the nanoparticle composition, Near Edge X-ray Absorption Fine Structure (NEXAFS) measurements were also performed, which obtained data comparable to the EELS spectra discussed for particles produced with the PAFS. The spectra obtained were compared to literature data for hematite, maghemite and magnetite, with the best fit provided by maghemite and magnetite spectra [*M. Nachbar, personal communication*]. Since the Fe:O ratio obtained through EDX spectroscopy was 2:3, the particles are assumed to be maghemite.

## 3.2.2 Data Analysis

### 3.2.2.1 Calculation of Particle Heat Up

Singly charged iron oxide nanoparticles were produced and held in a linear particle trap under controlled conditions. During an experiment, small numbers of particles were extracted with increasing trapping time and their mass was monitored using a TOF mass spectrometer. In successive experimental runs, irradiation of trapped particles under equivalent experimental conditions desorbs differing amounts of $H_2O$ from particles and plots such as Figure 3.11 can be generated, of the particle mass ($m(t)$) increase as a function of residence time ($t_{res}$). An empirical exponential expression is used to generate fits to the data;

E3.4
$$m(t) = m_0 + m_{ads} \cdot \left(1 - exp\left(\frac{-t_{res}}{\tau}\right)\right)$$

from which the initial mass of particles ($m_0$, kg) and the adsorbed mass of $H_2O$ molecules at equilibrium ($m_{ads}$, kg) can be extracted. Calculation of the nanoparticle radius ($r_N$, m), and hence surface area ($A_p = 4 \cdot \pi \cdot r_N^2$, m$^2$) from $m_0$, allows the surface concentration ($C_{H2O}$, m$^{-2}$) of $H_2O$ molecules to be calculated;

E3.5
$$r_N = \left(\frac{3m_0}{4\pi\rho}\right)^{\frac{1}{3}}$$

E3.6
$$C_{H2O} = \frac{m_{ads}}{m_{H2O} \cdot A_p}$$

where $\rho$ is the nanoparticle density (5200 kg m$^{-3}$) and $m_{H2O}$ is the mass of a $H_2O$ molecule (kg).
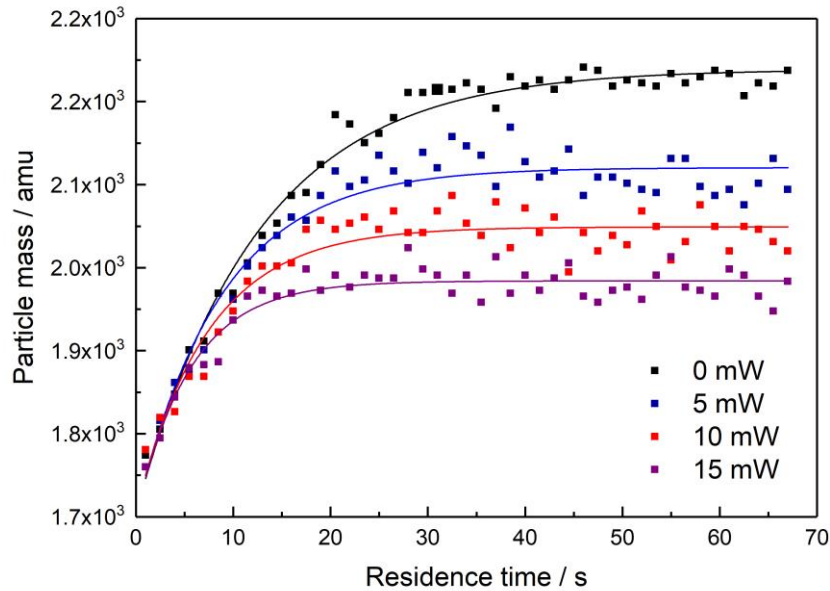


Figure 3.11: Nanoparticle mass as a function of residence time in the MICE, for experimental runs using increasing laser powers (0, 5, 10 and 15 mW (black, blue, red and purple respectively) at 405 nm, for $T_N$ = 144 K, $r_N$ = 1.69 nm.

During each experimental run where particles were not irradiated, the temperature of the nanoparticles ($T_N$) was equal to that of the environment i.e. the chamber ($T_{env}$), and an equilibrium between the adsorbing flux ($J_{ads}$, left-side of equation E3.7) and desorbing flux ($J_{des}$, right side of equation E3.7) of $H_2O$ molecules could be assumed ($J_{ads} = J_{des}$) [*Duft et al.*, 2019]:

E3.7
$$\frac{n_{H2O} \cdot v_{th}(T_{env})}{4} = C_{H2O} \cdot f \cdot exp\left(\frac{-E_{des}}{R \cdot T_N}\right) \cdot S_{eq}(r_N, T_N)$$

$v_{th}$ is the thermal velocity (m s$^{-1}$) of a gas-phase $H_2O$ molecule:

E3.8
$$v_{th} = \sqrt{\frac{8 \cdot k \cdot T_{env}}{\pi \cdot m_{H2O}}}$$

$S_{eq}$ is the equilibrium saturation over the particle surface:

E3.9
$$S_{eq} = exp\left(\frac{2 \cdot m_{H2O} \cdot \sigma}{k \cdot T_N \cdot \rho_{H2O} \cdot r_N}\right)$$

$n_{H2O}$ is the number density (cm$^{-3}$) of gas-phase $H_2O$, $f = 10^{13}$ Hz is the vibrational frequency of a $H_2O$ molecule on the particle surface [*Pruppacher and Klett*, 2010] and $R$ and $k$ are the gas constants (J K$^{-1}$ mol$^{-1}$ and J K$^{-1}$ respectively). $\sigma$ is the surface tension of amorphous solid water (mN m$^{-1}$), which is based on an extrapolation of data for supercooled $H_2O$ [*Nachbar et al.*, 2018a] and $\rho_{H2O}$ (g cm$^{-3}$) is the $H_2O$ ice density, which is based on a parameterisation for crystalline ice [*Pruppacher and Klett*, 2010]:

E3.10
$$\sigma = 114.81 - 0.144 \cdot T_N$$

E3.11
$$\rho_{ice} = 0.9167 - 1.75 \cdot 10^{-4} \cdot T_N(°C) - 5 \cdot 10^{-7} \cdot T_N(°C)^2$$

When $T_N = T_{env}$, the average desorption energy for a $H_2O$ molecule, $E_{des}$ (J molecule$^{-1}$), becomes the only unknown parameter in equation E3.7 – this was calculated for each particle size by solving for $E_{des}$. These calculated values for $E_{des}$ were then used for each irradiation experiment (where $T_N \neq T_{env}$) to calculate $T_N$, and the particle temperature increase upon irradiation ($\Delta T$) during that experimental run. This latter calculation was done in an iterative manner, by setting the initial value of $T_N$ to that of $T_{env}$. Two iterations were required before convergence in all cases.

### 3.2.2.2   Calculation of Particle Absorption

Assuming an equilibrium between radiative heating of the nanoparticles *via* absorption of laser light ($P_\lambda$, W), and cooling *via* collisions with the background gas, He ($P_{col}$, W) enables wavelength-dependent absorption cross sections ($C_{abs}$, m$^2$) to be calculated. The radiative heating (see equation E3.12) depends on the average irradiance ($I$, W m$^{-2}$) for each laser power used and on the absorption cross section. The description of collisional cooling used (equation E3.13) is presented in *Asmus et al.* [2014], where $n_{He}$ is the number of He molecules. $v_{th}$ is the thermal velocity of a He atom (E3.14, ms$^{-1}$), where $m_{He}$ is the mass of a He atom (kg). $A_{col}$ is the adsorption surface area (*E3.15*, m$^2$) where the collision radius ($r_{col}$) is the sum of the particle radius including the adsorbed $H_2O$, and the radius of He.

E3.12
$$P_\lambda = I \cdot C_{abs}$$

E3.13
$$P_{col} = A_{col} \cdot \frac{\alpha}{2} \cdot n_{He} \cdot \bar{v}_{th} \cdot k \cdot \Delta T$$

E3.14
$$v_{th} = \sqrt{\frac{8 \cdot k \cdot T_{env}}{\pi \cdot m_{He}}}$$

E3.15
$$A_{col} = 4 \cdot \pi \cdot (r_{col})^2$$

Absorption cross sections were calculated by equating $P_\lambda$ and $P_{col}$ (equations E3.12 and E3.13) and solving for $C_{abs}$.

### 3.2.3 Results and Discussion

For the comparison of the absorption across different sized particles, the absorption efficiency ($Q_{abs}$) is calculated; this provides a measure of how efficiently light is attenuated by a particle, and is defined as the absorption cross section normalised by the geometric cross section (E3.16). Figure 3.12 shows $Q_{abs}$ for nanoparticles with $r_N$ ~1-3 nm, generated with MICE/TRAPS at 405 nm (purple), 488 nm (blue) and 660 nm (red). The experimental $Q_{abs}$ values demonstrate an increase with increasing particle radius, and a decrease in $Q_{abs}$ with increasing wavelength. Because the nanoparticles are spherical and compact, Mie theory can be used to calculate absorption efficiencies using literature RIs, for comparison to the experimental data. These calculations have been performed using hematite RIs [*Bedidi and Cervelle*, 1993; *Hsu and Matijevic*, 1985; *Longtin et al.*, 1988; *Querry*, 1985], since these are the only RI data available for $Fe_2O_3$ particles. These data are shown in Figure 3.12 (dot-dashed dotted, short-dashed and dashed lines respectively), with the solid lines representing an average of these absorption efficiencies calculated at each wavelength. The average literature absorption data agrees fairly well with that from the experiment, given the large variation in the literature values and the experimental uncertainties. However, a more pronounced decrease is observed with increasing wavelength for the experimental $Q_{abs}$ – similar to the trend observed when comparing the PAFS OD to literature hematite data (using the RDG approximation with a fitted monomer concentration).

E3.16
$$Q_{abs} = \frac{C_{abs}}{C_{geom}}$$
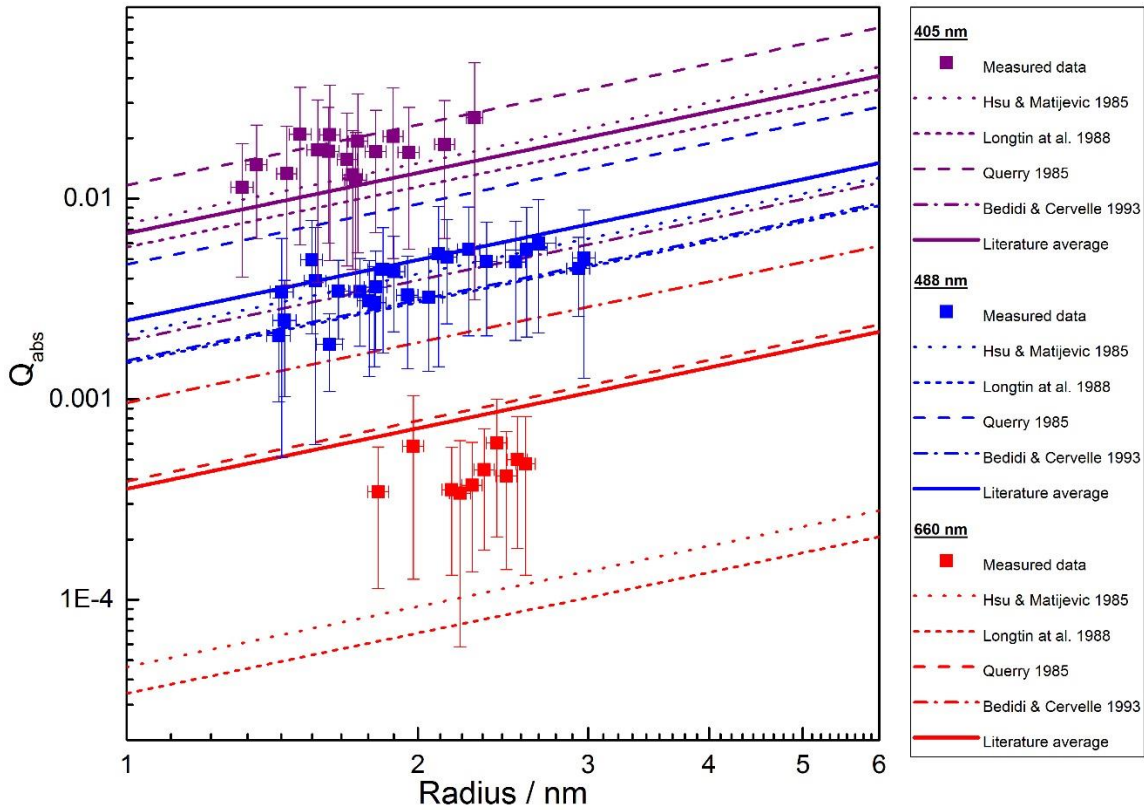
Figure 3.12: Absorption efficiencies at three wavelengths for a range of particle sizes: 405 nm (purple), 488 nm (blue) and 660 nm (red). Also shown are the absorption efficiencies calculated using literature data for hematite from Querry (dashed), Hsu and Matijevic (dotted), Bedidi and Cervelle (dot dash), Longtin et al. (short dash) and the average of these data (bold lines).

## 3.3   Photochemical Modelling

### 3.3.1   Derivation of Best-Fit Refractive Indices

In order to determine RIs for the iron oxide nanoparticles generated with both the PAFS and the MICE/TRAPS, a range of best-fit RIs were first calculated for the MICE/TRAPS data at 405 nm, 488 nm and 660 nm using an iterative procedure. At each wavelength, a range of possible RIs were used to calculate absorption cross sections ($C_{abs}$) using Mie theory, which were then compared to experimental data using E3.17. The RIs generating the smallest normalised squared difference ($\delta_{abs,\lambda}$) between the measured ($C_{abs,exp}$) and calculated ($C_{abs,calc}$) cross sections defined the best-fit RIs for the absorption measurements (Figure 3.13 dotted lines) at that wavelength.

E3.17
$$\delta_{abs,\lambda} = ((C_{abs,exp} - C_{abs,calc})/C_{abs,exp})^2$$
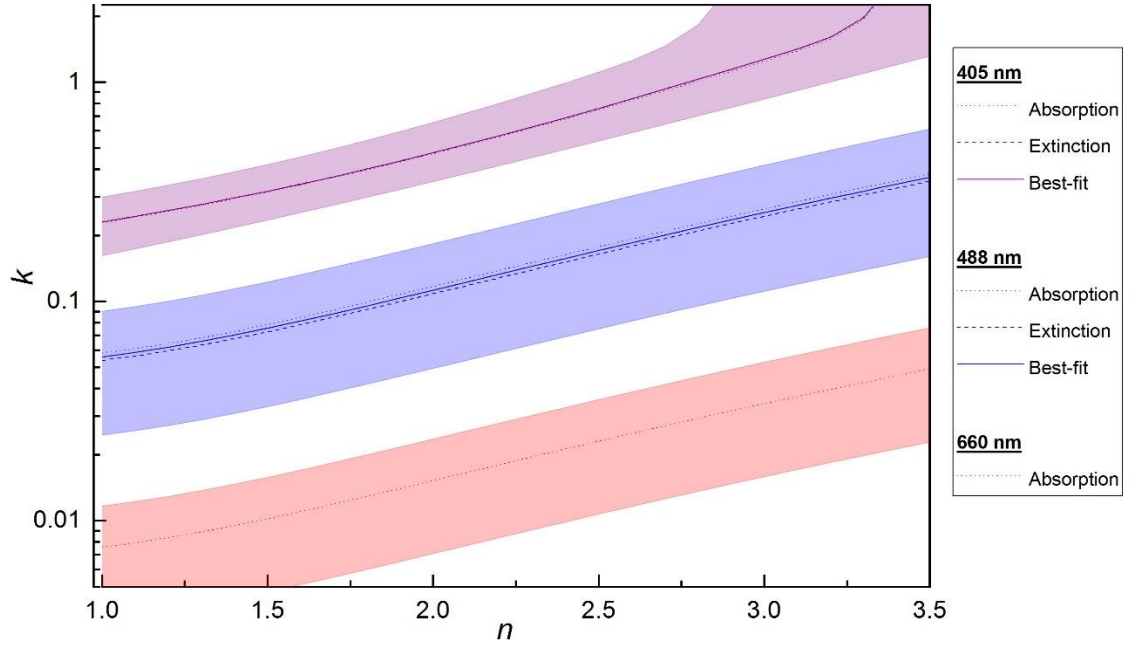
Figure 3.13. Best-fit real (n) and imaginary (k) RIs for absorption data (dotted lines), extinction data (dashed lines) and the two combined (solid lines) at 405 nm (purple), 488 nm (blue) and 660 nm (red). The shaded areas show where the resulting absorption and extinction cross sections are both within experimental error.

Since the primary particles from the PAFS are in an absorption dominated regime, the scattering component of the OD can be neglected and the extinction cross sections ($C_{ext}$) can be approximated using $C_{abs}$ for the MICE/TRAPS particles. This allows for the calculation of a best-fit primary particle concentration for the agglomerates. Using the best-fit RIs for MICE/TRAPS particles, the OD was calculated using the RDG approximation for a range of monomer concentrations at each of the two wavelengths where the measured OD was greater than the detection limit (405 nm and 488 nm). The normalised square difference ($\delta_{ext,\lambda}$) between the measured ($C_{ext,exp}$) and calculated ($C_{ext,calc}$) extinction cross sections was then computed:

E3.18
$$\delta_{ext,\lambda} = ((C_{ext,exp} - C_{ext,calc})/C_{ext,exp})^2$$

The final best-fit value was defined as the primary particle concentration that generated the smallest summed $\delta_{ext}$ over both wavelengths, 405 nm and 488 nm ($\chi^2_{ext}$):

E3.19
$$\chi^2_{ext} = \Sigma \delta_{ext,\lambda}$$

At each wavelength, this best-fit concentration ($3.14 \times 10^{10}$ cm$^{-3}$) was then used to calculate the OD for a range of RIs. The RIs giving the smallest normalised square difference, $\delta_{ext,\lambda}$ from the experimental data defined the best-fit RIs for the extinction at that wavelength (Figure 3.13, dashed lines). At 405 nm and 488 nm, the RIs giving the smallest combined square-difference ($\delta_\lambda$, equation E3.20) for both absorption and extinction were used (Figure 3.13, solid lines). At 660 nm, the best-fit RIs for the absorption data were used. The functions used to describe these final best-fit data are shown in Table 3.1, lines 1-3.

E3.20
$$\delta_\lambda = (\delta_{ext,\lambda} - \delta_{abs,\lambda})^2$$

Table 3.1. The functions used for fitting the imaginary refractive indices from best-fit real refractive indices at 405 nm, 488 nm and 660 nm (1-3). (4) shows the function used to derive the final wavelength dependent imaginary refractive indices for particles, using the three best-fit values at 405, 488 and 660 nm.

| | Wavelength / nm | Function |
|---|---|---|
| 1 | 405 | $y = y_0 + a_1 \cdot e^{(-x/t_1)} + a_2 \cdot e^{(-x/t_2)}$<br><br>where $y_0 = 0.121$, $a_1 = 1 \times 10^{-29}$, $t_1 = 0.0508$, $a_2 = 0.0337$, $t_2 = 0.850$ |
| 2 | 488 | $y = a \cdot e^{(-x/t)} + m \cdot x + c$<br><br>where $a = 0.300$, $t = -2.73$, $m = -0.242$, $c = -0.135$ |
| 3 | 660 | $y = a \cdot e^{(-x/t)} + m \cdot x + c$<br><br>where $a = 0.0563$, $t = -3.10$, $m = -0.0482$, $c = -0.0220$ |
| 4 | 350-660 | $y = a \cdot b^x$<br><br>where $a = 238$, $b = 0.986$ |

### 3.3.2 Derivation of Wavelength-Dependent Refractive Indices

Since it is possible to replicate the measured absorption and extinction data using multiple combinations of real and imaginary RIs, and there are only three wavelengths for which best-fit RIs have been established, it is difficult to determine a unique solution for the wavelength-dependence of the complex RIs. Multiple different functions to describe the wavelength dependence of both the real and imaginary RIs would need to be evaluated, for all possible combinations of the best-fit real-imaginary pairs across the three wavelengths studied. However, since the absorption dominates over scattering, the real refractive index has a much smaller impact on the resulting absorption and extinction. As such, the approach taken has been to first fix the wavelength dependence for the real RIs using the literature RIs for hematite. These data provided a reasonable fit to the absorption data, and provided the best fit to the experimental OD using the RDG approximation (Figure 3.9, solid red line). The OD calculated using hematite RIs was also very similar to the scaled absorbance data for maghemite (Figure 3.10).

Next, using these real RIs, the corresponding imaginary RI was selected from the best-fit data at 405 nm, 488 nm and 660 nm. The wavelength dependence of the imaginary RIs was then determined by fitting an exponential decay function through the three imaginary RIs (Table 3.1, line 4). The final RIs derived with this method are shown in Figure 3.14 (top panel). The uncertainties associated with these imaginary RIs were calculated by performing analogous calculations using the upper and lower limits of the best-fit RIs (from Figure 3.13). The ODs

given by the final RIs are shown in the bottom panel. The corresponding absorption data shows very good agreement with the experimental data (Figure 3.15); the absorption efficiencies calculated at 405 nm, 488 nm and 660 nm for a 1.65 nm particle are $1.59 \times 10^{-2}$, $3.19 \times 10^{-3}$ and $3.19 \times 10^{-4}$ respectively, compared to the measured values of $(1.60 \pm 1.15) \times 10^{-2}$, $(3.31 \pm 1.92) \times 10^{-3}$ and $(3.19 \pm 1.73) \times 10^{-4}$.
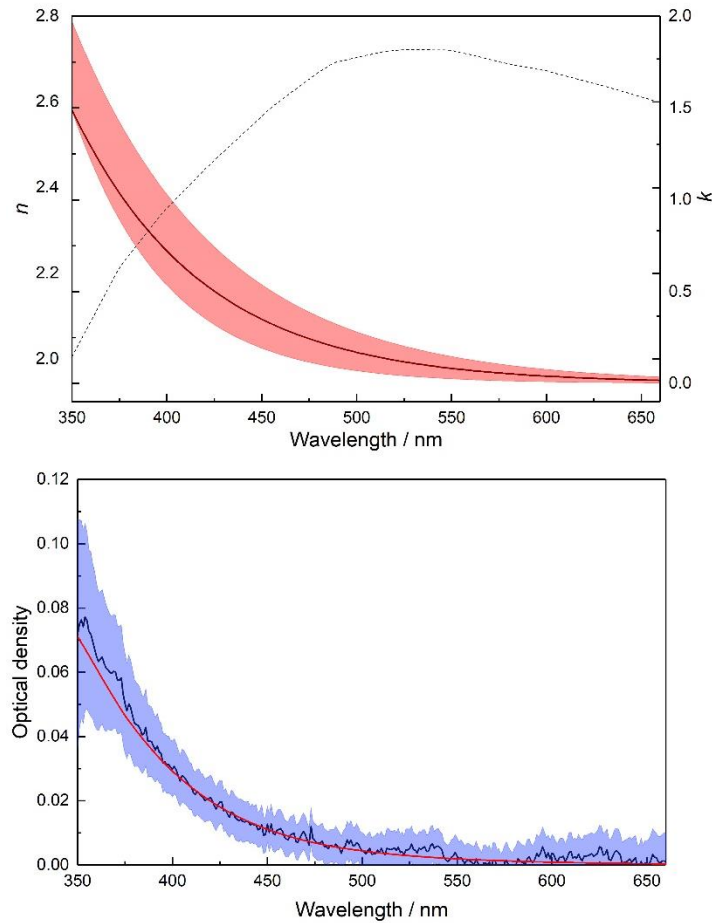


Figure 3.14. Top panel: Wavelength dependent real and imaginary RIs for maghemite particles. The real RI ($n$) is shown with the dashed line, and the imaginary RI ($k$) is given by the solid line. The experimental uncertainty is shown with red shading. Bottom panel: The experimental and calculated ODs using the wavelength dependent RIs for maghemite particles (blue and red lines respectively).
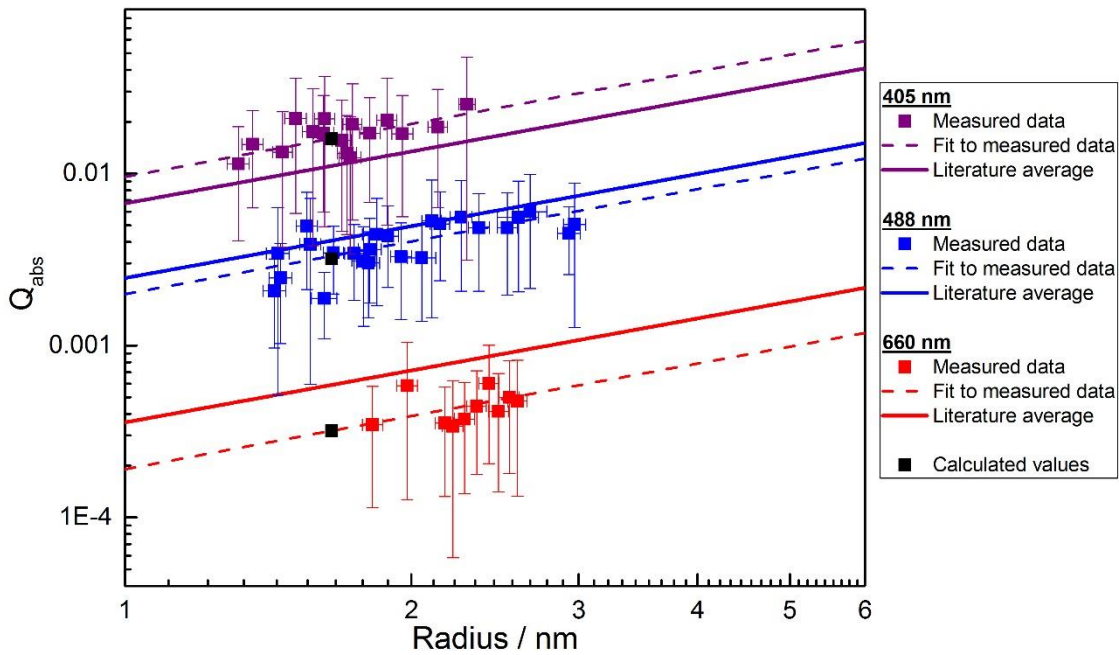
Figure 3.15. Measured Absorption efficiencies for a range of particle sizes at 405 nm (purple), 488 nm (blue) and 660 nm (red). The average absorption efficiencies calculated using literature data for hematite are shown with bold lines [*Bedidi and Cervelle*, 1993; *Hsu and Matijevic*, 1985; *Longtin et al.*, 1988; *Querry*, 1985]. Straight line fits thorough the experimental data are also shown for 405 nm, 488 nm and 660 nm with dashed lines. The black data points indicate absorption efficiencies calculated with the best-fit RIs at each wavelength.

## 3.4   Conclusions

Iron oxide meteoric smoke analogues were generated in the laboratory under atmospherically relevant conditions using two different experimental systems, the PAFS and the MICE/TRAPS. Nanoparticles produced with both experiments were collected and analysed using electron microscopy. For the PAFS, particles ranging in size from a few nanometres to a few microns were captured, that were highly fractal-like agglomerates composed of a number of primary spheres – the average radius of which was $1.65 \pm 0.15$ nm. EELS data were able to definitively exclude hematite-like and wüstite-like structures for the nanoparticles, with the EEL spectra showing good agreement with magnetite or maghemite literature data. The electron diffraction pattern corroborated this, showing concentric rings characteristic of the intense reflections for these iron oxide conformers. EDX confirmed the presence of Fe and O, though elemental quantification was not possible due to potential interference from Cu fluorescence. Unidentified contamination from an oxygen-rich hydrocarbon source, surface reactions, or incomplete restructuring of $FeO_3$ in the solid-phase could also be responsible for the quantification issues.

The optical extinction of PAFS particles was measured at wavelengths of 350 – 550 nm, demonstrating an approximate exponential decrease in OD with increasing wavelength. An optical analysis was performed using Mie theory and the RDG approximation to determine the most-likely particle composition using literature RI data for iron oxides. Using the measured size

distribution, neither Mie theory nor the RDG approximation were able to reproduce the measured extinction. However, the RDG approximation generated a good fit to data with a reduced primary particle concentration. Of the oxides for which RIs were available, hematite provided the best-match to the experimental data, though literature absorbance data for maghemite also provided a good fit to the measured extinction.

The MICE/TRAPS apparatus produced spherical, compact and singly charged nanoparticles with sizes ranging from 1-3 nm. NEXAFS measurements were able to exclude a hematite composition, with spectra best represented by maghemite or magnetite literature data, and quantification using EDX spectroscopy revealed a Fe:O ratio of 2:3. Consequently, the nanoparticles were concluded to be formed of maghemite. The optical absorption was measured at three wavelengths: 405 nm, 488 nm and 660 nm, with an increase in absorption efficiency observed with increasing particle size and decreasing wavelength. An optical analysis using literature RI data for hematite gave a reasonable fit to experimental data, though there was a wide range in the $Q_{abs}$ values calculated using literature data from different sources.

Wavelength-dependent complex RIs were derived for the maghemite MSP analogues using an iterative procedure. First, a range of best-fit RIs were determined at 405 nm, 488 nm and 660 nm using the absorption data. These RIs were used to optimise the best-fit primary particle concentration by calculating the optical extinction using the RDG approximation. The best-fit RIs at 405 nm and 488 nm were then adjusted such that they generated the best match to both experiments. Finally, wavelength-dependent complex RIs were derived across the wavelength range 350-660 nm, by first prescribing the wavelength-dependence of the real RI using literature absorption data for hematite. An exponential decay function was then used to obtain the wavelength-dependence for the imaginary part by fitting through imaginary RIs determined at 405 nm, 488 nm and 660 nm from the best-fit RIs.

## 3.5  Atmospheric Implications

Though a number of different iron oxide conformers have been considered to be some of the most likely constituents of MSPs, maghemite has not previously been examined as a candidate species due to the lack of optical data in the literature. However, the production of maghemite particles has been demonstrated in the laboratory using multiple production methods, operating under different conditions. This signifies that maghemite may have potential importance in the atmosphere, and should be an additional candidate species for MSPs. It also highlights the need for further studies to probe the formation, morphology, and optical properties of maghemite particles in this context. Furthermore, this study demonstrates that the RDG approximation is more appropriate than Mie theory to model the optical properties of fractal-like MSP analogues, since the latter of these techniques overpredicts the optical extinction by at least an order of magnitude. This supports the earlier work of  *Saunders et al.* [2007] and is an important

conclusion since the majority of studies relating to the optical properties of cosmic dust/MSPs rely on Mie theory to derive the OD – the parameter from which atmospheric implications are extrapolated. As a result, it is possible that the optical effects of such particles have been overestimated in a number of studies – for example, current MSP characterisation studies with the SOFIE satellite calculate MSP extinction using Mie theory for a distribution of spherical particles [*Hervig et al.*, 2017].

Although a unique solution to the wavelength-dependence of the real and imaginary RIs has not been established, the important parameter for the characterisation of MSPs in the atmosphere is the particle extinction. As such, since the derived RIs are able to reproduce both the measured extinction and absorption, these RIs should still be functional for this purpose over the wavelength range studied. Furthermore, the variation in the OD calculated at each of the three wavelengths (405 nm, 488 nm and 660 nm) with each of the possible combinations of real and imaginary best-fit RIs (Figure 3.3) is less than ~0.4 %, meaning no significant difference in the extinction would be observed for a different solution for the wavelength-dependent RIs.

The fact that the derived complex RIs were able to generate good matches to the absorption and extinction generated by crystalline and amorphous particles respectively lends confidence to the idea that it is appropriate to use the RIs for bulk species to represent amorphous MSPs for the purposes of their characterisation in the atmosphere. Nonetheless, in order for these RIs to be used with data from the SOFIE satellite, the wavelength range of the data would need to be extended further into both UV and IR wavelengths as the satellite channels currently used for this analysis are at $\lambda = 330$ nm, 867 nm and 1037 nm [*Hervig et al.*, 2017]. With the current data, extrapolation to 330 nm may be feasible but it is not possible to extrapolate to the other wavelengths used due to the unpredictable variation in RIs usually observed across wide wavelength ranges. However, it is possible that the RIs could be used in global climate models to probe the optical properties of meteoric smoke.

# Chapter 4
# Global Climate Modelling: Methods

A significant perturbation to the flux of Earth-bound dust from a comet's close passage could have implications for both atmospheric chemistry and dynamics. Indeed, the recent encounter of Comet Siding Spring with Mars provided evidence that the atmospheric perturbations caused by such an event are significant [*Schneider et al.*, 2015]. Sensitivity simulations have therefore been performed using the Whole Atmosphere Community Climate Model (WACCM) with an elevated Meteoric Input Function (MIF) to investigate such an encounter – specifically, the passage of Comet Halley past the Earth at a distance of 100,000 km (hereafter referred to as the 'Halley' model runs). The analytical model developed by *Moorhead et al.* [2014] has been used in conjunction with an atmospheric chemical ablation model – CABMOD [*Carrillo-Sanchez et al.*, 2016] – to provide the MIF of several meteoric species (Na, Fe, Si, Mg, S and MSPs) in the MLT for input into WACCM. Two different model configurations have been used to explore the key effects of this additional input on the atmosphere: impacts on the chemistry and dynamics of the upper and middle atmosphere have been probed using 'WACCM 1.06'; impacts on the middle atmosphere and surface deposition have been probed using 'WACCM-CARMA'. This chapter will present details of both model configurations and the simulations performed.

## 4.1   The Meteoric Input Function

The MIF describes the injection rate of meteoric material into the atmosphere as a function of time, latitude, longitude and altitude in units of atoms $cm^{-3} s^{-1}$. The 'standard' MIFs describing the input of meteoric species to the MLT are calculated using a chemical ablation model (CABMOD) developed at the University of Leeds [*Carrillo-Sanchez et al.*, 2016; *Vondrak et al.*, 2008] starting from the typical distribution of sporadic meteoroids as a function of time, mass, velocity and entry angle [*Carrillo-Sanchez et al.*, 2016]. These MIFs are used in all model runs, with additional 'Halley' MIFs calculated from CABMOD for the time period where the Earth passes through the coma of Comet Halley during the simulated close encounter. The particle flux used to calculate the Halley MIFs was itself calculated using a dust model developed for the Siding Spring encounter [*Moorhead et al.*, 2014].

### 4.1.1   Dust Model

Before the close passage of Comet Siding Spring past Mars in October 2014, a number of different groups developed dust models to predict the risk posed to spacecraft and the planet from ejected material. *Moorhead et al.* [2014] developed an analytical model that describes the spatial and size distributions of dust in a cometary coma. Whilst this model under-predicted the dust fluence for

the Siding Spring encounter, the model was able to successfully reproduce the dust fluence experienced by Giotto during the Halley flyby in 1986. A detailed description of the dust model used can be found in *Moorhead et al.* [2014]. In brief:

A power law is chosen for the size distribution;

E4.1
$$f(s) = Cs^{-k}$$

where $s$ is the particle radius (m) and the normalisation parameter ($C$, m$^{1.6}$) is defined as:

E4.2
$$C = \frac{g}{ah^\beta} \cdot 10^{-0.4(M1-m_{\odot,1au})} \cdot au^2 \cdot \frac{3-k}{s_{max}^{3-k} - s_{min}^{3-k}}$$

Assuming a constant flux of particles away from the comet, the number density ($N$, cm$^{-3}$) can be represented by an inverse-square dependence on cometocentric distance ($r$, m):

E4.3
$$N(r) = Dr^{-2}$$

where the coefficient of the spatial number density ($D$, m$^{-1}$) is equal to:

E4.4
$$D = C \cdot \frac{s_{max}^{1-k} - s_{min}^{1-k}}{4\pi r_c (1-k)}$$

Additional parameters used to define C and D are in are described in Table 4.1.

The particle flux ($\xi$/ m$^{-2}$ s$^{-1}$) is calculated from $N$ (cm$^{-3}$) and the encounter velocity ($v$/ m s$^{-1}$). This can be expressed in terms of the time, $t$, or distance, $x$, along a straight trajectory through the coma, from $-t_{max}$ to $t_{max}$, or $-x_{max}$ to $x_{max}$, where $t_{max}$ and $x_{max}$ are the time and distance from the edge of the coma to the point of closest approach respectively:

E4.5
$$t_{max} = \frac{x_{max}}{v} = \frac{\sqrt{r_c^2 - b^2}}{v}$$

The flux can be expressed in terms of the particle mass ($m$), as opposed to the radius; the time-dependent particle flux in each mass interval ($dm$) of the size distribution can be expressed as:

E4.6
$$\frac{d\xi(t)}{dm} = \frac{g}{ah^\beta} \cdot \left(\frac{2}{\pi}\right)^{\frac{1}{3}} \cdot \left(\frac{\rho}{3}\right)^{\frac{2}{3}} \cdot 10^{-0.4(M1-m_{\odot,1au})} \cdot au^2 \cdot \left(\frac{3-k}{3}\right) \cdot \left(\frac{m^{-(2+k)/3}}{m_{max}^{(3-k)/3} - m_{min}^{(3-k)/6}}\right) \cdot \left(\frac{v/r_c}{(v \cdot t)^2 + b^2}\right)$$

This can be integrated over the size distribution to get the total mass flux (g m$^{-2}$ s$^{-1}$) at each point in time (see Figure 4.1). Integration of the total mass flux over time obtains the total mass fluence along the trajectory (g m$^{-2}$). The fluence was multiplied by the area of one hemisphere ($A$/ m$^2$) as a circular target ($A=\pi r_e^2$, where $r_e$ is the radius of the Earth) to obtain the total integrated mass input to the Earth during the Halley encounter. Model calculations reveal that the Earth would spend just over 1 hour (~ 4000 s) inside the coma of Comet Halley. During this time, approximately 400 kt of dust (~10,000 times the daily input from sporadic meteors) would be deposited into the Earth's atmosphere. The dust flux increases with decreasing cometocentric distance, and decreases after the closest approach point in a symmetric manner.

Table 4.1. Model parameters used by Moorhead et al. [2014] and those that used in the current study.

| Parameter | Symbol | Value used for Siding Spring encounter | Reference | Value used for Halley-Earth encounter | Reference |
|---|---|---|---|---|---|
| Albedo | $a$ | 0.04 | *Fulle et al.* [2000] | 0.04 | *Fulle et al.* [2000] |
| Apparent solar magnitude at 1 au | $m_{O,1au}$ | -26.74 | | -26.74 | |
| Approach distance | $b$ | 131,000 km | NASA's Jet Propulsion Laboratory (JPL) | 100,000 km | |
| Astronomical uinit | $au$ | $150 \times 10^9$ m | | $150 \times 10^9$ m | |
| Coma radius | $r_c$ | Variable | *Fulle et al.* [2000] | 200,000 km | *Moorhead et al.* [2014] |
| Density | $\rho$ | 0.1 gcm$^{-3}$ | *Fulle et al.* [2000] | 2 gcm$^{-3}$ | |
| Dust contribution fraction to total brightness | $g$ | 1 | *Fulle et al.* [2000] | 1 | *Fulle et al.* [2000] |
| Heliocentric distance | $h$ | 1.4 au | JPL | 1 au | |
| Maximum dust mass | $m_{max}$ | 31.0 g | *Fulle et al.* [2000] | 31.0 g | *Fulle et al.* [2000] |
| Minimum dust mass | $m_{min}$ | $7.71 \times 10^{-9}$ g | *Fulle et al.* [2000] | $7.71 \times 10^{-9}$ g | *Fulle et al.* [2000] |
| Maximum dust radius | $S_{max}$ | 15.5 mm | *Fulle et al.* [2000] | 15.5 mm | *Fulle et al.* [2000] |
| Minimum dust radius | $S_{min}$ | 9.84 μm | *Fulle et al.* [2000] | 9.84 μm | *Fulle et al.* [2000] |
| Radial dependence exponent | $\beta$ | 2.4 | JPL | 2.4 | JPL |
| Size distribution exponent | $k$ | 2.6 | *Fulle et al.* [2000] | 2.6 | *Fulle et al.* [2000] |
| Total magnitude | $M1$ | 5.2 | JPL | 3.88 | *Hughes*, [1988] |
| Encounter velocity | $v$ | 55.96 km s$^{-1}$ | | 66.5 km s$^{-1}$ | *McDonnell et al.* [1987] |
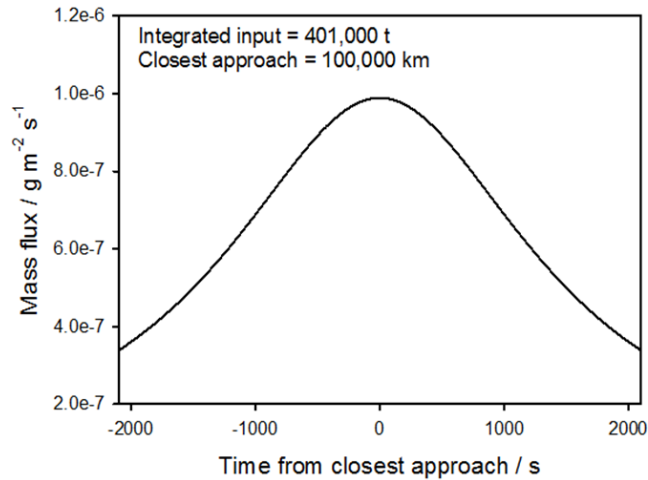
Figure 4.1. Total mass flux (g m$^{-2}$ s$^{-1}$) of the dust encountered by the Earth during passage through the coma of comet Halley as a function of time from closest approach.

### 4.1.2   Chemical Ablation Model

The Chemical Ablation Model (CABMOD) developed by *Vondrak et al.* [2008] and updated by *Carrillo-Sanchez et al.* [2016] considers a full treatment of the physics and chemistry of ablation: the sputtering of particles (i.e. ejection of surface atoms *via* inelastic collisions with air molecules); melting and evaporation of atoms and oxides; diffusion controlled migration of volatiles (Na and K); and impact ionization caused by collisions with atmospheric particles [*Vondrak et al.*, 2008]. The model framework is shown in Figure 4.2. Specific details including the equations used are discussed by *Vondrak et al.* [2008].
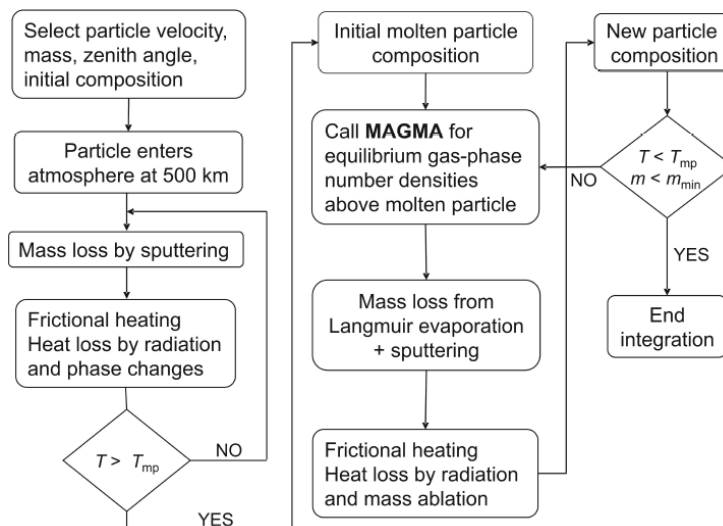


Figure 4.2. Flow diagram indicating the model architecture of CABMOD [Vondrak et al., 2008]. MAGMA is a chemical equilibrium code which calculates the vapour pressures of species evaporating from the meteoroid [Fegley and Cameron, 1987; Schaefer and Fegley, 2004; 2005].

The initial meteoroid composition for both the standard and Halley MIFs is assumed to be that of an ordinary chondrite ($Fe_2O_3$ (36.3 %), $SiO_2$ (34 %), MgO (24.2 %), $Al_2O_3$ (2.5 %), CaO (1.9 %) and $Na_2O$ (1 %)) based upon observations of dust from Comet Wild 2 [*Carrillo-Sanchez et al.*, 2015; *Gainsforth et al.*, 2015]. This composition is representative of the typical incoming meteor population. For the standard MIF, the initial particle distribution is generated from the six main sporadic meteoroid populations (33 % from the Apex, 22 % from the Helion, 22 % from the Anti-Helion, 11.5 % from the North Toroidal, and 11.5 % from the South Toroidal) [*Marsh et al.*, 2013a] which defines the angular and velocity distribution of the incoming particles at each latitude, longitude and time of year. From this initial distribution, the seasonally varying MIF can be calculated with CABMOD. This MIF has been validated against radar meteor head echo observations [*Janches et al.*, 2006] and is able to satisfactorily reproduce the observed metal layers in terms of peak concentration and seasonal variation. The average injection profiles for meteoric metals in the standard MIF are shown in Figure 4.3.

For the Halley-flyby, using the particle distribution defined from the dust model of *Moorhead et al.* [2014], CABMOD was used to predict the average elemental ablation profiles for the meteoric metals (Figure 4.3) using an entry velocity of 66 km s$^{-1}$ and a zenith angle of 35 °. Typically, around 20 % of incoming sporadic meteoroids are fully ablated in the MLT at altitudes between 70 and 100 km [*Carrillo-Sanchez et al.*, 2016]. However, the fast entry speeds of Halley meteoroids mean that the majority of the material ablates completely (Mg, Na, Si, Ca, Al, Ti, K and O: 100.0 %, Fe: 99.8 %, Al: 98.1%, J.D. Carillo Sánchez, personal communication 2018). For the Halley meteoroids, the peak ablation altitude is also around 10 km higher than that for the sporadic background population. Further differences can be seen in the altitude range over which ablation occurs, which is significantly narrower for Halley meteoroids. These differences are a result of the more energetic collisions that occur between the meteoric material and ambient molecules. This leads to greater heating rates, and means fewer collisions are required to vaporise the particles. As such, the material is ablated more rapidly/ at higher altitudes.
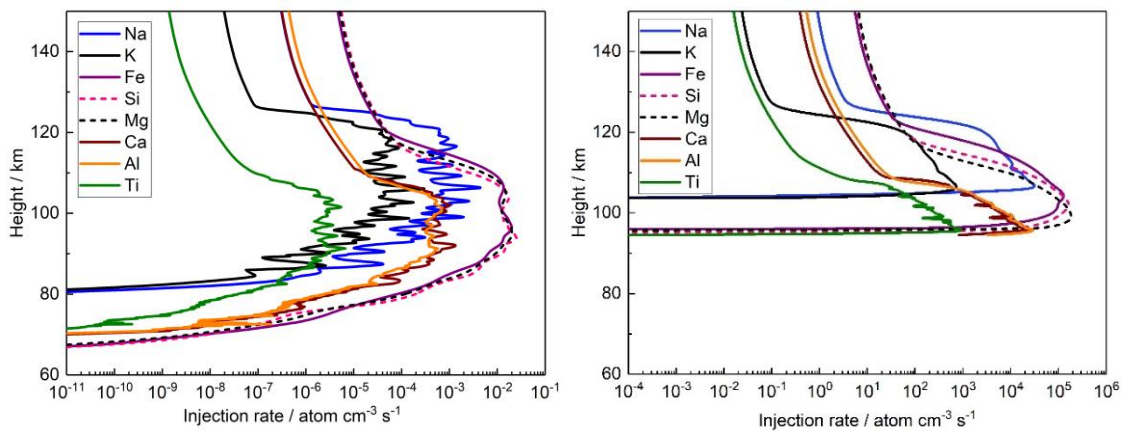


Figure 4.3. Ablation rate profiles for individual elements, integrated over the meteoroid mass range 10$^{-3}$ to 10$^{3}$ μg for the standard MIF (left) and the Halley MIF (right) as predicted by CABMOD. Note different horizontal scales.

## 4.2   WACCM 1.06

### 4.2.1   Model Setup

The Community Earth System Model version 1 (CESM1) is a fully coupled climate model incorporating five separate interacting components that model the Earth's atmosphere, ocean, land, land-ice and sea-ice [*Marsh et al.*, 2007]. The specific configuration used is CESM1.06 (hereafter referred to as WACCM 1.06), the most recent validated version of CESM1 with additional bug-fixes. The default configuration of CESM1 uses the Community Atmosphere Model version 4 (CAM4) as the atmospheric component. WACCM4, used in this work, represents an extension of CAM4 (hereafter referred to as WACCM). WACCM is a 'high-top' coupled chemistry-climate model that has a hybrid σ-pressure vertical coordinate with 66 levels – covering altitudes from the surface up to $5.1 \times 10^{-6}$ hPa (~140 km) [*Marsh et al.*, 2013b]. The vertical resolution in the MLT is approximately 3.5 km and the horizontal resolution is 1.9° latitude by 2.5° longitude.

WACCM contains a detailed description of dynamic, physical, chemical, radiative, and electrodynamic atmospheric processes in the middle and upper atmosphere [*Liu et al.*, 2010; *Marsh et al.*, 2007]. The interactive atmospheric chemistry module, which includes most known neutral and a number of ionic reactions, is based upon the Model for Ozone and Related Chemical Tracers, version 3 (MOZART) [*Kinnison et al.*, 2007] that contains compounds from the $O_x$, $NO_x$, $HO_x$, $ClO_x$, and $BrO_x$ chemical families, and also $CH_4$ (and its degradation products) [*Marsh et al.*, 2013b]. Additional metal chemistry has been added [*Bones et al.*, 2015; *Feng et al.*, 2017; *Plane et al.*, 2015; *Viehl et al.*, 2016] such that the model now contains 100+ chemical species and 400+ gas-phase reactions in total. A simple representation of tropospheric chemistry is used which includes only $CH_4$ and CO oxidation. A six constituent ion chemistry model is used to represent the E region ionosphere ($O^+$, $O_2^+$, $N^+$, $NO^+$, $N_2^+$ and $e^-$). WACCM uses the physical parameterisations from CAM4 for important processes not explicitly included in the model such as deep convection, cloud physics and forcing, gravity waves and solar proton events [*Feng et al.*, 2013; *Neale et al.*, 2013].

All model runs have used a 'free-running' configuration. The alternative configuration, 'specified dynamics', uses re-analysis meteorological data (surface pressure, temperature and winds [*Kinnison et al.*, 2018]) to constrain the model at every time step by mixing 1 % of model data fields with measured dynamical data below 60 km altitude. Generally, model output from simulations using both free-running and specified dynamics compare satisfactorily, although using a free-running model introduces a somewhat greater degree of natural variation between comparable model runs than using specified dynamics. Nevertheless, a free-running configuration was chosen as it prevents any 'nudging' of the model influencing atmospheric dynamics, meaning any dynamical changes observed can be attributed to the Halley perturbation with confidence.

## 4.2.2  MIF Implementation

The injection profiles calculated using CABMOD (atom $m^{-3}$ $s^{-1}$) for both the standard and Halley MIFs were interpolated onto the WACCM-grid prior to inclusion in the model. The Halley MIF was introduced in only one hemisphere (0-180 °E, chosen arbitrarily), to simulate the dust being preferentially deposited on the 'ram' hemisphere with respect to the direction of travel through the cometary coma. In contrast to the standard MIF, the Halley MIF was constant over latitude and longitude within the injection hemisphere. For all model runs, the standard MIF was implemented across all latitudes, longitudes, altitudes and times, with the Halley MIF additionally introduced on 2nd January at 00:00 UT (one day after the start of the simulations).

For the WACCM 1.06 model runs, the standard time step of 30 minutes was decreased to 5 minute resolution such that the Halley MIF could be introduced incrementally – both to ensure a more realistic representation of the injection and to prevent the sudden and dramatic increase in material causing model instability. The material was introduced over 4200 s, with the average Halley MIF multiplied by a time-dependent scaling factor ($M$) at each time step. The MIF factors used followed a Gaussian profile (equation E4.7, Figure 4.4) where $t$ is the time (s) at the start of each timestep, and $y_0$, $A$, $x_c$ and $w$ are fitted parameters with values 0.4611, 2104.6, 1361.5 and 0.7614 respectively. The magnitude of the scaling factors was such that the total integrated input (Na, K, Fe, Si, Mg, Ca, Al, Ti, O) was equal to 401,000 tons.

E4.7
$$M = y_0 + A \cdot exp\left(-0.5 * \left(\frac{((t+150)-x_c)}{w}\right)^2\right)$$
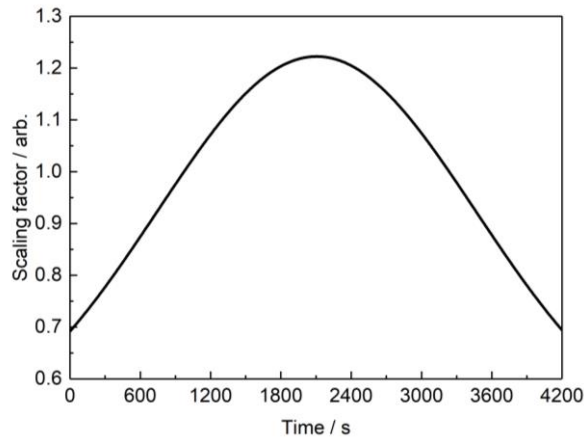


Figure 4.4. Time-dependent 'MIF factors' (scaling factors) used for the Halley MIF to define the ablation rate profiles during the 4200 s Halley encounter.

In practice, this meant only a fraction of this total amount was injected in the model runs; since only the major meteoric species Fe, Si, Mg and Na were introduced (which together account for approximately 243,000 tons, or ~61 % of the meteoric material). Of the remaining material, oxygen accounts for 36.3 % and the remaining 2.8 % is comprised of K, Ca, Al and Ti. Atomic oxygen was not introduced in addition to the other meteoric material as the concentration of

atomic O in the MLT is significantly higher than that which would be injected during the Halley encounter; the ambient O concentration is on the order of $1 \times 10^{10} - 5 \times 10^{11}$ atoms cm$^{-3}$ compared to an expected increase of $2.4 \times 10^9$ atoms cm$^{-3}$ for Halley at 100 km altitude.

A fraction of each meteoric metal was injected directly as ions, to account for the direct ionization of atoms occurring during atmospheric entry due to high speed collisions with $N_2$ and $O_2$ [*Janches et al.*, 2017]. Integrating over the mass distribution of incoming particles, the total ionization fraction for each metal was calculated to be 0.65, 0.62, 0.65 and 0.81 for Fe, Si, Mg and Na respectively (J.D. Carillo-Sánchez, personal communication, 2018). The final Halley MIF used for input into WACCM, for the meteoric metals Fe, Mg, Na and Si and their respective ions is shown in Figure 4.5.
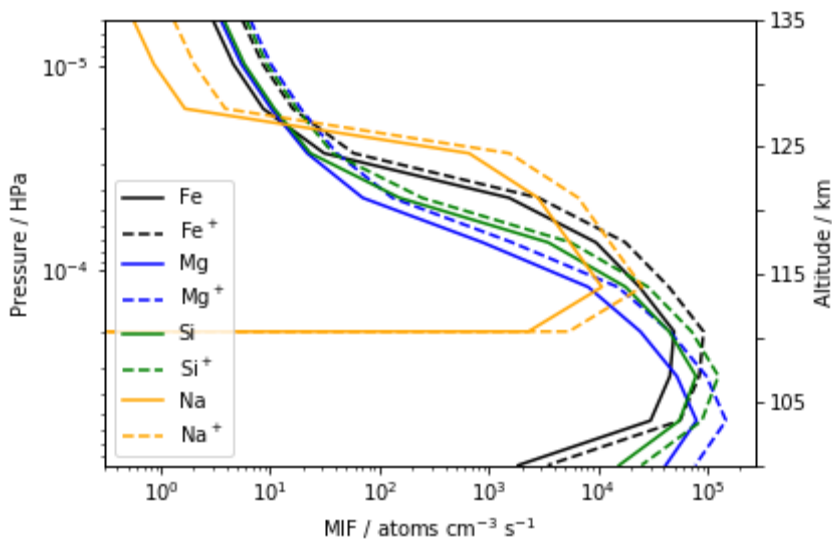


Figure 4.5. Average ablation rate profiles (atoms cm$^{-3}$ s$^{-1}$) for the individual elements Fe, Mg, Na, Si, and their respective ions, as a function of pressure (hPa) at the peak of the dust-input. Profiles were predicted by CABMOD and interpolated onto the WACCM model grid. The approximate altitude is shown on the right axis for reference.

## 4.2.3   Temperature Calculations

The cometary material injected into the atmosphere during the Halley encounter carries a significant amount of kinetic energy due to the high entry velocity of particles. This energy will be dispersed *via* processes such as phase transitions, ionization, translational energy and radiative emission. It is therefore important to consider the local temperature increase of the MLT during the Halley encounter. In order to evaluate a heating rate (K/s) which could be applied in the model, the following method was used to first estimate the amount of heat energy generated. Neglecting any energy lost in light production (approximately 0.2% [*Campbell-Brown and Koschny*, 2004]) and assuming all of the kinetic energy introduced is converted to heat (excepting the fraction consumed in phase transitions) the total heat produced ($Q_{tot}$/ J) was calculated for an initial

composition of meteoroid consisting of $Fe_2O_3$ (36.3 %), $SiO_2$ (34 %), MgO (24.2 %) and $Na_2O$ (1 %) *[Vondrak et al., 2008]*;

E4.8
$$Q_{tot} = \frac{1}{2} \cdot m \cdot v^2 - \Delta H_{fu} - \Delta H_{vap} - \Delta H_{at}$$

where $m$ is the mass of incoming material (kg), $v$ is the velocity (66,000 m s$^{-1}$), and $\Delta H_{fo}$, $\Delta H_{fu}$, $\Delta H_{vap}$ and $\Delta H_{at}$ are the heats of fusion, vaporization and atomisation respectively (J).

So that the temperature increase could be introduced to the model over the appropriate altitude range, the total heat energy was split over the altitude range spanned by the MIF ($z_{min}$ - $z_{max}$). At each altitude level the heat fraction ($Q_{frac}$ / J) was determined (equation E4.9) by multiplying the total heat ($Q_{tot}$ / J) by a fractional scaling factor calculated from the total MIF ($MIF_{tot}$ / atoms cm$^{-3}$ s$^{-1}$) – the sum of the MIFs for the meteoric metals, Fe, Si, Mg and Na.

E4.9
$$Q_{frac} = Q_{tot} \cdot \left( \frac{MIF_{tot}}{\sum_{z_{min}}^{z_{max}} MIF_{tot}} \right)$$

Division of $Q_{frac}$ by the total number of injected atoms at each altitude level yields the average energy carried by each atom;

E4.10
$$Q_{at} = \frac{Q_{frac}}{MIF_{tot} \cdot V_{lev} \cdot t} \cdot M$$

where $V_{lev}$ is the volume of the altitude level for the injection hemisphere (cm$^3$) and $t$ is the total encounter time (4200 s). At each timestep, the average energy input per injected atom is multiplied by the MIF factor, $M$, such that the time-dependent energy input ($Q_{at}$ / J atom$^{-1}$) follows the same Gaussian profile as the incoming material (Figure 4.4). This energy, $Q_{at}$, multiplied by the total MIF yields the energy input rate to the atmosphere ($E_{in}$/ J cm$^{-3}$ s$^{-1}$):

E4.11
$$E_{in} = Q_{at} \cdot MIF_{tot}$$

The atmospheric density ($\rho$/ kg cm$^{-3}$) and the heat capacity at constant pressure ($C_p$/ J Kg$^{-1}$ K$^{-1}$) are then used to calculate the atmospheric heating rate ($HR$/ K s$^{-1}$), as shown in Figure 4.6:

E4.12
$$HR = \frac{E_{in}}{\rho \cdot C_p}$$
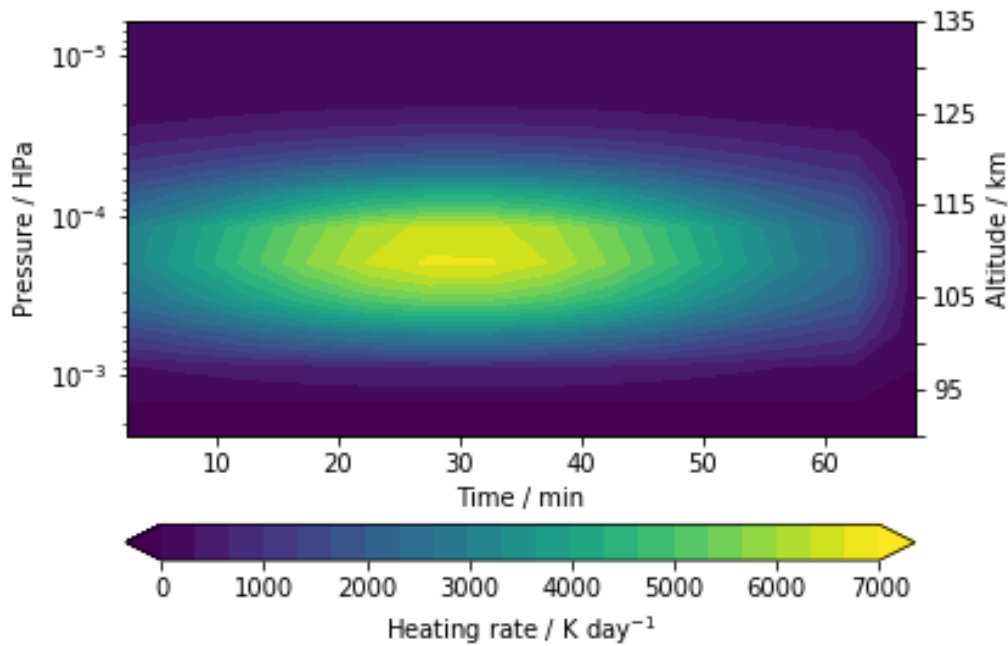
Figure 4.6. The heating rate (K day$^{-1}$) added to WACCM during the Halley encounter, as a function of pressure (hPa) and time (minutes). Approximate altitudes (km) are shown for reference on the right axis.

### 4.2.4   Model Simulations

WACCM 1.06 was used to probe the effects of different aspects of the Halley encounter on the chemistry and dynamics of the MLT. The model was spun up so as to include additional metal chemistry [*Bones et al.*, 2015; *Feng et al.*, 2017; *Plane et al.*, 2015; *Viehl et al.*, 2016]. This model run was continued after the spin-up period, such that it could serve as a control run (run B – the 'baseline' run) for comparison with the 'Halley runs', runs A, C and D – simulations completed with added chemical and/or dynamical perturbations, representing the different predicted consequences of the Halley encounter. These modifications were implemented in separate model runs such that the effects of each perturbation could be examined individually.

The chemical perturbation was added in run C – the four principal meteoric metals, Fe, Si, Mg and Na were injected, with a fraction injected directly as ions (as discussed in section 4.2.2). The dynamical perturbation was added in run D – implementing a heating tendency (K s$^{-1}$) calculated from the kinetic energy carried by the incoming material (discussed in section 4.2.3). Run A combined 'all' these effects – both the chemical and dynamical perturbations (see Table 4.2). All simulations were run for a total time of one year. An additional test simulation (run $A_m$) was performed for a duration of one month to assess the impacts of including reaction enthalpies for key metal reactions (see section 5.3).

Table 4.2. List of WACCM 1.06 runs with a short description.

| Run No. | Model Run | Description |
|---------|-----------|-------------|
| A | All | Halley metal injection (Fe, Si, Mg, Na) + heating tendency ($\Delta T$) |
| B | Baseline | Control run – no additional modifications |
| C | Chemistry | Halley metal injection (Fe, Si, Mg, Na) |
| D | Dynamics | Halley heating tendency ($\Delta T$) |
| $A_m$ | All + $\Delta H_m$ | 1 month test simulation - repeat of run A, including reaction enthalpies from key metal reactions |

## 4.3  WACCM-CARMA

### 4.3.1  Model Setup

CESM v1.2.2 and WACCM (CAM v5.3.7) were used to evaluate the effects of an injection of meteoric sulfur and MSPs to the atmosphere [*Brooke et al.*, 2017; *Gómez Martín et al.*, 2017]. A free-running configuration was used, with aerosol microphysics treated by coupling WACCM to a sectional microphysics model based on the Community Aerosol and Radiation Model (CARMA) [*Toon et al.*, 1988] – the specific model configuration used is hereafter referred to as WACCM-CARMA. CARMA is coupled to WACCM by passing the model's state in each column across to CARMA, where microphysical processes alter the state of the constituents. These changes are then passed back to WACCM where the model's state is adjusted accordingly [*Bardeen et al.*, 2008].

The horizontal resolution of WACCM-CARMA is the same as WACCM 1.06, however 88 vertical levels are used, covering altitudes up to ~140 km. As was the case for WACCM 1.06, the chemistry of the middle atmosphere is based on MOZART. However, in contrast to WACCM 1.06, mesospheric metal chemistry was not included. There are 66 species in total which interact *via* a range of gas-phase, heterogeneous and photolytic reactions [*Lamarque et al.*, 2012]. Neutral sulfur chemistry includes 8 gas-phase species (S, SO, $SO_2$, $SO_3$, $HSO_3$, $HSO_4$, OCS and DMS) and 22 reactions [*English et al.*, 2011] and the ionic sulfur chemistry was updated as per *Gómez Martín et al.* [2017]. Natural and anthropogenic emissions of DMS, $SO_2$, $NO_2$, NO and CO are specified from *Lamarque et al.* [2012]; *Mills et al.* [2016]. A pre-industrial component set (FW1850) was used to define natural and anthropogenic emissions of DMS, $NO_2$, NO and CO. Since $SO_2$ emissions were not included, the initial $SO_2$ emissions were set to present day levels. A spin-up period of 4 years allowed these to relax to pre-industrial levels.

In CARMA, aerosols are defined into three 'groups': pure sulfate (PURE), mixed sulfate (MIXED), and MSP cores (DUST), see Table 4.3. This representation is similar to that used by *Brooke et al.* [2017], where two aerosol groups are defined. However, where *Brooke et al.* [2017] treated MSP cores as a mixed sulfate particle with no adsorbate, the treatment applied here classifies an element of this type within its own aerosol group (DUST). The mixed sulfate group contains two elements, mixed sulfate aerosol (MIXSUL) and MSP cores (CORE). This aerosol classification scheme was developed by Charles Bardeen (based at the University Corporation for Atmospheric Research (UCAR), Boulder, Colorado, ©2009 - 2013). A sectional representation of aerosols is used, whereby aerosols in all groups are split into 28 size bins, the mass of which increases by a factor of 1.37 between successive bins, varying in size from 0.34 nm to 1.62 μm. Particle densities are 2.0 and 1.9 g cm$^{-3}$ for pure and mixed sulfate respectively. Aerosol microphysics such as nucleation, evaporation, condensation and coagulation are calculated within CARMA, as described by *English et al.* [2012] and the resulting aerosol surface area densities are used to define the rates of heterogeneous reactions in WACCM. Coagulation occurs within and between all aerosol groups. Condensation and evaporation of $H_2SO_4$ occur from both mixed sulfate and pure sulfate aerosol groups, though evaporation from mixed sulfate aerosol only occurs if the core fraction is below 0.5, to mimic the reaction of $H_2SO_4$ and metal atoms in MSPs [*Saunders et al.*, 2012]. Homogeneous nucleation of $H_2SO_4$ and $H_2O$ controls the entry of particles to the smallest size bin for the pure sulfate group. For the DUST group, MSPs are injected into the smallest size bin using a predefined production rate scaled to the global input rate from ablation [*Kalashnikova et al.*, 2000] (Figure 4.7).

Table 4.3. Particle groups used to define aerosols within CARMA, and the elements within each group, including a short description of each particle type.

| Group | Group elements & description – this work | Group elements & description – *Brooke et al.* [2017] |
|---|---|---|
| PURE | PURE - pure sulfate aerosol | PURE - pure sulfate aerosol |
| MIXED | MIXSUL - mixed sulfate aerosol<br><br>CORE - MSP core within a mixed sulfate particle | MIXSUL - Mixed sulfate aerosol<br><br>CORE - MSP core within a mixed sulfate particle.<br><br>A MSP core with no adsorbed sulfate is equivalent to a particle within the DUST group |
| DUST | DUST - MSP | - |
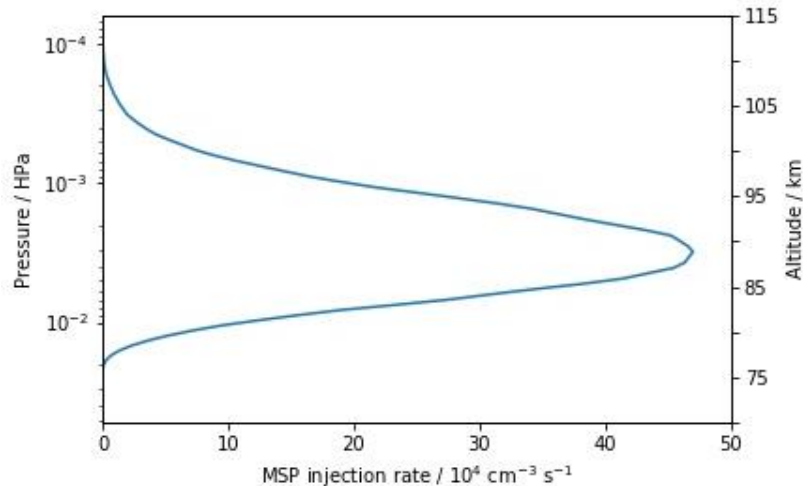
Figure 4.7. The injection rate of MSPs (R, $10^4$ atom cm$^{-3}$ s$^{-1}$) with a radius of 1.37 nm, used to define both the Halley MSP-MIF and the standard MSP-MIF, as defined by *Kalashnikova et al.* [2000].

Aerosol deposition was calculated as per the standard deposition scheme specified in *Brooke et al.* [2017]. Sedimentation velocities are calculated within CARMA for all aerosol sizes, in each model grid box. In the lowest model grid box for each column, CARMA estimates the deposition velocity using sedimentation velocities for all aerosol particles, with a parametrisation from *Zhang and Brook* [2001] and the land and ocean fractions from WACCM. Sedimentation velocities in all other grid boxes are used to define the change in concentration within each grid box across each time step. The total change for the column defines the dry deposition flux. Wet deposition is calculated by WACCM, and uses below-cloud (impaction) and in-cloud (nucleation) scavenging to generate both convective and stratiform precipitation.

### 4.3.2 MIF Implementation

In the Halley run (run A$_s$), 21,700 tons of sulfur (~5.4% of the incoming mass [*Jessberger et al.*, 1988]) was injected uniformly across one hemisphere (0-180 °E) on the 1$^{st}$ January at 00:00 UT, using a sulfur MIF (the Halley S-MIF) obtained from CABMOD, by scaling the Na-MIF generated for the Halley encounter by a factor of 2.10. This factor is derived from a combination of the ratio in the abundances of the material (5.425/1.8544) and the relative atomic masses (22.9897/32.066). In an analogous manner to the meteoric metals, a fraction of the ablated S will be subsequently ionized by collisions. However, sulfur-containing ions (S$^+$, SO$^+$ etc.) are all converted to neutral sulfur species below 90 km [*Gómez Martín et al.*, 2017], which is the relevant part of the atmosphere for investigating the impacts of sulfur from the cometary dust. The WACCM-CARMA simulations were intended to explore the long-term effects of the Halley encounter, so the model time step was kept at the standard value of 30 minutes. Thus, in order to

introduce the material incrementally, the Halley S-MIF was implemented across a timeframe of two hours, scaling the MIF during each time step by factors detailed in Figure 4.8.
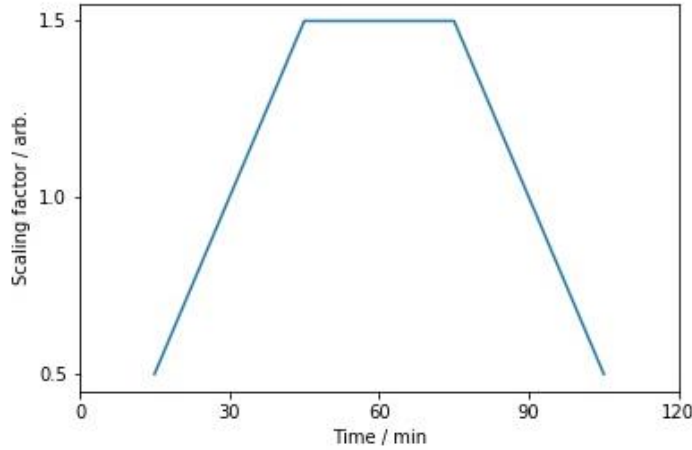


Figure 4.8. Scaling factors used for the S-MIF in the Halley WACCM-CARMA model run (run $A_s$) as a function of time (minutes).

In addition to the sulfur input, 401,000 tonnes of MSPs were also injected uniformly into the smallest DUST size bin ($r_{min} = 0.34$ nm). This Halley MSP-MIF was added to the model over the course of one week (approximately the timescale of MSP formation), assuming that all of the incoming material subsequently formed MSPs. The altitude profile of the injected material in both the Halley MSP-MIF and the standard MSP-MIF follows that in Figure 4.7 [*Kalashnikova et al.*, 2000]. However, since the $r_{min}$ used in CARMA is different to the radius specified in *Kalashnikova et al.* [2000], the input rate defined in Figure 4.7 ($R$, cm$^{-3}$ s$^{-1}$) was scaled appropriately, before multiplication by the bin mass ($m_{bin}$, g) to obtain a mass flux ($R_m$, kg m$^{-3}$ s$^{-1}$):

E4.13
$$R_m = R \times (1.37^3/0.34^3) \times m_{bin} \times 10^3$$

The mass flux was then scaled such that the integrated mass influx over the column was consistent with the appropriate total mass influx. For the standard MIF, the mass influx of ablated material is ~7.9 t day$^{-1}$ (2.9 kt yr$^{-1}$). For the Halley MSP-MIF, a total injection of 401,000 tons gives an input rate of 20.9 Mt yr$^{-1}$, though this is only implemented for one week. The standard MSP-MIF was also multiplied by an additional scaling factor, representing the typical seasonal variation in the MSP-MIF (see Figure 4.9).
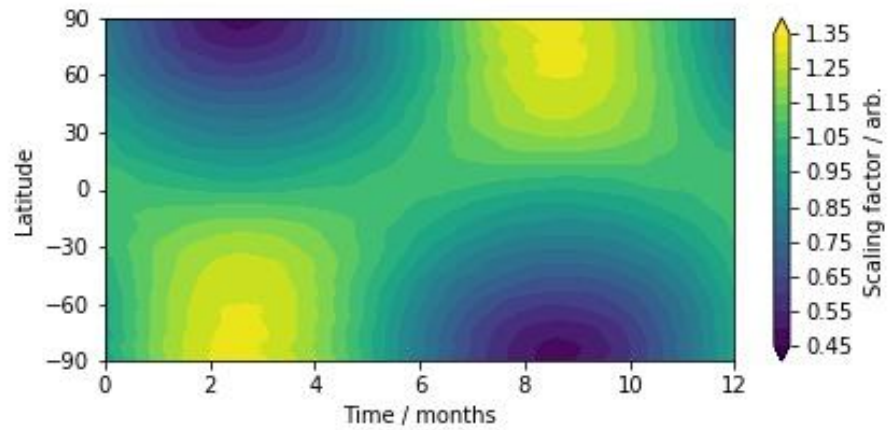
Figure 4.9. Scaling factor used to define the seasonal variation in the global input rate of MSPs for the standard MSP-MIF.

### 4.3.3 Model Simulations

WACCM-CARMA was used to probe the effects of the Halley S-MIF and MSP-MIFs on both gas-phase chemistry and aerosol properties in the mesosphere and stratosphere, and additionally to determine whether a measurable deposition of sulfur was observed. Two sensitivity simulations were performed: a 'Halley' run (run $A_s$) including both the S-MIF and the MSP-MIF, and a control run (run $B_s$) including standard versions of these MIFs. 7 year simulations were performed in both cases.

# Chapter 5

# Cometary Impacts on the Upper Atmosphere

In this chapter, the impacts on the MLT of a chemical and a dynamical perturbation resulting from the simulated Halley encounter will be discussed. Four one-year WACCM simulations were completed to explore this. The chemical perturbation involved adding a metal injection to the model above ~95 km, introducing the four main meteoric metals, Fe, Mg, Na and Si. The dynamical perturbation involved adding a heating tendency to the model (which initiates a temperature response), at similar altitudes to the injected material. Of the four model simulations, run C included the chemical perturbation and run D included the dynamical perturbation. Run A added both the chemical and dynamical perturbations, and run B served as a control simulation. An additional test simulation is then discussed, which explores the effects of including in the model the chemical heating terms from a number of metal reactions.

## 5.1   Chemical Changes

### 5.1.1   Metals

#### 5.1.1.1   Vertical Distribution

Figure 5.1 shows the vertical distributions of the global average metal densities ($cm^{-3}$) in run A, before and after the added perturbations, for each of the four main meteoric metals ([Fe], [Mg], [Na] or [Si]), their atomic ions ([$Fe^+$], [$Mg^+$], [$Na^+$] or [$Si^+$]) and the reservoir species ([FeOH], [$Mg(OH)_2$], [$NaHCO_3$] or [$OSi(OH)_2$]) [*Plane et al.*, 2015]. These plots, and all subsequent plots showing a vertical distribution, are plotted on a pressure axis, with log-pressure altitudes shown for reference on the right-hand axes. These altitudes were calculated with equation R5.1, where $Z$ is the altitude (km), $H$ is the approximate scale height (7 km), $P$ is the pressure and $P_0$ is the pressure at height $Z$=0 km (1013 hPa) [*Bhatnagar and Livingston*, 2005]. To aid with intuitive understanding in subsequent discussions, phenomena are discussed in terms of altitude changes rather than pressure changes – a reference to 'increasing altitude' should be taken to mean 'decreasing pressure' since the approximate altitude values shown may differ slightly from the geopotential altitudes in each model grid box.
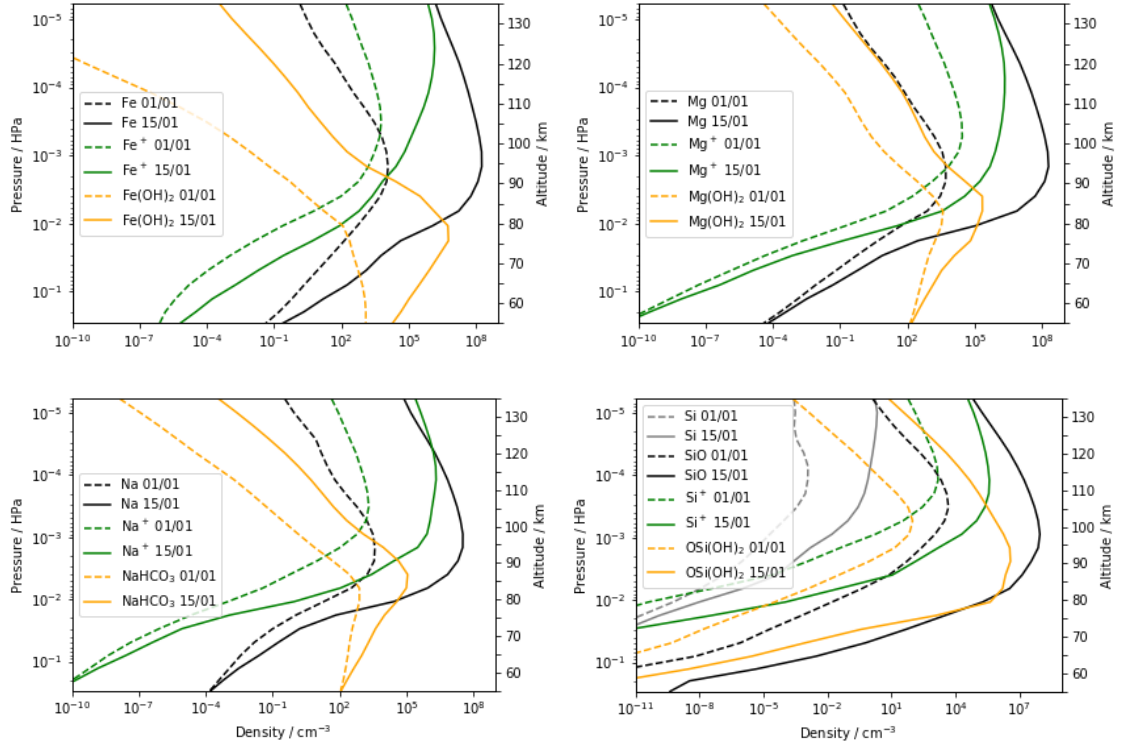
Figure 5.1. Global average densities (cm$^{-3}$) for the atomic metal (Fe, Mg, Na, black), the atomic ion (Fe$^+$, Mg$^+$, Na$^+$ and Si$^+$, green) and the reservoir species (Fe(OH)$_2$, Mg(OH)$_2$, NaHCO$_3$ and O(Si(OH)$_2$, yellow) for each of the four main meteoric metals. For Si, the atomic metal is shown in grey, and the counterpart to the other neutral metals, SiO, is shown in black. Dashed lines represent densities from 1$^{st}$ January, before the Halley perturbations, and the solid lines represent densities from 15$^{th}$ January, two weeks after the Halley perturbations were implemented. Note different horizontal scale for the Si panel.

R5.1    $Z = -H \cdot \log(P/P_0)$

From Figure 5.1, some differences can be observed in the distribution of metals before and after the metal injection. For the neutral atomic metals, an increase in metal density is observed largely at the peak of the metal layer and at higher altitudes, with a smaller increase below the peak of the layer. The metal layers thus occur at slightly higher altitudes and are somewhat broader as a result. These differences are due to the higher ablation altitudes determined for the Halley dust, compared to the typical ablation of sporadic meteoroids. For Fe, Mg and Na, this elevation in the neutral layers leads to a similar pattern being observed for the altitude profiles of both the ionic metals and the reservoir species, since their chemistry is interlinked [*Feng et al.*, 2013; *Langowski et al.*, 2015; *Marsh et al.*, 2013a; *Plane et al.*, 2016]. In contrast to the other metals, for Si$^+$ there is little difference in the vertical distribution before and after the injection. This is because for Fe$^+$, Mg$^+$ and Na$^+$, the main ionization pathway is *via* charge transfer between the neutral metal and NO$^+$ or O$_2^+$. However, the main route to Si$^+$ is *via* charge transfer with SiO [*Plane et al.*, 2016] which is itself formed by reaction with O$_3$ – the density of which falls rapidly with height above ~95 km. In the first month of the simulations the O$_3$ density is also reduced by changes to metal and HO$_x$ chemistry (see section 5.1.2.1). The resulting altitude decrease for the SiO layer

thus suppresses an altitude increase for $Si^+$, and leads to a corresponding decrease in the peak altitude of the $OSi(OH)_2$ layer.

## 5.1.1.2 Duration

To explore the duration of the perturbation to the metal layers, global-average total column densities ($[M_{tot}]$, $cm^{-2}$) were calculated for each of the four main metal species. These are calculated from the sum of the respective global-average column densities for the neutral metal atom, the atomic ion and the reservoir species. For each metal, an increase in the total column density was observed in both runs A and C, with a larger overall increase in run A (Figure 5.2, top panel). In both cases, the largest increase in metal species was seen immediately after the additional metal injection. The largest increase was seen for $[Fe_{tot}]$ and $[Mg_{tot}]$, and the smallest increase was observed for $[Na_{tot}]$, which is consistent with the amount of material injected during the Halley encounter and the typical ambient concentrations. The metal densities then decay in an approximately exponential manner, with $[Fe_{tot}]$, $[Na_{tot}]$ and $[Mg_{tot}]$ returning to background concentrations after a period of 6-7 months. The Si species ($[Si_{tot}]$) were removed much more rapidly, due to the formation of $Si(OH)_4$ from $OSi(OH)_2$ *via* the addition of $H_2O$, returning to background levels after around 2 months. Note the main loss mechanism is *via* the dimerization of the reservoir species - this is a proxy for the formation of MSPs, which is not represented explicitly in the model. The e-folding lifetimes for each metal are shown in Table 5.1. The lifetimes for the total metals are significantly reduced in runs A and C compared to run B as a result of the increase in metal density, which causes an increase in the rate of removal of the reservoir species (which is approximately second-order in the reservoir species concentration). In both runs A and C, the metals were removed at approximately the same rate ($<$ ~5% difference between runs) though for Fe and Mg, the metals were removed more slowly in run A compared to run C. For Na and Si, the opposite was observed, with the metals removed slightly more quickly in run A.

Similar increases in the global-average column densities of metal ions are observed in runs A and C as a result of the chemical perturbation. In an analogous manner to the total metals, the metal ions decayed approximately exponentially, the $[Fe^+]$, $[Mg^+]$ and $[Na^+]$ returning to baseline levels after 6 to 7 months and the $[Si^+]$ after 2 months. In contrast to the neutral species, for which the largest density increase was observed with Fe, the largest increase was observed for $Na^+$ since this is the most efficiently ionized of the four metals (the ionization potentials for Fe, Si, Mg and Na are 760, 787, 738 and 496 $kJmol^{-1}$, respectively [*Weast et al.*, 1984]). Furthermore, in contrast to the other metals, $Na^+$ does not react with $O_3$ to form the metal oxide ion, which can then undergo dissociative recombination (see Figure 1.17) [*Feng et al.*, 2013; *Langowski et al.*, 2015; *Marsh et al.*, 2013a; *Plane et al.*, 2016]. The metal ions produced as a result of the chemical perturbation are the dominant charge carrier in the MLT for a period of 2-3 months. This is demonstrated in

Figure 5.2 (bottom panel) where the profile of the global-average total column density for the four metals Fe, Si, Mg and Na ($[M^+_{tot}]$) follows that of the electrons for this period of time. The electron density recovers around 1-2 months faster than that of the metal ions. At this point, the $e^-$ density is controlled by other ionic species such as $O_2^+$ and $NO^+$, which normally dominate the chemistry of the E region (95-170 km) [*Brasseur and Solomon*, 1986; *Plane et al.*, 2015; *Shuman et al.*, 2015].
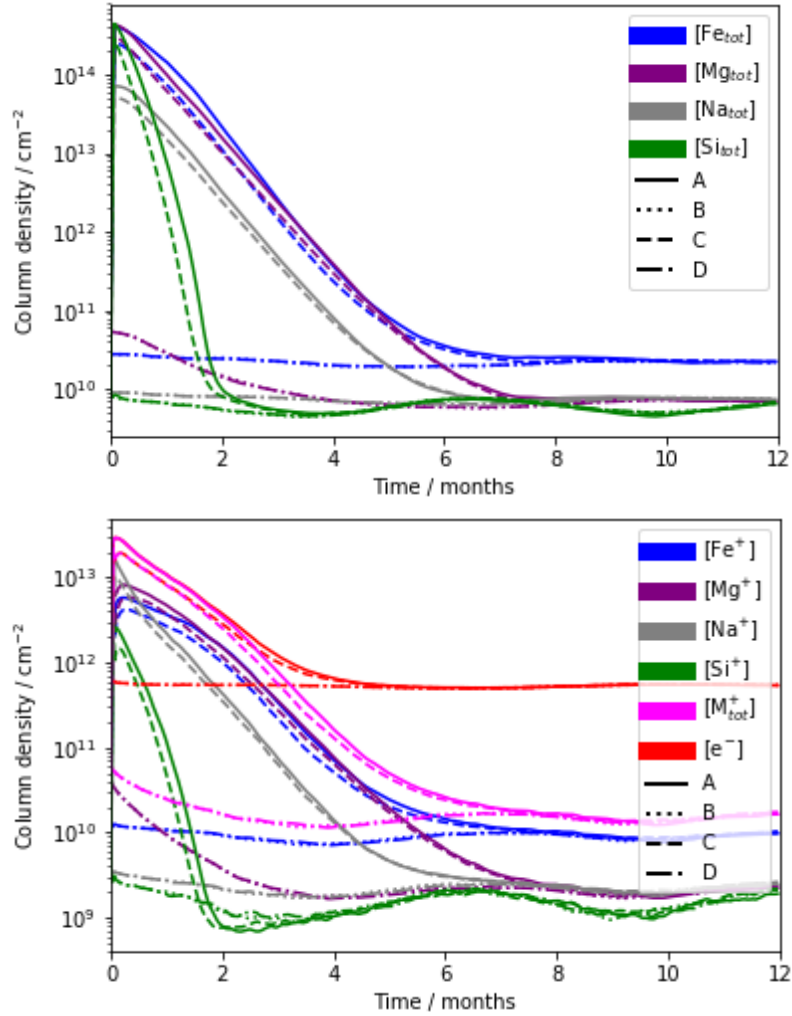


Figure 5.2. Top panel: Time series for the global-average total column densities (cm$^{-2}$) for [Fe$_{tot}$] (blue), [Mg$_{tot}$] (purple), [Na$_{tot}$] (grey) and [Si$_{tot}$] (green) where [Fe$_{tot}$] = [Fe] + [Fe$^+$] + [FeOH], [Mg$_{tot}$] = [Mg] + [Mg$^+$] + [Mg(OH)$_2$], [Na$_{tot}$] = [Na] + [Na$^+$] + [NaHCO$_3$] and [Si$_{tot}$] = [Si] + [SiO] + [Si$^+$] + [OSi(OH)$_2$]. Bottom panel: Time series for the global-average column densities (cm$^{-2}$) for [Fe$^+$] (blue), [Mg$^+$] (purple), [Na$^+$] (grey), [Si$^+$] (green) [M$^+_{tot}$] (pink) and [e$^-$] (red) where [M$^+_{tot}$] = [Fe$^+$] + [Mg$^+$] + [Na$^+$] + [Si$^+$]. For both panels, run A is shown with solid lines, run B is shown with dotted lines, run C is shown with dashed lines and run D is shown with dash-dot lines.

Table 5.1. E folding lifetimes for Fe, Mg, Na and Si, calculated in month 2 of the simulation for runs A, B, and C.

|  | RUN A | RUN C | % change, A & C | RUN B |
|---|---|---|---|---|
| Total Fe | 16.8 days ± 5 hrs | 16.4 days ± 3 hrs | 2.3 | 41.4 days ± 12 hrs |
| Total Mg | 17.5 days ± 1 hrs | 17.3 days ± 2.5 hrs | 1.3 | 120.7 days ± 23.1 hrs |
| Total Na | 16.4 days ± 2 hrs | 16.9 days ± 2.5 hrs | -3.7 | 47.6 days ± 10.9 hrs |
| Total Si | 4.1 days ± 0.2 hrs | 4.4 days ± 2.5 hrs | -5.6 | 2.5 days ± 3.1 hrs |

### 5.1.1.3  Meridional Distribution

Though the initial increase in $M_{tot}$ was larger in run A compared to run C, the resulting distribution for the total metals was similar in the two simulations, and for all metal species (Figure 5.3). The largest fraction of metals persisted in the summer (southern) hemisphere at low to mid latitudes, despite the uniform distribution of metals over the northern and southern hemisphere during the added perturbation (at 0-180 °E). The similarities in the metal distributions in runs A and C suggest this effect is chemical rather than dynamical in origin – or, to be more precise, it is a dynamical effect caused by the chemical perturbation.
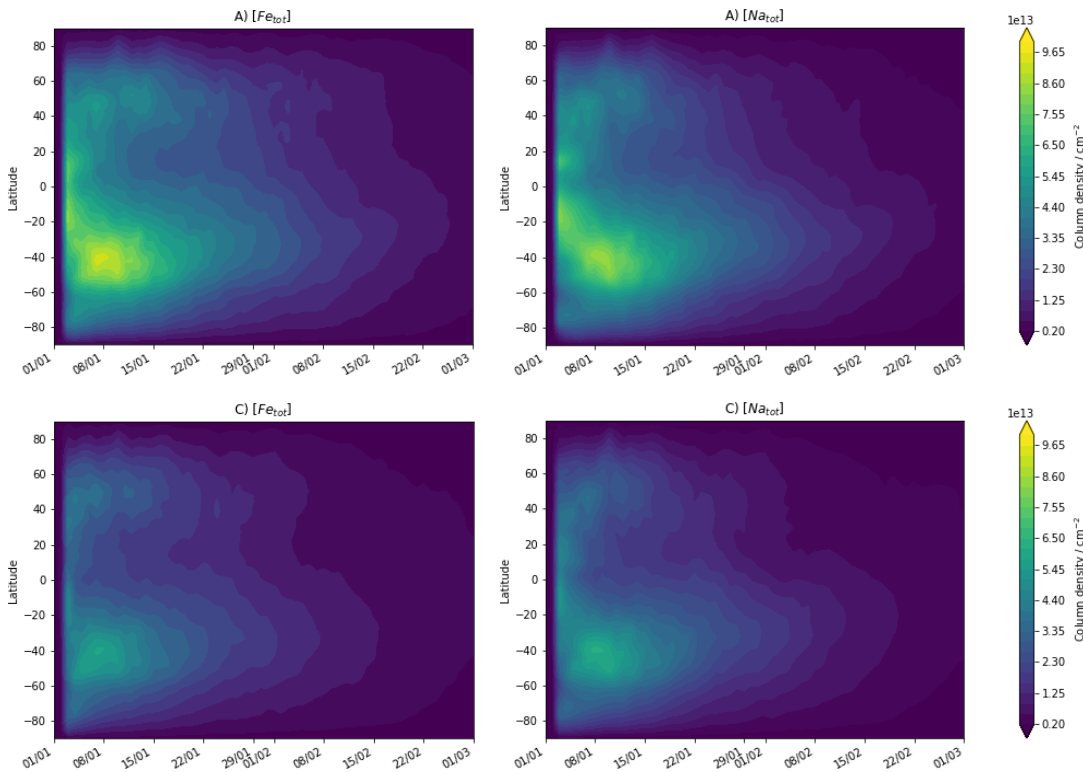


Figure 5.3. Time series showing the meridional distribution of the area-weighted, zonally-averaged column density (cm$^{-2}$) for the total metals [Fe$_{tot}$] and [Na$_{tot}$] - run A (top panels) and run C (bottom panels).

A summer minimum and winter maximum is typically observed in the metal layers (Fe, Mg & Na), the peak of which occurs at an altitude of around ~90-95 km (Figure 5.4, run B), resulting from the residual circulation carrying material from the summer to winter pole [*Feng et al.*, 2013; *Langowski et al.*, 2015; *Marsh et al.*, 2013a]. In contrast, the Halley runs exhibit a summer maximum and winter minimum (see Figure 5.4, runs A and C). The altitude of the metal layers is also elevated by around 5 km due to the increased ablation altitude of Halley dust. The material takes around 10 days to settle down to an altitude of approximately 95-100 km. Usually at high latitudes in the summer hemisphere, an upwelling of air feeds the residual meridional circulation from the summer to winter pole at altitudes below around 95 km (Figure 5.4, run B). Little to no net transport is typically observed in the altitude range 95-110 km. However, above ~110 km there is a small net transport from the winter to summer pole, where at high latitudes an additional upwelling of air feeds further transport from the summer to winter pole at altitudes above ~120-125 km.

During the first week after the Halley perturbation in both runs A and C, a winter-to-summer circulation was induced at altitudes of 100-110 km where previously there was no significant transport. This southwards air-flow is responsible for the increased burden of metal species in the southern hemisphere (Figure 5.4, runs A & C) since it corresponds to the highest density of metal species during the initial injection of material. The thermospheric summer-to-winter transport (>125 km) is reduced as a result of these circulation changes, as there is strong disruption to the transport at summer high latitudes above 95 km. The upwelling of air from the summer pole below 95 km (and residual transport to the winter pole) prevents further sedimentation of the metals in the southern hemisphere, and after 10 days, the typical summer to winter transport resumes (though with an increased magnitude), serving to re-establish atmospheric equilibrium. Material is moved back towards the winter (northern) hemisphere, along the metal mixing ratio gradient. No significant changes to the meridional circulation are observed as a result of the temperature perturbation (Figure 5.4, run D).
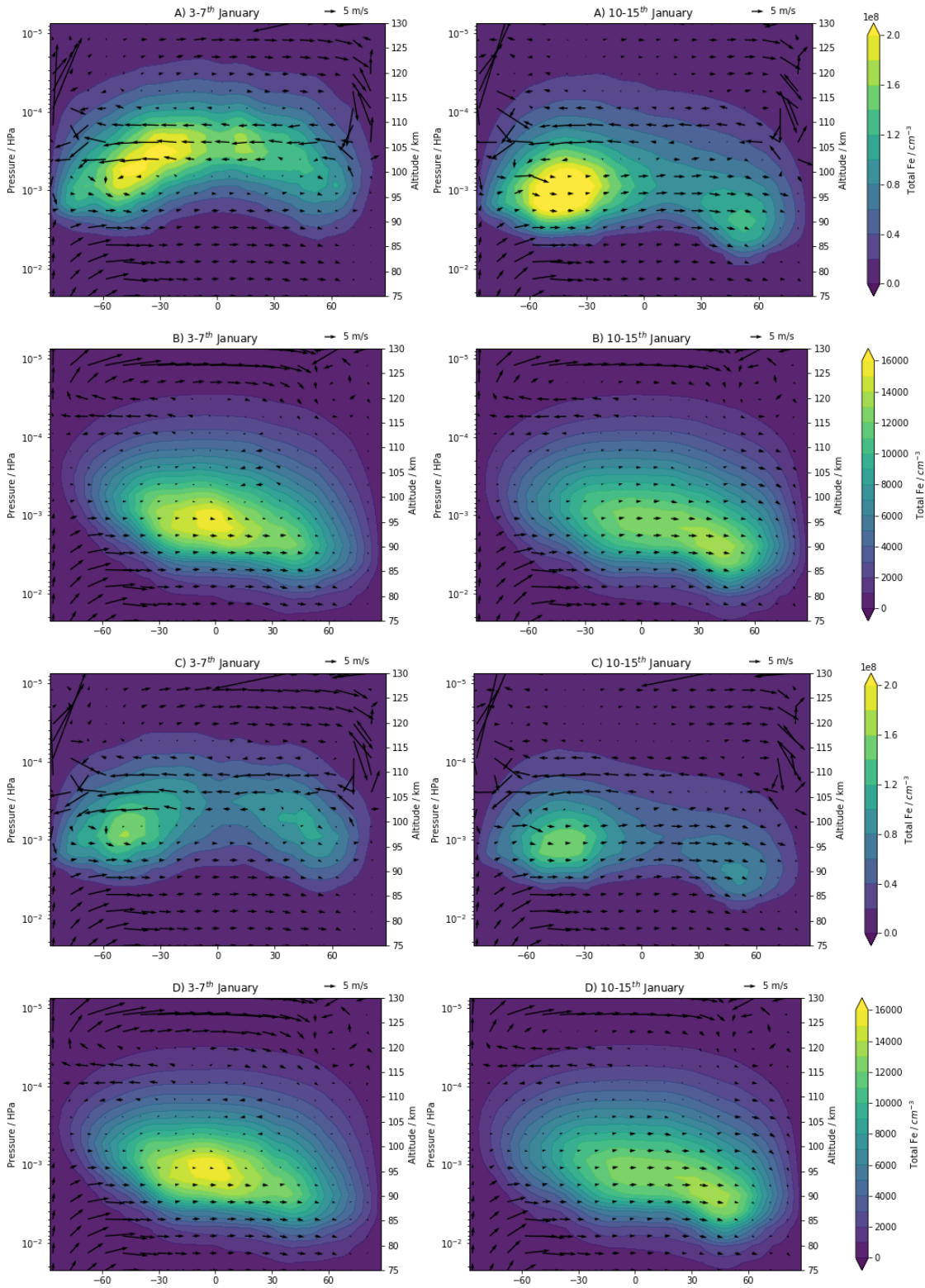
Figure 5.4. Number density for the area-weighted, zonally averaged total Fe ([$Fe_{tot}$]) as a function of pressure (hPa) for runs A, B, C and D. Approximate altitudes (km) are shown for reference. Also shown are the meridional wind vectors combining the horizontal winds $v$ and the vertical winds $w$. The vertical winds are multiplied by 100 for clarity. Note the different colour-bar scales between runs A & C and B & D.

## 5.1.2   $O_x$ and $HO_x$

### 5.1.2.1   Changes to O and $O_3$

A decrease in the global-average atomic O density of up to 17 % and 19 % was observed for runs C and A, respectively, with the density taking around 4-5 months to return to baseline levels (Figure 5.5). For $O_3$ (above 80 km) a decrease of up to 30 % and 34 % was observed for runs C and A, respectively, in the first month of the simulation, with the largest decrease occurring after ~2 weeks. After this minimum, the density relaxed back to the baseline level, though it continued to increase such that a maximum density increase of 60 % and 75 % was observed for runs C and A, respectively, just under 2 months after the initial perturbation. For both model runs, the dramatic increase in metal densities caused by the added perturbation leads to significant increases in the reaction rates for both the neutral and ionic metal reactions.

With regard to the neutral chemistry, the sequential oxidation of Me through MeO to $MeO_2$ (where Me is Fe, Mg and Na) and $FeO_2$ to $FeO_3$ (see Figure 1.17) effectively catalyses the slow reaction $O + O_3 \rightarrow 2O_2$. For Si, the oxidation reactions destroy $O_3$ though there are no analogous reduction reactions. The interconversion of the atomic metals and the monoxide species proceeds the fastest (reactions R5.2 and R5.3), due to both the large rate constants and the high concentration of neutral metal species in the MLT. Thus, these are the metal reactions that are largely responsible for the destruction of O and $O_3$ observed. An equivalent cycle is observed for the ionic metals, which also contributes to the O and $O_3$ removal (R5.4 and R5.5). Note that the density of $O_3$ in Figure 5.5 (for all model runs) increases across the course of the year – this is likely to be due to the model spin-up not being performed for long enough. A similar phenomenon is also observed for $H_2O$ (see Figure 5.9). In both cases this should not affect the results of this study since any changes observed are discussed in terms of the differences from the baseline run, and all the simulations display similar behaviour across the course of the year.

R5.2    $Me + O_3 \rightarrow MeO + O_2$    (where Me is Fe, Mg, Na, Si)

R5.3    $MeO + O \rightarrow Me + O_2$    (where Me is Fe, Mg, Na)

R5.4    $Me^+ + O_3 \rightarrow MeO^+ + O_2$    (where Me is Fe, Mg, Si)

R5.5    $MeO^+ + O \rightarrow Me^+ + O_2$    (where Me is Fe, Mg, Na, Si)
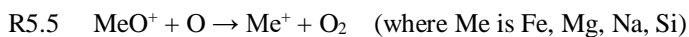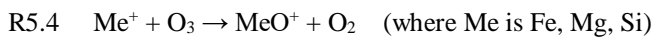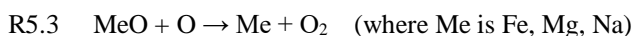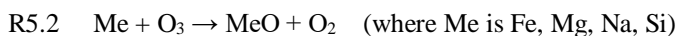

The decrease in O and $O_3$ has implications for both $O_x$ and $HO_x$ reaction rates and densities. For example, a reduction in reaction R1.3 ($O+O_2 (+M) \rightarrow O_3 (+M)$) causes additional decreases in $O_3$, which causes a reduction in R1.4 and R1.5 (the interconversion of H and OH), and other $HO_x$ reactions. This disrupts the catalytic removal of atomic O *via* both catalytic cycles (R1.3-R1.4-R1.5 and R1.6-R1.7-R1.5), leading to an increase in the ratio of O:$O_3$ relative to run B (Figure 5.6, runs A and C). Since the majority of reactions involving $O_x$ and $HO_x$ are exothermic, a reduction in their densities leads to a decrease in the model heating rates (Q) – more specifically the heat produced from chemical reactions ($Q_c$). This in turn leads to a reduction in temperature

(see section 5.2). Complex feedback pathways exist between all of these effects (see Figure 5.7), which directly or indirectly cause feedbacks to the metal chemistry, since some of these reactions have significant temperature dependences and involve $O_x$ or $HO_x$. It should be noted that the standard version of WACCM used does not include the chemical heating from metal reactions (indicated with a red arrow). However, as discussed later (see section 5.3), a test run has been performed to assess the implications of including these reaction enthalpies in the simulations.
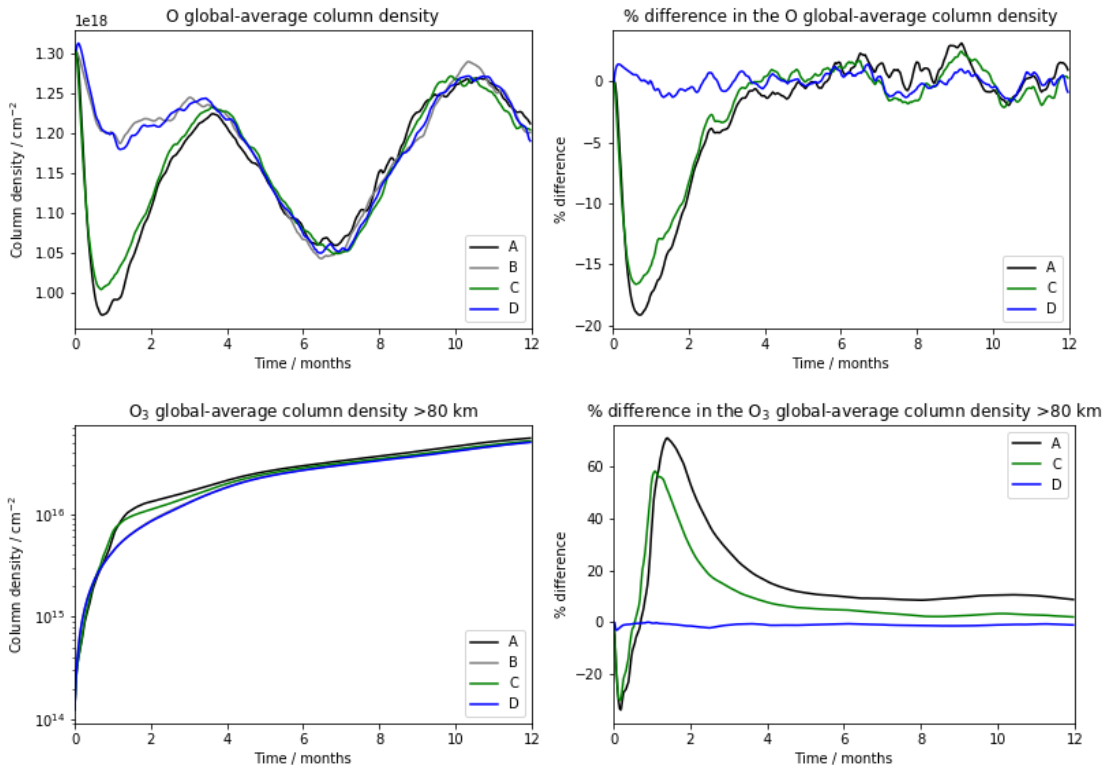


Figure 5.5. Time series for the global-average total column densities for O ($\times 10^{18}$ cm$^{-2}$) (top left) and $O_3$ above 80 km (cm$^{-2}$) (bottom left), for runs A (black), B (grey), C (green) and D (blue). Also shown is the percentage difference between each of runs A (black) C (green) and D (blue) with run B, for O (top right) and $O_3$ above 80 km (bottom right).
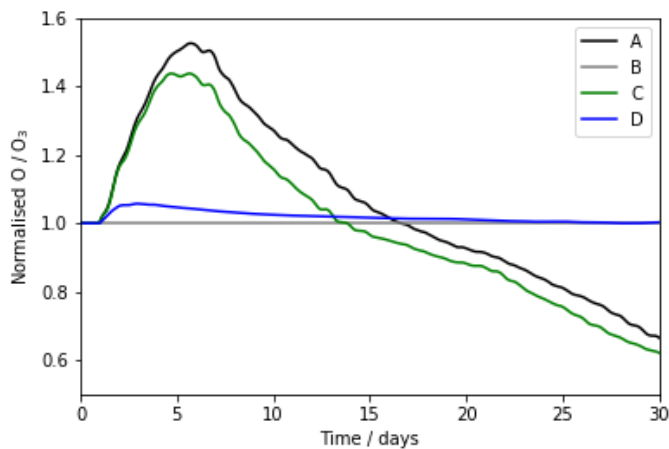


Figure 5.6. O:$O_3$ ratios calculated using the global-average column densities from model runs A (black), C (green) and D (blue) relative to that from run B (grey) during the first month of the simulations.
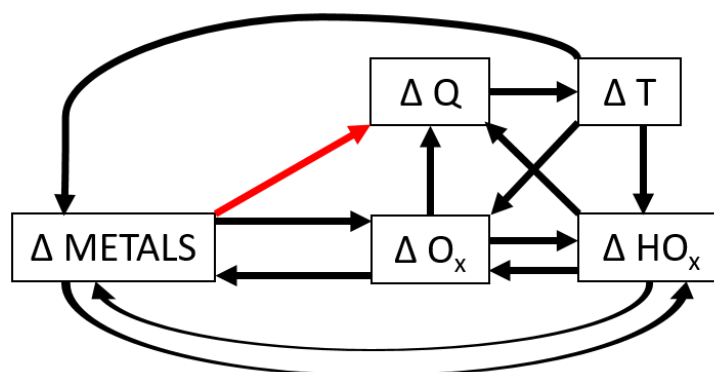
Figure 5.7. Schematic diagram showing the possible feedback pathways between mesospheric metal chemistry, $O_x$ chemistry, $HO_x$ chemistry, changes to the heating (Q) and temperature (T). The red arrow indicates the chemical heating from metal reactions, which is not represented in the standard version of WACCM.

For run D, although there was no perturbation to the metal densities, some small changes were still observed in the densities of O and $O_3$ (Figure 5.5). This is due to changes to $O_x$ and $HO_x$ chemistry similar to those induced by the metal chemistry in runs A and C, as an increase in O and corresponding decrease in $O_3$ is initiated by a decrease in reaction R1.3 ($O+O_2$ (+M) → $O_3$ (+M)) with increasing temperature. Further increases in O result from changes to the rates of other $HO_x$ reactions, and disruption to the catalytic removal of O. This increases the ratio of $O:O_3$ (Figure 5.6, run D), decreases $HO_x$ reaction rates and causes a subsequent decrease in chemical heating ($Q_c$). Thus, the temperature decreases until atmospheric equilibrium is restored (see section 5.2). This increase in $O/O_3$ resulting from the temperature perturbation leads to the differences observed between runs A and C. A relative decrease in the rate of oxidation of neutral metals to metal oxides compared to the rate of reduction leads to an increase in neutral atoms relative to the oxides. As such, the metals are able to destroy more O and $O_3$ because of a relative increase in the turnover of Me↔MeO (where Me is Fe or Mg) compared to MeO↔MeO$_2$ and FeO$_2$↔FeO$_3$. These reactions proceed the fastest of all the neutral and ionic metal reactions, and as such are largely responsible for the destruction of O and $O_3$ observed. This additional destruction of O and $O_3$ in run A causes an amplification of the effects on $O_x$ and $HO_x$ chemistry previously described.

The increase in the global-average column density of $O_3$ (> 80 km) observed after ~1 - 2 months (Figure 5.5) is in fact largely due to an increase in $O_3$ density centred at ~80 km. This starts to become more dominant when the $O_3$ density at ~85 - 120 km begins to recover from the ~100 % destruction observed in the first month (Figure 5.8, top panels). Though there is also a comparable relative increase in $O_3$ observed above ~120 km, this is a very small absolute increase (~$10^2$ compared to ~$10^9$ at 80 km), since the density of $O_3$ falls rapidly with height in the thermosphere [*Plane et al.*, 2015]. The $O_3$ density increase at ~80 km coincides with an increase in O density (Figure 5.8, bottom right panel) and is due to a decrease in the reaction R5.6. This is a result of the temperature decrease caused by the chemical perturbation (see section 5.2.1), since R5.6

exhibits a very strong positive temperature dependence [*Brasseur and Solomon*, 1986]. Since the density of O is higher than that for $O_3$ in the MLT, only a ~30 % decrease in O density is observed after the perturbation, centred at ~90-95 km, near the peak of the metal layers (Figure 5.8, bottom left panel).

R5.6    $O + O_3 (+M) \rightarrow 2O_2$
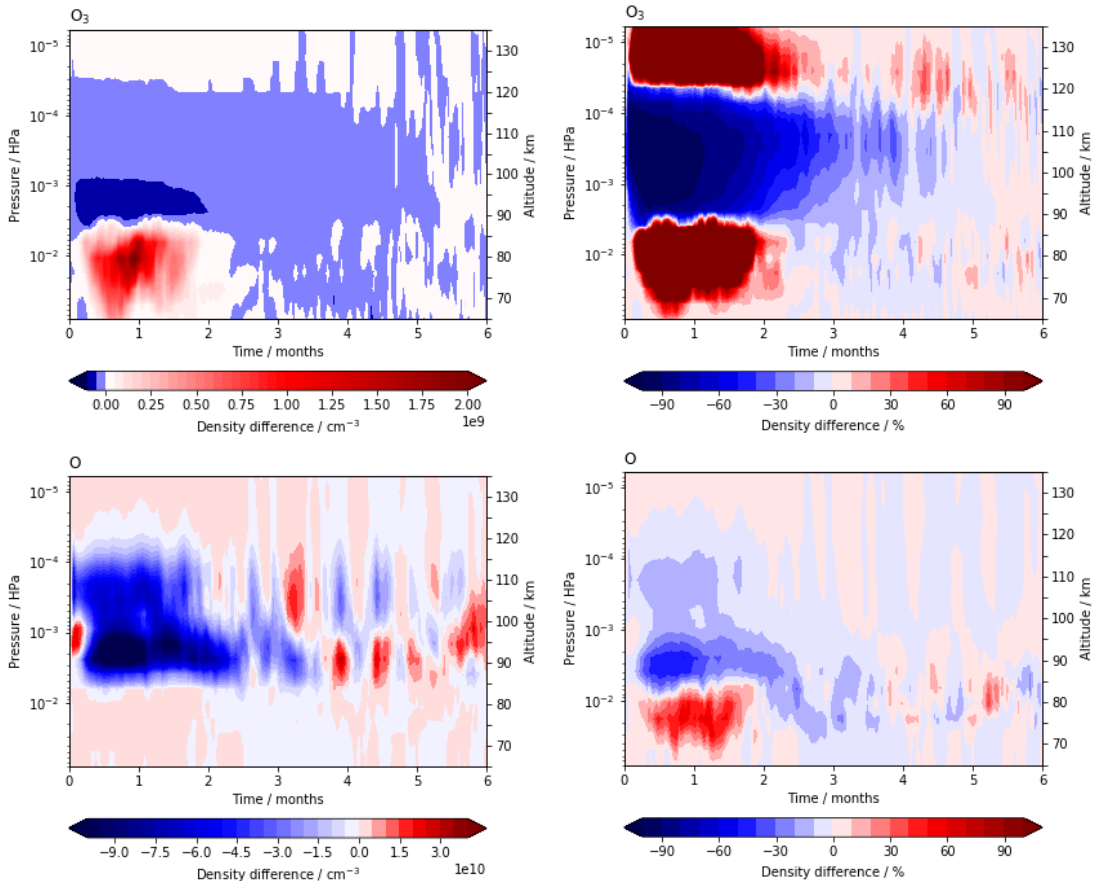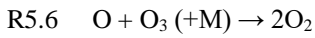


Figure 5.8. The absolute (left panels) and percentage (right panels) difference in the global-average $O_3$ (top panels) and O (bottom panels) densities between runs A and B (A minus B), as a function of height and time.

### 5.1.2.2   Changes to H and $H_2O$

A decrease of up to 68 % and 78 % was observed in the global-average column density of atomic H in runs C and A, respectively, with the minimum density occurring two weeks to one month after the perturbation (Figure 5.9). The H density relaxes back to baseline levels after around three months. Above 80 km, decreases of up to 25 % and 36 % were observed for $H_2O$ in runs C and A, respectively, with the largest decrease occurring around one month after the perturbation. For run A, the $H_2O$ concentration did not completely recover by the end of the simulation, where the concentrations remained approximately 10 % below that in the baseline run. Upon inspection of the global-average densities of H and $H_2O$ as a function of altitude, it can be seen that the observed density decreases represent losses of up to 100 % above ~80 km in the first 1 - 2 months for both

species (Figure 5.10, right panels). For H, the absolute difference in density is greatest at ~85 - 100 km, collocated with the metal layers (Figure 5.10, top left panel). For $H_2O$, though the relative decrease is greater than that for H above 80 km, the largest absolute differences are observed below ~85 km (Figure 5.10, bottom left panel). However, these latter changes represent variations of less than ± 10 %. This is due to the contrasting behaviour of the two species: for H, the density typically increases up to an altitude of 80-90 km, above which it decreases with increasing altitude; for $H_2O$, the density typically decreases with increasing altitude in the MLT.

H is removed through the reactions of metal hydroxides – for example, by the formation and destruction of MeOH *via* reactions R5.7 to R5.11. It is ultimately removed from the system by dimerization, which functions as a proxy for the formation of MSPs in WACCM [*Feng et al.*, 2013; *Plane et al.*, 2015]. In runs A and C, a significant increase in the rates of these reactions is observed due to the overall increase in speed of the metal reactions after the chemical perturbation. This leads to the observed drop in H density, since the only metal reactions known to reform H is reaction R5.11 (see Figure 1.17).

R5.7   $Me(OH)_2 + H \rightarrow MeOH + H_2O$   (where Me is Fe or Mg)

R5.8    $MeO_3 + H \rightarrow MeOH + O_2$    (where Me is Fe or Mg)

R5.9    $MeOH + H \rightarrow Me + H_2O$   (where Me is Fe or Mg)

R5.10    $FeOH + H \rightarrow FeO + H_2$

R5.11    $NaO + H_2 \rightarrow NaOH + H$
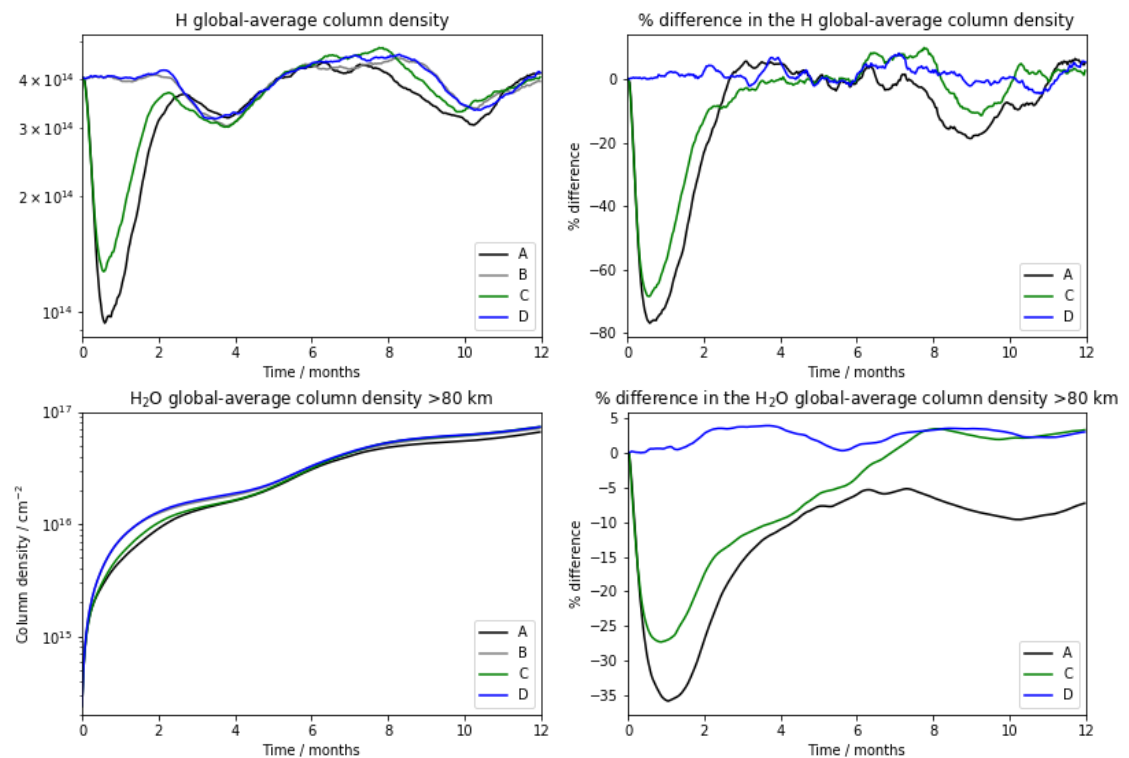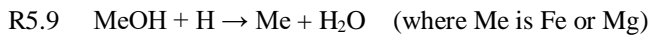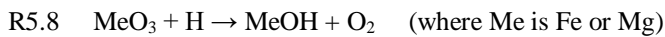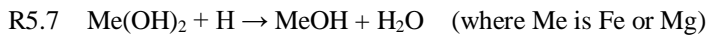


Figure 5.9. Time series for the global-average total column densities ($cm^{-2}$) for H (top left) and $H_2O$ above 80 km (bottom left), for runs A (black), B (grey), C (green) and D (blue). Also shown is the percentage difference between each of runs A (black) C (green) and D (blue) with run B, for H (top right) and $H_2O$ above 80 km (bottom right).
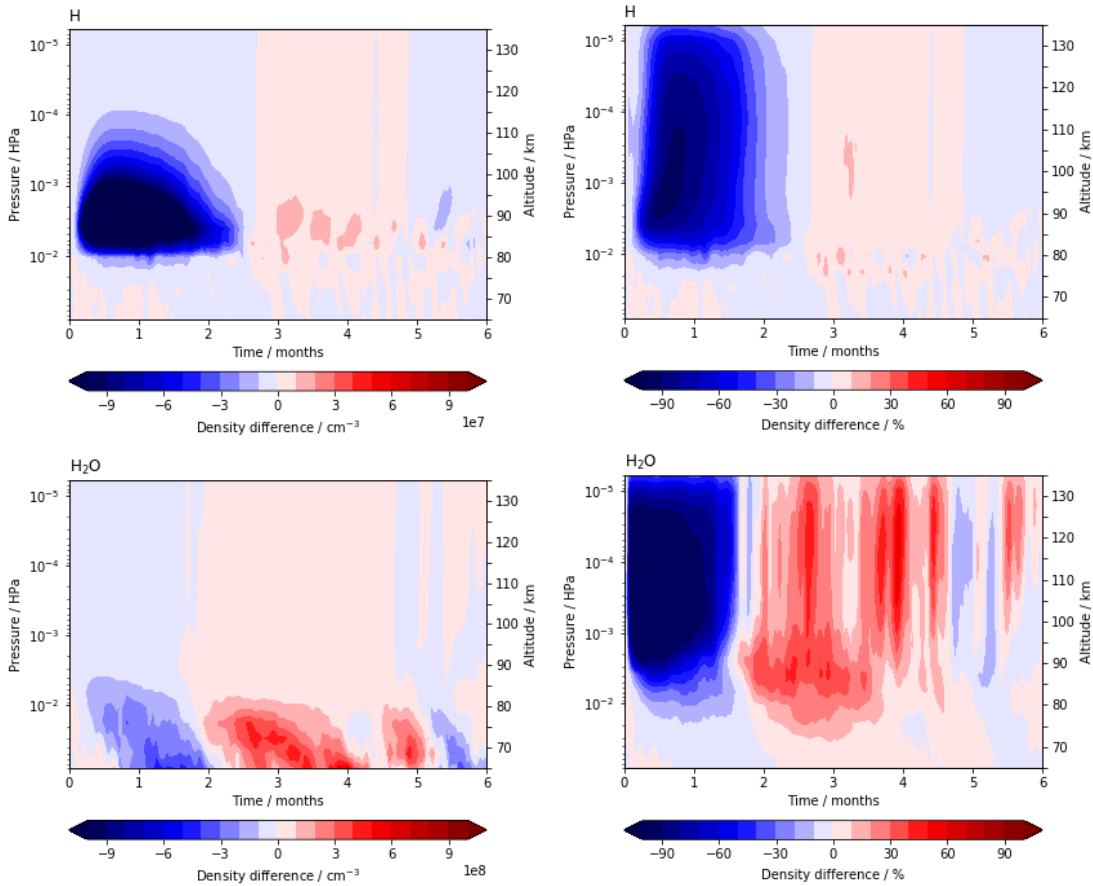
Figure 5.10. The absolute (left panels) and percentage (right panels) difference in the global-average H (top panels) and H$_2$O (bottom panels) densities between runs A and B (A minus B), as a function of height and time.

Changes to the metal chemistry leads to a net removal of H$_2$O, *via* reactions R5.12 - R5.16 [*Feng et al.*, 2013; *Langowski et al.*, 2015; *Marsh et al.*, 2013a; *Plane et al.*, 2015]. Additionally, the rates of the metal reactions which re-form H$_2$O are affected by the decrease in H density. Once the H becomes substantially depleted, reactions R5.7 and R5.9 slow down, leading to an increase in Me(OH)$_2$ relative to MeOH, and a resulting decrease in H$_2$O. The H$_2$O is removed from the system by dimerization – in essence, for a period of time the metal chemistry is catalysing the transformation of H and H$_2$O (and O$_3$) into 'MSPs' (hydroxide dimers).

R5.12  MeO + H$_2$O (+M) → Me(OH)$_2$  (where Me is Fe or Mg)

R5.13  MeO$_3$ + H$_2$O → Me(OH)$_2$ + O$_2$  (where Me is Fe or Mg)

R5.14  NaO + H$_2$O → NaOH + OH

R5.15  SiO$_2$ + H$_2$O (+M) → OSi(OH)$_2$

R5.16  OSi(OH)$_2$ + H$_2$O (+M) → Si(OH)$_4$
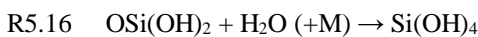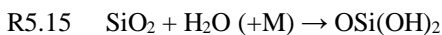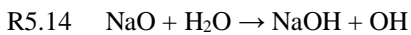
There are additional feedbacks on the densities of H and H$_2$O from HO$_x$ chemistry. The reduction in H$_2$O leads to a decrease in H$_2$O photolysis (R1.10, H$_2$O + $hv$ → H + OH) and thus further decreases in H. The reduction in H causes a decrease in the rate of interconversion of H with OH

and $HO_2$, which not only contributes to the aforementioned decrease in chemical heating and therefore temperature, but also leads to an additional decrease in $H_2O$ density since $H_2O$ is reformed chemically from these species *via* R5.17 and R5.18. Furthermore, other than reaction R1.5 (O + OH → H + $O_2$) which decreases as a result of the removal of O and $O_3$, H can only be reformed by photolysis of $H_2O$.

R5.17    OH + $HO_2$ → $H_2O$ + $O_2$

R5.18    H + $HO_2$ → $H_2O$ + O

## 5.2    Dynamical Changes

### 5.2.1    Vertical Distribution

When added in isolation (run D), the dust heating tendency caused a maximum increase in the global mean temperature of ~180 K around 110 km, three hours after the heating rate was implemented (Figure 5.11, run D). The highest temperature increase is observed close to the altitude at which the largest injection of metals occurs in the MIF. After the initial rise, the temperature decreased with time and the perturbation persisted for around 5 days after the heating tendency was added. The chemical perturbation also induced dynamical effects in the simulations – dynamical effects were observed in runs A, C and D, despite the temperature perturbation only being added to runs A and D. In run C, a small temperature increase was observed, centred at an altitude of ~100 km and lasting for ~1 week (Figure 5.11, run C), though the magnitude was much smaller than that resulting from the dynamical perturbation (< 4 K). The prevalent effect, however, was a net decrease in the global mean temperature. A small but pervasive temperature decrease was present above ~70 km, with larger decreases in temperature focused at two distinct altitudes. The first of these was centred between 90-95 km (up to ~12 K), the second was centred at around 125 km (up to ~38 K). It should be noted that although the magnitude of the temperature decrease at 125 km is greater than that at 90 km, the relative magnitudes are similar (~6-9 %). In run A, when the dynamical and chemical perturbations were combined, the duration of the initial temperature response to the added heating tendency was similar to that in run D. However, the response this triggered in the model lasted significantly longer – including the temperature perturbation amplified both the chemical and dynamical effects observed in run C. In terms of the dynamics, the magnitude and duration of the temperature decrease observed at ~90 km were slightly greater in run A than in run C, though the changes were only on the order of a few K/week (Figure 5.11, run A).
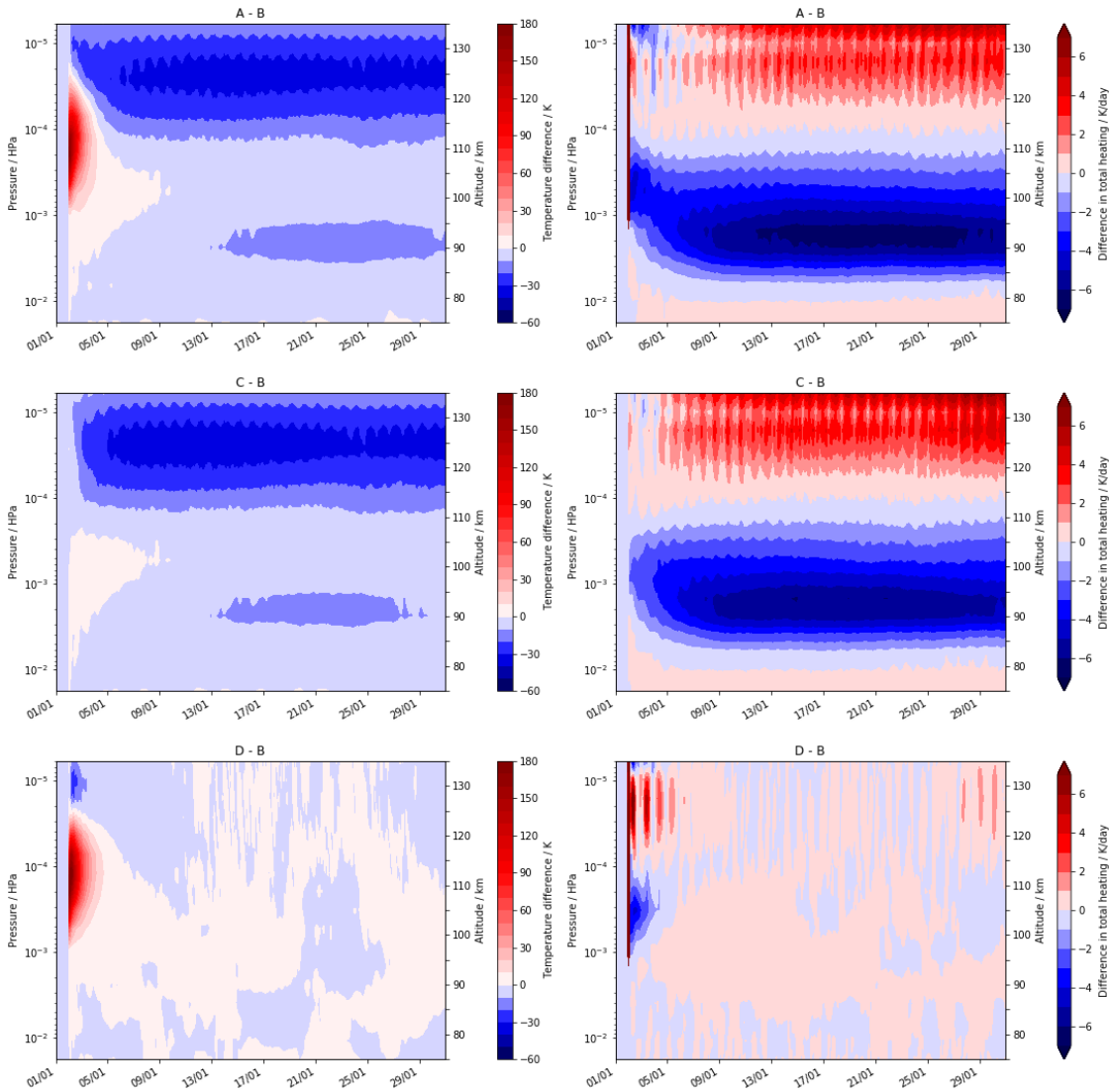
Figure 5.11. Left panels: time series showing the global mean temperature difference (dT/ K) from the control run B, as a function of pressure (hPa) for runs A, C and D (A, C, or D minus B). Right panels: time series showing the global mean difference in the total atmospheric heating (dQ$_{tot}$/ K day$^{-1}$) from the control run B, as a function of pressure (hPa) for runs A, C and D (A, C, or D minus B). Approximate altitudes (km) are shown for reference on the right axis.

The temperature decrease at ~90 km was a result of a decrease in the total shortwave heating (Q$_{tot}$/ K day$^{-1}$) in the model (Figure 5.11, runs A and C). The different terms contributing towards Q$_{tot}$ can be separated, enabling the source of the effect to be established. The observed differences are predominantly caused by a decrease in chemical heating (Q$_c$), as shown by Figure 5.12, which shows the global average Q$_c$ for runs A, B and C at four different altitudes, compared to the decrease in the global-average temperature. A slightly greater decrease in Q$_c$ is observed in run A compared to run C, at ~90 km, 100 km, and 110 km, with the biggest difference at 90 km close to the peak of the global metal layers. This leads to the subsequent differences in the temperature response between these runs. In addition to the changes in Q$_c$, there is also a small contribution (< 1 K day$^{-1}$) to Q$_{tot}$ from a reduction in the heating from non-EUV (extreme ultra-violet) photolysis (Q$_p$) of O$_3$ (not shown). Both of these effects can be explained in terms of changes to

HO$_x$ chemistry, caused by the chemical perturbation. As discussed above, an increase in the metal chemistry triggers the removal of O, O$_3$ and H, causing a reduction in the rates of O$_x$ and HO$_x$ reactions – most of which are exothermic. This leads to the observed decrease in chemical heating (and further feedbacks on the density of these and other HO$_x$ species). The reduction in O$_3$ also causes a decrease in the absorption of longwave (>200 nm) radiation *via* the two O$_3$ photolysis channels (R1.11 and R1.12) causing the decrease in Q$_p$.
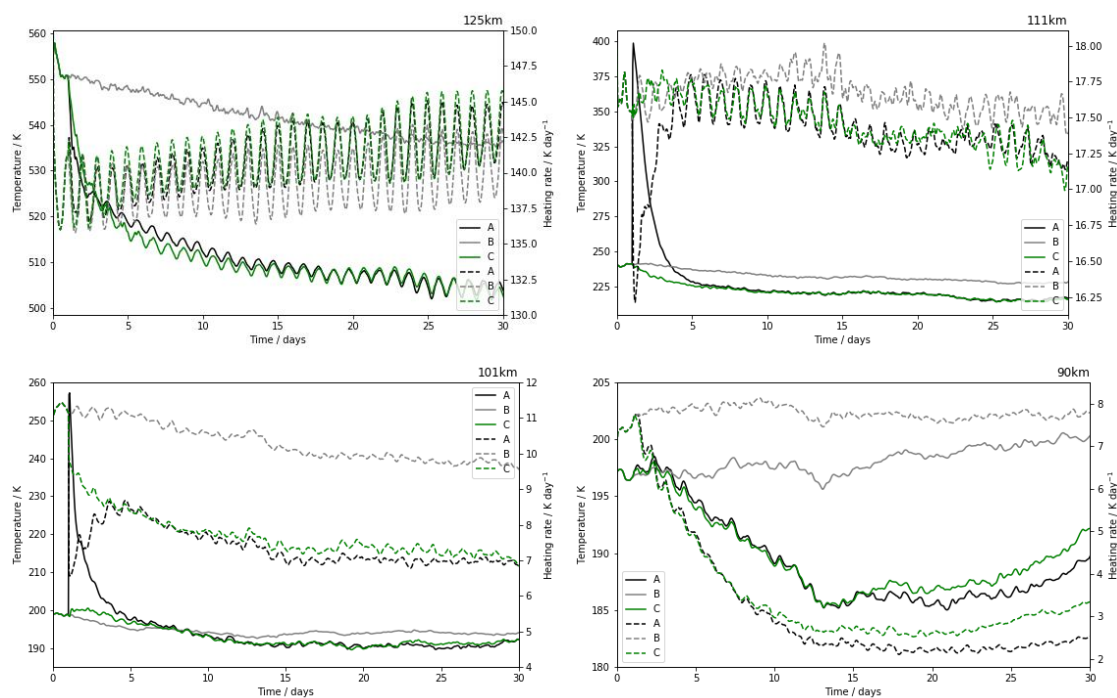


Figure 5.12. The global-average temperature (K) during the first month of the simulations, for runs A (black), B (grey) and C (green) at 125 km, 111 km, 101 km and 90 km (solid lines). Also shown (right axis/dashed lines) is the chemical heating rate (Q$_c$) in K day$^{-1}$.

The temperature decrease at ~125 km cannot be explained in the same manner, because rather than decrease in Q$_{tot}$ and Q$_c$, increases are observed – though the absolute magnitude of the increases are smaller than the decreases below ~100 km, and the relative change is much less significant – at 90 km, the change in Q$_{tot}$ for run A represents up to a 60 % decrease compared to the control run B, whereas at 125 km it constitutes only < 3%. Again, the change in Q$_{tot}$ is largely due to a change in Q$_c$, with a small contribution from non-EUV photolysis (Q$_p$) – in this case, from O$_2$ rather than O$_3$ (*via* R1.1 and R1.2).

The increase in Q$_c$ is a result of an increase in thermospheric O$_x$ and NO$_x$ reactions, which are highly exothermic (between -70 and -510 kJ mol$^{-1}$ [*Atkinson et al.*, 2004; *Roble*, 1995]) such as the recombination of NO$^+$ and O$_2^+$ ions with electrons (R5.19, R5.20). After the chemical perturbation there is a significant increase in plasma density in the MLT, and the atmosphere functions to neutralise itself. At 125 km, the dominant ions are NO$^+$ and O$_2^+$, and their

recombination with electrons proceeds *via* dissociative electron recombination (rate constant $k \sim$ 1.6 - 4.2 $\times$ $10^{-7}$ cm$^3$ s$^{-1}$) [*Roble*, 1995]. This is the main loss process for ionization in the lower thermosphere [*Rees*, 1989; *Shuman et al.*, 2015], proceeding significantly faster than the dielectronic recombination of metal ions ($k \leq \sim 10^{-11}$ cm$^3$ s$^{-1}$) and the dissociative recombination of molecular ions (e.g. FeO$^+$, FeO$_2^+$, FeN$_2^+$, $k \sim 1.8 \times 10^{-7}$ cm$^3$ s$^{-1}$) given the low concentrations of these latter species above 120 km [*Bones et al.*, 2016; *Plane et al.*, 2015]. R5.19 and R5.20 form both ground-state and electronically excited N and O, which can react *via* a number of pathways, releasing kinetic energy – through exothermic chemical reactions, as translational energy, and *via* radiative emission [*Rees*, 1989]. The release of energy from these processes leads to the increase in Q$_c$ observed. However, this increase in Q$_c$ does not explain why a temperature decrease is observed at high altitudes. It may be that these effects are anomalous, since at the top of the model the temperature and atomic O density are constrained by a boundary condition based on the Mass Spectrometer-Incoherent Scatter (MSIS) model [*Hedin*, 1987; 1991]. Thus, a significant perturbation to the temperature, atomic O density or the density of other species could have a spurious effect at the model-top (above 120 km), where the dissipation of energy by longwave emission is very inefficient [*Neale et al.*, 2010].

R5.19 O$_2^+$ + e$^-$ $\rightarrow$ O (57.5 %) + O$^1$D (42.5 %)

R5.20 NO$^+$ + e$^-$ $\rightarrow$ N$^2$D (80 %) + N (20 %) + O
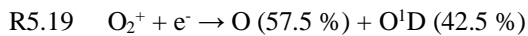
## 5.2.2  Duration

Though the short-term temperature increase in runs A and D lasted only ~5 days, the duration of the temperature decrease in runs A and C lasted approximately the same amount of time as the perturbation to O$_x$ and HO$_x$ due to the changes to metal chemistry. This is demonstrated by Figure 5.13, which shows the global-average temperature at different altitudes for runs A, B, C and D. Though the magnitude of the temperature changes varies at each altitude, the time taken for the temperature to return to the baseline levels was approximately 3 - 4 months in each case. As discussed before, this is primarily due to changes in model heating rates such as Q$_c$ causing changes to the temperature.
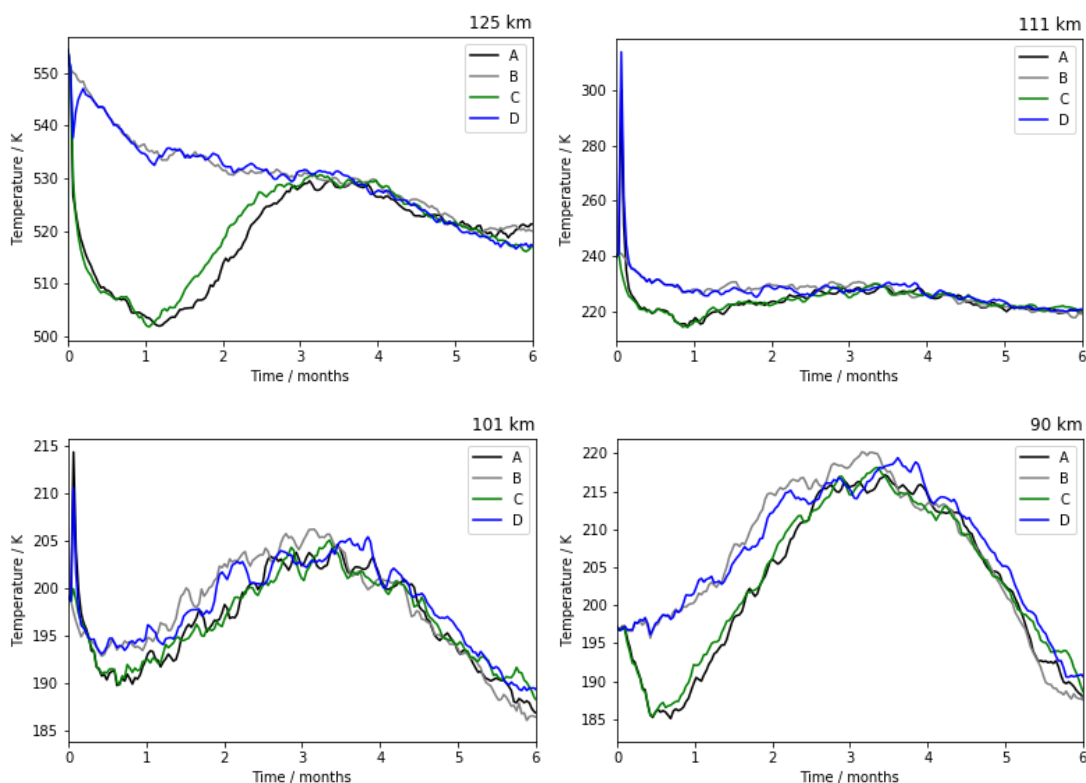
Figure 5.13. Time series showing the global average temperature (K) at 125 km, 111 km, 101 km and 90 km, for runs A (black), B (grey), C (green) and D (blue).

## 5.3 Metal Reaction Enthalpies Test Run

The standard version of WACCM used does not include reaction enthalpies for any of the mesospheric metal chemistry, since the background densities of these species in the MLT are too small to cause heating in comparison with exothermic reactions involving species such as $O_x$, $HO_x$ and $NO_x$. However, since the metal densities in the Halley simulations were so elevated, a one month test simulation (run $A_m$) was performed to establish whether the inclusion of these reaction enthalpies significantly altered the heating rates or thermal balance in the MLT. The enthalpies for the metal reactions which catalyse the transformation of O and $O_3$ into $O_2$, were added to this simulation as detailed in Table 5.2.

Figure 5.14 shows the global-average temperature and the global-average heating rate from chemical reactions ($Q_c$) for runs $A_m$, A, B and C at four altitudes. It can be seen that including the additional metal reaction enthalpies has an effect on $Q_c$ and therefore the temperature. At ~110 km and below, the decrease in $Q_c$ observed in run $A_m$ is smaller than that in run A, the equivalent run without the added reaction enthalpies. At ~90 km, there is also a slight increase in $Q_c$ in run $A_m$ relative to run B. This is caused by an increase in heat released from the metal reactions, which offsets the decrease in heat produced from $HO_x$ chemistry. At 125 km, there are minimal differences between $Q_c$ in runs $A_m$ and A. The changes to $Q_c$ lead to an initial increase in temperature for run $A_m$ (relative to run B) at ~90 km, followed by a smaller temperature decrease

than was observed in run A. At 100 km, the initial temperature increase decayed away more slowly, such that by the end of the month the temperature had approximately converged to the baseline, in contrast to runs A and C, which exhibited a temperature decrease after the first week. At 125 km, since the changes to $Q_c$ were negligible, the temperature response was similar in the two runs. This is because at high altitudes, any changes to $Q_c$ become dominated by changes to non-metal reactions.

The effect of these changes on the metal densities was to cause the metals to be removed more slowly (Figure 5.15); by the end of the first month, the global-average total metal column densities in run $A_m$ were ~10 - 30 % higher than run A. However, this is not enough to make a substantial difference to the long-term decay of the metals or their removal lifetimes. Some differences are also observed in $O_x$ and $HO_x$ densities (Figure 5.16). The largest effect was on $O_x$ – a ~15 % decrease in the global-average total column density of atomic O was observed in run $A_m$, compared to ~20 % in run A. For $O_3$, whilst the decrease observed is not significantly altered in run $A_m$, the duration of the effect is longer than in run A. Small differences are present in the H and $H_2O$ densities, though these are relatively insignificant, being on the order of a few percent. The changes to the densities observed between runs $A_m$ and A are a result of the temperature changes induced by changes to $Q_c$. This affects $O_x$, $HO_x$ and metal reaction rates, as per Figure 5.7. Inclusion of this heating would give a more complete representation of the simulated encounter. However, though there are some changes to the densities and temperature, it is unlikely that the omission of this additional effect would significantly affect the conclusions of this study.

Table 5.2. Reaction enthalpies (kJ mol$^{-1}$) for the neutral and ionic metal reactions added to WACCM during the test-simulation, run $A_m$.

| Reaction | Enthalpy change / kJ mol$^{-1}$ | Reference |
|---|---|---|
| $Fe + O_3 \rightarrow FeO + O_2$ | -302 | *Helmer and Plane* [1994] |
| $FeO + O \rightarrow Fe + O_2$ | -91 | *Helmer and Plane* [1994] |
| $Mg + O_3 \rightarrow MgO + O_2$ | -149 | *Plane and Whalley* [2012] |
| $MgO + O \rightarrow Mg + O_2$ | -244 | *Plane and Whalley* [2012] |
| $Na + O_3 \rightarrow NaO + O_2$ | -152 | *Plane et al.* [2012] *Gómez Martín et al.* [2016] |
| $NaO + O \rightarrow Na + O_2$ | -241 | *Cox and Plane* [1999] |
| $Fe^+ + O_3 \rightarrow FeO^+ + O_2$ | -240 | *Rollason and Plane* [1998] |
| $FeO^+ + O \rightarrow Fe^+ + O_2$ | -153 | *Woodcock et al.* [2006] |
| $Mg^+ + O_3 \rightarrow MgO^+ + O_2$ | -116 | *Whalley et al.* [2011] |
| $MgO^+ + O \rightarrow Mg^+ + O_2$ | -277 | *Whalley et al.* [2011] |
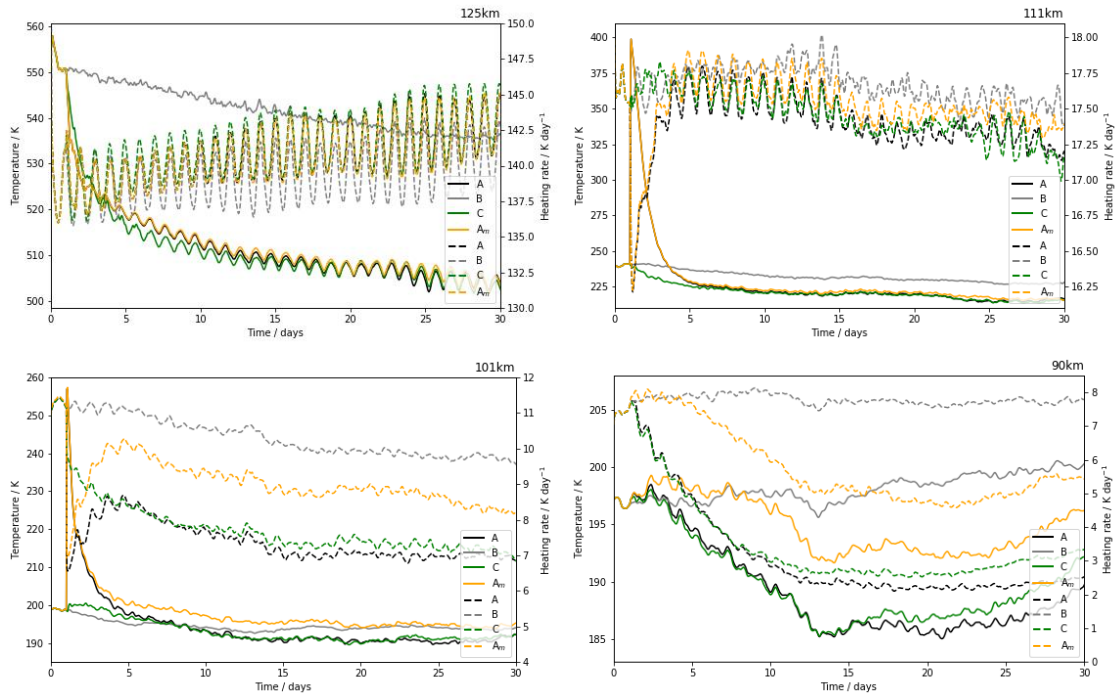
Figure 5.14. The global-average temperature (K) during the first month of the simulations, for runs $A_m$ (yellow), A (black), B (grey) and C (green) at 125 km, 111 km, 101 km and 90 km (solid lines). Also shown (right axis) is the chemical heating rate ($Q_c$) in K day$^{-1}$ (dashed lines).
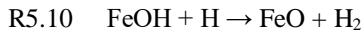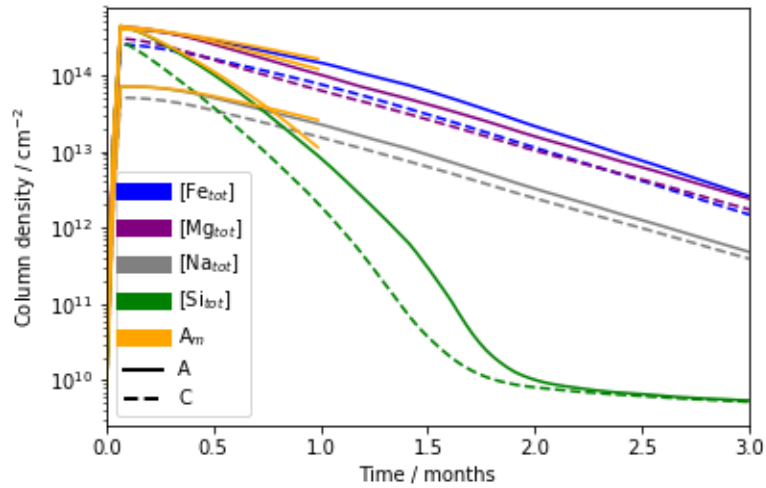


Figure 5.15. Time series for the global-average total column densities (cm$^{-2}$) for run A (solid lines) and run C (dashed lines): [Fe$_{tot}$] (blue), [Mg$_{tot}$] (purple), [Na$_{tot}$] (grey) and [Si$_{tot}$] (green) where [Fe$_{tot}$] = [Fe] + [Fe$^+$] + [FeOH], [Mg$_{tot}$] = [Mg] + [Mg$^+$] + [Mg(OH)$_2$], [Na$_{tot}$] = [Na] + [Na$^+$] + [NaHCO$_3$] and [Si$_{tot}$] = [Si] + [SiO] + [Si$^+$] + [OSi(OH)$_2$]. Also shown is the global-average total column densities for run $A_m$ (yellow lines) for [Fe$_{tot}$], [Mg$_{tot}$], [Na$_{tot}$] and [Si$_{tot}$].
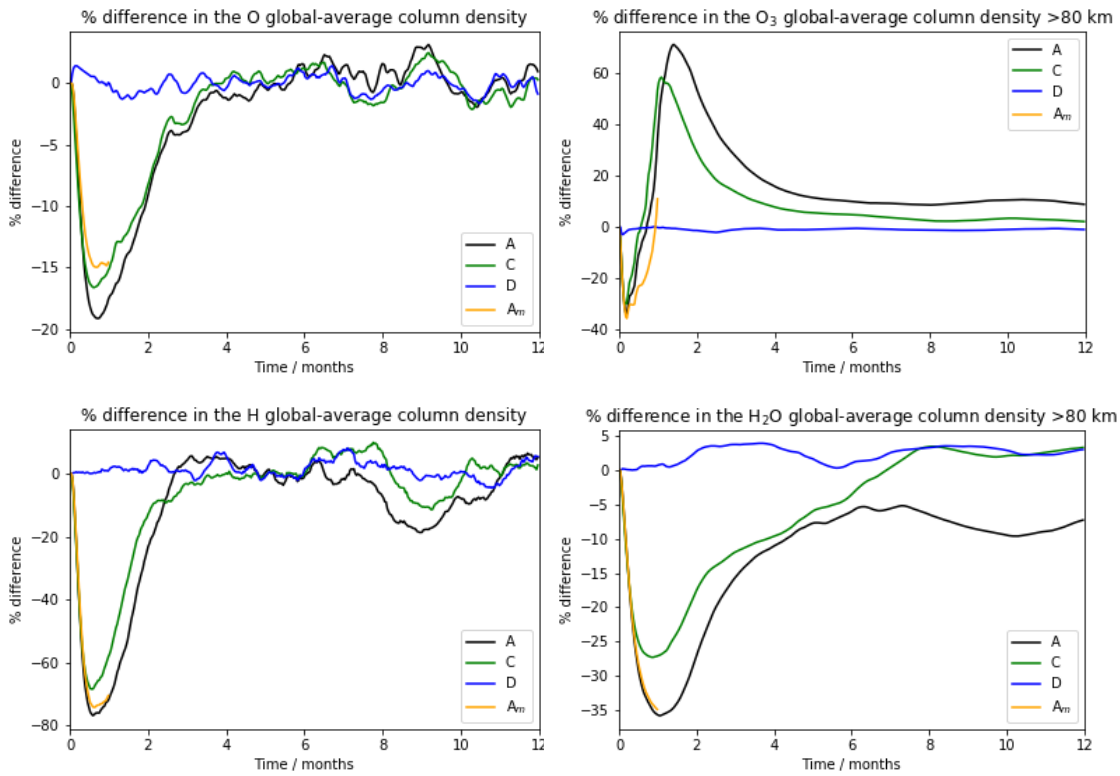
Figure 5.16. Time series showing the percentage difference in the global-average total column densities for O (top left) and $O_3$ above 80 km (top right), H (bottom left) and $H_2O$ (bottom right) for runs $A_m$ (yellow), A (black), C (green) and D (blue).

## 5.4   Conclusions

Four simulations were performed in which the effects of both a chemical and dynamical perturbation were explored. The chemical perturbation (metal injection) was implemented in run C, and the dynamical perturbation (heating tendency) was implemented in run D. Run A combined the two effects, and in run B no additional changes were included, such that this served as a background simulation. The chemical perturbation added to runs A and C generated an increase (by a factor of $\sim 10^5$) in the global-average total column densities of Fe, Mg, Na and Si species. For both simulations, the removal of the metals *via* dimerization proceeded more rapidly than in the control run B, with a small difference between the removal rates between A and C. The Fe, Mg and Na densities took approximately 6-7 months to return back to baseline levels, whereas Si was removed much more rapidly, forming the stable $Si(OH)_4$ in a timeframe of approximately 2 months.

The chemical perturbation also generated changes to the residual circulation in the MLT. In runs A and C, a net transport from winter-to-summer was induced at around 100-110 km where previously there was no significant transport. These circulation changes resulted in an increased burden of metal species in the southern (summer) hemisphere, in contrast to the usual winter maximum observed (for Fe, Mg and Na). Despite a significant temperature increase being

observed in the first few days of Run D, this dynamical perturbation did not induce any longer-term dynamical changes – run D did not display any significant changes to the residual circulation.

Both the chemical and dynamical perturbations induced changes in $O_x$ densities. Metal chemistry in the MLT causes a net removal of O and $O_3$ through the interconversion of the neutral and ionic metals and their oxides. The elevated metal densities and faster reaction rates lead to ~17 % and 30 % decreases in the global-average column densities of O and $O_3$ respectively for run C. A slightly greater destruction of O and $O_3$ was observed in run A (19 % and 34 % respectively) as a result of the inclusion of the dynamical perturbation. These changes constituted decreases of up to 30 % and 100 % in the global-average O and $O_3$ densities respectively, between approximately 85 and 115 km in altitude. In runs A and D, the dramatic increase in temperature added to the model lead to a decrease in the pressure dependent recombination of O and $O_2$ to form $O_3$, leading to an increase in $O/O_3$ ratio. This caused an increase in the neutral metal densities relative to the oxides, and lead to the destruction of additional O and $O_3$ during run A compared to run C. This was predominantly a result of an increase in the interconversion of Me and MeO, since these reactions proceed the fastest of all the metal reactions [*Plane et al.*, 2015].

A net destruction of H and $H_2O$ is also typically observed as a result of the MLT metal chemistry due to the formation and reaction of metal hydroxides. Thus, the elevated metal densities lead to a significant decrease in the H and $H_2O$ global-average column densities (up to 68 % and 25 % respectively for run C). In run A, the changes to $O_x$ species resulting from the inclusion of the dynamical perturbation amplified the effects of the chemical perturbation, leading to greater destruction of H and $H_2O$ (up to 78 % and 36 % decreases respectively in the global-average column densities). Above 80 km, this represented up to 100 % removal of both species in the first 1-2 months (run A). H is exclusively consumed by metal reactions, with the exception of the reaction of NaO with $H_2$ to form NaOH, which is the only metal reaction to reform H. For $H_2O$, a net destruction is observed through the formation and dimerization of $Mg(OH)_2$, $Si(OH)_4$ and $NaHCO_3$. Furthermore, though $H_2O$ is both consumed and produced in the production of FeOH, its formation from $Fe(OH)_2$ involves reaction with H, which becomes severely depleted after the chemical perturbation. Thus, the reactions of Fe also contribute to the net removal of $H_2O$.

In run D, the added heating tendency caused an increase in the global-average temperature of up to ~180 K, peaking at ~110 km, close to the altitude at which the highest amount of metals were injected by the MIF. The temperature increase decayed away over approximately 5 days, with minimal effects on the temperature observed after this time. In runs A and C, the chemical perturbation also had an effect on the temperature. The depletion in O, $O_3$, H and $H_2O$ from the metal chemistry causes a net reduction in the rates of $O_x$ and $HO_x$ reactions, which has feedbacks to both the metal chemistry and the densities of these species. It also causes a reduction in both chemical ($Q_c$) and photochemical ($Q_p$) heating. Thus, a net decrease in temperature is observed due to the chemical perturbation, which has additional feedbacks on both metal and ambient chemistry. However, below 100 km the temperature decrease should be considered an upper limit

– inclusion of $Q_c$ from key metal reactions counteracts the temperature decrease observed. In an analogous manner, the decreases observed in O, $O_3$, H and $H_2O$ represent upper limits for the removal of these species, though the only significant overestimation is in the O density by omission of this effect. Contrastingly, the metal densities are slightly underestimated through not including the metal heating rates, though this is unlikely to make a significant difference on the duration of the overall decay in the total metals.

# Chapter 6

## Cometary Impacts on the Middle Atmosphere and Surface Deposition

In this chapter, the longer-term effects of the simulated Halley encounter will be explored through a 7 year WACCM-CARMA simulation, in which a meteoric sulfur (S) injection and an injection of meteoric smoke particles (MSPs) to the upper atmosphere were implemented. This simulation will be referred to as the 'Halley' simulation, or run $A_S$. A background (control) simulation was also performed in which no additional changes were applied: run $B_S$. Effects on the gas-phase sulfur chemistry of the mesosphere and stratosphere will be discussed, and effects on the density and size distributions of stratospheric sulfate aerosol will be examined, including discussion of changes to the available surface area. Lastly, the deposition of MSPs will be analysed, to determine if a close cometary encounter could cause - or contribute to - the increased S deposition observed in the $6^{th}$ century, when a period of severe global cooling took place.

## 6.1 Gas Phase Species

In the Halley simulation, run $A_s$, the sulfur injection produced an increase in the global average column density of S and SO of around 3 and 2.5 orders of magnitude respectively (Figure 6.1). The S is rapidly oxidised to SO, the maximum density of which is observed after one to two weeks. Further oxidation is assumed to occur *via* the typical pathways described in *Gómez Martín et al.* [2017]; oxidation of SO to $SO_2$ occurs *via* reaction with $O_2$, $O_3$ or OH and the maximum densities of $SO_2$ and $SO_3$ are observed 6 to 7 months after the S injection. The S density decayed back to baseline levels in 10 months to 1 year after the Halley perturbation, and that of the oxides took on the order of 1.5 years. After this time, the oxide densities continued to decay such that a decrease of up to 18 %, 22 % and 52 % was observed for SO, $SO_2$ and $SO_3$, respectively, between 1.5 and 2 years after the initial injection.

The sequential oxidation of the injected material is demonstrated more clearly when looking at altitude profiles showing the difference between the two model runs. Figure 6.2 shows global average time series as a function of altitude, where with increasing time and decreasing altitude, the S is converted from S through to $SO_2$ and $SO_3$. The maximum in the aforementioned density decrease of the oxides can be seen, for $SO_2$ and $SO_3$, to be localised at approximately 35-45 km, above the stratospheric aerosol layer. $HSO_3$, produced as an intermediate in the formation of $SO_3$ from $SO_2$, exhibits similar behaviour to the oxides. A large increase followed by a smaller (~20 %) decrease after 1.5 years is observed. A decrease of up to ~70 % is observed in gaseous $H_2SO_4$, lasting on the order of 2 years. Though the relative decrease is greater than that observed for $SO_2$, $SO_3$ and $HSO_3$, the maximum density decrease for $H_2SO_4$ is located at a similar altitude (35 - 45 km).
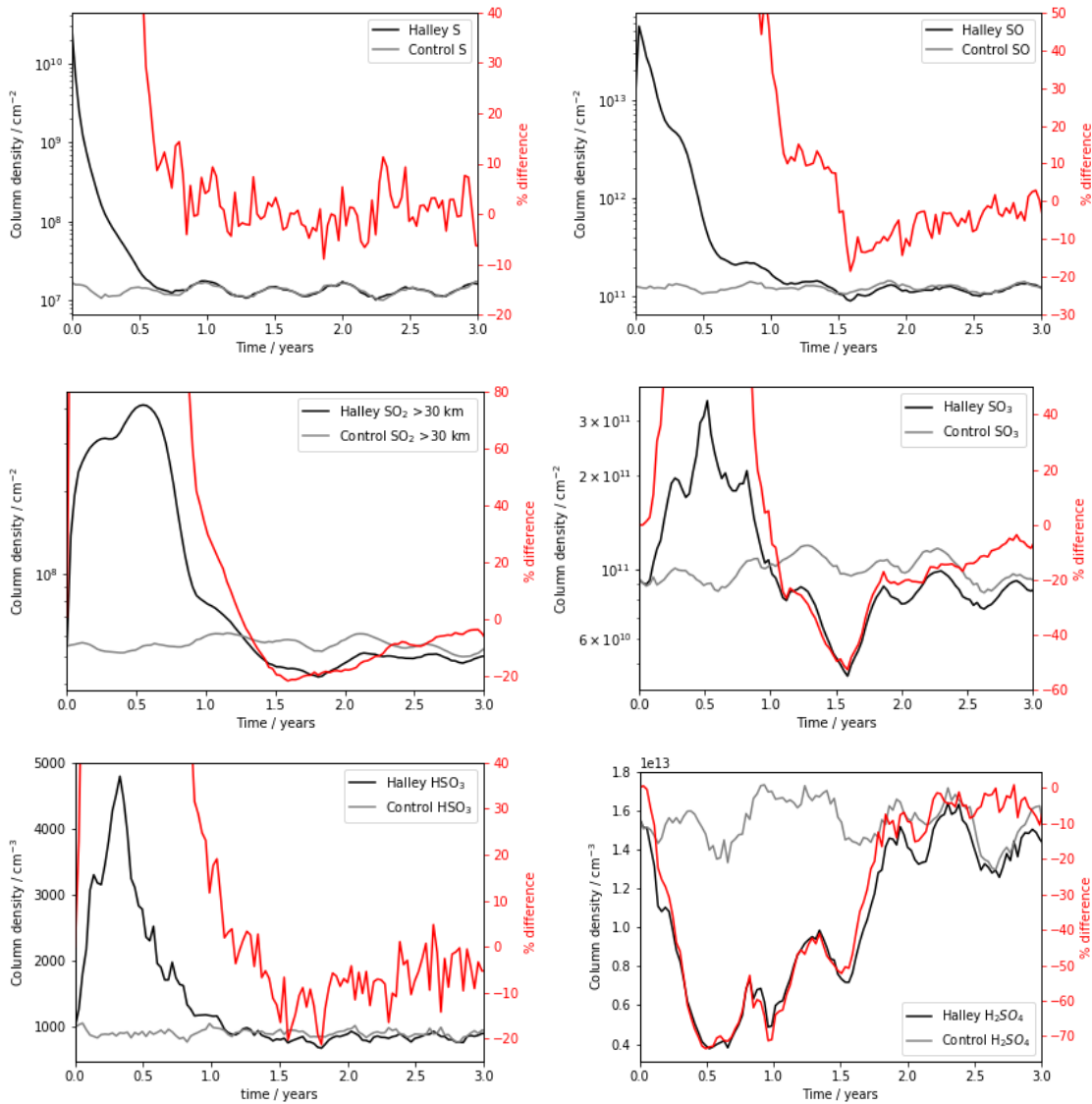
Figure 6.1. Time series showing the global average column densities for the gaseous sulfur species S, SO, SO$_2$, SO$_3$, HSO$_3$ (cm$^{-2}$) and H$_2$SO$_4$ ($\times 10^{13}$ cm$^{-2}$) for the Halley (black) and control (grey) simulations (A$_s$ and B$_s$). The percentage increase is also shown (red) on the right axis. For SO$_2$, the column density above an altitude of 30 km is plotted, due to the high concentrations of SO$_2$ observed in the stratospheric aerosol layer, which are significantly greater than the densities at higher altitudes.

For all the gas-phase sulfur species (excepting H$_2$SO$_4$), the increase and subsequent decay in the densities are caused by two competing effects. Initially, the elevated production rates resulting from the increased levels of sulfur precursors (formed from the injected meteoric sulfur) dominate over the rates of removal *via* gas phase reactions (the material is being formed faster than it is destroyed). After a period of time, defined by the rates of production and removal for each species, the removal processes dominate and the density for each species decreases until it returns to the baseline level. The densities of the gaseous sulfur species are also affected by changes to aerosol processes; since H$_2$SO$_4$ undergoes uptake onto MSPs, pure sulfate and mixed sulfate aerosol (see section 6.2.1.1, reactions *c*, *d*, *f* and *g*, Table 6.1) and the aerosol densities are significantly elevated from the start of the model run, a large (up to 70 %) decrease in H$_2$SO$_4$ density is

observed lasting around 2 years. This then has implications for the densities of SO, $SO_2$, $SO_3$ and $HSO_3$; these species can be interconverted and as such, reaction rates are affected. A combination of these two phenomena leads to the density decreases observed after approximately 1.5 years. The uptake of $H_2SO_4$ onto meteoric smoke in the atmosphere typically increases with decreasing altitude, though uptake can occur at altitudes above 45 km [*Neely et al.*, 2011; *Saunders et al.*, 2012]. In the Halley simulation ($A_s$), the decrease in gas phase S species above the aerosol layer, centred at around 40 - 45 km, is therefore caused by an increase in uptake to aerosol at higher altitudes than the control run $B_s$ (up to ~ 50 - 55 km) as a result of the higher density of both sulfur species and meteoric material available.
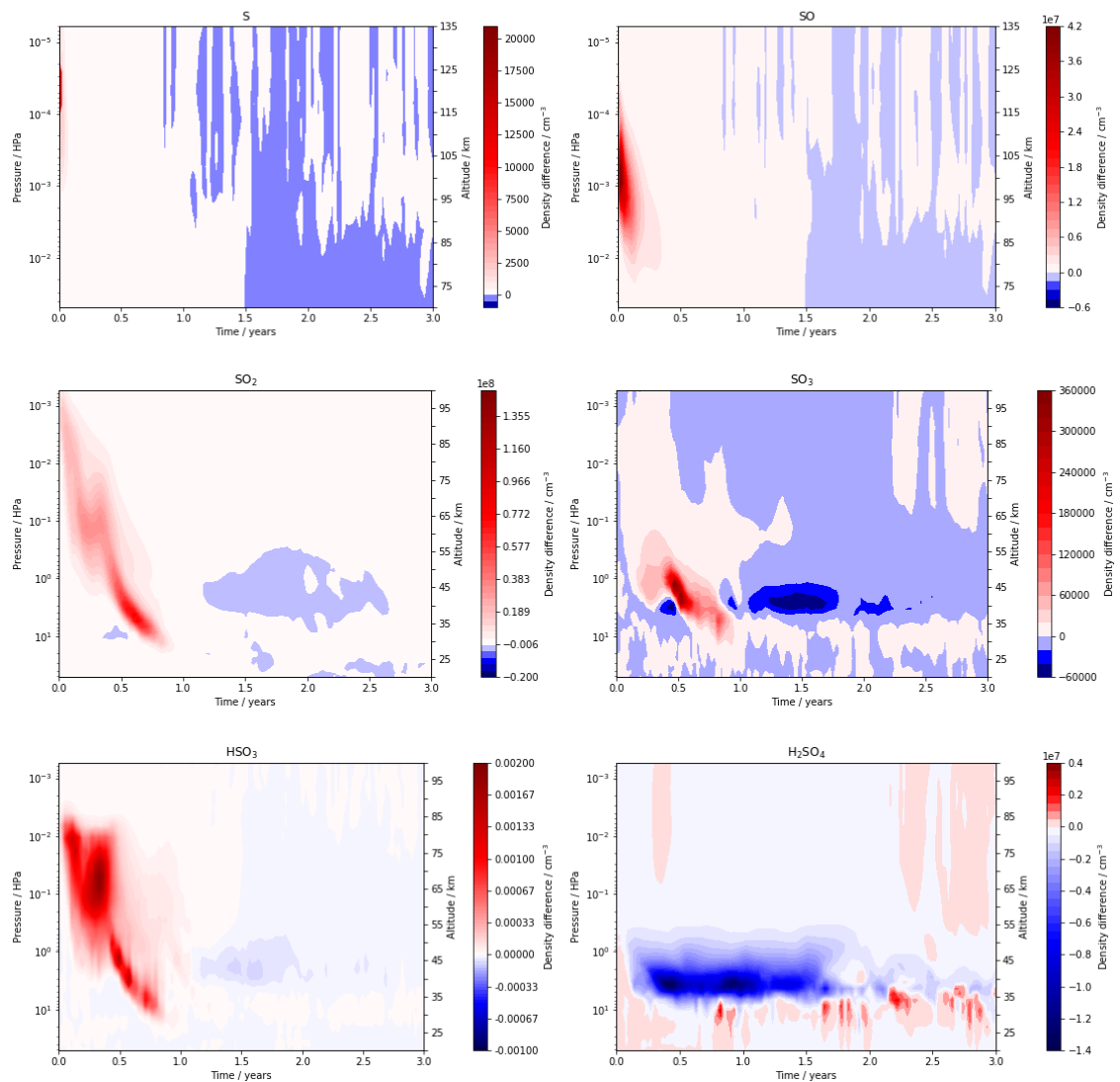


Figure 6.2. Time series showing the difference in the global average densities of gaseous sulfur species S ($cm^{-3}$), SO ($\times 10^7 cm^{-3}$), $SO_2$ ($\times 10^8 cm^{-3}$), $SO_3$ ($cm^{-3}$), $HSO_3$ ($cm^{-3}$) and $H_2SO_4$ ($\times 10^7 cm^{-3}$) between the Halley and control simulations ($A_s$ and $B_s$) as a function of pressure (hPa). Approximate altitudes (km) are shown for reference. Note different height scales used for the top two panels.

## 6.2   Aerosols

### 6.2.1   Particle Size distributions

#### 6.2.1.1   MSPs

A rapid increase in the global-average total mass density of MSPs is observed in run $A_s$ (Figure 6.3, top left panel). This represents a global-average of the mass density integrated over all particle size bins. After this initial increase, the mass density decreases fairly steadily, returning to the baseline after three to four years. A relatively smaller increase in the total mass density is also observed at the start of the second year. The initial increase in mass density is a result of the initial injection. This is followed by rapid coagulation of particles – in the model, this is the only process where MSPs (DUST) can grow to larger sizes (reaction $l$, Table 6.1). This is demonstrated in Figure 6.3 (middle left & bottom left panels) where in the first few months after the injection the MSPs, which were initially injected into the smallest size bin (0.34 nm), grow rapidly such that the larger size bins become more populated and the smaller size bins become less populated relative to those in the control run, $B_s$. As the particles grow to increasingly larger sizes, the rate of coagulation slows down because although most of the mass is concentrated into the largest particles, there are fewer particles of these sizes formed (Figure 6.3, middle right and bottom right panels); the number density decreases with increasing particle size in both model runs $A_s$ and $B_s$. It should be noted that in the model it is not possible for particles to exceed the maximum size bin available, and any particles that do are still classed in this last size bin. As such, it may be possible that there would be a population of particles with sizes exceeding the maximum radius which are not captured by the model. Inspection of the mass density in Figure 6.3 shows that the size distribution in run $A_s$ takes approximately 6-7 years to recover, though towards the end of the simulation the changes are much less pronounced.

In contrast to the mass density, the global-average total number density of MSPs exhibits a decrease in the first month (Figure 6.3, top right panel). The initial increase due to the MSP injection is not captured in the global average and there is rapid coagulation reducing the total number of particles in run $A_s$ compared to run $B_s$. This coagulation is observed in the size distribution (Figure 6.3 middle right and bottom right panels) where there is an increased number of larger particles in run $A_s$ compared to $B_s$. In the same manner as the mass density, although the number density in run $A_s$ takes around 5 years to completely return to the baseline the effect on the average total number density is only significant closer to the start of the model run (Figure 6.3, top-right panel).
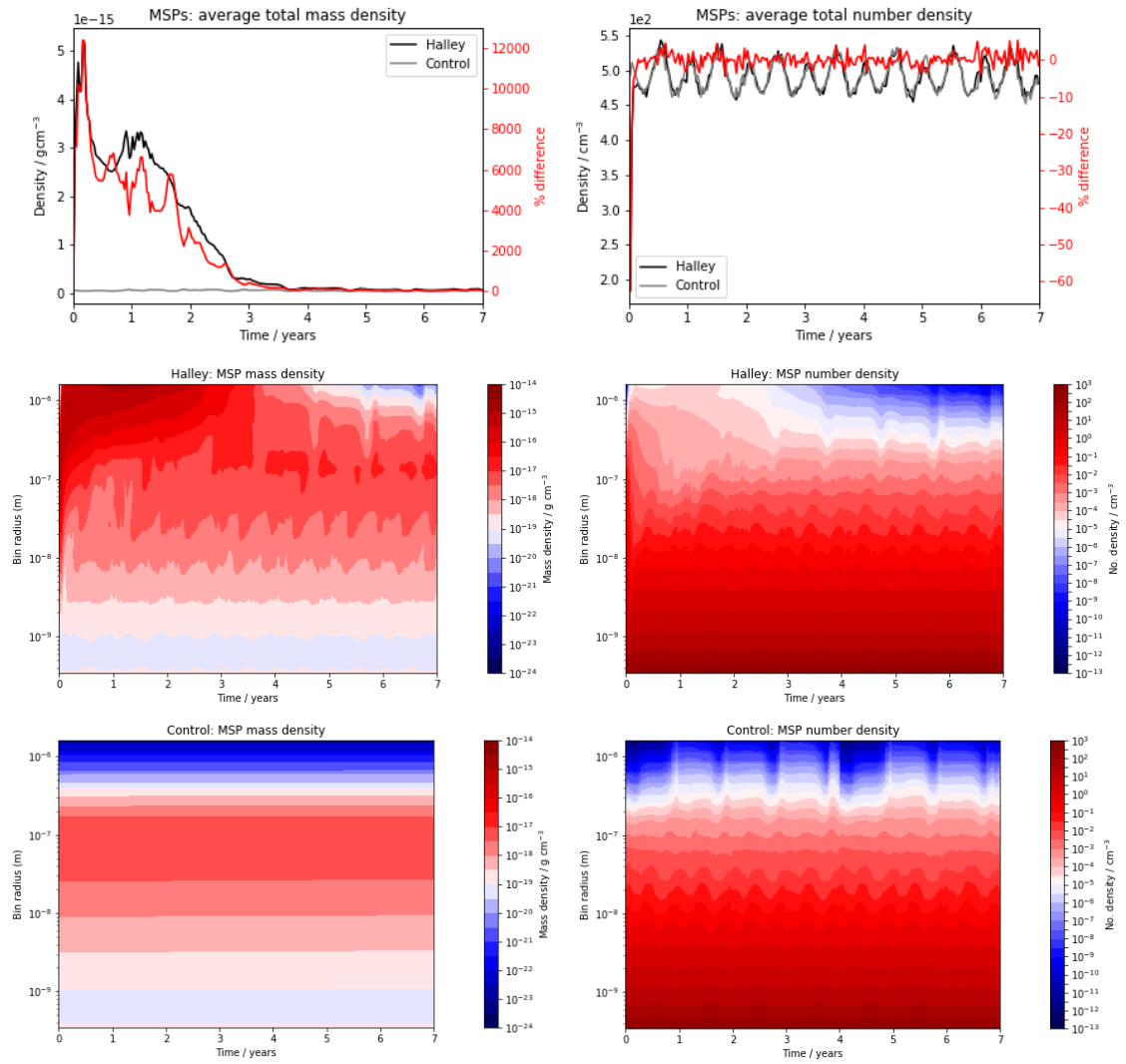
Figure 6.3. Top panels: the global-average MSP total mass density (×10⁻¹⁵ g cm⁻³, left panel) and number density (cm⁻³, right panel). Middle panels: particle mass (left) and number (right) densities for run A_s as a function of size (radius/ m) and of time (years). Bottom panels: particle mass (left) and number (right) densities (cm⁻³) for run B_s as a function of size (radius/ m) and time (years).

Table 6.1. Allowed aerosol processes in WACCM-CARMA involving the four aerosol types (PURE, CORE, MIXSUL, and DUST) and gaseous $H_2SO_4$ [*Bardeen et al.*, 2008; *Brooke et al.*, 2017].

| Particle type | Formation processes | Destruction processes |
|---|---|---|
| $H_2SO_4$ | *a)* $PURE \xrightarrow{evaporation} PURE + H_2SO_4$ <br> *b)* $CORE \xrightarrow{evaporation} DUST + H_2SO_4$ | *c)* $PURE + H_2SO_4 \xrightarrow{homo\,nuc} PURE$ <br> *d)* $PURE + H_2SO_4 \xrightarrow{growth} PURE$ <br> *f)* $DUST + H_2SO_4 \xrightarrow{het\,nuc} CORE$ <br> *g)* $MIXED + H_2SO_4 \xrightarrow{growth} MIXED$ |
| PURE | *c)* $PURE + H_2SO_4 \xrightarrow{homo\,nuc} PURE$ <br> *d)* $PURE + H_2SO_4 \xrightarrow{growth} PURE$ <br> *e)* $PURE + PURE \xrightarrow{growth} PURE$ | *a)* $PURE \xrightarrow{evaporation} PURE + H_2SO_4$ <br> *h)* $MIXED + PURE \xrightarrow{growth} MIXED$ <br> *k)* $DUST + PURE \xrightarrow{growth} MIXED$ |
| CORE | *f)* $DUST + H_2SO_4 \xrightarrow{het\,nuc} CORE$ | *b)* $CORE \xrightarrow{evaporation} DUST + H_2SO_4$ |
| MIXSUL | *g)* $MIXED + H_2SO_4 \xrightarrow{growth} MIXED$ <br> *h)* $MIXED + PURE \xrightarrow{growth} MIXED$ <br> *i)* $MIXED + MIXED \xrightarrow{growth} MIXED$ <br> *j)* $MIXED + DUST \xrightarrow{growth} MIXED$ <br> *k)* $DUST + PURE \xrightarrow{growth} MIXED$ | *m)* $MIXED \xrightarrow{evaporation} MIXED + H_2SO_4$ |
| DUST | *l)* $DUST + DUST \xrightarrow{growth} DUST$ <br> *b)* $CORE \xrightarrow{evaporation} DUST + H_2SO_4$ | *f)* $DUST + H_2SO_4 \xrightarrow{het\,nuc} CORE$ <br> *j)* $MIXED + DUST \xrightarrow{growth} MIXED$ <br> *k)* $DUST + PURE \xrightarrow{growth} MIXED$ |

## 6.2.1.2 Mixed sulfate

For mixed sulfate aerosol, an increase in the global-average total mass density is observed, peaking after 1 to 2 years (Figure 6.4, top left panel). The increase observed for mixed sulfate is delayed compared to that seen for MSPs since the MSPs must be transported from their injection altitude down to the lower mesosphere/stratosphere, where there is a higher density of $H_2SO_4$ and other aerosols before an appreciable mass of mixed sulfate is formed. Looking at the mass density size distribution (middle left and bottom left panels), it can be seen that there is a decrease in the mass in small size bins (<10 nm) for years 1 and 2 in run $A_s$. This could be due to more rapid coagulation of small particles, or because more large particles are formed directly relative to small ones due to the increased coagulation of MSPs (or both). The peak of the size distribution in run $A_s$ does not increase relative to run $B_s$, indicating that the formation of larger particles is limited by a combination of decreasing $H_2SO_4$, the low concentration of large MSP cores, and the faster sedimentation rates of large particles.
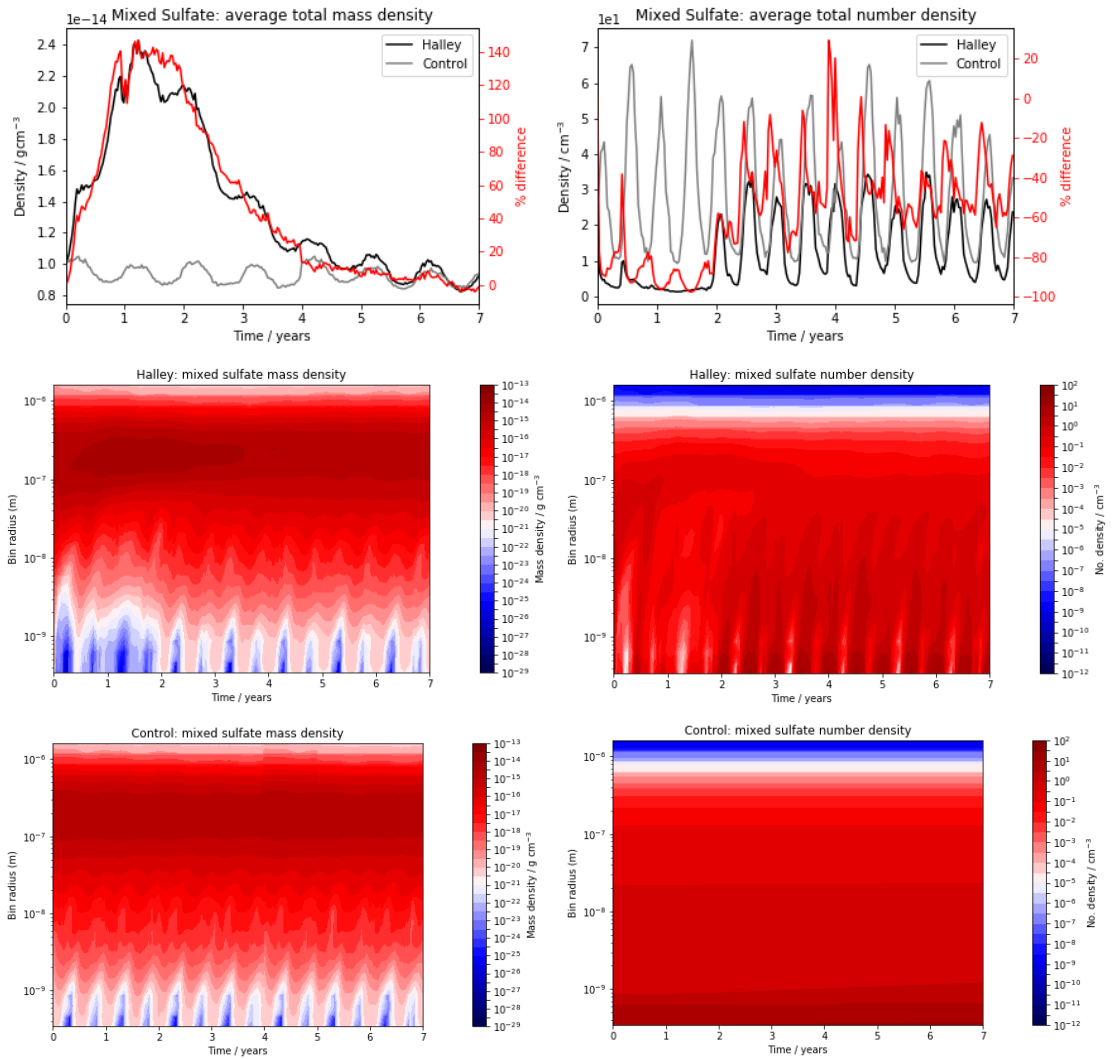
Figure 6.4. Top panels: the global-average mixed sulfate total mass density ($\times 10^{-14}$ g cm$^{-3}$, left panel) and number density ($\times 10^{-1}$ cm$^{-3}$, right panel). Middle panels: particle mass (left) and number (right) densities for run A$_s$ as a function of size (radius/ m) and of time (years). Bottom panels: particle mass (left) and number (right) densities (cm$^{-3}$) for run B$_s$ as a function of size (radius/ m) and time (years).

The global-average total number density of mixed sulfate is dramatically reduced in the first two years of run A$_s$ and does not fully recover by the end of the simulation (Figure 6.4, top right panel). In line with the changes seen for the mass density, inspection of the number density size distributions for the first two years (Figure 6.4, middle right and bottom right panels) shows a decrease in the number density of small particles in run A$_s$, and an increase in the number density of particles with sizes on the order of 100 nm. A pronounced semi-annual fluctuation is observed in the number density for run A$_s$, whereby two cycles of increasing/decreasing number density occur each year. This corresponds to a similar pattern seen in the mass density. The decreases in number density occur with the decreases in mass density, and *vice versa*. This is a result of increased particle growth (*via* reactions *g* to *k,* Table 6.1) as material is transported down the winter polar vortices. This concentrates the material into a smaller volume and the increased densities lead to higher coagulation rates [*Bardeen et al.*, 2008].

### 6.2.1.3  Pure sulfate

No marked changes can be seen in the global-average total mass or number densities for pure sulfate aerosol (Figure 6.5, top panels). However, looking at the size distributions some differences are evident, though these are small compared to the differences in the mixed sulfate particles. In run $B_s$ there is little variation in the particle mass densities with time, and the peak of the distribution lies at a radius of around 20-100 nm. In run $A_s$, a regular pattern of increased coagulation can be seen in each year of the simulation for both the mass and number densities (Figure 6.5, middle panels), which is timed with the coagulation observed for the mixed sulfate aerosol. An increase in the amount of pure sulfate aerosol resulting from increased uptake of $H_2SO_4$ (*c* and d, Table 6.1) will lead to additional aerosol growth (*e,* Table 6.1). However, these changes to the aerosol processes do not have a large effect on either the peak particle radius, or the average numbers of particles of each size, since the pure sulfate aerosol is dominated by material from terrestrial sources; the average number density of pure sulfate aerosol is ~30,000 $cm^{-3}$ compared to ~30 $cm^{-3}$ for mixed sulfate aerosol. Furthermore, since the increased formation of pure sulfate aerosol coincides with an increase in both MSPs and mixed sulfate, an increase in destructive processes is also observed, leading to the formation of mixed sulfate from pure sulfate aerosol (*h* and *k*, Table 6.1).
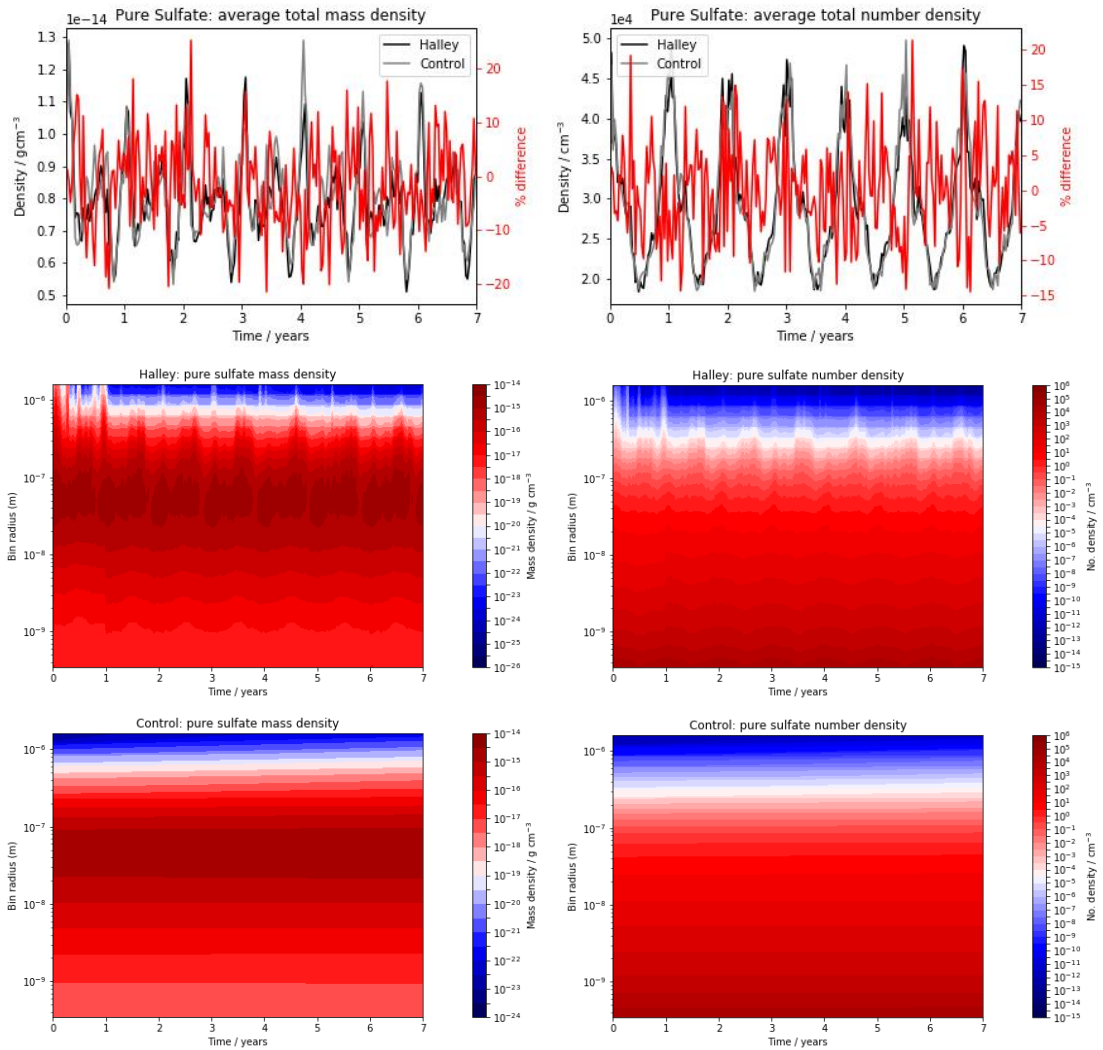
Figure 6.5. Top panels: the global-average pure sulfate total mass density ($\times 10^{-14}$ g cm$^{-3}$, left panel) and number density (cm$^{-3}$, right panel). Middle panels: particle mass (left) and number (right) densities for run A$_s$ as a function of size (radius/ m) and of time (years). Bottom panels: particle mass (left) and number (right) densities (cm$^{-3}$) for run B$_s$ as a function of size (radius/ m) and time (years).

## 6.2.2 Available Surface Area

The surface area density (SAD) defines the surface area available for homo- or heterogeneous reaction. Figure 6.6 shows the global average surface area density for MSPs, mixed sulfate and pure sulfate aerosol. For MSPs, a large increase in SAD is observed at the start of run A$_s$. The SAD then decreases, initially very rapidly, but with the rate of decay decreasing with time. The initial increase in SAD is a result of the injection of MSPs. Rapid coagulation then reduces the available surface area. The reduction in the coagulation rate, as the MSPs agglomerate to increasingly larger sizes, is reflected in the rate at which the SAD decays. With increasing time (decreasing altitude) an increasing amount of MSPs are converted into mixed sulfate aerosol, which will also reduce the coagulation rate of MSPs (and hence affect SAD).

An ~80 % increase in the SAD of mixed sulfate aerosol is observed, with the maximum increase observed after approximately 1 year. This increase in SAD occurs concurrently with the increase in mass density of the mixed sulfate. Typically, higher rates of coagulation lead to a reduction in SAD. However, the increase in SAD observed demonstrates that the increase in SAD resulting from additional formation of mixed sulfate (*g, h, j & k*, Table 6.1) dominates over any reduction in SAD from increased coagulation of mixed sulfate (*i*, Table 6.1). For pure sulfate aerosol, the SAD decreased by ~10-15 % in the first year of run $A_s$. Increased uptake of $H_2SO_4$ *via* reaction *c* (Table 6.1) leads to an increased amount of pure sulfate aerosol, which subsequently agglomerates to larger sizes. However, in contrast to the mixed sulfate, where the dramatic increase in MSPs leads to an increase in the mass and number density, this increase in MSPs causes additional destruction of pure sulfate *via* reaction *k*, Table 6.1.

An increase in aerosol SAD may have knock-on effects on gas phase chemistry as stratospheric aerosol can catalyse a number of heterogeneous reactions; although heterogeneous $NO_x$ chemistry was not included in the simulations in the present work, previous studies have shown using a variation of WACCM-CARMA that uptake of $HNO_3$ onto MSPs leads to periodic losses of over 80 % of $HNO_3$ across the winter hemisphere, and up to 60 % of $HO_2$ in the winter polar vortex below approximately 0.1 hPa (~65 km), with standard (background) aerosol concentrations [*Frankland et al.*, 2015; *James*, 2016]. These losses represent upper limits to the removal since the uptake of $H_2SO_4$ onto MSPs deactivates the MSP surfaces towards $HNO_3$ uptake, and this was not included in the model runs from these studies. Furthermore, there is still uncertainty in the uptake coefficients due to the lack of knowledge regarding the composition of MSPs. The uptake of $HNO_3$ has knock-on effects on other gaseous species, namely $NO_2$, $NO_3$, $N_2O_5$, OH and $HO_2$ since the chemistry of these species is interlinked [*James*, 2016]. Since in the Halley simulation the MSP density is dramatically elevated above typical ambient concentrations, it is likely that there will be a significant effect on stratospheric $NO_x$ and $HO_x$ in the mesosphere and upper stratosphere, with the greatest impact seen towards the start of the simulation.

The elevated SAD resulting from the high levels of MSPs and mixed sulfate aerosol could impact on the formation of polar stratospheric clouds in the winter polar vortex, leading to changes in $O_3$ as a result of heterogeneous chemistry and denitrification [*James et al.*, 2018]. If more PSCs are produced, this will activate chlorine radicals that themselves destroy $O_3$, by facilitating heterogeneous reactions (e.g. $ClNO_3 + H_2O \rightarrow HNO_3 + HOCl$) on the surfaces of cloud droplets. Furthermore, removing nitrates from the gas-phase - temporarily *via* condensation or permanently *via* sedimentation - prevents the destruction of radicals *via* the formation of the inactive $ClONO_2$ [*Solomon*, 1999; *Wegner et al.*, 2012]. Because the elevated SAD and smoke concentration in the sulfate aerosol last for around three years, this could be an important impact of the cometary flyby, and is an avenue for future research.
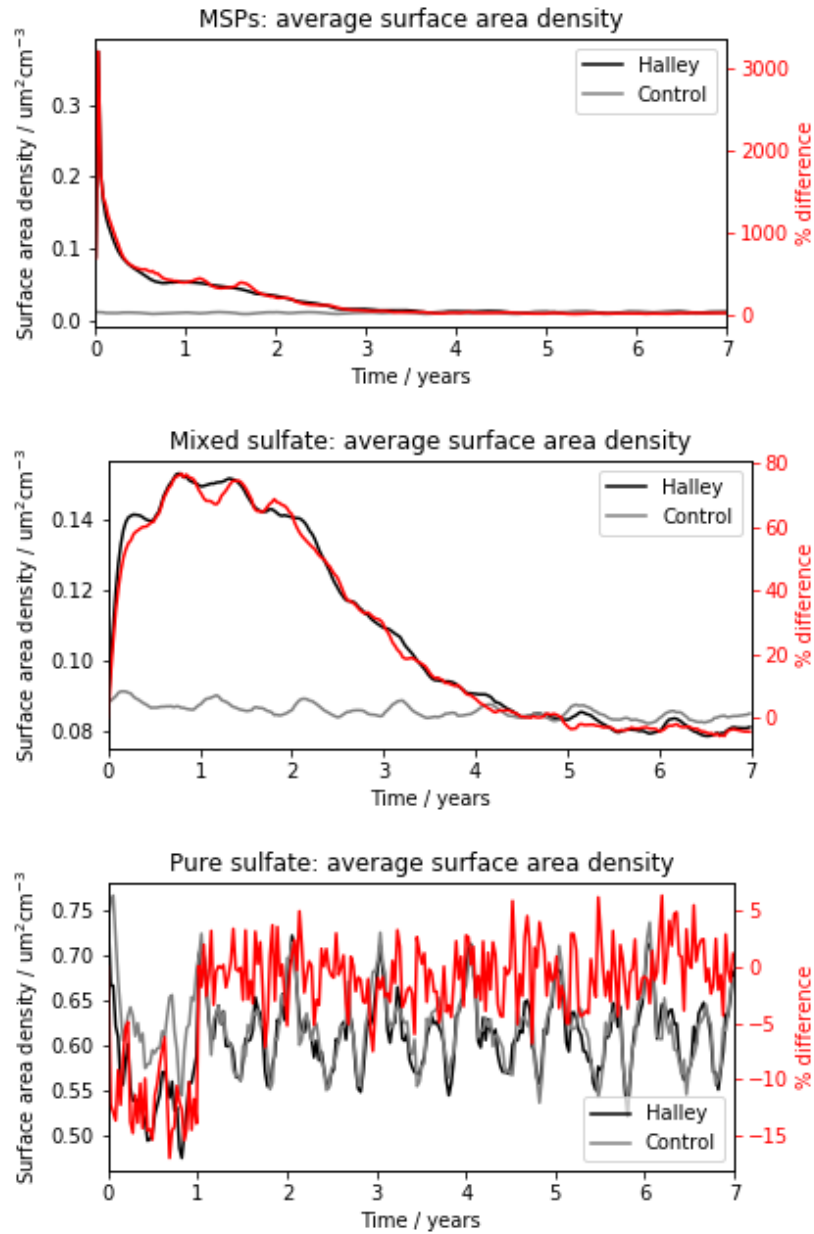
Figure 6.6. The global-average surface area density of MSPs (top panel), mixed sulfate (middle panel) and pure sulfate (bottom panel) for run $A_s$ (black) and $B_s$ (grey). Also shown is the percentage difference observed in run $A_s$ relative to that in run $B_s$ (red).

## 6.3 Deposition

### 6.3.1 Aerosol Deposition

There is a longstanding debate as to the cause of a severe and protracted global climate anomaly in A.D. 536-550. Although it is widely held that the 'mystery cloud' responsible for this global cooling is volcanic in origin [*Sigl et al.*, 2015], the case has also been made for an extra-terrestrial cause [*Abbott et al.*, 2014b; *Rigby et al.*, 2004]. As such, the surface deposition in the WACCM-CARMA runs was examined to assess whether the aerosol from the simulated close

encounter would be detectable against the background deposition of MSPs and sulfate aerosol. The total deposition ($d_{tot}$) over the 7 year simulations was therefore calculated for both model runs, $A_s$ and $B_s$ ($d_{tot}$ represents the total integrated deposition for mixed sulfate, pure sulfate and MSPs). Figure 6.7 shows the total deposition for run $A_s$ (top panel), where it can be seen that the highest levels of deposition occur at low to mid latitudes. This is because most stratosphere-troposphere exchange occurs along the mid-latitude storm tracks [*Brooke et al.*, 2017; *Lanci et al.*, 2012]. In WACCM-CARMA, two deposition mechanisms are employed: dry deposition, where material is deposited *via* sedimentation down a column, and wet deposition, where material is deposited in precipitation, either *via* in-cloud (nucleation) or *via* below-cloud (impaction) scavenging [*Brooke et al.*, 2017]. Wet deposition dominates over dry deposition, leading to the geographical variation in the deposition pattern [*Lanci et al.*, 2012].

Inspection of Figure 6.7 (middle and bottom panels) demonstrates that although the largest absolute differences occur at low to mid latitudes, these generally represent changes of less than ± 10 % from run $B_s$. The largest absolute increases in deposition are collocated adjacent to the largest decreases in deposition, suggesting these changes are simply due to differences in the precipitation patterns between the two free-running simulations. The largest relative differences in deposition occur at high latitudes, with increases of up to 40 % observed in both the northern and southern hemispheres. However, as the total deposition at high latitudes is significantly lower than at low and mid latitudes, these changes only represent a very small absolute change to the deposition.

A statistical t-test demonstrates that these high latitude fluctuations are not significant at the 95 % confidence level, relative to the typical variability seen over the 7 year period. For the total deposition in each year ($d_y$, where $y = 1 \dots 7$), the fraction of data points that have a t-value ($t$) greater than a critical t-value ($t_{crit}$) can be determined using equation E6.1, where $\bar{d}$ and $\sigma^2$ are the mean deposition and the variance respectively for run $B_s$, and $N_1$ and $N_2$ are the number of samples considered in the calculation for each simulation (1 and 7 for runs $A_s$ and $B_s$ respectively). The critical t-value of 2.447 is defined according to the chosen confidence limit (in this case, $2\sigma$, or 95 %). It can be seen from the example plot (Figure 6.8) showing the deposition map for year 3 in run $A_s$, where only data with $t > t_{crit}$ are shown, that only a very small number of data-points exceed this limit at high latitudes. This plot is representative of that for the other years in the simulation. In each year, although some data-points at low and mid latitudes do exceed this limit, as mentioned previously these represent relatively small changes which are likely to be due to the free-running configuration leading to changes in precipitation.
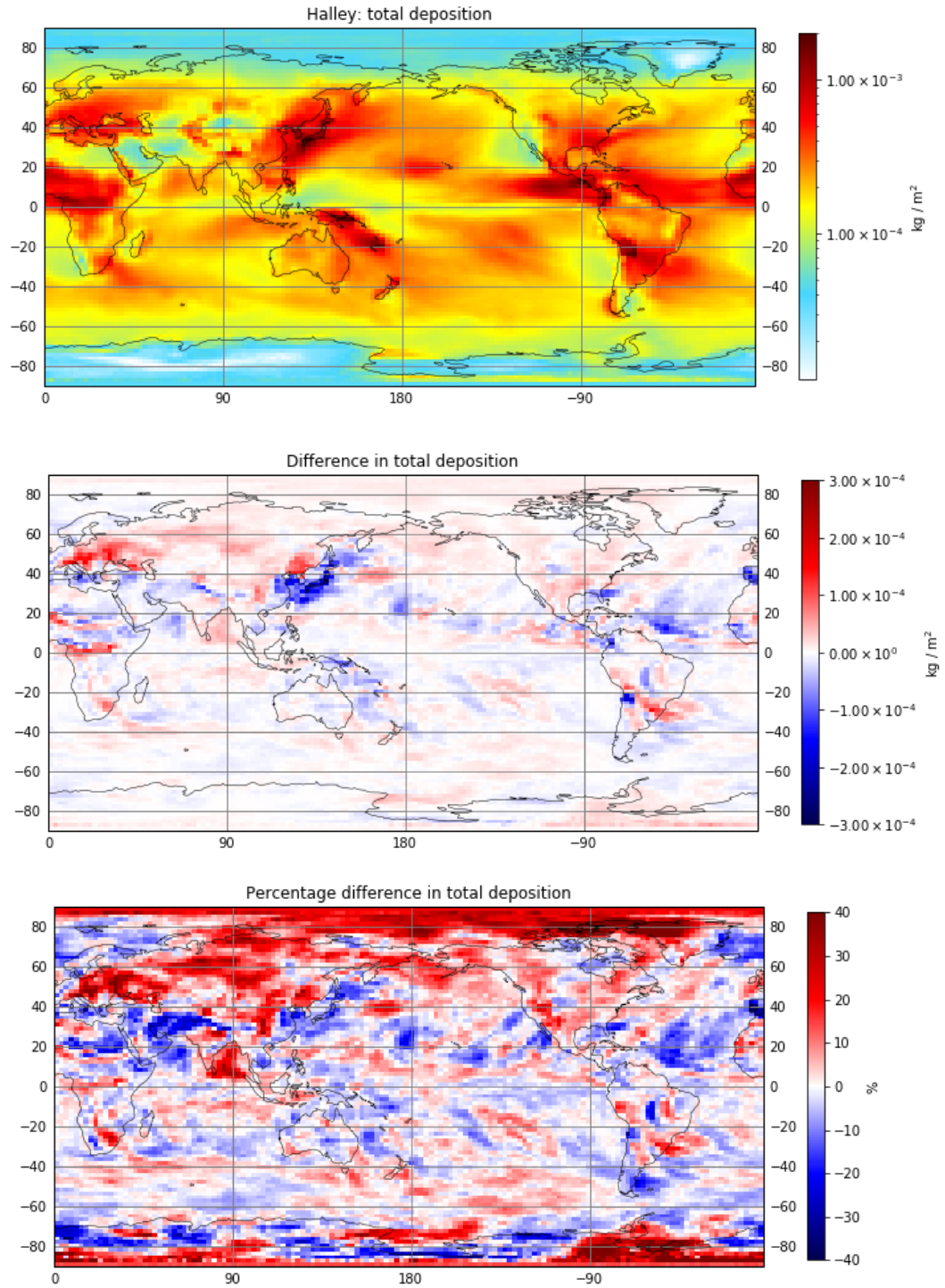
Figure 6.7. Top panel: The total deposition across the 7 year simulation for the Halley run ($A_s$). Middle panel: the difference in the total deposition between the Halley and control simulations ($A_s$ and $B_s$). Bottom panel: The percentage difference in the total deposition between the Halley and control simulations ($A_s$ and $B_s$).

E6.1
$$t = \frac{(d_y - \bar{d})}{\sqrt{\frac{\sigma^2}{N_1} + \frac{\sigma^2}{N_2}}}$$
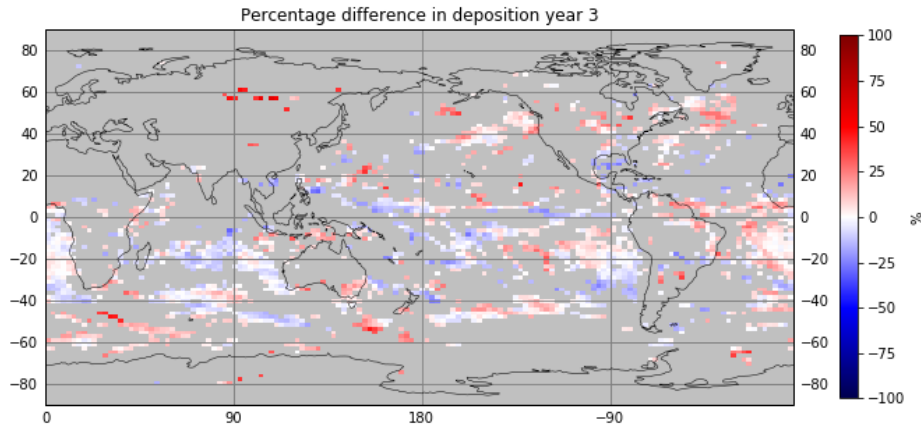
Figure 6.8. The percentage difference in the total deposition between the Halley and control simulations ($A_s$ and $B_s$), where grey areas indicate where $t < t_{crit}$, i.e. the data lies within $2\sigma$ variation for run $B_s$.


## 6.3.2 Sulfur Deposition

The total sulfate deposition rate resulting from the deposition of mixed sulfate aerosol can be calculated from that for the mixed sulfate aerosol ($d_{ms}$) minus that for the MSP cores ($d_c$). The sum of this and the deposition rate of sulfate from pure sulfate aerosol ($d_{ps}$) yields the total sulfate deposition rate ($d_{sf}$, equation E6.2), which can be converted into a S concentration (ppb) for comparison with the non sea-salt sulfur (nssS) deposition rates recorded in ice-cores. Two ice-cores have been chosen for this comparison: NEEM-2011-S1 in Greenland (77.45 °N, 51.06 °W, hereafter referred to as NEEM) and WDC (79.47 °S 112.09 °W) in Antarctica [*Sigl et al.*, 2015].

E6.2  $d_{sf} = (d_{ms} - d_c) + d_{ps}$

Upon inspection of the year to year deposition in the model runs at the two ice-core sites (Figure 6.9) a high degree of variability can be seen. As such, only a small number of points are significant at the 95% confidence interval (red data points). The required level of deposition to be deemed significant at this confidence level is indicated with purple dotted lines. In Antarctica, the deposition for the significant points is only marginally greater than this critical concentration, meaning it is unlikely that any deposition from the Halley encounter could be unambiguously detected against the background deposition in this Antarctic ice-core. However, for the Greenlandic ice-core, the deposition in years 1, 2 and 7 exceeds the critical concentration by a reasonable amount, with the deposition in year 2 being the most prominent.

## NEEM
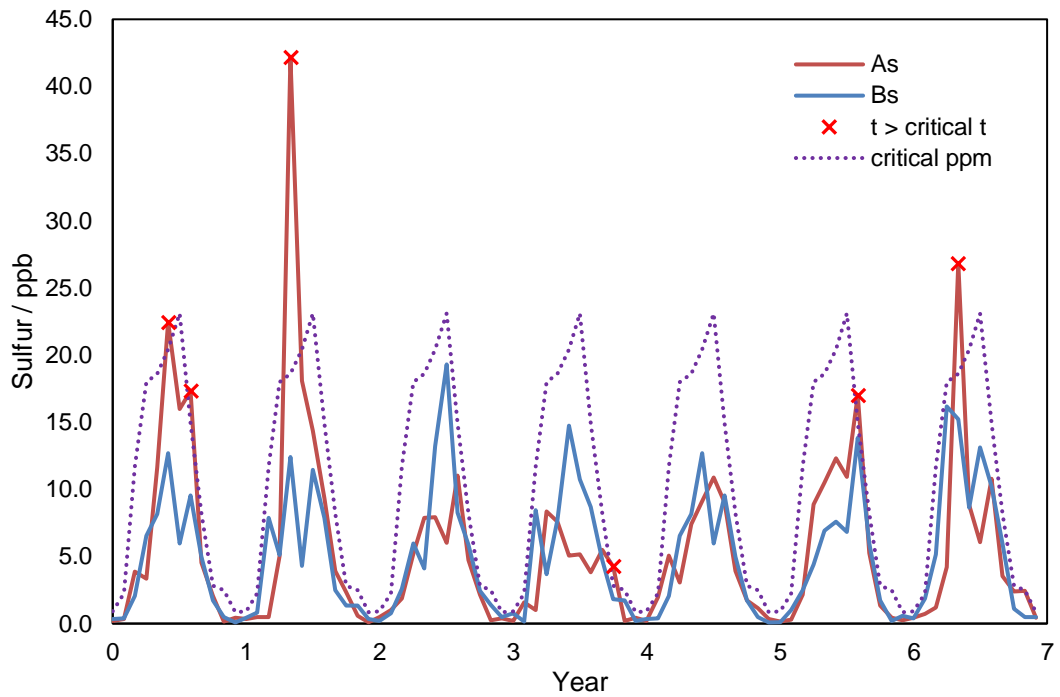


## WDC
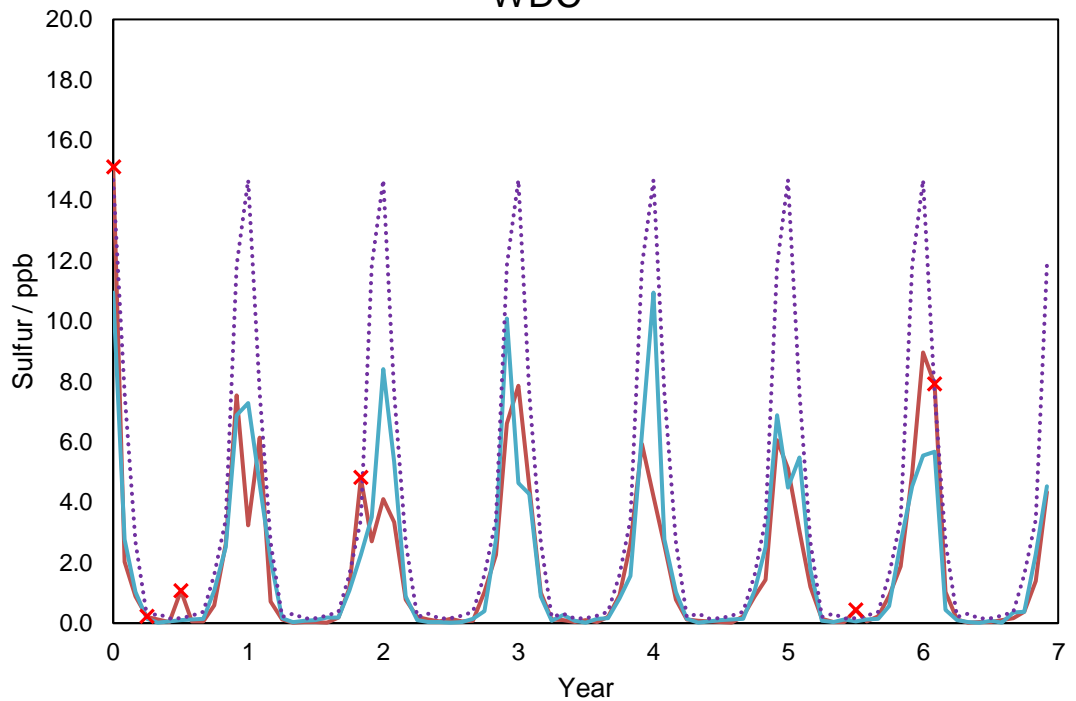
Figure 6.9. Calculated S deposition (ppb) from the Halley simulation ($A_s$, red) and the control simulation ($B_s$, blue) at the locations of the NEEM (top panel) and WDC (bottom panel) ice-cores. Data points from run $A_s$ that are deemed significant at the 95 % confidence level are indicated with red crosses. The concentration required to obtain a significant level of deposition is indicated with the purple dotted lines.

The measured deposition at the two ice-core sites is shown in Figure 6.10 (black lines). The lack of seasonality observed is a result of the deposited layers 'smearing out' over time, as they are compressed in the snow/firn, a process which is not captured in the model deposition. Weathering processes will also affect the amount of sulfur deposited in each year. To make a comparison between the modelled and observed deposition, the model data (from Figure 6.9) was averaged to obtain the yearly average deposition. The data were also arbitrarily transposed such that they began in the year A.D. 536. In general, the nssS deposition in the model runs agrees reasonably well with the baseline deposition in the ice-core record (years 530-535). However, the model underestimates the recorded deposition (more so in the WDC ice-core). This is to be expected, since WACCM-CARMA is known to underestimate MSP deposition, particularly at high latitudes [*Brooke et al.*, 2017]. As such, the modelled deposition was scaled by factors of 2.5 and 6.5 at NEEM and WDC respectively, such that the measured baseline deposition is well represented by the model data.
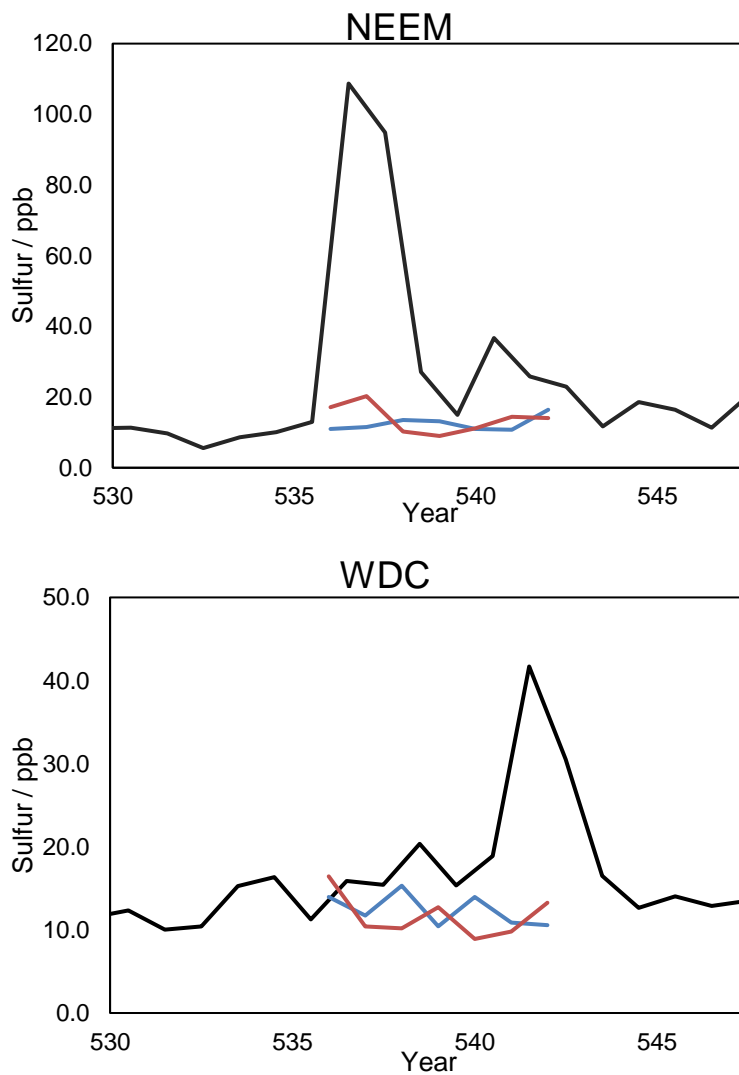


Figure 6.10. Yearly average S deposition (ppb) from the Halley simulation (A$_s$, red) and the control simulation (B$_s$, blue) compared to nssS measurements (black) from the NEEM (top panel) WDC (bottom panel) ice-cores. Model data from the NEEM and WDC ice-cores has been scaled by factors of 2.5 and 6.5 respectively. Ice-core deposition data obtained from *Sigl et al.* [2015].

In order to quantify the cometary S deposition at each location, in each year, the difference in yearly average deposition between runs $A_s$ and $B_s$ was compared to the peak deposition in the ice-core record – for NEEM, this was 108.7 ppb and 36.6 ppb in the years 536 and 540 AD respectively. For WDC this was 41.7 ppb in the year 541 AD (see Figure 6.10). In this manner, the relative (percentage) contribution of the Halley S to the peak recorded deposition was established (see Table 6.2). This analysis demonstrates that the simulated encounter could have contributed up to $8.0 \pm 4.6$ % and $23.6 \pm 13.6$ % to the 536 AD and 540 AD peaks in the NEEM ice-core record. For WDC, the maximum contribution was $6.6 \pm 8.2$ %. As mentioned before, this means that it would be unlikely that any anomalous S deposition from the simulated encounter could be unambiguously detected in the Antarctic ice-core. However, it is possible that the additional S deposition would be measurable in Greenland.

Table 6.2. The relative contribution of the cosmic S to the peak deposition in the NEEM and WDC ice-core records for the years indicated. Negative percentages indicate that the deposition decreased in the Halley run relative to the control run. The maximum contribution to the deposition for each ice-core is indicated in bold.

| Year | NEEM: percentage of 536 AD ice-core deposition | NEEM: percentage of 540 AD ice-core deposition | WDC: percentage of 541 AD ice-core deposition |
|---|---|---|---|
| 536 | 5.6 | 16.7 | 5.9 |
| 537 | **8.0** | **23.6** | -3.1 |
| 538 | -3.0 | -8.9 | -12.3 |
| 539 | -3.9 | -11.6 | 5.5 |
| 540 | 0.2 | 0.5 | -12.2 |
| 541 | 3.4 | 10.2 | -2.6 |
| 542 | -2.1 | -6.2 | **6.6** |

Given the scarce historical records from this time period, it is possible that a close encounter event could have occurred without being documented (or without any records being found) – for example, if the deposition was centred over the western or southern hemisphere eg. North/South America, Africa, Australasia or Antarctica. In the western hemisphere, no recorded observations of meteor showers have been found from any pre-Hispanic civilization, though the ancient Maya civilisation clearly had the capacity to record such events; information regarding Venus, solar and lunar eclipses and seasonal cycles has been found in the few remaining ancient books not destroyed by the Spanish after their arrival into Maya territory in the 16th century [*Kinsman and Asher*, 2017]. It therefore cannot be ruled out that a close cometary encounter could have contributed to the observed sulfate deposition in the 6th century, though it is unlikely that such an event would be the sole cause.

Further investigation is required to determine the radiative effects of a cometary dust-loading in the atmosphere, and whether such an event could have contributed to the dark skies or temperature decreases observed in the 6th century. Though there may not have been any observable deposition after such an event, it is possible that the additional meteoric dust injected during a close encounter

could have exacerbated the climatic effects from volcanic eruptions during this time period. It could be that such an event may account for the difficulties in reproducing the observed temperature anomalies with recent volcanic forcing reconstructions *Toohey et al.* [2016].

## 6.4 Conclusions

21,700 tons of meteoric sulfur were injected into WACCM-CARMA at altitudes above approximately 110 km across a time period of 2 hours. Rapid oxidation of the S to SO was then observed. Slower oxidation to $SO_2$ and $SO_3$ followed, leading to the maximum density increases for these species being observed after ~ 6 months at altitudes of between about 40 and 45 km. A 70% decrease in $H_2SO_4$ density was observed, centred at ~35 - 45 km, extending upwards to 55 km. This was a result of increased uptake on MSPs to form SSA. A result of this and the interconversion of gas phase S species caused corresponding decreases in $HSO_3$, $SO_3$ and $SO_2$ at a similar altitude.

401,000 tons of MSPs were also injected to the model, over the course of 1 week. Inspection of aerosol size distributions showed that a rapid increase in the global average mass density of MSPs was observed. The mass density then decreased at a steady rate, returning to approximately baseline levels after 3-4 years. In contrast, a ~60 % drop in the global average MSP number density was observed, as a result of rapid coagulation of particles. After this initial decrease no significant differences were observed compared to the baseline run $B_s$. Increased coagulation of particles was demonstrated in the mass and number size distributions for the MSPs which both showed an increased population of large particles and a decreased population of small particles following the Halley injection.

Mixed sulfate aerosol also exhibited an increase in the global average mass density, which peaked in the second year of the simulation and took 6-7 years to return to baseline levels. The delay in the peak of the mixed sulfate mass density relative to that for MSPs is due to the time required to both chemically produce $H_2SO_4$ from injected S, and to transport the relevant species to lower altitudes where the uptake to MSPs proceeded at a faster rate. Significantly increased coagulation was observed in the first 3 years, as demonstrated by a decrease of ~90 % in the global average number density and a decrease in the population of small particles compared to the baseline run (and *vice versa* for large particles). A decreased population of small particles was also observed in the mass density size distribution. However, the peak of the distribution was not shifted to larger sizes, showing instead an increased population of particles at comparable sizes to the peak of the distribution in the baseline run. This indicates that the formation of large mixed sulfate particles is limited by the availability of the precursor species (MSPs, pure sulfate or gas phase $H_2SO_4$) and aerosol sedimentation rates.

Though there were no significant changes to the global average mass or number densities for pure sulfate aerosol, regular patterns of increased coagulation were observed each year, timed with that seen for the mixed sulfate aerosol. However, this did not cause any significant changes to the overall mass or number size distributions, since the increase in pure sulfate aerosol from increased uptake of $H_2SO_4$ is countered by increased formation of mixed sulfate aerosol by reaction with MSPs or mixed sulfate particles. Furthermore, the number density of pure sulfate is significantly higher than that of MSPs or mixed sulfate and it is dominated by aerosol from terrestrial sources. Any changes resulting from the meteoric injection were therefore masked by this aerosol.

A rapid increase in MSP SAD was observed after the Halley injection, with the SAD then decreasing with time as it was reduced by particle coagulation. The SAD returned to baseline levels after 3-4 years. For mixed sulfate, an ~80 % increase in SAD was observed, peaking around a year after the injection. Though coagulation was also observed for mixed sulfate particles, the dominant effect was an increase in SAD due to increased aerosol formation (from MSPs and pure sulfate aerosol). For pure sulfate, though an increase in the uptake of $H_2SO_4$ would be expected to increase the SAD, the high concentrations of MSPs leads to increased mixed sulfate formation, and thus a decrease in SAD of 10-15 % was observed. The effects on SAD are likely to have implications for the uptake of gas-phase species such as $HNO_3$, $HO_2$ and the formation of polar stratospheric clouds – with potentially serious implications for $O_3$ depletion. These effects have not been investigated further in this study because a parameterization of the role of MSP/mixed sulfate particles in freezing PSCs is not available, although this is being determined in a current project at the University of Leeds.

The deposition pattern of aerosols was investigated to determine whether any record of the cometary flyby would be observable in ice-cores. The largest absolute total deposition was observed in mid-latitudes as a result of stratosphere-troposphere exchange and wet deposition. The most significant differences from the baseline run were collocated with this strong deposition in the Halley run, suggesting this was merely a result of changes in precipitation between the two free-running simulations. The largest relative increase in deposition (~ 40 %) was located at the poles, though these changes were not deemed significant at the 95 % confidence level, since there was a high degree of variability in the total annual deposition at high latitudes.

The total sulfur deposition in the WACCM simulations (originating from both pure and mixed sulfate aerosols) was calculated across the 7 years after the Halley injection. No significant increase was observed in the modelled S deposition at the location of the Antarctic ice-core site. However, an increase in deposition was observed at the NEEM Greenlandic ice-core after the Halley encounter, with the maximum effect occurring in the second year after the injection. Analysis of the yearly average deposition at the NEEM ice-core site indicated that the simulated encounter could have contributed up to $8.0 \pm 4.6$ % and $23.6 \pm 13.6$ % to the peak deposition in 536 AD and 540 AD respectively. At WDC, the maximum possible contribution to the deposition in 540 AD was $6.6 \pm 8.2$ %.

Due to the high degree of variability in such events, the simulated cometary encounter is unlikely to be an accurate representation of any close encounter that may have occurred in the 6th century. Nonetheless, this result demonstrates that the possible implications of a cometary encounter on deposition are non-negligible, and that a cometary dust-loading event could have contributed towards the anomalous S deposits recorded in the 6th century ice-cores. Further investigation is required to quantify possible encounter scenarios, and to quantify any radiative effects that the cometary material may have in the atmosphere, compared to the effects of volcanic eruptions. However, an extra-terrestrial event of this nature could help to explain the anomalous climatic effects observed during the early 6th century.

# Chapter 7
# Conclusions and Future Work

Cometary material is implicated in a range of chemical and dynamical processes during its passage through the Earth's atmosphere. Chapter 1 of this thesis introduced our current understanding of these processes and identified the key role that meteoric smoke particles (MSPs) play in a number of these processes. The areas that were investigated in the rest of the thesis, using a combined experimental and modelling approach, were also presented. The laboratory techniques used to investigate the optical properties of iron oxide MSP analogues were set out in chapter 2, and results from the two experimental systems used - the PAFS and the MICE/TRAPS – were discussed in chapter 3. Chapter 4 presented details of the modelling approach used to simulate a close encounter with Halley's comet at a closest-approach distance of 100,000 km. Two different model configurations were used, to simulate various effects on the upper and middle atmospheres respectively, with the latter also probing the effects on surface deposition. The results from these simulations were discussed in chapters 5 and 6. More details regarding the conclusions of each chapter are presented below, including recommendations for future work to further the findings of this study.

## 7.1 Laboratory Studies: The Optical Properties of Iron Oxide Meteoric Smoke Analogues

### 7.1.1 Conclusions

Iron oxide MSP analogues were produced using two laboratory techniques: the PAFS and the MICE/TRAPS. In the PAFS, particles were produced photochemically from neutral gas at ambient pressures whereas in the MICE/TRAPS, singly charged nanoparticles were produced in a low-pressure microwave plasma. The PAFS particles were poorly crystalline agglomerates having sizes that ranged from a few nanometres to a few microns, composed of a number of primary spheres with an average radius of $1.65 \pm 0.15$ nm. The MICE/TRAPS particles were spherical and crystalline, with radii of 1-3 nm. Microscopic analysis of particles collected from both systems suggested the most likely composition to be maghemite, despite the different production mechanisms used in each experiment. Comparison to literature EEL spectra showed good agreement with maghemite or magnetite literature data; for PAFS particles this was corroborated by the electron diffraction pattern which showed the intense reflections expected from a spinel crystal structure. The MICE/TRAPS particles exhibited a Fe:O ratio of 2:3, confirming the maghemite composition. Problems with elemental quantification for the PAFS particles due to contamination from Cu fluorescence meant that an exact Fe:O ratio could not be established, though previous work using comparable conditions produced particles with a Fe:O

ratio of 2:3. The presence of additional oxygen in the sample was observed upon comparison of the EDX spectrum to that for a maghemite standard. This could be a result of contamination from an unidentified oxygen-rich hydrocarbon, surface oxidation or incomplete formation from $FeO_3$.

The optical extinction of nanoparticles was measured with the PAFS at wavelengths of 330-550 nm. An approximately exponential increase in OD was observed with decreasing wavelength across this range. An analysis using Mie theory and the RDG approximation was performed to determine the most likely particle composition from available literature RI data for iron oxide particles. Using the measured size distribution, neither level of theory was able to reproduce the measured data. However, when using a reduced primary particle concentration, the RDG approximation was able to generate a good fit to the experimental data using hematite RIs. Although no maghemite RIs were available, scaled absorbance data from maghemite particles was also able to generate a good fit to the measured OD. The optical absorption of particles was measured using the MICE/TRAPS at 405 nm, 488 nm and 660 nm. An increase in absorption efficiency was observed with increasing particle radius and decreasing wavelength. Analysis with Mie theory using the average literature RIs for hematite gave a reasonable fit to the measured data, though data from different sources resulted in a wide range of $Q_{abs}$ values.

An iterative model was developed to derive complex RIs for the MSP analogues. This model was used first to establish a range of best-fit RIs for the absorption data at 405 nm, 488 nm and 660 nm. Optimisation of a best-fit primary particle concentration for the extinction data was then possible, by neglecting the scattering component of the extinction. Using this primary particle concentration, the best-fit RIs at 405 nm and 488 nm were adjusted iteratively to deduce the best-match to the measured data for both experiments. Lastly, wavelength-dependent complex RIs were derived by prescribing the wavelength-dependence of the real RIs using those for hematite particles. The imaginary RIs were then generated in the wavelength range 350 – 660 nm by fitting an exponential decay through the corresponding best-fit imaginary RIs at 405 nm, 488 nm and 660 nm. The results obtained from this study support the notion that amorphous MSPs can be represented with the RIs of crystalline particles, when using the RDG approximation rather than Mie theory to calculate the OD. Nonetheless, more work is required to extend the wavelength range of the derived maghemite RIs to cover the appropriate wavelengths used for the characterisation of MSPs in the atmosphere.

### 7.1.2  Future work

Through the experiments performed with the MICE/TRAPS and PAFS, maghemite has been shown to be a potentially important candidate species for atmospheric MSPs, highlighting the need for further studies probing the formation, agglomeration and optical properties of this iron oxide conformer in this context. Accordingly, the studies performed with both systems could be extended for this purpose. For the MICE/TRAPS, both additional measurements at the three

wavelengths already studied, and further experiments at different wavelengths throughout the UV, visible and IR spectral regions would be particularly useful. The latter of these experiments would help constrain the RIs derived using the photochemical model by reducing the degrees of freedom when fitting the imaginary RI.

Additional experiments with the PAFS would also be of value. Firstly, repeat measurements would aid in reducing the experimental uncertainties. Secondly, additional experiments extending the measurements into the UV and IR would augment the usefulness of the optical parameters derived for the particles. Furthermore, additional analysis with TEM, EELS and EDX would help constrain the particle composition, aiding with 1) establishing a definitive Fe:O ratio for the particles, 2) establishing the source of any additional oxidation that may be present within the particles and 3) constraining the particle size distribution, for example determining the fractal dimension ($D_f$) of the agglomerates (a measure of the space-filling properties of particles). The latter of these points would be relevant for atmospheric MSP characterisation since a knowledge of the 3-D $D_f$ value would help to establish a primary particle concentration to be used in optical calculations.

With respect to the first two points, it is important to determine whether the additional oxidation present in the samples was a result of external contamination or if it was present within the particles, i.e. whether this is a repeatable phenomenon resulting from the formation mechanism, and if so whether this process is likely to occur for atmospheric MSPs. It is possible that particle oxidation could have led to the formation of a core-shell structure. This possibility could be assessed using EDX mapping techniques, though these are typically used for much thicker particles (~100 nm) than those in this study (~10 nm) and as such, the signal may be too weak to generate usable data. The difficulties encountered with the elemental quantification could be a result of the software used (Brucker) as quantification packages make certain assumptions regarding the nature of the material to be quantified. Quantification using alternative software packages (e.g. Velox) could therefore be attempted to assess any errors incurred in this manner.

Once the optical properties of iron oxide particles have been satisfactorily analysed, both the techniques employed in this study could be extended to other particle compositions, such as iron, magnesium or mixed silicates. Additionally, for the PAFS, the effects of changing the flow conditions on particle composition and morphology could be assessed, since characterisation efforts in the atmosphere demonstrate a possible relation between particle size (i.e. particles analysed from different pressures) and changes to the optical extinction [*Hervig et al.*, 2017].

## 7.2   Modelling studies

This thesis represents a significant advance in knowledge regarding the possible outcomes of a cometary flyby past the terrestrial atmosphere, since to the authors knowledge it represents the

first and only study of its kind. This work provides an overview of the important and interesting effects of such an encounter, providing a general base upon which to develop interesting avenues for future research. Whilst the effects of the simulated encounter on the upper and middle atmosphere have been presented in a quantitative manner, if these results are to be extended to other cometary encounters the conclusions should be interpreted qualitatively, due to the high degree of variability in the parameters used to define various aspects of the encounter and gaps in the current knowledge regarding the processes likely to be involved.

To simulate the Halley encounter, a MIF defining the amount and distribution of material entering the Earth's atmosphere was developed for several meteoric species: Fe, Mg, Na, Si, $Fe^+$, $Mg^+$, $Na^+$, $Si^+$, $e^-$, S and MSPs. First, a dust flux was derived using the model of *Moorhead et al.* [2014] – designed for assessing the risk posed to spacecraft during the Siding Spring encounter and calibrated against the dust flux experienced by Giotto during its encounter with Halley's comet. This flux was then used in a chemical ablation model (CABMOD) to predict the vertical distribution of meteoric metals resulting from the atmospheric entry of the 401,000 tons of cometary material. The S MIF was calculated based upon the expected distribution of Na, as per *Gómez Martín et al.* [2017], and that of MSPs was based upon the total fluence of material, assuming complete conversion of the ablated material to MSPs. These Halley MIFs were then implemented in a number of simulations with the global climate model WACCM. Two different model configurations were used: WACCM 1.06 and WACCM-CARMA. The former of these probed the effects of the injection of Fe, Mg, Na, Si, $Fe^+$, $Mg^+$, $Na^+$, $Si^+$ and $e^-$ on the upper atmosphere, and additionally the effects of an added heating tendency. The latter of these investigated the effects of the injection of S and MSPs on the middle atmosphere, and any effects on surface deposition.

### 7.2.1   Cometary Impacts on the Upper Atmosphere

### 7.2.1.1   Conclusions

Four sensitivity simulations were performed using WACCM to investigate the effects of both a chemical and dynamical perturbation on the MLT. The chemical perturbation comprised the metal injection discussed above. The dynamical perturbation was calculated using the MIF for the meteoric metals, assuming all of the kinetic energy contained in the incoming material was dissipated as heat in the atmosphere, accounting for the energy consumed in phase transitions. The total energy input (J $cm^{-3}$ $s^{-1}$) as a function of time and altitude was calculated and used to derive an atmospheric heating rate (K $s^{-1}$). The chemical and dynamical perturbations were implemented in separate simulations (runs C and D respectively) before investigating the combined effects (run A). A background simulation (run B) was also performed.

The chemical perturbation produced a $\sim 10^5$ increase in the global-average total column densities of Fe, Mg, Na and Si species. A corresponding increase in removal processes (dimerization) was observed, as a result of the increased metal densities. The Fe, Mg and Na decayed over approximately 6-7 months. However, the removal of Si proceeded significantly faster, forming the stable $Si(OH)_4$, decaying back to baseline levels after $\sim$ 2 months. The chemical perturbation produced significant changes to the residual meridional circulation, inducing a net thermospheric transport from the winter to summer pole (at $\sim$100-110 km). This produced a maximum in the metal densities in the summer hemisphere, in contrast to the typical distributions observed for Fe, Mg and Na. After $\sim$ 2 weeks, an additional circulation developed from the summer to winter pole that served to re-establish atmospheric equilibrium, transporting material along the mixing ratio gradient back towards the northern hemisphere. Though a significant temperature increase was observed in run D, no notable changes to the meridional circulation were observed.

Changes to the densities of O and $O_3$ were observed as a result of both the chemical and dynamical perturbations. In runs A and C, a net removal of both these species resulted from the interconversion of the neutral and ionic metals and their respective oxides; the increased metal densities led to decreases of $\sim$19 % and 34 % ($\sim$17 % and 30 %) in the global-average column densities of O and $O_3$ respectively for run A (run C). The additional depletion in run A was due to a decrease in the pressure-dependent recombination of O and $O_2$ which led to an increase in the $O/O_3$ ratio. In run A, this destruction represented decreases of up to $\sim$30 % and 100 % in the global-average densities of O and $O_3$ respectively, at altitudes of $\sim$85-115 km. For both O and $O_3$, a density increase was also observed at $\sim$80 km due to a decrease in the rate of the pressure-dependent recombination of O and $O_3$, which has a strong temperature dependence.

A net destruction of H and $H_2O$ was also observed as a result of the increased metal densities following the chemical perturbation; decreases in the global-average column densities of up to 78 % and 36 % (68 % and 25 %) respectively were observed in run A (run C). The changes in both runs A and C resulted from the formation and destruction of metal hydroxides, and above $\sim$80 km, these constituted up to 100 % removal of both species. All but one of the metal reactions involving H consume this species, and although $H_2O$ is reformed by a couple of these reactions, a net destruction is still observed, as the depletion of H means these reactions proceed slowly.

The dynamical perturbation added to run D led to an increase in the global-average temperature of $\sim$180 K (at $\sim$110 km), which decayed away over around 5 days. The chemical perturbation also induced changes to the temperature, with decreases of $\sim$6-9 % (up to $\sim$12 K and $\sim$38 K) centred at $\sim$90 km and 125 km respectively, that lasted for around 3-4 months. The depletion of $O_x$ and $HO_x$ led to corresponding decreases in the rates of ambient reactions, with feedbacks on both the metal chemistry and the densities of these species. This decrease in reaction rates led to a reduction in chemical (and photochemical) heating rates, resulting in the temperature changes observed (the effects on temperature were slightly greater and more prolonged in run A than run C). The inclusion of chemical heating rates for the metal reactions leads to differences in the

magnitude and duration of these effects, though the only significant effects were on the temperature (i.e. chemical heating rates) and the O density. The omission of these heating rates therefore does not significantly affect the conclusions of this study.

### 7.2.1.2   Future Work

Future work regarding the upper atmosphere should begin with the current simulations. For example, changes to the densities of minor species, and changes to transport and mixing could be investigated further to solidify the understanding of the processes affected by the perturbations. Additionally, possible effects on radio transmission resulting from the increased electron density could be explored, deriving the 'critical frequency' of radiation that would be able to penetrate through the enhanced layer of plasma in the MLT. Additional simulations could also be performed to model the Halley encounter. In the first instance, the test simulation including the reaction enthalpies for the metal reactions should be extended, in order to accurately gauge the effects of the encounter. The other runs (B, C and D) should also be repeated with these processes included. The effects of changing the deposition hemisphere could also be explored – for example, injecting the material in the winter or summer hemisphere, or injecting the material at different times of year, etc.

The MIF could also be extended to other meteoric species, such as including an injection of $H_2O$; though all of the $H_2O$ contained within interplanetary dust particles is expected to have evaporated at 1 au, a significant fraction of $H_2O$ may remain trapped within fresh cometary dust particles. For the simulated encounter with Halley's comet, any O injected in this manner is unlikely to have a significant effect on the atmosphere, since this would represent <1 % of the typical atmospheric O density. However, the injected H would represent approximately 20 % of the ambient H density in the altitude range over which ablation occurs, and therefore may be more significant. Other encounter scenarios could also be explored, changing various parameters such as: the closest approach distance; the comet encountered, i.e. the dust density and coma radius; or the nature of the orbit, i.e. the entry speed, angle, etc.

### 7.2.2   Cometary Impacts on the Middle Atmosphere and Surface Deposition

### 7.2.2.1   Conclusions

Halley MIFs for meteoric S and MSPs were injected into WACCM-CARMA, over 2 hours and 1 week respectively. Significant increases in S species were observed, with the S sequentially oxidised to SO, $SO_2$ and $SO_3$. The maximum densities in the latter two species were observed after ~6 months at ~40 – 45 km. A ~70 % decrease in $H_2SO_4$ was observed, centred at ~35 – 45 km, as a result of increased uptake onto MSPs. Corresponding decreases in $HSO_3$, $SO_3$ and $SO_2$

were also observed, though these had smaller magnitudes. A rapid increase in the global average mass density of MSPs was observed after the injection, and this decayed back to background levels after 3-4 years. However, a ~60 % drop in the global average number density was observed as a result of rapid coagulation, though this effect was short-lived. The particle coagulation could be seen in the both the mass and number size distributions, which both exhibited an increased population of large particles and a decreased population of small particles after the injection.

An increase in the global average mass density was also observed for the mixed sulfate aerosol. However, the maximum density for this aerosol type was observed in the second year of the simulation, due to the time required to form and transport the relevant species to lower altitudes. As for the MSPs, increased coagulation was observed, as demonstrated by the aerosol size distributions. This led to a 90 % decrease in the global average number density that was more prolonged than that observed for the MSPs (~2 years). In contrast to the MSPs, the peak in the size distributions was not shifted to larger particles – the formation of large mixed sulfate particles is limited by the availability of the precursors and sedimentation velocities. There were no significant changes to the global average mass or number densities for pure sulfate. However, increased coagulation could be observed, coincident with that seen for the mixed sulfate. This coagulation did not lead to any significant changes to the overall size distributions, as the increased formation of pure sulfate is counteracted by more rapid formation of mixed sulfate aerosol. Furthermore, pure sulfate is dominated by aerosol from terrestrial sources.

A pronounced and rapid increase in MSP SAD (up to ~3000 %) was observed after the Halley injection that remained elevated for around 3-4 years. For mixed sulfate, around an ~80 % increase in the SAD was observed, with the maximum occurring after around a year. For pure sulfate, although increased uptake of $H_2SO_4$ would increase the SAD, the increased formation of mixed sulfate dominates, leading to a decrease in SAD of around 10-15 %. These changes to the SAD are likely to impact on the uptake of gas phase species such as $HNO_3$ and $HO_2$, and also affect the formation of polar stratospheric clouds, which could have potentially significant effects on $O_3$.

Upon inspection of the aerosol deposition pattern it could be seen that the strongest deposition occurred at mid-latitudes. Wet deposition dominated over dry deposition, with the differences between the Halley and baseline runs being a result of changes to precipitation patterns. The largest relative increase in deposition (~40 %) occurred at high latitudes, though these changes were not significant at the 95 % confidence level. The total S deposited from mixed and pure aerosol was compared with that recorded in two ice-cores: NEEM and WDC. At the WDC ice-core site (Antarctica), there was no pronounced deposition increase in the Halley run compared to the control run. However, at the NEEM ice-core site (Greenland), the additional S deposited from the Halley encounter could have contributed up to $8.0 \pm 4.6$ % and $23.6 \pm 13.6$ % to the deposition in the years 536 AD and 540 AD respectively. This result demonstrates it is possible that a dust-loading from a cometary close encounter could have contributed to the anomalous S

140

deposits from the early 6th century; the lack of historical records documenting such an event do not rule it out as such an exogenous event may not have been documented at the time, or if it was, records may have been lost. Further studies are required to quantify possible encounter scenarios and establish any radiative effects of the atmospheric aerosol. However, a close encounter event may help to explain the anomalous climatic effects observed during this time period.

### 7.2.2.2 Future Work

There is much that could still be probed in the current simulations. For example, investigating any zonal and meridional variation in the investigated parameters (the gas-phase concentrations, aerosol size distributions, and SAD). The current simulations (for both the middle and upper atmosphere) could also be adapted such as to investigate other encounter scenarios, or probe any differences observed upon changing the deposition hemisphere or timing of the event. With regard to the deposition, it may be advantageous to run an ensemble of simulations and use the average result in order to eliminate the pronounced variability observed between the two free running simulations. However, this may not be practical, since this would be very computationally expensive to do. One adaptation to the model runs simulating the Halley encounter that may be worthwhile is to include the explicit formation of MSPs from metal atoms. This would enable a more realistic assessment of the effects on gas-phase and aerosol chemistry since the simulations performed with the two model configurations could effectively be combined. As such, any effects on the chemistry or dynamics of the middle atmosphere that are initiated by the chemical or dynamical perturbations in the upper atmosphere could be assessed. Work to include the explicit formation of MSPs into WACCM has already been started. However, a rigorous testing of this methodology has not yet been performed.

As discussed previously, future work relating to the aerosol model runs should aim to investigate the effects of the uptake and reaction of gas-phase species such as $HNO_3$, $HO_2$ and additionally HCl, by inclusion of the relevant heterogeneous processes in the model simulations. It would be preferable to perform these simulations once appropriate uptake coefficients have been definitively established. However, approximations for these parameters are available based on observations and experimental work, which could be used until this point. Any corresponding effects on $O_3$ resulting from changes to gas-phase chemistry could therefore be quantified. Once appropriate parametrisations for the formation and activity of PSCs have been established, any additional effects on $O_3$ through interactions on solid particles and denitrification could also be determined. Investigating the radiative properties of the cometary aerosol is another avenue for future research. Any changes to the radiative forcing of the atmosphere, either directly (*via* interaction of the aerosols with light) or indirectly (through influencing cloud properties or the $O_3$ concentration) should be determined. This analysis could be performed online in WACCM, or

offline using the current model data. Alternatively, a dedicated radiative forcing model could be employed for this purpose.

# References

A'Hearn, M. F., et al. (2005), Deep Impact: Excavating Comet Tempel 1, *Science*, *310*(5746), 258.

A'Hearn, M. F., et al. (2011), EPOXI at Comet Hartley 2, *Science*, *332*(6036), 1396.

Abbott, D. H., D. Breger, P. E. Biscaye, and R. A. Juhl (2014a), Calendar-year dating of the Greenland Ice Sheet Project 2 (GISP2) ice core from the early sixth century using historical, ion, and particulate data, *Geological Society of America Special Papers*, *505*, 411-420.

Abbott, D. H., D. Breger, P. E. Biscaye, R. A. Juhl, and P. McCafferty (2014b), What caused terrestrial dust loading and climate downturns between A.D. 533 and 540?, *The Geological Society of America*, *505*, 421-437.

Alvarez, L. W., W. Alvarez, F. Asaro, and H. V. Michel (1980), Extraterrestrial Cause for the Cretaceous-Tertiary Extinction, *208*(4448), 1095-1108.

Andrews, D. G., J. R. Holton, and C. B. Leovy (1987), *Middle atmosphere dynamics*, Academic Press, Orlando.

Arijs, E., D. Nevejans, J. Ingels, and P. Frederick (1983), Negative-Ion Composition and Sulfuric-Acid Vapor in the Upper-Stratosphere, *Planetary and Space Science*, *31*(12), 1459-1464.

Arijs, E., D. Nevejans, J. Ingels, and P. Frederick (1985), Recent Stratospheric Negative-Ion Composition Measurements between 22 km and 45 km Altitude, *J Geophys Res-Atmos*, *90*(4), 5891-5896.

Asmus, H., H. Wilms, B. Strelnikov, and M. Rapp (2014), On the heterogeneous nucleation of mesospheric ice on meteoric smoke particles: Microphysical modeling, *J. Atmos Sol-Terr Phy*, *118*, 180-189.

Atkinson, R., D. L. Baulch, R. A. Cox, J. N. Crowley, R. F. Hampson, R. G. Hynes, M. E. Jenkin, M. J. Rossi, and J. Troe (2004), Evaluated kinetic and photochemical data for atmospheric chemistry: Volume I - gas phase reactions of $O_x$, $HO_x$, $NO_x$ and $SO_x$ species, *Atmos. Chem. Phys.*, *4*(6), 1461-1738.

Babadzhanov, P. B., I. P. Williams, and G. I. Kokhirova (2008), Near-earth objects in the taurid complex, *Mon Not R Astron Soc*, *386*(3), 1436-1442.

Bailey, M. E., V. Clube, and W. M. Napier (1990), *The origin of comets*, Pergamon.

Baillie, M. G. L. (2007), The case for significant numbers of extraterrestrial impacts through the late Holocene, *Journal of Quaternary Science*, *22*(2), 101-109.

Baillie, M. G. L., and J. McAneney (2015), Tree ring effects and ice core acidities clarify the volcanic record of the first millennium, *Clim Past*, *11*(1), 105-114.

Bardeen, C. G., O. B. Toon, E. J. Jensen, D. R. Marsh, and V. L. Harvey (2008), Numerical simulations of the three-dimensional distribution of meteoric dust in the mesosphere and upper stratosphere, *J Geophys Res-Atmos*, *113*(D17).

Bardyn, A., et al. (2017), Carbon-rich dust in comet 67P/Churyumov-Gerasimenko measured by COSIMA/Rosetta, *Mon Not R Astron Soc*, *469*(Suppl. 2), S712-S722.

Baumann, W., B. Thekedar, H.-R. Paur, and H. Seifert (2006), Characterization of nanoparticles synthesized in the microwave plasma discharge process by particle mass spectrometry and transmission electron microscopy, paper presented at Proceedings of AiChE Fall and Annual Meeting, San Francisco, CA, USA.

Bedidi, A., and B. Cervelle (1993), Light scattering by spherical particles with hematite and goethitelike optical properties: Effect of water impregnation, *J. Geophys. Res.-Solid Earth*, *98*, 11941-11952.

Beer, A. (1852), *Tabulae curvarum quarti ordinis symmetricarum, asymptotis rectis et linea fundamentali recta praeditarum, quas delineavit et expositione illustravit*

Bentley, M. S., et al. (2016), Aggregate dust particles at comet 67P/Churyumov–Gerasimenko, *Nature*, *537*, 73.

Bézard, B. (1997), Long-term response of Jupiter's thermal structure to the SL9 impacts, *Planetary and Space Science*, *45*(10), 1251-1270.

Bhatnagar, A., and W. C. Livingston (2005), *Fundamentals of solar astronomy*, World Scientific, Hackensack, NJ.

Biermann, L. (1951), Kometenschweife Und Solare Korpuskularstrahlung, *Z Astrophys*, *29*(3), 274-286.

Biermann, L., B. Brosowski, and H. U. Schmidt (1967), The interaction of the solar wind with a comet, *Solar Physics*, *1*(2), 254-284.

Bohren, C. F., and D. R. Huffman (1983), *Absorption and scattering of light by small particles*, Wiley, New York; Chichester.

Bones, D., J. M. C. Plane, and W. Feng (2015), *Dissociative Recombination of FeO(+) With Electrons: Implications for Plasma Layers in the Ionosphere*.

Bones, D. L., J. M. C. Plane, and W. Feng (2016), Dissociative Recombination of FeO+ with Electrons: Implications for Plasma Layers in the Ionosphere, *The Journal of Physical Chemistry A*, *120*(9), 1369-1376.

Bönisch, H., A. Engel, T. Birner, P. Hoor, D. W. Tarasick, and E. A. Ray (2011), On the structural changes in the Brewer-Dobson circulation after 2000, *Atmos. Chem. Phys.*, *11*(8), 3937-3948.

Brasseur, G., and S. Solomon (1986), *Aeronomy of the middle atmosphere : chemistry and physics of the stratosphere and mesosphere*, 2nd ed. ed., Reidel, Dordrecht; Lancaster.

Briffa, K. R., T. S. Bartholin, D. Eckstein, P. D. Jones, W. Karlen, F. H. Schweingruber, and P. Zetterberg (1990), A 1,400-Year Tree-Ring Record of Summer Temperatures in Fennoscandia, *Nature*, *346*(6283), 434-439.

Brooke, J. S. A., W. Feng, J. D. Carrillo-Sanchez, G. W. Mann, A. D. James, C. G. Bardeen, and J. M. C. Plane (2017), Meteoric Smoke Deposition in the Polar Regions: A Comparison of Measurements With Global Atmospheric Models, *J Geophys Res-Atmos*, *122*(20), 11112-11130.

Brown, A. P., R. G. C. Moore, and R. Brydson (2001), *Characterisation of iron oxide nanoparticles using EELS*, in Electron microscopy and analysis 2001: proceedings of the Institute of Physics Electron Microscopy and Analysis Group Conference, University of Dundee, 5-7 September 2001, Bristol.

Brown, A. P., S. Hillier, and R. M. D. Brydson (2017), Quantification of Fe-oxidation state in mixed valence minerals: a geochemical application of EELS revisited, *Journal of Physics: Conference Series*, *902*, 012016.

Brown, J. T., and F. D. Schowengerdt (1979), Analysis of a Continuous-Flow Parallel Plate Thermal-Diffusion Cloud Chamber, *J Aerosol Sci*, *10*(3), 339-348.

Brown, P. G., et al. (2013), A 500-kiloton airburst over Chelyabinsk and an enhanced hazard from small impactors, *Nature*, *503*, 238.

Brownlee, D., et al. (2006), Comet 81P/Wild 2 Under a Microscope, *Science*, *314*(5806), 1711.

Bruner, R. (2018), Scientists Have Identified the Actual Worst Year in History. And No, It's Not 2018, edited, https://www.yahoo.com/news/scientists-identified-actual-worst-history-172042812.html?guce_referrer=aHR0cHM6Ly93d3cudGhlZ3VhcmRpYW4uY29tL2NvbW1lnRpc2ZyZWUvMjAxOC9ub3YvMjMvMjAxOC13b3JzdC15ZWFyLWV2ZXItNTM2LXdvcm

xkLXN1bg&guce_referrer_sig=AQAAAA4dlOFcn8S9A2gzv3tsRAFjaB-
V1fnB0GsPC8YSymve6VtrPiMIGQczeRM_5RHEGMQhPlTxOy9HpXX2UtIryRFpml1GnkGl
8ty-e-9oZugH8yKohJYICzJSzfjm1OpY9NU-
Xnu51vRmLJEf68RPAN28ju2BjQg17P_JsQsMUKBy&_guc_consent_skip=1554224939&guc
counter=1, Accessed on 04.04.2019.

Budge, E. A. W. (1932), *Bar-Hebraeus Chronology (transl. Budge, E. A. W.)*, Oxford University Press, London.

Büntgen, U., L. Wacker, K. Nicolussi, M. Sigl, D. Güttler, W. Tegel, P. J. Krusic, and J. Esper (2014), Extraterrestrial confirmation of tree-ring dating, *Nature Climate Change*, *4*, 404.

Burke, D. J., and W. A. Brown (2010), Ice in space: surface science investigations of the thermal desorption of model interstellar ices on dust grain analogue surfaces, *Phys Chem Chem Phys*, *12*(23), 5947-5969.

Burrows, J. P., A. Richter, A. Dehn, B. Deters, S. Himmelmann, S. Voigt, and J. Orphal (1999), Atmospheric remote-sensing reference data from GOME-2. Temperature dependent absorption cross sections of O3 in the 231-794 nm range, *Journal of Quantitative Spectroscopy and Radiative Transfer*, *61*(4), 509-517.

Campbell-Brown, M. D., and D. Koschny (2004), Model of the ablation of faint meteors, *Astron Astrophys*, *418*(2), 751-758.

Carrillo-Sanchez, J. D., J. M. C. Plane, W. Feng, D. Nesvorný, and D. Janches (2015), On the size and velocity distribution of cosmic dust particles entering the atmosphere, *Geophys Res Lett*, *42*(15), 6518-6525.

Carrillo-Sanchez, J. D., D. Nesvorný, P. Pokorný, D. Janches, and J. M. C. Plane (2016), Sources of cosmic dust in the Earth's atmosphere, *Geophys Res Lett*, *43*(23), 11979-11986.

Chabot, J.-B. (1901), *Michael the Syrian Chronicle (Translated into French)*, Paris.

Chambers, J. E. (1999), A hybrid symplectic integrator that permits close encounters between massive bodies, *Mon Not R Astron Soc*, *304*(4), 793-799.

Chambó, J. J. (2016), Comet Catalina Tails, APOD, edited, Accessed on 30.01.16, http://apod.nasa.gov/apod/ap160101.html.

Chapman, C. R., and D. Morrison (1994), Impacts on the Earth by Asteroids and Comets - Assessing the Hazard, *Nature*, *367*(6458), 33-40.

Chou, C., and J. Phillips (1992), Plasma production of metallic nanoparticles, *Journal of Materials Research*, *7*(8), 2107-2113.

Clausen, H. B., C. U. Hammer, C. S. Hvidberg, D. Dahl-Jensen, J. P. Steffensen, J. Kipfstuhl, and M. Legrand (1997), A comparison of the volcanic records over the past 4000 years from the Greenland Ice Core Project and Dye 3 Greenland ice cores, *Journal of Geophysical Research: Oceans*, *102*(C12), 26707-26723.

Collins, R. L., J. Li, and C. M. Martus (2015), First lidar observation of the mesospheric nickel layer, *Geophys Res Lett*, *42*(2), 665-671.

Cooper, C. L., G. e. T. Swindles, I. P. Savov, A. Schmidt, and K. L. Bacon (2018), Evaluating the relationship between climate change and volcanism, *Earth-Science Reviews*, *177*, 238-247.

Cox, R. M., and J. M. C. Plane (1999), An experimental and theoretical study of the reactions $NaO+H_2O(D_2O) \rightarrow NaOH(D)+OH(OD)$, *Phys Chem Chem Phys*, *1*(20), 4713-4720.

Crawford, D. A., M. B. Boslough, T. G. Trucano, and A. C. Robinson (1995), The impact of periodic comet shoemaker-levy 9 on jupiter, *International Journal of Impact Engineering*, *17*(1), 253-262.

Crismani, M. M. J., N. M. Schneider, J. S. Evans, J. M. C. Plane, J. D. Carrillo-Sánchez, S. Jain, J. Deighan, and R. Yelle (2018), The Impact of Comet Siding Spring's Meteors on the Martian Atmosphere and Ionosphere, *Journal of Geophysical Research: Planets*, *123*(10), 2613-2627.

David, B., N. Pizurova, O. Schneeweiss, E. Santavá, V. Kudrle, and O. Jašek (2012), *gamma-Fe2O3 Nanopowders Synthesized in Microwave Plasma and Extraordinarily Strong Temperature Influence on Their Mossbauer Spectra*, 9277-9285 pp.

DeCarlo, P. F., J. G. Slowik, D. R. Worsnop, P. Davidovits, and J. L. Jimenez (2004), Particle morphology and density characterization by combined mobility and aerodynamic diameter measurements. Part 1: Theory, *Aerosol Sci. Tech.*, *38*(12), 1185-1205.

Dewing, H. B. (1916), *Procopius: History of the Wars (transl. Dewing, H. B.)*, Harvard University Press, Cambridge, Massachusetts.

Dhomse, S. S., R. W. Saunders, W. Tian, M. P. Chipperfield, and J. M. C. Plane (2013), Plutonium-238 observations as a test of modeled transport and surface deposition of meteoric smoke particles, *Geophys Res Lett*, *40*(16), 4454-4458.

Draine, B. T. (2003), Interstellar dust grains, *Annu Rev Astron Astr*, *41*, 241-289.

Duft, D., M. Nachbar, and T. Leisner (2019), Unravelling the microphysics of polar mesospheric cloud formation, *Atmos. Chem. Phys.*, *19*(5), 2871-2879.

Duft, D., M. Nachbar, M. Eritt, and T. Leisner (2015), A Linear Trap for Studying the Interaction of Nanoparticles with Supersaturated Vapors, *Aerosol Sci Tech*, *49*(9), 682-690.

Dymond, K. F., K. D. Wolfram, S. A. Budzien, A. C. Nicholas, R. P. McCoy, and R. J. Thomas (2003), Middle ultraviolet emission from ionized iron, *Geophys Res Lett*, *30*(1).

English, J. M., O. B. Toon, and M. J. Mills (2012), Microphysical simulations of sulfur burdens from stratospheric sulfur geoengineering, *Atmos. Chem. Phys.*, *12*(10), 4775-4793.

English, J. M., O. B. Toon, M. J. Mills, and F. Yu (2011), Microphysical simulations of new particle formation in the upper troposphere and lower stratosphere, *Atmos. Chem. Phys.*, *11*(17), 9303-9322.

Engrand, C., et al. (2016), Variations in cometary dust composition from Giotto to Rosetta, clues to their formation mechanisms, *Mon Not R Astron Soc*, *462*(Suppl_1), S323-S330.

ESA (2013), Giotto overview, edited, Accessed on 28.03.2019, https://www.esa.int/Our_Activities/Space_Science/Giotto_overview.

ESA (2014), Kuiper Belt and Oort Cloud in Context, edited, Accessed on 01.11.2015, http://www.esa.int/spaceinimages/Images/2014/12/Kuiper_Belt_and_Oort_Cloud_in_context.

Farias, T. L., Ü. Ö. Köylü, and M. G. Carvalho (1996), Range of validity of the Rayleigh–Debye–Gans theory for optics of fractal aggregates, *Applied Optics*, *35*(33), 6560-6567.

Feng, W., D. R. Marsh, M. P. Chipperfield, D. Janches, J. Hoffner, F. Yi, and J. M. C. Plane (2013), A global atmospheric model of meteoric iron, *J Geophys Res-Atmos*, *118*(16), 9456-9474.

Feng, W., B. Kaifler, D. R. Marsh, J. Höffner, U.-P. Hoppe, B. P. Williams, and J. M. C. Plane (2017), Impacts of a sudden stratospheric warming on the mesospheric metal layers, *J Atmos Sol-Terr Phy*, *162*, 162-171.

Ferris, D. G., J. Cole-Dai, A. R. Reyes, and D. M. Budner (2011), South Pole ice core record of explosive volcanic eruptions in the first and second millennia A.D. and evidence of a large eruption in the tropics around 535 A.D, *116*(D17).

Fontijn, W. F. J., P. J. vanderZaag, M. A. C. Devillers, V. A. M. Brabers, and R. Metselaar (1997), Optical and magneto-optical polar Kerr spectra of $Fe_3O_4$ and $Mg^{2+}$- or $Al^{3+}$-substituted $Fe_3O_4$, *Phys Rev B*, *56*(9), 5432-5442.

Frankland, V. L., A. D. James, W. Feng, and J. M. C. Plane (2015), The uptake of HNO$_3$ on meteoric smoke analogues, *J Atmos Sol-Terr Phy*, *127*, 150-160.

Fulle, M., A. C. Levasseur-Regourd, N. McBride, and E. Hadamcik (2000), In Situ Dust Measurements From within the Coma of 1P/Halley: First-Order Approximation with a Dust Dynamical Model, *The Astronomical Journal*, *119*(4), 1968-1977.

Funke, B., et al. (2011), Composition changes after the "Halloween" solar proton event: the High Energy Particle Precipitation in the Atmosphere (HEPPA) model versus MIPAS data intercomparison study, *Atmos. Chem. Phys.*, *11*(17), 9089-9139.

Gabrielli, P., et al. (2006), A climatic control on the accretion of meteoric and super-chondritic iridium–platinum to the Antarctic ice cap, *Earth and Planetary Science Letters*, *250*(3), 459-469.

Gabrielli, P., et al. (2004), Meteoric smoke fallout over the Holocene epoch revealed by iridium and platinum in Greenland ice, *Nature*, *432*(7020), 1011-1014.

Gainsforth, Z., et al. (2015), Constraints on the formation environment of two chondrule-like igneous particles from comet 81P/Wild 2, *Meteorit Planet Sci*, *50*(5), 976-1004.

Galeev, A. A., et al. (1986), Position and Structure of the Comet Halley Bow Shock - Vega-1 and Vega-2 Measurements, *Geophys Res Lett*, *13*(8), 841-844.

Ganapathy, R., D. E. Brownlee, and P. W. Hodge (1978), Silicate Spherules from Deep-Sea Sediments: Confirmation of Extraterrestrial Origin, *Science*, *201*(4361), 1119.

Geiss, J., and K. Altwegg (1998), Giotto: A unique ESA science mission, *Esa Sp Publ*, *431*, 103-131.

Gerding, M., S. Daly, and J. M. C. Plane (2019), Lidar Soundings of the Mesospheric Nickel Layer Using Ni($^3$F) and Ni($^3$D) Transitions, *Geophys Res Lett*, *46*(1), 408-415.

Gi, N., P. Brown, and M. Aftosmis (2018), The frequency of window damage caused by bolide airbursts: A quarter century case study, *Meteorit Planet Sci*, *53*(7), 1413-1431.

Gibbons, A. (2018), Eruption made 536 'the worst year to be alive', *Science*, *362*(6416), 733.

Giesen, B., H. Wiggers, A. Kowalik, and P. Roth (2005), Formation of Si-nanoparticles in a microwave reactor: Comparison between experiments and modelling, *J Nanopart Res*, *7*(1), 29-41.

Gómez Martín, J. C., S. A. Garraway, and J. M. C. Plane (2016), Reaction Kinetics of Meteoric Sodium Reservoirs in the Upper Atmosphere, *The Journal of Physical Chemistry A*, *120*(9), 1330-1346.

Gómez Martín, J. C., J. S. A. Brooke, W. Feng, M. Hopfner, M. J. Mills, and J. M. C. Plane (2017), Impacts of meteoric sulfur in the Earth's atmosphere, *J Geophys Res-Atmos*, *122*(14), 7678-7701.

Goodhew, P. J., R. Beanland, and F. J. Humphreys (2001), *Electron microscopy and analysis*, 3rd ed. ed., Taylor & Francis, London.

Greenberg, J. M., and A. Li (1998), Evolution of interstellar dust and its relevance to life's origin: laboratory and space experiments, *Uchu Seibutsu Kagaku*, *12*(2).

Hamilton, F. J., and E. W. Brooks (1899), *The Syriac Chronicle known as that of Zachariah of Mitylene*, Methuen and Co., Byzantine Texts, London.

Hammer, C. U. (1984), Traces of icelandic eruptions in the Greenland ice sheet, *Jökull*, *34*, 51-65.

Hammer, C. U., H. B. Clausen, and C. C. Langway (1997), 50,000 years of recorded global volcanism, *Climatic Change*, *35*(1), 1-15.

Hansen, J., R. Ruedy, M. Sato, and K. Lo (2010), Global surface temperature change, *Rev Geophys*, *48*(4).

Haynes, P. (2005), Stratospheric Dynamics, *37*(1), 263-293.

Hedin, A. E. (1987), MSIS-86 Thermospheric Model, *92*(A5), 4649-4662.

Hedin, A. E. (1991), Extension of the MSIS Thermosphere Model into the middle and lower atmosphere, *96*(A2), 1159-1172.

Helama, S., et al. (2018), Volcanic dust veils from sixth century tree-ring isotopes linked to reduced irradiance, primary production and human health, *Scientific Reports*, *8*(1), 1339.

Helmer, M., and J. M. C. Plane (1994), Kinetic study of the reaction between Fe and $O_3$ under mesospheric conditions, *Journal of the Chemical Society, Faraday Transactions*, *90*(1), 31-37.

Henning, T., and H. Mutschke (1997), Low-temperature infrared properties of cosmic dust analogues, *Astron. Astrophys.*, *327*, 743-754.

Hervig, M. E., J. S. A. Brooke, W. Feng, C. G. Bardeen, and J. M. C. Plane (2017), Constraints on Meteoric Smoke Composition and Meteoric Influx Using SOFIE Observations With Models, *J. Geophys. Res.-Atmos.*, *122*(24), 13495-13505.

Hervig, M. E., R. E. Thompson, M. McHugh, L. L. Gordley, J. M. Russell, and M. E. Summers (2001), First confirmation that water ice is the primary component of polar mesospheric clouds, *Geophys Res Lett*, *28*(6), 971-974.

Hervig, M. E., L. L. Gordley, L. E. Deaver, D. E. Siskind, M. H. Stevens, J. M. Russell, S. M. Bailey, L. Megner, and C. G. Bardeen (2009), First Satellite Observations of Meteoric Smoke in the Middle Atmosphere, *Geophys Res Lett*, *36*.

Hildebrand, A. R., D. A. Kring, W. V. Boynton, G. T. Penfield, M. Pilkington, A. Camargo Z., and S. B. Jacobsen (1991), Chicxulub Crater: A possible Cretaceous/Tertiary boundary impact crater on the Yucatán Peninsula, Mexico, *Geology*, *19*(9), 867-871.

Hsieh, H. H., and D. Jewitt (2006), A Population of Comets in the Main Asteroid Belt, *Science*, *312*(5773), 561.

Hsu, W. P., and E. Matijevic (1985), Optical properties of monodispersed hematite hydrosols, *Appl. Opt.*, *24*(11), 1623-1630.

Huffman, D. R., and J. L. Stapp (1973), Optical Measurements on Solids of Possible Interstellar Importance, in *Interstellar Dust and Related Topics*, edited by J. M. Greenberg and H. C. Van De Hulst, pp. 297-301, Springer Netherlands, Dordrecht.

Hunten, D. M. (1967), Spectroscopic studies of twilight airglow, *Space Sci Rev*, *6*(4), 493-&.

Hurrell, J. W., et al. (2013), The Community Earth System Model: A Framework for Collaborative Research, *Bulletin of the American Meteorological Society*, *94*(9), 1339-1360.

Imoto, S., and I. Hasegawa (1958), Historical Records of Meteor Showers in China, Korea, and Japan, *Smithsonian Contribution to Astrophysics*, *2*, 131.

Jacobson, M. Z. (2005), *Fundamentals of Atmospheric Modeling, 2nd edn.*, Cambridge Univ. Press, New York.

Jain, P. K., Y. H. Xiao, R. Walsworth, and A. E. Cohen (2009), Surface Plasmon Resonance Enhanced Magneto-Optics (SuPREMO): Faraday Rotation Enhancement in Gold-Coated Iron Oxide Nanocrystals, *Nano Lett*, *9*(4), 1644-1650.

James, A. D. (2016), Impacts of Meteoric Material on Earth's Atmosphere, University of Leeds.

James, A. D., J. S. A. Brooke, T. P. Mangan, T. F. Whale, J. M. C. Plane, and B. J. Murray (2018), Nucleation of nitric acid hydrates in polar stratospheric clouds by meteoric material, *Atmos. Chem. Phys.*, *18*(7), 4519-4531.

James, A. D., D. R. Moon, W. Feng, P. S. J. Lakey, V. L. Frankland, D. E. Heard, and J. M. C. Plane (2017), The uptake of $HO_2$ on meteoric smoke analogues, *Journal of Geophysical Research: Atmospheres*, *122*(1), 554-565.

Janches, D., L. P. Dyrud, S. L. Broadley, and J. M. C. Plane (2009), First observation of micrometeoroid differential ablation in the atmosphere, *Geophys Res Lett*, *36*.

Janches, D., C. J. Heinselman, J. L. Chau, A. Chandran, and R. Woodman (2006), Modeling the global micrometeor input function in the upper atmosphere observed by high power and large aperture radars, *111*(A7).

Janches, D., N. Swarnalingam, J. D. Carrillo-Sanchez, J. C. Gomez-Martin, R. Marshall, D. Nesvorný, J. M. C. Plane, W. Feng, and P. Pokorný (2017), Radar Detectability Studies of Slow and Small Zodiacal Dust Cloud Particles. III. The Role of Sodium and the Head Echo Size on the Probability of Detection, *The Astrophysical Journal*, *843*(1), 1.

Janzen, C., H. Kleinwechter, J. Knipping, H. Wiggers, and P. Roth (2002), Size analysis in low-pressure nanoparticle reactors: comparison of particle mass spectrometry with in situ probing transmission electron microscopy, *J Aerosol Sci*, *33*(6), 833-841.

Jessberger, E. K., A. Christoforidis, and J. Kissel (1988), Aspects of the major element composition of Halley dust, *Nature*, *332*(6166), 691-695.

Johnson, K. S. (2001), Iron supply and demand in the upper ocean: Is extraterrestrial dust a significant source of bioavailable iron?, *15*(1), 61-63.

Jones, G. H., M. M. Knight, A. Fitzsimmons, and M. G. G. T. Taylor (2017), Cometary science after Rosetta, *Philosophical transactions. Series A, Mathematical, physical, and engineering sciences*, *375*(2097), 20170001.

Jones, W. (1997), Theoretical and observational determinations of the ionization coefficient of meteors, *Mon Not R Astron Soc*, *288*(4), 995-1003.

Jucks, K. W., D. G. Johnson, K. V. Chance, W. A. Traub, and R. J. Salawitch (1999), Nitric acid in the middle stratosphere as a function of altitude and aerosol loading, *104*(D21), 26715-26723.

Junge, C. E., and J. E. Manson (1961), Stratospheric aerosol studies, *Journal of Geophysical Research*, *66*(7), 2163-2182.

Junge, C. E., C. W. Chagnon, and J. E. Manson (1961), Stratospheric Aerosols, *J Meteorol*, *18*(1), 81-108.

Kalashnikova, O., M. Horanyi, G. E. Thomas, and O. B. Toon (2000), Meteoric smoke production in the atmosphere, *Geophys Res Lett*, *27*(20), 3293-3296.

Keller, H. U., R. Kramm, and N. Thomas (1988), Surface-features on the nucleus of Comet Halley, *Nature*, *331*(6153), 227-231.

Keller, H. U., D. Britt, B. J. Buratti, and N. Thomas (2004), *In Situ Observations of Cometary Nuclei*, 211-222 pp., University of Arizona Press, Tuscon

Keller, H. U., et al. (1986), 1st Multicolor camera imaging results from Giotto *Nature*, *321*(6067), 320-326.

Kinnison, D. E., R. Wang, J. Anderson, and R. A. Fuller (2018), Evaluation of CESM1 (WACCM) free-running and specified-dynamics atmospheric composition simulations using global multi-species satellite data records, *Atmos. Chem. Phys. Discuss.*, *2018*.

Kinnison, D. E., et al. (2007), Sensitivity of chemical tracers to meteorological parameters in the MOZART-3 chemical transport model, *J Geophys Res-Atmos*, *112*(D20).

Kinsman, J. H., and D. Asher (2017), *Evidence of Eta Aquariid Outbursts Recorded in the Classic Maya Hieroglyphic Script Using Orbital Integrations*.

Kissel, J., et al. (1986a), Composition of comet Halley dust particles from Giotto observations *Nature*, *321*(6067), 336-337.

Kissel, J., et al. (1986b), Composition of comet Halley dust particles from Vega observations, *Nature*, *321*(6067), 280-282.

Kopp, E. (1997), On the abundance of metal ions in the lower ionosphere, *Journal of Geophysical Research: Space Physics*, *102*(A5), 9667-9674.

Kronk, G. W. (1984), *Comets: a descriptive catalog*, Enslow Publishers, Hillside, N.J.

Kyte, F. T. (2002), Tracers of the extraterrestrial component in sediments and inferences for Earth's accretion history, in *Catastrophic events and mass extinctions: impacts and beyond*, edited by C. Koeberl and K. G. MacLeod, p. 0, Geological Society of America.

Lamarque, J. F., et al. (2012), CAM-chem: description and evaluation of interactive atmospheric chemistry in the Community Earth System Model, *Geosci Model Dev*, *5*(2), 369-411.

Lambert, J. H. (1760), *Photometria, sive de mensura et gradibus luminis, colorum et umbræ*.

Lancelot, C., A. de Montety, H. Goosse, S. Becquevort, V. Schoemann, B. Pasquer, and M. Vancoppenolle (2009), Spatial distribution of the iron supply to phytoplankton in the Southern Ocean: a model study, *Biogeosciences*, *6*(12), 2861-2878.

Lanci, L., and D. V. Kent (2006), Meteoric smoke fallout revealed by superparamagnetism in Greenland ice, *33*(13).

Lanci, L., D. V. Kent, and P. E. Biscaye (2007), Meteoric smoke concentration in the Vostok ice core estimated from superparamagnetic relaxation and some consequences for estimates of Earth accretion rate, *Geophys Res Lett*, *34*(10).

Lanci, L., B. Delmonte, D. V. Kent, V. Maggi, P. E. Biscaye, and J. R. Petit (2012), Magnetization of polar ice: a measurement of terrestrial dust and extraterrestrial fallout, *Quaternary Science Reviews*, *33*, 20-31.

Langevin, Y., M. Hilchenbach, N. Ligier, S. Merouane, K. Hornung, C. Engrand, R. Schulz, J. Kissel, J. Rynö, and P. Eng (2016), Typology of dust particles collected by the COSIMA mass spectrometer in the inner coma of 67P/Churyumov Gerasimenko, *Icarus*, *271*, 76-97.

Langowski, M. P., C. von Savigny, J. P. Burrows, W. Feng, J. M. C. Plane, D. R. Marsh, D. Janches, M. Sinnhuber, A. C. Aikin, and P. Liebing (2015), Global investigation of the Mg atom and ion layers using SCIAMACHY/Envisat observations between 70 and 150 km altitude and WACCM-Mg model results, *Atmos. Chem. Phys.*, *15*(1), 273-295.

Larsen, L. B., et al. (2008), New ice core evidence for a volcanic cause of the AD 536 dust veil, *Geophys Res Lett*, *35*(4).

Levasseur-Regourd, A.-C., et al. (2018), Cometary Dust, *Space Sci Rev*, *214*(3), 64.

Lisse, C. M. (2015), Comet Siding Spring, up close and personal, *Science*, *350*(6258), 277-278.

Liu, H. L., et al. (2010), Thermosphere extension of the Whole Atmosphere Community Climate Model, *J Geophys Res-Space*, *115*.

Liu, Y., and P. H. Daum (2008), Relationship of refractive index to mass density and self-consistency of mixing rules for multicomponent mixtures like ambient aerosols, *J Aerosol Sci*, *39*(11), 974-986.

Longtin, D. R., E. P. Shettle, J. r. Hummel, and , and J. D. Pryce (1988), *A Wind Dependent Desert Aerosol Model: Refractive Properties*, 115 pp., Air Force Syst. Command, Air Force Geophys. Lab., Hanscom Air Force Base, USA.

Loveluck, C. P., et al. (2018), Alpine ice-core evidence for the transformation of the European monetary system, AD 640–670, *Antiquity*, *92*(366), 1571-1585.

Majima, T., G. Santambrogio, C. Bartels, A. Terasaki, T. Kondow, J. Meinen, and T. Leisner (2012), Spatial distribution of ions in a linear octopole radio-frequency ion trap in the space-charge limit, *Physical Review A*, *85*(5), 053414.

Manca, F., P. Sicoli, and A. Testa (2016), Close encounters among asteroids, comets, Earth-Moon system and inner planets: the cases of (99942) Apophis and Comet C/2013 A1, *Mem. Soc. Ast. Ital.*, *87*(72).

Marsh, D. R., D. Janches, W. Feng, and J. M. C. Plane (2013a), A global model of meteoric sodium, *J Geophys Res-Atmos*, *118*(19), 11442-11452.

Marsh, D. R., M. J. Mills, D. E. Kinnison, J. F. Lamarque, N. Calvo, and L. M. Polvani (2013b), Climate Change from 1850 to 2005 Simulated in CESM1(WACCM), *J Climate*, *26*(19), 7372-7391.

Marsh, D. R., R. R. Garcia, D. E. Kinnison, B. A. Boville, F. Sassi, S. C. Solomon, and K. Matthes (2007), Modeling the whole atmosphere response to solar cycle changes in radiative and geomagnetic forcing, *J Geophys Res-Atmos*, *112*(D23).

McDonnell, J. A., et al. (1987), The dust distribution within the inner coma of comet P/Halley 1982i: encounter by Giotto's impact detectors, *Astron Astrophys*, *187*(1-2), 719-741.

McGrath, M., R. V. Yelle, and Y. Betremieux (1996), *Long-term Chemical Evolution of the Jupiter Stratosphere Following the SL9 Impacts*, American Astronomical Society, DPS meeting #28, id.22.41; Bulletin of the American Astronomical Society, Vol. 28, p.1149.

Megner, L. (2008), Meteoric Aerosols in the Middle Atmosphere, 32 pp, Stockholm University, Stockholm.

Meinen, J., S. Khasminskaya, E. Ruhl, W. Baumann, and T. Leisner (2010a), The TRAPS Apparatus: Enhancing Target Density of Nanoparticle Beams in Vacuum for X-ray and Optical Spectroscopy, *Aerosol Sci Tech*, *44*(4), 316-328.

Meinen, J., S. Khasminskaya, M. Eritt, T. Leisner, E. Antonsson, B. Langer, and E. Ruhl (2010b), Core level photoionization on free sub-10-nm nanoparticles using synchrotron radiation, *Rev Sci Instrum*, *81*(8).

Millán, L., S. Wang, N. Livesey, D. Kinnison, H. Sagawa, and Y. Kasai (2015), Stratospheric and mesospheric HO$_2$ observations from the Aura Microwave Limb Sounder, *Atmos. Chem. Phys.*, *15*(5), 2889-2902.

Mills, M. J., O. B. Toon, J. Lee-Taylor, and A. Robock (2014), Multidecadal global cooling and unprecedented ozone loss following a regional nuclear conflict, *Earth's Future*, *2*(4), 161-176.

Mills, M. J., O. B. Toon, V. Vaida, P. E. Hintze, H. G. Kjaergaard, D. P. Schofield, and T. W. Robinson (2005), Photolysis of sulfuric acid vapor by visible light as a source of the polar stratospheric CN layer, *J Geophys Res-Atmos*, *110*(D8).

Mills, M. J., et al. (2016), Global volcanic aerosol properties derived from emissions, 1990-2014, using CESM1(WACCM), *J Geophys Res-Atmos*, *121*(5), 2332-2348.

Minor-Planet-Center, I. (2019), Closest Approaches to the Earth by Comets, edited, accessed on 30.01.2019, https://minorplanetcenter.net//iau/lists/ClosestComets.html.

Moorhead, A. V., P. A. Wiegert, and W. J. Cooke (2014), The meteoroid fluence at Mars due to Comet C/2013 A1 (Siding Spring), *Icarus*, *231*, 13-21.

Morbidelli, A. (2005), Origin and dynamical evolution of comets and their reservoirs, *Astrophysics*.

Morice, C. P., J. J. Kennedy, N. A. Rayner, and P. D. Jones (2012), Quantifying uncertainties in global and regional temperature change using an ensemble of observational estimates: The HadCRUT4 data set, *Journal of Geophysical Research: Atmospheres*, *117*(D8).

Murphy, D. M., D. J. Cziczo, P. K. Hudson, and D. S. Thomson (2007), Carbonaceous material in aerosol particles in the lower stratosphere and tropopause region, *J Geophys Res-Atmos*, *112*(D4).

Murray, B. J., and J. M. C. Plane (2005), Uptake of Fe, Na and K atoms on low-temperature ice: implications for metal atom scavenging in the vicinity of polar mesospheric clouds, *Phys Chem Chem Phys*, *7*(23), 3970-3979.

Murray, B. J., and E. J. Jensen (2010), Homogeneous nucleation of amorphous solid water particles in the upper mesosphere, *J Atmos Sol-Terr Phy*, *72*(1), 51-61.

Myhre, G., et al. (2013), *Anthropogenic and Natural Radiative Forcing, Climate Change 2013: The Physical Science Basis. Contribution of Working Group I to the Fifth Assessment Report of the Intergovernmental Panel on Climate Change*, Cambridge University Press, Cambridge, United Kingdom and New York, NY, USA.

Nachbar, M. (2018), The microphysics of mesospheric cloud formation on Earth and Mars - Laboratory experiments, University of Heidelberg, Germany.

Nachbar, M., D. Duft, and T. Leisner (2018a), Volatility of Amorphous Solid Water, *The Journal of Physical Chemistry B*, *122*(43), 10044-10050.

Nachbar, M., D. Duft, A. Kiselev, and T. Leisner (2018b), Composition, Mixing State and Water Affinity of Meteoric Smoke Analogue Nanoparticles Produced in a Non-Thermal Microwave Plasma Source, *Zeitschrift für Physikalische Chemie*, *232*, 635-648.

Nachbar, M., D. Duft, T. P. Mangan, J. C. G. Martin, J. M. C. Plane, and T. Leisner (2016), Laboratory measurements of heterogeneous $CO_2$ ice nucleation on nanoparticles under conditions relevant to the Martian mesosphere, *J Geophys Res-Planet*, *121*(5), 753-769.

Nachbar, M., H. Wilms, D. Duft, T. Aylett, K. Kitajima, T. Majima, J. M. C. Plane, M. Rapp, and T. Leisner (2019), The impact of solar radiation on polar mesospheric ice particle formation, *Atmos. Chem. Phys.* , *19*, 4311-4322.

Nadeem, K., H. Krenn, T. Traussnig, R. Würschum, D. V. Szabó, and I. Letofsky-Papst (2012), Spin-glass freezing of maghemite nanoparticles prepared by microwave plasma synthesis, *Journal of Applied Physics*, *111*(11), 113911.

Napier, W. M. (2010), Palaeolithic extinctions and the Taurid Complex, *Mon Not R Astron Soc*, *405*(3), 1901-1906.

Napier, W. M. (2015), Giant comets and mass extinctions of life, *Mon Not R Astron Soc*, *448*(1), 27-36.

Napier, W. M., and D. Asher (2009), The Tunguska impact event and beyond, *Astron Geophys*, *50*(1), 1.18-11.26.

Navrotsky, A., L. Mazeina, and J. Majzlan (2008), Size-driven structural and thermodynamic complexity in iron oxides, *Science*, *319*(5870), 1635-1638.

Neale, R. B., J. Richter, S. Park, P. H. Lauritzen, S. J. Vavrus, P. J. Rasch, and M. H. Zhang (2013), The Mean Climate of the Community Atmosphere Model (CAM4) in Forced SST and Fully Coupled Experiments, *J Climate*, *26*(14), 5150-5168.

Neale, R. B., et al. (2010), Description of the NCAR Community Atmosphere Model (CAM 5.0), NCAR Technical note.

Neely, R. R., J. M. English, O. B. Toon, S. Solomon, M. Mills, and J. P. Thayer (2011), Implications of extinction due to meteoritic smoke in the upper stratosphere, *Geophys Res Lett*, *38*.

Nesvorný, D., and F. Roig (2017), Dynamical Origin and Terrestrial Impact Flux of Large Near-Earth Asteroids, *The Astronomical Journal*, *155*(1), 42.

Nesvorný, D., P. Jenniskens, H. F. Levison, W. F. Bottke, D. Vokrouhlický, and M. Gounelle (2010), Cometary origin of the zodiacal cloud and carbonaceous micrometeorites. Implications for hot debris disks, *The Astrophysical Journal*, *713*(2), 816–836.

Nesvorný, D., D. Janches, D. Vokrouhlický, P. Pokorný, W. F. Bottke, and P. Jenniskens (2011), Dynamical Model for the Zodiacal Cloud and Sporadic Meteors, *The Astrophysical Journal*, *743*.

Neukum, G., B. A. Ivanov, and W. K. J. S. S. R. Hartmann (2001), Cratering Records in the Inner Solar System in Relation to the Lunar Reference System, *96*(1), 55-86.

Pavlov, A. A., O. B. Toon, A. K. Pavlov, J. Bally, and D. Pollard (2005), Passing through a giant molecular cloud: "Snowball" glaciations produced by interstellar dust, *Geophys Res Lett*, *32*(3).

Peter, T. (1997), Microphysics and heterogeneous chemistry of polar stratospheric clouds, *Annu Rev Phys Chem*, *48*, 785-822.

Peter, T., and J.-U. Grooβ (2012), Polar Stratospheric Clouds and Sulfate Aerosol Particles: Microphysics, Denitrification and Heterogeneous Chemistry, in *Stratospheric ozone depletion and climate change*, edited by R. Müller, pp. 108-144, RSC Publishing, Cambridge.

Plane, J. M. C. (2003), Atmospheric chemistry of meteoric metals, *Chem Rev*, *103*(12), 4963-4984.

Plane, J. M. C. (2012), Cosmic dust in the earth's atmosphere, *Chem Soc Rev*, *41*(19), 6507-6518.

Plane, J. M. C., and C. L. Whalley (2012), A New Model for Magnesium Chemistry in the Upper Atmosphere, *The Journal of Physical Chemistry A*, *116*(24), 6240-6252.

Plane, J. M. C., W. Feng, and E. C. M. Dawkins (2015), The Mesosphere and Metals: Chemistry and Changes, *Chem Rev*, *115*(10), 4497-4541.

Plane, J. M. C., B. J. Murray, X. Z. Chu, and C. S. Gardner (2004), Removal of meteoric iron on polar mesospheric clouds, *Science*, *304*(5669), 426-428.

Plane, J. M. C., J. C. Gómez-Martín, W. Feng, and D. Janches (2016), Silicon chemistry in the mesosphere and lower thermosphere, *Journal of Geophysical Research: Atmospheres*, *121*(7), 3718-3728.

Plane, J. M. C., H. Oetjen, M. de Miranda, A. Saiz-Lopez, M. Gausa, and B. Williams (2012), On the sodium D line emission in the terrestrial nightglow, *J Atmos Sol-Terr Phy*, *74*, 181-188.

Plane, J. M. C., et al. (2014), A combined rocket-borne and ground-based study of the sodium layer and charged dust in the upper mesosphere, *J Atmos Sol-Terr Phy*, *118*, 151-160.

Pokorný, P., D. Vokrouhlický, D. Nesvorný, M. Campbell-Brown, and P. Brown (2014), Dynamical model for the toroidal sporadic meteors, *The Astrophysical Journal*, *789*(25), 1-20.

Prasad, M. S., N. G. Rudraswami, and D. K. Panda (2013), Micrometeorite flux on Earth during the last ~50,000 years, *118*(11), 2381-2399.

Prather, M. J., and J. M. Rodriguez (1988), Antarctic Ozone - Meteoric Control of Hno3, *Geophys Res Lett*, *15*(1), 1-4.

Pruppacher, H. D., and J. D. Klett (2010), *Microphysics of Clouds and Precipitation*, 2 ed., XXII, 954 pp., Springer Netherlands.

Querry, M. R. (1985), *Optical Constants, Contractor report*, 415 pp., US Army Chemical Research, Development and Engineering Center (CRDC), Aberdeen Proving Ground, MD, USA.

Rampino, M. R., S. Self, and R. B. Stothers (1988), Volcanic Winters, *Annu Rev Earth Pl Sc*, *16*, 73-99.

Rapp, M., J. M. C. Plane, B. Strelnikov, G. Stober, S. Ernst, J. Hedin, M. Friedrich, and U. P. Hoppe (2012), In situ observations of meteor smoke particles (MSP) during the Geminids 2010: constraints on MSP size, work function and composition, *Ann Geophys-Germany*, *30*(12), 1661-1673.

Rapp, M., et al. (2011), Microphysical Properties of Mesospheric Aerosols: An Overview of In Situ-Results from the ECOMA Project, in *Aeronomy of the Earth's Atmosphere and Ionosphere*, edited by M. A. Abdu and D. Pancheva, pp. 67-74.

Rapp, M., et al. (2010), Rocket-borne in situ measurements of meteor smoke: Charging properties and implications for seasonal variation, *J. Geophys. Res.-Atmos.*, *115*, art. no.: D00I16.

Rees, M. H. (1989), *Physics and chemistry of the upper atmosphere*, Cambridge University Press.

Rigby, E., M. Symonds, and D. Ward-Thompson (2004), A comet impact in AD 536?, *Astron Geophys*, *45*(1), 23-26.

Roble, R. G. (1995), Energetics of the Mesosphere and Thermosphere, in *The Upper Mesosphere and Lower Thermosphere: A Review of Experiment and Theory*, edited by R. M. Johnson and T. L. Killeen.

Robock, A., L. Oman, G. L. Stenchikov, O. B. Toon, C. Bardeen, and R. P. Turco (2007), Climatic consequences of regional nuclear conflicts, *Atmos. Chem. Phys.*, *7*(8), 2003-2012.

Rollason, R. J., and J. M. C. Plane (1998), A study of the reactions of $Fe^+$ with $O_3$, $O_2$ and $N_2$, *Journal of the Chemical Society, Faraday Transactions*, *94*(20), 3067-3075.

Rotundi, A., et al. (2015), Dust measurements in the coma of comet 67P/Churyumov-Gerasimenko inbound to the Sun, *Science*, *347*(6220), aaa3905.

Rowan-Robinson, M., and B. May (2013), An improved model for the infrared emission from the zodiacal dust cloud: cometary, asteroidal and interstellar dust, *Mon Not R Astron Soc*, *429*(4), 2894-2902.

Saunders, R. W., and J. M. C. Plane (2006), A laboratory study of meteor smoke analogues: Composition, optical properties and growth kinetics, *J Atmos Sol-Terr Phy*, *68*(18), 2182-2202.

Saunders, R. W., and J. M. C. Plane (2010), The formation and growth of $Fe_2O_3$ nanoparticles from the photo-oxidation of iron pentacarbonyl, *J Aerosol Sci*, *41*(5), 475-489.

Saunders, R. W., and J. M. C. Plane (2011), A photo-chemical method for the production of olivine nanoparticles as cosmic dust analogues, *Icarus*, *212*(1), 373-382.

Saunders, R. W., P. M. Forster, and J. M. C. Plane (2007), Potential climatic effects of meteoric smoke in the Earth's paleo-atmosphere, *34*(16).

Saunders, R. W., S. Dhomse, W. S. Tian, M. P. Chipperfield, and J. M. C. Plane (2012), Interactions of meteoric smoke particles with sulphuric acid in the Earth's stratosphere, *Atmos Chem Phys*, *12*(10), 4387-4398.

Schneider, N. M., et al. (2015), MAVEN IUVS observations of the aftermath of the Comet Siding Spring meteor shower on Mars, *Geophys Res Lett*, *42*(12), 4755-4761.

Scuderi, L. A. (1993), A 2000-Year Tree-Ring Record of Annual Temperatures in the Sierra-Nevada Mountains, *Science*, *259*(5100), 1433-1436.

Self, D. E., and J. M. C. Plane (2003), A kinetic study of the reactions of iron oxides and hydroxides relevant to the chemistry of iron in the upper mesosphere, *Phys Chem Chem Phys*, *5*(7), 1407-1418.

Self, S., M. R. Rampino, and J. J. Barbera (1981), The Possible Effects of Large 19th-Century and 20th-Century Volcanic-Eruptions on Zonal and Hemispheric Surface Temperatures, *J Volcanol Geoth Res*, *11*(1), 41-60.

Shuman, N. S., D. E. Hunton, and A. A. Viggiano (2015), Ambient and Modified Atmospheric Ion Chemistry: From Top to Bottom, *Chem Rev*, *115*(10), 4542-4570.

Sigl, M., et al. (2015), Timing and climate forcing of volcanic eruptions for the past 2,500 years, *Nature*, *523*, 543.

Smetacek, V., et al. (2012), Deep carbon export from a Southern Ocean iron-fertilized diatom bloom, *Nature*, *487*, 313.

Smith, A. K. (2012), Global Dynamics of the MLT, *Surveys in Geophysics*, *33*(6), 1177-1230.

Soderblom, L. A., et al. (2002), Observations of comet 19P/Borrelly by the Miniature Integrated Camera and Spectrometer Aboard Deep Space 1, *Science*, *296*(5570), 1087-1091.

Solomon, S. (1999), Stratospheric ozone depletion: A review of concepts and history, *Rev Geophys*, *37*(3), 275-316.

Sorensen, C. M. (2001), Light Scattering by Fractal Aggregates: A Review, *Aerosol Sci Tech*, *35*(2), 648-687.

Stothers, R. B. (1984), Mystery Cloud of Ad-536, *Nature*, *307*(5949), 344-345.

Stothers, R. B., and M. R. Rampino (1983), Volcanic-Eruptions in the Mediterranean before Ad 630 from Written and Archaeological Sources, *Journal of Geophysical Research*, *88*(Nb8), 6357-6371.

Swingedouw, D., J. Mignot, P. Ortega, M. Khodri, M. Menegoz, C. Cassou, and V. Hanquiez (2017), Impact of explosive volcanic eruptions on the main climate variability modes, *Global and Planetary Change*, *150*, 24-45.

Tang, J., M. Myers, K. A. Bosnick, and L. E. Brus (2003), Magnetite $Fe_3O_4$ nanocrystals: Spectroscopic observation of aqueous oxidation kinetics, *J Phys Chem B*, *107*(30), 7501-7506.

Taylor, S., J. H. Lever, and R. P. Harvey (1998), Accretion rate of cosmic spherules measured at the South Pole, *Nature*, *392*(6679), 899-903.

Taylor, S., J. H. Lever, and R. P. Harvey (2000), Numbers, types, and compositions of an unbiased collection of cosmic spherules, *Meteorit Planet Sci*, *35*(4), 651-666.

Thomas, G. E., and J. Olivero (2001), Noctilucent clouds as possible indicators of global change in the mesosphere, *Advances in Space Research*, *28*(7), 937-946.

Toohey, M., K. Krüger, M. Sigl, F. Stordal, and H. Svensen (2016), Climatic and societal impacts of a volcanic double event at the dawn of the Middle Ages, *Climatic Change*, *136*(3), 401-412.

Toon, O. B., R. P. Turco, D. Westphal, R. Malone, and M. S. Liu (1988), A Multidimensional Model for Aerosols - Description of Computational Analogs, *J Atmos Sci*, *45*(15), 2123-2143.

Toon, O. B., K. Zahnle, D. Morrison, R. P. Turco, and C. Covey (1997), Environmental perturbations caused by the impacts of asteroids and comets, *35*(1), 41-78.

Tricarico, P., N. H. Samarasinha, M. V. Sykes, J. Y. Li, T. L. Farnham, M. S. P. Kelley, D. Farnocchia, R. Stevenson, J. M. Bauer, and R. E. Lock (2014), Delivery of Dust Grains from Comet C/2013 A1 (Siding Spring) to Mars, *Astrophys J Lett*, *787*(2).

Turco, R. P., O. B. Toon, C. Park, R. C. Whitten, J. B. Pollack, and P. Noerdlinger (1981), Tunguska Meteor Fall of 1908: Effects on Stratospheric Ozone, *Science*, *214*(4516), 19.

Vaubaillon, J., L. Maquet, and R. Soja (2014), Meteor hurricane at Mars on 2014 October 19 from comet C/2013 A1, *Mon Not R Astron Soc*, *439*(4), 3294-3299.

Veverka, J., et al. (2013), Return to Comet Tempel 1: Overview of Stardust-NExT results, *Icarus*, *222*(2), 424-435.

Viehl, T. P., J. M. C. Plane, W. Feng, and J. Hoffner (2016), The photolysis of FeOH and its effect on the bottomside of the mesospheric Fe layer, *Geophys Res Lett*, *43*(3), 1373-1381.

Vincent, R. A. (2015), The dynamics of the mesosphere and lower thermosphere: a brief review, *Progress in Earth and Planetary Science*, *2*(1), 4.

Vondrak, T., J. M. C. Plane, S. Broadley, and D. Janches (2008), A chemical model of meteoric ablation, *Atmos Chem Phys*, *8*(23), 7015-7031.

Wachsmuth, C. E. (1897), *On Portents 9c, translated from Teubner, Leipzig, 1863*.

Weast, R. C., M. J. Astle, and W. H. Beyer (1984), *CRC handbook of chemistry and physics*, 69th ed. / editor-in-chief Robert C. Weast / associate editors Melvin J. Astle, William H. Beyer. ed., CRC Press, Boca Raton, Florida.

Wegner, T., J. U. Grooß, M. von Hobe, F. Stroh, O. Sumińska-Ebersoldt, C. M. Volk, E. Hösen, V. Mitev, G. Shur, and R. Müller (2012), Heterogeneous chlorine activation on stratospheric aerosols and clouds in the Arctic polar vortex, *Atmos. Chem. Phys.*, *12*(22), 11095-11106.

Weigel, R., C. M. Volk, K. Kandler, E. Hösen, G. Günther, B. Vogel, J. U. Grooß, S. Khaykin, G. V. Belyaev, and S. Borrmann (2014), Enhancements of the refractory submicron aerosol fraction in the Arctic polar vortex: feature or exception?, *Atmos. Chem. Phys.*, *14*(22), 12319-12342.

Whalley, C. L., J. C. G. Martín, T. G. Wright, and J. M. C. Plane (2011), A kinetic study of $Mg^+$ and Mg-containing ions reacting with $O_3$, $O_2$, $N_2$, $CO_2$, $N_2O$ and $H_2O$: implications for magnesium ion chemistry in the upper atmosphere, *Phys Chem Chem Phys*, *13*(13), 6352-6364.

Whipple, F. L. (1940), Photographic Meteor Studies. III. The Taurid Shower, *Proceedings of the American Philosophical Society*, *83*(5), 711-745.

Whipple, F. L. (1950), A comet model 1. the acceleration of comet Encke *Astrophysical Journal*, *111*(2), 375-394.

Whipple, F. L. (1951), A comet model 2. physical relations for comets and meteors *Astrophysical Journal*, *113*(3), 464-474.

Whipple, F. L. (1954), Photographic meteor orbits and their distribution in space, *Astronomical Journal*, *59*(6), 201-217.

Williams, D. A., and E. Herbst (2002), It's a dusty Universe: surface science in space, *Surf Sci*, *500*(1-3), 823-837.

Williams, D. A., W. A. Brown, S. D. Price, J. M. C. Rawlings, and S. Viti (2007), Molecules, ices and astronomy, *Astron Geophys*, *48*(1), 25-34.

Williams, K. (2018), You think 2018 is the worst year ever? Try the real dark age: 536, in *The Guardian*, edited, https://www.theguardian.com/commentisfree/2018/nov/23/2018-worst-year-ever-536-world-sun#comments, Accessed on 04.04.2019.

Wolbach, W. S., et al. (2018), Extraordinary Biomass-Burning Episode and Impact Winter Triggered by the Younger Dryas Cosmic Impact ~12,800 Years Ago. 1. Ice Cores and Glaciers, *The Journal of Geology*, *126*(2), 165-184.

Woodcock, K. R. S., T. Vondrak, S. R. Meech, and J. M. C. Plane (2006), A kinetic study of the reactions $FeO^+ + O$, $Fe^+ \cdot N_2 + O$, $Fe^+ \cdot O_2 + O$ and $FeO^+ + CO$: implications for sporadic E layers in the upper atmosphere, *Phys Chem Chem Phys*, *8*(15), 1812-1821.

Yang, H. G., and M. Ishiguro (2015), Origin of Interplanetary Dust through Optical Properties of Zodiacal Light, *The Astrophysical Journal*, *813*(2), 9.

Ye, Q. Z., and M. T. Hui (2014), An Early Look of Comet C/2013 A1 (Siding Spring): Breathtaker or Nightmare?, *Astrophysical Journal*, *787*(2).

Yumoto, K., T. Saito, and T. Nakagawa (1986), Hydromagnetic waves near $O^+$ (or $H_2O^+$) ion cyclotron frequency observed by Sakigake at the closest approach to comet Halley, *Geophys Res Lett*, *13*(8), 825-828.

Zhang, L., and J. R. Brook (2001), The effect of subgrid velocity scale on site-specific/subgrid area and grid-averaged dry deposition velocities, *Atmospheric Environment*, *35*(22), 3841-3850.

Zielinski, G. A., P. A. Mayewski, L. D. Meeker, S. Whitlow, M. S. Twickler, M. Morrison, D. A. Meese, A. J. Gow, and R. B. Alley (1994), Record of Volcanism since 7000-Bc from the Gisp2 Greenland Ice Core and Implications for the Volcano-Climate System, *Science*, *264*(5161), 948-952.